HAL
open science

Vers la conception des matériaux amortissants : une apporche micromécanique

Michaël Haberman

To cite this version:

Michaël Haberman. Vers la conception des matériaux amortissants : une apporche micromécanique. Autre. Université Paul Verlaine - Metz, 2006. Français. NNT : 2006METZ023S . tel-01752465

HAL Id: tel-01752465

https://hal.univ-lorraine.fr/tel-01752465v1

Submitted on 29 Mar 2018

HAL is a multi-disciplinary open access archive for the deposit and dissemination of scientific research documents, whether they are published or not. The documents may come from teaching and research institutions in France or abroad, or from public or private research centers.

L'archive ouverte pluridisciplinaire **HAL**, est destinée au dépôt et à la diffusion de documents scientifiques de niveau recherche, publiés ou non, émanant des établissements d'enseignement et de recherche français ou étrangers, des laboratoires publics ou privés.

UNIVERSITÉ DE LORRAINE

AVERTISSEMENT

Ce document est le fruit d'un long travail approuvé par le jury de soutenance et mis à disposition de l'ensemble de la communauté universitaire élargie.

Il est soumis à la propriété intellectuelle de l'auteur. Ceci implique une obligation de citation et de référencement lors de l'utilisation de ce document.

D'autre part, toute contrefaçon, plagiat, reproduction illicite encourt une poursuite pénale.

Contact : ddoc-theses-contact@univ-lorraine.fr

LIENS

Code de la Propriété Intellectuelle. articles L 122. 4
Code de la Propriété Intellectuelle. articles L 335.2- L 335.10
http://www.cfcopies.com/V2/leg/leg_droi.php
http://www.culture.gouv.fr/culture/infos-pratiques/droits/protection.htm

LABORATOIRE DE PHYSIQUE ET MECANIQUE DES MATERIAUX

Georgia Institute of Technology

THESE

Présenté à

Paul Verlaine Université - Metz

par

Michael R. HABERMAN

Pour l'obtention du grade de :

DOCTEUR DE L'UNIVERSITE PAUL VERLAINE - METZ

Specialité : Physique et Science pour l'ingénieur
Option : Mécanique

Vers la conception des matériaux amortissants : Une approche micromécanique

À soutenir le 14 Avril 2006 devant le jury composé de :

Professeur M.CHERKAOUI (Directeur de thèse), Georgia Tech/LPMM
Professeur E. M. DAYA (co-Directeur de thèse), LPMM
Professeur S. AHZI (Rapporteur), IMFS Strasbourg
Professeur B. HOSTEN (Rapporteur), LMP Bordeaux, Directeur de recherche CNRS
Professeur Y. BERTHELOT (Examinateur), Georgia Institute of Technology
Dr. M. KHALEEL (Examinateur), Laboratory Fellow and Division Director at PNNL

VERS LA CONCEPTION DES MATERIAUX AMORTISSANTS:

2006 068 S

UNE APPROCHE MICROMECANIQUE

S/Mz 06/23
mg. l'étage

Approuvé:

Dr. Mohammed CHERKAOUI, Directeur
Professeur des Universités
Laboratoire de Physique et Mécanique des Matériaux
Université de Paul Verlaine - Metz
&
Department of Mechanical Engineering
Georgia Institute of Technology

Dr. El Mostafa DAYA, Co-Directeur
Professeur des Universités
Laboratoire de Physique et Mécanique des Matériaux
Université de Paul Verlaine - Metz

Dr. Bernard HOSTEN
Directeur de Recherche CNRS
Directeur Adjoint LMP
Laboratoire de Mécanique Physique
Université de Bordeaux I

Dr. Saïd AHZI
Professeur des Universités
Institute de Mécanique des Fluides et Solides
Université Louis Pasteur - Strasbourg

Dr. Yves H. BERTHELOT
Directeur Georgia Tech Lorraine
Professor
Woodruff School of Mechanical Engineering
Georgia Institute of Technology

Dr. Moe KHALEEL
Laboratory Director and Fellow
Pacific Northwest National Laboratory

Date de la Soutenance: 14 Avril 2006

ACKNOWLEDGEMENTS

I am grateful to many people for their help and support. I would like to first thank my thesis advisors Dr. Cherkaoui and Dr. Berthelot. The insight, direction, and encouragement from these two individuals has driven this research and a significant amount of peripheral work. They have also provided me with a very unique educational experience by allowing me to work simultaneously at the Université Paul Verlaine in Metz and Georgia Institute of Technology for three unforgettable years. I would also like to thank Dr. Daya for his support in several aspects of this research and for providing much needed support in the final hour of manuscript preparation. I am forever grateful for the unwavering support provided by my parents throughout the years. They have inspired my achievements in countless ways. I would finally like to express my utmost thanks to my fiancé, Tänya, for her patience, love, and support during this hectic period of study, I owe you one.

TABLE OF CONTENTS

ACKNOWLEDGEMENTS III

TABLE OF CONTENTS IV

LIST OF TABLES VII

LIST OF FIGURES IX

SUMMARY XVI

RESUME DE LA THESE XVII

1 CHAPTER I 1

INTRODUCTION 1

1.1 OBJECTIVE AND MOTIVATION 1
1.2 HYPOTHESIS AND STRATEGY 3
1.3 THESIS OVERVIEW 4

2 CHAPTER II 9

BIBLIOGRAPHIC REVIEW AND PRINCIPLES 9

2.1 DAMPING MATERIALS 9
2.1.1 Strain energy methods for approximating damping capacity 17
2.1.2 Acoustic scattering methods for approximating damping capacity 24
2.2 MICROMECHANICAL HOMOGENIZATION OF PARTICULATE COMPOSITES 29
2.2.1 Pertinent micromechanical modeling developments 31
2.3 HOMOGENIZATION OF PARTICULATE COMPOSITES THROUGH ACOUSTIC SCATTERING 35
2.3.1 Single scattering models 35
2.3.2 Multiple scattering models 39
2.4 MATERIAL BY DESIGN 41

3 CHAPTER III 44

MICROMECHANICAL MODELING OF VISCOELASTIC COMPOSITES CONTAINING COATED INCLUSIONS 44

3.1 INTRODUCTION 44
3.2 DERIVATION OF QUASI-STATIC THREE PHASE SELF-CONSISTENT MODEL 45
3.2.1 Localization and the integral equation 49
3.2.2 Interfacial operators 55
3.2.2.1 Application to local strain fields 59
3.2.3 Localization: Average strain fields in the inclusion and coating 61
3.2.4 Homogenization and the self-consistent approximation 68
3.3 GENERALIZATION USING DILUTE STRAIN CONCENTRATION TENSORS 73
3.3.1 Localization and the integral equation 75
3.3.2 Interfacial operators and average strain fields of coated inclusion families 80
3.3.3 Homogenization and effective material properties 85

4 CHAPTER IV 90

VALIDATION AND APPLICATION OF THE SELF-CONSISTENT MODEL IN THE QUASI-STATIC DOMAIN **90**

4.1 OVERVIEW 90
4.2 COMPLEX BOUNDS AND THE SELF-CONSISTENT MODEL 91
4.2.1 Complex shear and bulk modulus bounds proposed by Roscoe *93*
4.2.2 Complex bounds using variational and translational techniques *101*
4.2.2.1 Complex bounds on the bulk modulus of bi-phase media 102
4.2.2.2 Complex bounds on the shear modulus of bi-phase media 103
4.3 VALIDATION OF THE GENERAL SC MODEL IN THE QUASI-STATIC DOMAIN 104
4.3.1 Elementary validation of quasi-static SC model *105*
4.3.2 Comparison of modeling results with experimental TL data: Oriented ellipsoidal inclusions *113*
4.3.3 Identical coated inclusions with a known orientational distribution *125*
4.3.3.1 Approximation of globally isotropic properties 127
4.3.3.2 Approximation of globally anisotropic properties 133
4.3.3.3 Comparison with experiment 136
4.3.4 Sub-micron → Micro → Macro Modeling *139*
4.3.4.1 Comparison with experiment 141
4.3.5 Distribution of coating thicknesses *144*
4.3.5.1 Comparison with experiment 147
4.4 COMMENTS ON NUMERICAL IMPLEMENTATION OF SC MODEL 149

5 CHAPTER V **153**

TOWARDS SELF-CONSISTENT MODEL IMPLEMENTATION IN A MATERIAL BY DESIGN STRATEGY **153**

5.1 OVERVIEW 153
5.2 MULTISCALE WINDSHIELD MODELING 154
5.3 PART LEVEL MODELING: DAMPED FLEXURAL WAVES IN A SANDWICH PLATE 156
5.3.1 Approximation of the effective bending modulus of a sandwich plate *158*
5.3.2 RKU Model Sensitivity Analysis *169*
5.4 STRUCTURE LEVEL MODELING 171
5.4.1 Analysis of the lossy behavior of simplified structures *176*
5.4.1.1 Forced vibration of a beam with elastic boundary conditions 177
5.4.1.2 Forced vibration of an elastically constrained circular plate 180
5.5 MICROSTRUCTURAL INFLUENCE ON STRUCTURAL DAMPING CAPACITY 184
5.5.1 Microstructure → Part level modeling *186*
5.5.2 Microstructure → Structure level modeling *190*

6 CHAPTER VI **198**

CONCLUSIONS, PERSPECTIVES, AND SUGGESTIONS FOR FUTURE WORK **198**

6.1 GENERAL CONCLUSION AND PERSPECTIVES 198
6.1.1 Quasi-static model development *199*
6.1.2 Model validation *201*
6.1.2.1 Homogenization of composites containing oriented ellipsoidal inclusions 202
6.1.2.2 Homogenization through DSCT formulation: Orientation distribution, multiple scale modeling, and coating thickness variations 203
6.1.3 Towards the implementation of the SC model as a material by design tool *205*
6.2 PERSPECTIVES AND SUGGESTIONS FOR FUTURE WORK 207
6.2.1.1 Suggestions for future work 208
6.2.1.2 Comments on material by design 211

7 APPENDIX A 212

FOURIER TRANSFORMATION APPROXIMATION OF $\hat{\mathbf{T}}^{I}\left(\hat{\mathbf{C}}^{X}\right)$ 212

8 APPENDIX B 216

TENSOR ROTATION AND EULER ANGLES 216

9 APPENDIX C 219

SUMMARY OF COMPLEX BOUNDS 219

10 APPENDIX D 227

RKU MODEL EVALUATION ALGORITHM 227

11 APPENDIX E 230

FORCED VIBRATION OF ELASTICALLY CONSTRAINED BEAMS AND CIRCULAR PLATES 230

12 REFERENCES 244

LIST OF TABLES

Table 4-1: Constituent material properties of the viscoelastic composites studied by Baird *et al* [76]. 95

Table 4-2: Material properties of coating and inclusion for material modeled in Figure 4-18. 122

Table 4-3: Minor radius ratios for composite modeled in Figure 4-18. 123

Table 4-4: Material properties of the constituent phases of shale studied by Hornby et al. Material data taken from various sources: clay [78], quartz and feldspar [154], pyrite [155]. 137

Table 4-5: Experimental data and results of effective stiffness coefficients of shale (GPa) for various modeling techniques. DSCT = Dilute strain concentration tensor; SC = Self-Consistent; GSC = Generalized Self-Consistent. 138

Table 4-6: Observed and calculated values of the coefficients of the stiffness tensor (GPa) for Al-SiC composite of Ledbetter and Datta [79]. (DSCT = Dilute strain concentration tensor; GSC = Generalized Self-Consistent; MT = Mori-Tanaka; LD = Ledbetter and Datta) 143

Table 5-1: Layer properties representing windshield constituent properties and geometry. 163

Table 5-2: Generic layer and plate properties used to approximate resonant behavior. $v \sim$ Poisson ratio, $L \sim$ sample length, and $W \sim$ sample width. 172

Table 5-3: Approximate sandwich plate resonant frequencies from LOM and RKU model homogenization. 172

Table 5-4: Sandwich beam geometry and properties for analytic and FE study in Figure 5-16. 178

Table 5-5: Plate geometry and material properties for parametric studies of component influence on structural damping. 183

Table 5-6: Material properties used to produce Figure 5-20 - Figure 5-24 and Figure 5-26. The viscoelastic properties are calculated from (V.3.9) and the HN coefficients given in the associated paragraph for an exciting frequency of 1 kHz. 186

Table E-1: First three eigenvalues taken from literature and comparison with current model. 234

Table E-2: First four eigenvalues of clamped circular plate taken from literature [171] and comparison with current model. $\nu = 0.30$ 242

Table E-3: First four eigenvalues of a simply-supported circular plate taken from literature [171] and comparison with current model. $\nu = 0.30$ 242

Table E-4: First five eigenvalues of free circular plate taken from literature [171] and comparison with current model. $\nu = 0.25$ 242

LIST OF FIGURES

Figure R-2: Schéma de la décomposition d'un matériau composite particulaire par DSCT xxv

Figure R-3: Bornes dans le plan complexe du module d'élasticité volumique calculé par les bornes de Gibiansky et Lakes [72] et l'approximation par le modèle AC, . Les bornes sont délimité par quatre courbes, $\kappa^{(1\text{-}4)}$, qui parfois se recouvrent xxvii

Figure R-4: Bornes du module de cisaillement dans le plan complexe depuis Milton et Berryman [71]. Borne supérieure; Borne inférieure. Le modèle AC, , rentre dans les limites xxviii

Figure R-5: IAA d'une dalle du matériau viscoélastique composite d'une épaisseur 1 cm. La matrice viscoélastique contient 13% des inclusions enrobées oblates. L'orientation des inclusions est telle que les axes longs sont perpendiculaires aux ondes incidentes. Etude paramétrique sur la variation du rapport des axes : $a/c = 1$, $a/c = 1.5$, $a/c = 2$, $a/c = 2.5$ xxix

Figure R-6: Coefficient d'affaiblissement en fonction d'angle de propagation dans le plan x_1-x_3 dans un matériau composite viscoélastique avec 10% par volume d'inclusions de verre enrobée par Lucite (θ = 0 représente l'axe x_3). La fréquence des ondes incidentes est 50 kHz. xxx

Figure R-7: IAA calculé avec le modèle AC et AC DSCT comparée avec les données expérimentales de Baird *et al* [76]. xxxii

Figure R-8: L'approche de la modélisation multi-échelle d'un pare-brise. xxxiv

Figure R-9: Le facteur de perte du premier mode d'une poutre sandwiche encastrée dans un matériau viscoélastique. Résultats analytique par une hiérarchie de modèles comparé avec une analyse par éléments fini employant le modèle de Daya et Potier-Ferry [83] xxxvi

Figure R-10: La fraction d'amplitude d'une onde de flexion amorti par longueur d'onde dans une plaque sandwiche en fonction de la fraction volumique des vides dans la couche viscoélastique approximée par les modèles RKU et micromécanique AC xxxvii

Figure R-11: La variation du facteur de perte du premier mode d'une plaque sandwiche circulaire en fonction de la fraction volumique des vides dans la couche viscoélastique, ϕ xxxviii

Figure R-12: L'approximation de l'IAA d'une pare-brise dont la couche PVB comprend les petites fractions volumique d'inclusions instables ($\mu_I = -1.1\mu_{PVB}$) xxxix

Figure 2-1: Evolution of the strain, ε, of a bar under constant stress, σ_0 (creep response). I, II, and III represent the three stages of creep. ε_0 is the value of the elastic strain. 11

Figure 2-2: Stress relaxation, $\sigma(t)$, in a bar under constant strain, ε_0. σ_0 is the value of the elastic stress and σ_∞ is the limiting value of $\sigma(t)$ as $t \rightarrow \infty$ 11

Figure 2-3: Time domain response of a one dimensional sample of viscoelastic material to an imposed cyclic strain. 16

Figure 2-4: Composite sphere of inner and outer radii a and b respectively. The material has a bulk and shear moduli denoted as K and μ respectively. The boundary conditions at $r = a$ can be changed and are designated as χ. 19

Figure 2-5: Ratio of strain energy in matrix material of composite sphere for three different values of Poisson's ratio with rigid BC at $r = a$ as a function of volume fraction, $f = a^3/b^3$. 22

Figure 2-6: Ratio of strain energy in matrix material of composite sphere for three different values of Poisson's ratio with pressure release ($\sigma_{rr} = 0$) BC at $r = a$ as a function of volume fraction, $f = a^3/b^3$ 23

Figure 2-7: Illustration of the dominant physical mechanisms that take place when a longitudinal plane wave impinges on an material inhomogeneity. 25

Figure 2-8: RVE for the SC model of Cherkaoui *et al* [23]. λ_x and μ_x represent the Lamé constants and ρ_x the density of material x. C^{eff}_{ijkl} is the effective stiffness tensor and I, C, and M specify respectively the inclusion, coating, and matrix. 30

Figure 2-9: RVE of composite material consisting of a matrix containing coated ellipsoidal inclusions. 34

Figure 2-10: The composite material, (a), and the RVE, (b), for the single scattering approach introduced by Chaban [46]. 37

Figure 2-11: Schematic representation of the two approaches to design, taken from Olsen [15, 90]. 41

Figure 2-12: Schematic of complete system design, including the design of materials. Figure from Seepersad [20], Cochran [141], Randle [142], and Piscanec [143]. 42

Figure 3-1: Topology of a coated inclusion embedded in a limitless matrix. Σ_{ij} and E_{ij} represent the macroscopically applied stresses and strains, respectively. 47

Figure 3-2 : Schematic of the interface of two viscoelastic solids used in the derivation of interfacial operators. 56

Figure 3-3: The SC model RVE consists of a coated inclusion surrounded by the homogeneous effective medium. The inclusion and coating are fully described by their viscoelastic properties $\hat{\mathbf{C}}^I$ and $\hat{\mathbf{C}}^C$, an average strain field $\hat{\varepsilon}^I_{ij}$ and $\hat{\varepsilon}^C_{ij}$, and volume fractions f^I and f^C, respectively. The effective medium is submitted to macroscopic stress and strain fields, $\hat{\Sigma}_{ij}$ and $\hat{E}_{ij}$, and has viscoelastic stiffness tensor $\hat{\mathbf{C}}^{eff}$ 69

Figure 3-4: Schematic representation of DSCT formulation of the SC model as the sum of N different RVE's corresponding to each coated inclusion family. 74

Figure 3-5: Topology of a particulate viscoelastic composite with N coated inclusion families. 76

Figure 4-1: Real and imaginary parts of the effective shear modulus as function of coated inclusion volume fraction for a fixed frequency. SC model approximation shown with the upper and lower bounds proposed by Roscoe. (Lower bound of imaginary part is zero everywhere). 97

Figure 4-2: Real and imaginary parts of the effective bulk modulus as a function of coated inclusion volume fraction for a fixed frequency. SC model approximation shown with the upper and lower bounds proposed by Roscoe. (Lower bound of imaginary part is zero everywhere). 98

Figure 4-3: Real and imaginary parts of the effective shear modulus as a function of frequency for a fixed coated inclusion volume fraction. SC model approximation shown with the upper and lower bounds proposed by Roscoe. (Lower bound of imaginary part is zero everywhere). 99

Figure 4-4: Real and imaginary parts of the effective bulk modulus as a function of frequency for a fixed coated inclusion volume fraction. SC model approximation shown with the upper and lower bounds proposed by Roscoe. (Lower bound of imaginary part is zero everywhere). 100

Figure 4-5: Bounds in the complex bulk modulus plane calculated from reference [72] and SC model approximation, , of same composite. Bounds are delineated by four, sometimes overlapping, lines: $\kappa^{(1\text{-}4)}$ 103

Figure 4-6: Bounds on the complex effective shear modulus given in reference [71]. Upper bound; Lower bound. Calculated SC model point, , is shown to fall within ellipsoidal bounded area. 104

Figure 4-7: Effective complex shear modulus of a voided viscoelastic material as a function of frequency. The pure matrix response is shown together with three differnent values of void fraction. 106

Figure 4-8: General characteristics of the frequency dependent shear modulus of viscoelastic. The modulus is approximated by the Havriliak-Negami model [147]. Damping capacity of the viscoelastic material is a monotonically increasing function of frequency for $0 < f < f_{crit}$ 108

Figure 4-9: Increase in the specific strain energy of voided composites due to pure shear loading. The ratio shown is the ratio of the specific strain energy in a voided composite to the strain energy in a homogeneous material submitted to the same shear stress. 110

Figure 4-10: Attenuation coefficients for shear and longitudinal wave propagation in a pure polymer compared with the effective behavior of three different voided composites approximated by the SC model. 111

Figure 4-11: The imaginary part of the inverted shear and longitudinal moduli of a pure polymer compared with the effective behavior of three different voided composites as approximated by the SC model. 112

Figure 4-12: (a) Representation of a viscoelastic matrix slab containing identically oriented ellipsoidal inclusions. (b) Incident, reflected, and transmitted plane-wave visualization used to calculate the TL of the composite material layer. 114

Figure 4-13: SC and BKT model estimates of TL for a 1 cm thick slab of viscoelastic composite submerged in water. Experimental data taken by Baird *et al* [76]. 117

Figure 4-14: Transmission loss of 1 cm thick slab of composite material oriented as shown in Figure 4-12(a) and containing 13% by volume of oblate coated inclusions of varying aspect ratios. $a/c=1$, $a/c=1.5$, $a/c=2$, $a/c=2.5$. 118

Figure 4-15: Geometry of oblate spheroids and their orientation with respect to the global coordinate system. 119

Figure 4-16: Attenuation coefficient as a function of angle in the x_1-x_3 plane of material containing oblate ellipsoidal inclusions of varying aspect ratios ($\theta = 0$ coincides with x_3-axis). The volume fraction of inclusions is 13% and the frequency of the incident wave is 50 kHz. $a/c=1$, $a/c=1.5$, $a/c=2$, $a/c=2.5$ 120

Figure 4-17: Real and imaginary parts of effective complex longitudinal wave speed in x_3-direction as function of frequency for a volume fraction inclusions of 13%. $a/c=1$, $a/c=1.5$, $a/c=2$, $a/c=2.5$ 122

Figure 4-18: Attenuation coefficient as a function of angle in the x_1-x_3 plane for a composite consisting of a viscoelastic matrix with Lucite coated glass ellipsoidal inclusions of different forms (θ = 0 coincides with x_3-axis). The volume fraction of inclusions is 10% and the frequency of the incident wave is 50 kHz. 124

Figure 4-19: Compressional and shear wave speeds and Q^{-1} values as a function of volume fraction calculated using the SC DSCT model and Berryman's model [51] for the case of prolate rock inclusions in water where a/b = a/c = 10.....129

Figure 4-20: Compressional and shear wave speeds and Q^{-1} values as a function of volume fraction calculated using the SC DSCT model and Berryman's model [51] for the case of oblate rock inclusions in water where a/b = 1 and a/c = 10. 130

Figure 4-21: Orientation of prolate glass inclusions. θ is the azimuthal angle. 134

Figure 4-22: Variation of attenuation coefficient as a function of azimuthal angle for glass/polymer composite with varying degrees of anisotropy. Volume fraction of prolate inclusions φ = 10%, $a/b = a/c = 5$, frequency inspected f = 25 kHz. 135

Figure 4-23: Micrograph of shale studied by Horby *et al* [78] (image from reference).....137

Figure 4-24: Composite material studied by Ledbetter and Datta (image taken from reference [79]). The material consists of a non-uniform distribution of sub-micron prolate SiC particles in an aluminum matrix. (a) Micrograph of

material, SiC particles are dark areas, (b) Schematic of modeling approach employed. 142

Figure 4-25: Transmission loss calculated using SC and SC DSCT with experimental data from reference [76]. 148

Figure 5-1: Multiscale windshield modeling approach. 156

Figure 5-2: (a) Differential element of a sandwich plate ; (b) Cross sectional geometry. 159

Figure 5-3: DMTA data and HN curve fits for PVB material 163

Figure 5-4: Variation of sandwich plate complex bending modulus as a function of the thickness ratio, *H*. Parametric study on the shear loss factor of the interlayer 164

Figure 5-5: Variation of sandwich plate complex flexural wavenumber as a function of the thickness ratio, *H*. Parametric study on the shear loss factor of the interlayer 165

Figure 5-6: Variation of sandwich plate complex shear parameter as a function of the thickness ratio, *H*. Parametric study on the shear loss factor of the interlayer 165

Figure 5-7: Complex effective flexural modulus calculated with BKT model as a function of the shear parameter's loss factor, γ for fixed values of g' 167

Figure 5-8: Optimally lossy complex effective bending modulus calculated as a function of $\hat{g}'$. The material properties employed are those given in Table 5-1 168

Figure 5-9: Sensitivity of the complex shear parameter to changes in the thickness ratio and the shear loss factor of the interlayer. Partial derivatives of g' and γ with respect to H and β_2 are shown. For (a) and (c), $\beta_2 = 0.13$; for (b) and (d), $H = 0.4$. 170

Figure 5-10: Schematic of general set-up used for SAE J1400 TL testing. 173

Figure 5-11: TL due to four different windshield samples. Notches in TL at ~ 500 Hz and ~ 1000 Hz agree well with RKU model approximation 174

Figure 5-12: TL experimental setup. Sample window contains stainless steel plug. Note red clamps and isolation putty around exterior of test window. 175

Figure 5-13: TL results for S1 with different boundary conditions. Viscoelastic BC show a substantial increase in observed TL. 176

Figure 5-14: Schematic of an elastically constrained beam. 177

Figure 5-15: Approximation of viscoelastic boundary conditions as linear and rotational springs. 178

Figure 5-16: Viscoelastically constrained beam LF as function of the LF of constraining and interlayer materials. Multiscale model comparison with FEA model derived by Daya and Potier-Ferry [83] 179

Figure 5-17: Schematic of elastically constrained circular plate.....181

Figure 5-18: Approximation of viscoelastic boundary conditions as linear and rotational springs.....182

Figure 5-19: Modal loss factor of vibrating plate as a function of each contributing element. PS1 indicates the influence of the rotational spring loss factor, PS2 indicates the effect of the linear spring's loss factor, and PS3 indicates the beam loss factor's influence.....184

Figure 5-20: Effective bending modulus as a function of layer thickness ratio for varying values of interlayer void fraction at f = 1 kHz.....187

Figure 5-21: Effective flexural wavenumber as a function of the thickness ratio at f = 1 kHz for a several different void fractions.....188

Figure 5-22: Measure of damping amplitude attenuation per flexural wavelength for layered plate homogenized using RKU model with a voided interlayer.....189

Figure 5-23: Effective shear parameter as a function of the layer thickness ratio for several values of interlayer void fraction at f= 1 kHz.....189

Figure 5-24: Variation of the loss factor of the 1st mode of vibration for a cantilever beam as a function of interlayer void fraction, ϕ.....191

Figure 5-25: General characteristics of TL versus frequency for a panel (figure from Buerhle *et al* [165]).....192

Figure 5-26: Theoretical TL of layered windshield as a function of frequency for an incident angle of $\theta_I = 60°$. Slight improvements are predicted for voided PVB near coincidence frequency.....194

Figure 5-27: Transmission Loss of sandwich panel when PVB interlayer contains small volume fractions of negative stiffness inclusions ($\mu_I = -1.1\mu_{PVB}$). Coincidence notch moves to dramatically lower frequencies and nearly vanishes.....196

Figure 6-1: Schematic of a meta-model mapping procedure. The microscale variables represent, from top to bottom, the constituent material properties, the volume fractions, the inclusion form, the inclusion orientation, and any other variables to be defined.....210

Figure B-1: Visualization of Euler angles employed in the x-convention [148].....216

Figure E-1: Schematic of elastically constrained beam.....230

Figure E-2: Approximation of boundary conditions as linear spring and rotational spring. b is the beam width.....232

Figure E-3: Sign conventions used in the derivation of the beam bending problem.....232

Figure E-4: Schematic of elastically constrained circular plate.....235

Figure E-5: Approximation of boundary conditions as linear spring and rotational spring. *a* is the plate radius, *h* is the plate thickness, and *t* is the radial thickness that the plate is embedded in the elastic boundary. 239

SUMMARY

This study focuses on the micromechanical modeling of particulate viscoelastic composite materials in the quasi-static frequency domain to approximate macroscopic damping behavior and has two main objectives. The first objective is the development of a robust multiscale model in the quasi-static domain. For this purpose, the static three phase self-consistent (SC) model introduced by Cherkaoui *et al* [J. Eng. Mater. Technol. 116, 274-278 (1994)] is extended to the quasi-static domain by employing the elastic-viscoelastic correspondence principle. The model is then generalized by employing dilute strain concentration tensor formulation. The developed model is validated by comparison with complex bounds from literature, acoustic and static experimental data, and established models. The second objective is a study of the SC model as a tool for the design of high loss materials. This objective is met by presenting a case study of the lossy behavior of a multiscale structure in the form of a vibrating sandwich plate representing an automobile windshield. This multiscale structure is modeled with a nested hierarchy of models which is validated by comparison with finite element approximations. Parametric studies of damping behavior at structural and part length scales are performed which provide information for the design of constituent sandwich plate materials. The effects of microstructural variation on structure level damping predicted by the SC model are quantified and discussed. The work concludes by summarizing important results and contributions and giving perspectives and suggestions for future work.

RESUME DE LA THESE

Chapitre I : Introduction

Objectif

L'objectif principal de cette thèse est la dérivation, développement, et validation d'un modèle micromécanique auto-cohérent quasi-statique afin de faciliter l'exploration et génération des spécifications pour la conception des matériaux amortissants.

Les applications pratiques nécessitant des matériaux possédants une forte capacité d'amortir l'énergie acoustique et vibrationnelle concernent presque toutes les industries. Les industries automobile [1] et aérienne [2], par exemple, se servent des matériaux amortisseurs afin de remplir éléments structurels creux. De tels matériaux renforcent la structure et amortissent les vibrations et bruits simultanément. Les matériaux amortissants présentent des avantages d'absorption aussi en les employant en forme de couches ou de plies. Quelques exemples des structure traités avec les couches ou plies de matériau amortissant sont les chambres de tranquillisation pour diminuer le bruit des tuyères [3], les structures vibrantes [4], et les pare-brises automobiles [5]. De plus, il est connu que la capacité amortissante d'un matériau peut être amélioré en introduisant des hétérogénéités [6], et de ce fait en créant un matériaux composite particulaire.

La modélisation des matériaux composites viscoélastiques est, donc, d'un grand intérêt du fait du grand nombre d'applications pour des matériaux amortissants. Cela explique pourquoi la modélisation est un domaine de recherche très actif depuis presque cinquante ans [7, 8]. La recherche actuelle suggère la possibilité de créer les composites qui possèdent une capacité amortissante extrêmement élevée [9-13] et le

potentiel réel de concevoir des matériaux pour des applications spécifiques [14, 15]. Ces deux développements donnent une impulsion renouvelée à la modélisation des matériaux composites viscoélastique.

La capacité amortissante d'un système viscoélastique, qu'il s'agisse d'une structure ou d'un matériau composite, est une fonction de l'état de déformation des éléments viscoélastique de la structure. Cet état de déformation peut être approximé par plusieurs méthodes différentes mathématiquement, mais fondamentalement il est important de noter qu'une augmentation de l'énergie de déformation des éléments viscoélastique conduit à une augmentation de la capacité amortissante du système globale [16]. En effet, les recherches récentes montrent que les inclusions instable [9, 10, 12], ou bistables [17, 18], induisent de grandes déformations du matériau hôte dans le voisinage des inclusions et ainsi contribuent fortement à une augmentation important du comportement amortissant macroscopique. *Le développement d'un modèle multi-échelle robuste est un élément principal de cette thèse. Celui-ci permettra l'étude des effets de la forme, d'orientation, et du comportement constitutif des inclusions sur le comportement macroscopique des composites particulaires.*

La sélection des matériaux, qui est un élément clé du processus de la conception traditionnelle des systèmes [19], est un aspect très limitatif de la conception. En effet l'approche classique de la conception des systèmes, qui prévaut dans la communauté de la conception, suppose que la conception des éléments est limitée par les propriétés physiques des matériaux disponibles [20]. Ce paradigme change quand l'approche de la conception des systèmes est prolongée pour inclure *la conception des matériaux* pour les applications multi-physiques et multi-fonctionnelles [14, 15]. Cette nouvelle approche s'appelle la conception inductive. Une méthodologie inductive dans le domaine de la conception implique la conception des matériaux pour la fabrication, tandis que les méthodes traditionnelles fabrique les matériaux pour les utiliser dans la conception (approche déductive) [21]. Les modèles multi-échelles robustes peuvent fournir des informations utiles pour la conception des matériaux [14]. Cet élément est un très important dans cette approche émergeante. La

conception effective des matériaux nécessite des modèles capables de faire la transition entre les échelles de temps et longueur disparates (les échelles de longueurs entre l'atomique et le macroscopique et les échelles de temps entre les pico-secondes et les années). De tels modèles n'existent pas et ne seront pas disponibles dans un proche avenir. L'approche actuelle consiste en l'implémentation d'une hiérarchie des modèles différents imbriqués ou chacun effectue une, ou plusieurs, transitions d'échelle [20]. Cette méthodologie est difficile à cause d'un manque d'information concernant, ou d'un comportement complexe, des modèles dans l'espace de la conception [21]. Ces difficultés limitent l'implémentation d'un grand nombre de modèles dans une stratégie de conception complète. Un moyen de surmonter cette difficulté consiste à effectuer plusieurs études multi-échelles élémentaires utilisant des modèles rigoureux afin d'observer les tendances. Les tendances ainsi obtenues peuvent être approximées par des modèles simplifiés, les meta-modèls, et ainsi être intégrées dans une stratégie de conception des matériaux. Cette approche présentent un moyen efficace d'explorer l'espace de conception [22]. Sans se soucier de la méthode employée, tout processus de conception des matériaux nécessite à la fois des modèles multi-échelles robustes et une connaissance du comportement d'un matériau composite dans l'espace de conception fournie par ces modèles. *L'objectif de cette thèse est donc le développement d'un modèle multi-échelle (micro → macro) des matériaux amortissants à l'aide d'un schéma auto-cohérent (AC) statique à partir d'un modèle existant [23, 24] et de l'intégrer dans un hiérarchie de modèles d'échelles de longueurs différentes afin de mettre en évidence les effets microstructuraux sur l'amortissement des structures. Un pas vers la conception des matériaux amortissants.*

Hypothèse

Le développement d'un modèle auto-cohérent micromécanique robuste dans le domaine fréquentielle quasi-statique fournira un outil à la conception des matériaux composites amortissants.

Afin de valider cette hypothèse, il faut d'abord développer le modèle AC dans le domaine fréquentiel quasi-statique pour les applications d'amortissement divers. Il faut que ce modèle puisse prendre en compte les propriétés viscoélastique des matériaux constituants ainsi que la forme et l'orientation des hétérogénéités afin de simuler le comportement global. Le modèle droit être validé en le comparant avec d'autres modèles d'homogénéisation, les bornes complexes, ainsi qu'avec les données expérimentales. Il est ensuite nécessaire de mettre en œuvre un exemple simple de structure multi-échelle et d'y intégrer le modèle AC. Enfin, il faut effectuer plusieurs études sur le comportement de la structure à chaque échelle. L'effet de la microstructure qui se propage à travers des échelles de longueurs et qui se manifeste sur comportement structurel est étudié à ce stade.

Chapitre II: Revue Bibliographique et principes

Le deuxième chapitre présente un résumé des principes utilisés dans cette thèse. Ce chapitre commence par une discussion concernant la dissipation de l'énergie dans les matériaux. Pour cela, nous présentons les sources différentes de dissipation dans les matériaux homogènes et hétérogènes ainsi que les mesures de cette dissipation d'énergie. Les principes physiques de la dissipation sont ensuit introduits dans le cadre de l'énergie de déformation, qui est une approche souvent employée souvent dans le domaine des vibration des structures. Le chapitre poursuite par la présentation de quelques approches acoustiques basées sur les principes de la dispersion des ondes décrivant les principes physiques de l'amortissement des composites particulaires. Ce chapitre se termine par une synthèse bibliographique des deux domaines principaux de la thèse : (*i*) la modélisation des matériaux composites

particulaires à partir des méthodes micromécaniques statiques et des méthodes acoustiques de dispersion simple et multiple, et (*ii*) les développements importants des méthodes de la conception des matériaux avec une approche multi-échelle et multi-fonctionnelle.

Chapitre III : Modélisation micromécanique dans le domaine quasi-statique

Le modèle proposé dans cette thèse est une approche micromécanique d'homogénéisation AC. L'approche AC des composites particulaires fait parti d'une classe de modèles dit champs moyenné [25]. La modélisation par champs moyenné consiste en deux opérations fondamentaux : (*i*) la localisation et (*ii*) la homogénéisation [26, 27]. Ces opérations nécessitent l'existence de deux échelles de longueurs intrinsèque tel que le comportement et la structure du matériau à l'échelle de longueur microscopique, qui représente l'échelle des particules, n'a qu'un effet moyenné sur le comportement du matériau à l'échelle macroscopique [27]. Le travail d'Eshelby a fournit la perspicacité et outils mathématiques pour résoudre le problème de la localisation d'un chargement mécanique macroscopique imposé à l'infini à l'échelle microscopique via le tenseur de localisation appelé le tenseur d'Eshelby, S_{ijkl}, et la méthode d'inclusion équivalente. La capacité d'effectuer une localisation des chargements mécaniques imposé à l'échelle macroscopique à l'échelle microscopique est un besoin fondamental de l'étape d'homogénéisation. Les propriétés effectives d'un matériau composite sont obtenues depuis les champs moyens volumétriques de contrainte et de déformation d'un matériau hétérogène. Le moyen volumique est obtenu depuis les champs locaux des déformations et des contraintes calculés pendant l'étape de localisation [28-30].

La contribution fondamental d'Eshelby est suivi par une grande gamme de modèles, dont quelques exemples représentatives sont ceux de Kröner [31], Budiansky [32], Wu [28], et Mori et Tanaka [33]. Zeller et Dederichs ont amélioré la méthode d'inclusions équivalentes en introduisant un formalisme de Green qui permet

le calcul de la contrainte et la déformation en chaque point d'un milieux hétérogène à l'échelle microscopique [34]. Mura [35] et Willis [36] ont ajouté la déformation plastique à l'approche de Zeller et Dederichs et Berveiller *et al* [37] ont généralisé l'approche au cas de deux inclusions ellipsoïdales plastiques et désorientées. Une autre amélioration importante de l'approche des inclusions équivalentes est l'introduction des opérateurs interfaciaux qui relient l'état de contrainte et déformation à travers d'une interface de deux matériaux différents [38, 39]. La combinaison de ces deux techniques mathématiques fournit un outil de modélisation des phénomènes physiques à l'échelle microscopique extrêmement puissant. Le résultat important pour ce travail est que ces outils améliorent les opérations de moyen volumétriques nécessaire pour effectuer l'homogénéisation. Le modèle AC introduit par Cherkaoui *et al* [23, 40] doit sa précision au fait qu'il s'est servi de ces outils. Le modèle développé dans cette thèse est une extension au domaine fréquentiel quasi-statique de leur modèle.

Tous les modèles micromécaniques nécessitent la sélection d'un volume élémentaire représentatif (VER). Le VER représente le plus petit volume du matériau hétérogène qui se comporte de la même manière que le matériau macroscopique. Chaque modèle est obtenu en appliquant les lois de comportement au VER spécifique au modèle et en servant des outils mathématiques décris dessus. Un matériau composite constitué d'inclusions ellipsoïdales enrobées plongées dans un milieu homogène de référence peut être représenté par le VER montré par Figure R-1. Le modèle de Mori et Tanaka suppose que le matériau de référence dans Figure R-1 soit une matrice avec les propriétés élastiques, $\mathbf{C}^M$. Le matériau de

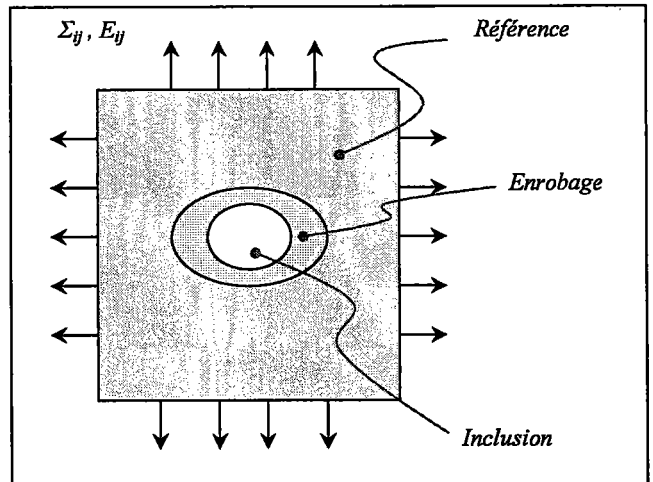

Figure R-1: VER d'un matériau composite constitué des inclusions enrobées plongées dans une milieu infini de référence.

référence subit une déformation macroscopique, E_{ij}, qui est la même que celle dans la matrice ε_{ij}^{M} [33]. Le modèle Mori-Tanaka est, donc, limité aux applications ou la fraction volumique des inclusions, f_I, est faible. Un grand nombre d'autres modèles sont limités aux cas de concentration diluée d'inhomogénéités parce qu'ils supposent qu'il n'y a pas d'interaction entre les champs de déformation des inclusions [41]. Plusieurs moyens existent pour surmonter cette limitation. Par exemple, une approximation numérique depuis une maille périodique basé sur des calcules par éléments finis. Cette approche prend compte l'interaction des hétérogénéités d'une manière explicite mais elle nécessite les calcules intensifs [25]. Un autre exemple est le modèle proposé par Molinari et El Mouden [42] qui applique le formalisme de Green d'une paire d'inclusions ellipsoïdales de Berveiller *et al* [37]. Leur modèle fiable obtiens les constants effectives du comportement des composites particulaires avec une concentration d'inclusions élevée. Les modèles AC représentent une autre démarche qui peut être employé pour simuler le comportement d'une composite particulaire avec une concentration d'inhomogénéités élevée. L'approche AC suppose que le milieu de référence du VER en Figure R-1 se comporte selon les propriétés élastiques effectives macroscopiques, $\mathbf{C}^{eff}$, et qu'elles sont inconnues [41]. Kröner a proposé cette démarche afin d'approximer le comportement des matériaux polycristallins car la définition de la matrice n'est pas claire [31]. Budiansky [32] et Hill [43, 44] ont amélioré l'approche de Kröner et finalement Christensen et Lo l'ont généralisé [45]. La démarche AC n'est pas limitée au comportement statique des matériaux composites. Chaban [46], Kuster et Toksoz [47], et Gaunaurd et Überall [48, 49] ont tous proposé des modèles d'homogénéisation AC fiables par des méthodes acoustiques. Les modèles micromécaniques AC obtiennent les équations implicite qui engendre, parfois, les instabilités numériques [50]. Pour certains cas, ces modèles peuvent aboutir à des valeurs erronés [51, 52]. Cependant, les modèles micromécaniques AC restent fiables, commode et, en particulier, donnent de bonnes approximations du comportement des composites ayant une haute fraction volumique d'inclusions. Pour ces raisons le modèle AC de Cherkaoui *et al* [23] est développé ici

dans le domaine fréquentiel quasi-statique, présenté par l'Équation (R.1), afin d'approximer le comportement des composites viscoélastique [50, 53].

$$\hat{\mathbf{C}}^{eff} = \hat{\mathbf{C}}^{M} + f_I\left[\hat{\mathbf{C}}^{I} - \hat{\mathbf{C}}^{M}\right] : \hat{\mathbf{A}}^{I}\left(\hat{\mathbf{C}}^{eff}\right) + f_C\left[\hat{\mathbf{C}}^{C} - \hat{\mathbf{C}}^{M}\right] : \hat{\mathbf{A}}^{C}\left(\hat{\mathbf{C}}^{eff}\right) \qquad \text{(R.1)}$$

Dans cette relation les propriétés viscoélastique de la matrice, des inclusions, et de l'enrobage sont notées par les teneurs de rigidité complexes $\mathbf{C}^{M}(\omega)$, $\mathbf{C}^{I}(\omega)$, et $\mathbf{C}^{C}(\omega)$ respectivement, f_I et f_C représentent respectivement les fractions volumiques des inclusions et de l'enrobage, et $\mathbf{A}^{I}(\omega)$ et $\mathbf{A}^{C}(\omega)$ sont les tenseurs de localisation des déformations de l'inclusion et l'enrobage. De plus, l'équation (R.1) utilise la notation simplifiée $\mathbf{C}^{x}(\omega) \Leftrightarrow \hat{\mathbf{C}}^{x}$.

Le modèle introduit par Cherkaoui *et al* [23, 40, 54] se limite aux cas des inclusions enrobées sphériques ou bien ellipsoïdales. Malheureusement, quand les inclusions sont ellipsoïdales, le modèle est limité aux applications ou les phases constitutives possèdent les propriétés viscoélastiques *identiques* et les inclusions sont toutes orientées *identiquement*. Etant donner que la majorité des vrais matériaux n'appartiennent à ni l'un ni l'autre de ces classifications, il est intéressant de généraliser le modèle. Spécifiquement, il est intéressant de développer le modèle afin de simuler le comportement effectif d'un matériau qui consiste en une matrice contenant les plusieurs types d'inclusions enrobées qui ont une distribution d'orientation connu. Il est possible d'arriver à ce niveau de généralité en étendant le VER du modèle AC du Figure R-1 pour inclure toutes « familles » d'inclusions enrobées différentes. Cette démarche s'appelle la formulation par tenseurs de localisation des déformations diluées (où « Dilute Strain Concentration Tensors », DSCT). Le VER utilisé pour la dérivation d'un modèle AC DSCT peut être décomposer selon le schéma montré dans le Figure R-2 [55-57].

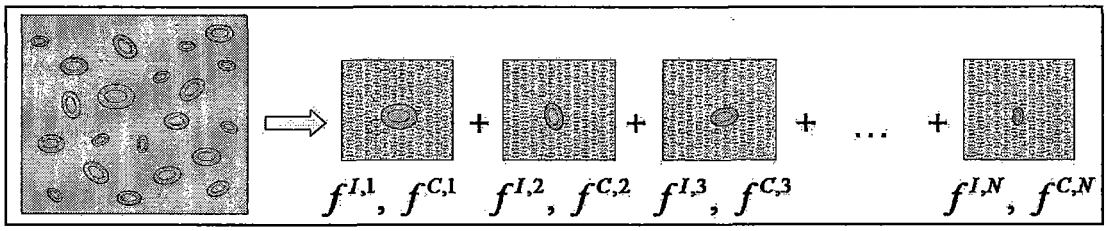

Figure R-2: Schéma de la décomposition d'un matériau composite particulaire par DSCT.

Le modèle AC quasi-statique provenant de la formulation par DSCT est décrit par l'Equation (R.2).

$$\hat{\mathbf{C}}^{eff} = \hat{\mathbf{C}}^{M} + \sum_{i=1}^{N} \left\{ f^{I,i} \left(\hat{\mathbf{C}}^{I,i} - \hat{\mathbf{C}}^{M} \right) : \hat{\mathbf{A}}^{I,i} + f^{C,i} \left(\hat{\mathbf{C}}^{C,i} - \hat{\mathbf{C}}^{M} \right) : \hat{\mathbf{A}}^{C,i} \right\} \qquad \text{(R.2)}$$

Equation (R.2) montre que le modèle DSCT prédit le comportement effectif avec une sommation des effets de N familles d'inclusions enrobées différentes. Cette approche raffine les approximations du modèle AC donnée par Equation (R.1) en permettant de se rapprocher de la vraie composition des matériaux composites particulaires.

Chapitre IV: Validation et application du modèle auto-cohèrent QS

Avant d'intégrer le modèle micromécanique AC dans une stratégie de conception des matériaux, il est d'abord nécessaire de valider le modèle. Le but de ce chapitre est la validation du modèle AC quasi-statique qui s'accompli en deux étapes. La première étape compare le modèle AC avec les bornes analytiques des milieux hétérogènes complexes prises de la littérature. La comparaison avec les bornes complexe commence par une introduction des méthodes les plus applicables aux matériaux étudiés dans cette thèse. Ensuit les valeurs obtenues par le modèle AC dans le domaine quasi-statique pour plusieurs matériaux hypothétiques sont comparé avec ces bornes complexes. L'accord entre les bornes complexes et le mode AC assure la validité du modèle dans le domaine fréquentiel quasi-statique. La deuxième partie de la validation du modèle consiste en des études paramétriques et comparaison

avec l'expérience. L'accord avec les données expérimentales montre la précision et la flexibilité du modèle pour son application aux divers problèmes. Le chapitre se termine avec une discussion de l'implémentation numérique du modèle AC. Cette partie discute quelques problèmes rencontrés, suggère les méthodes pour implémentation du modèle AC quasi-statique, et discute des observations sur les instabilités numériques rencontrées.

Comparaison avec bornes complexes

Les techniques qui définissent les limites de validité des modèles d'homogénéisation des composites élastiques sont bien connues, voir par exemple, Hashin et Shtrikman [58], Walpole [59], Hill [60, 61], et pour une revue détaillée Hashin [62]. De plus, l'approche AC rentre dans les bornes acceptés pour le cas élastique (c'est-à-dire, les tenseurs de rigidité de chaque phase d'un composite particulaire n'ont que les composants réelles) [43]. Par contre, il existe comparativement peu de travail qui concerne les bornes du comportement effectif complexe des composites viscoélastique. Hashin [8, 63, 64], Christensen [7], Roscoe [65, 66] ont abordé le sujet avec leur études fondamentaux sur le sujet des composites viscoélastique et les bornes complexes simples. Plus récemment, les techniques basées sur méthodes variationelles et translationelles ont fait leur apparition. Cherkaev et Gibiansky [67] ont introduit cette approche rigoureuse qui est liée au travail de Milton [68] et aussi celui de Miller [69]. Le résultat de leur travail ont stimulé plusieurs contributions concernant le développement des bornes complexes, notamment celles de Gibiansky et Milton [70], Milton et Berryman [71], Gibiansky et Lakes [72, 73] et Gibiansky et Torquato [74]. Toutes ces méthodes limitent les valeurs effectives des modules de cisaillement et d'élasticité volumique dans une zone du plan complexe décrit par des arcs. Les arcs sont les fonctions des modules complexes des phases constituantes et les fractions volumiques. Le

désavantage des ces méthodes est qu'elles sont limitées à l'application à chaque fraction volumique et chaque fréquence d'intérêt d'un matériaux composite.

Cette section de la thèse met en évidence que le modèle AC quasi-statique n'enfreint aucune loi physique. Il est montré que le modèle est situé entres les bornes de Roscoe en fonction de la fréquence et aussi bien que la fraction volumique. De plus, il est montré que le modèle est en accord avec les bornes rigoureuses du module de d'élasticité volumique proposé par Gibiansky et Lakes [72], Figure R-3, et du module de cisaillement de Milton et Berryman [71], Figure R-4.

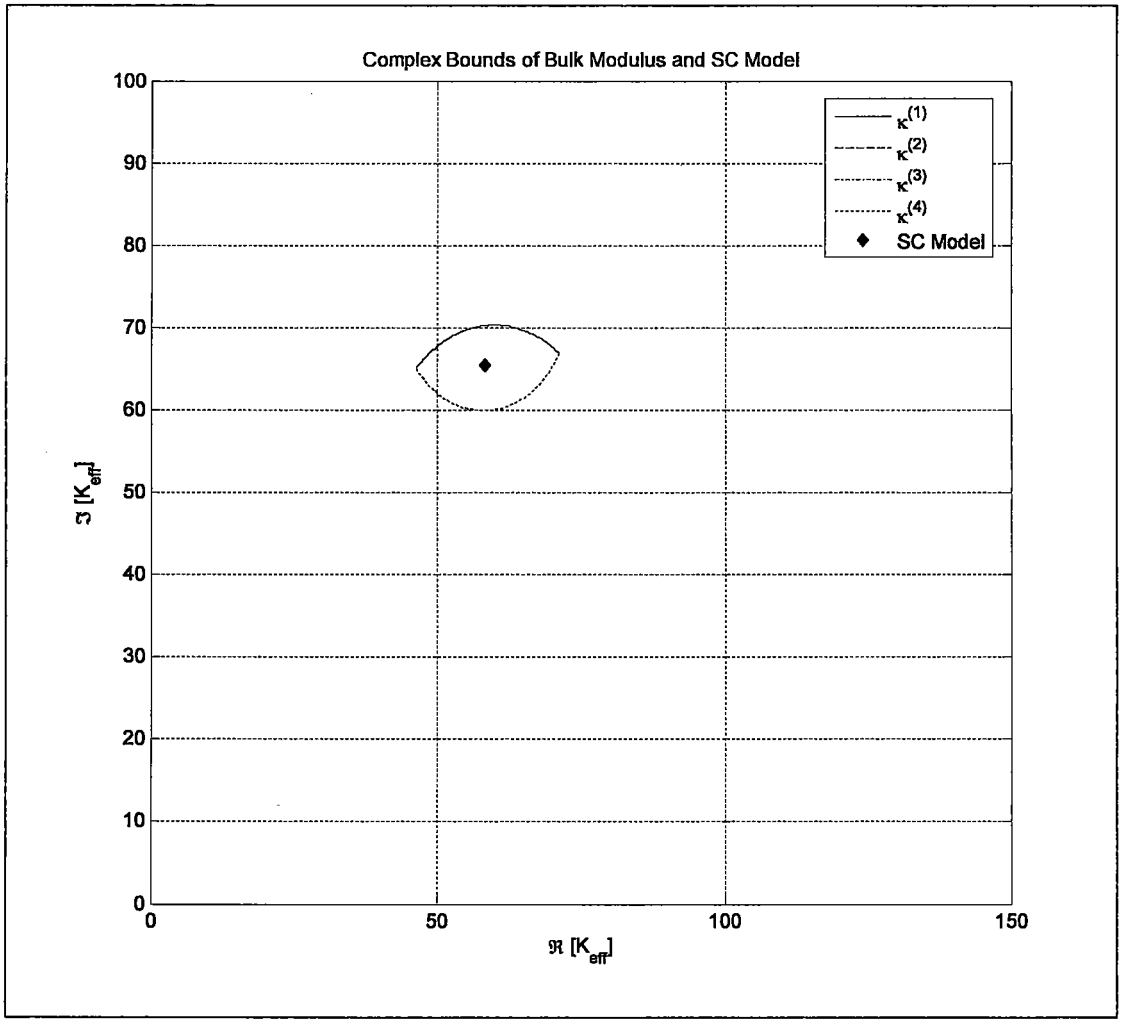

Figure R-3: Bornes dans le plan complexe du module d'élasticité volumique calculé par les bornes de Gibiansky et Lakes [72] et l'approximation par le modèle AC, ◆. Les bornes sont délimité par quatre courbes, $\kappa^{(1-4)}$, qui parfois se recouvrent.

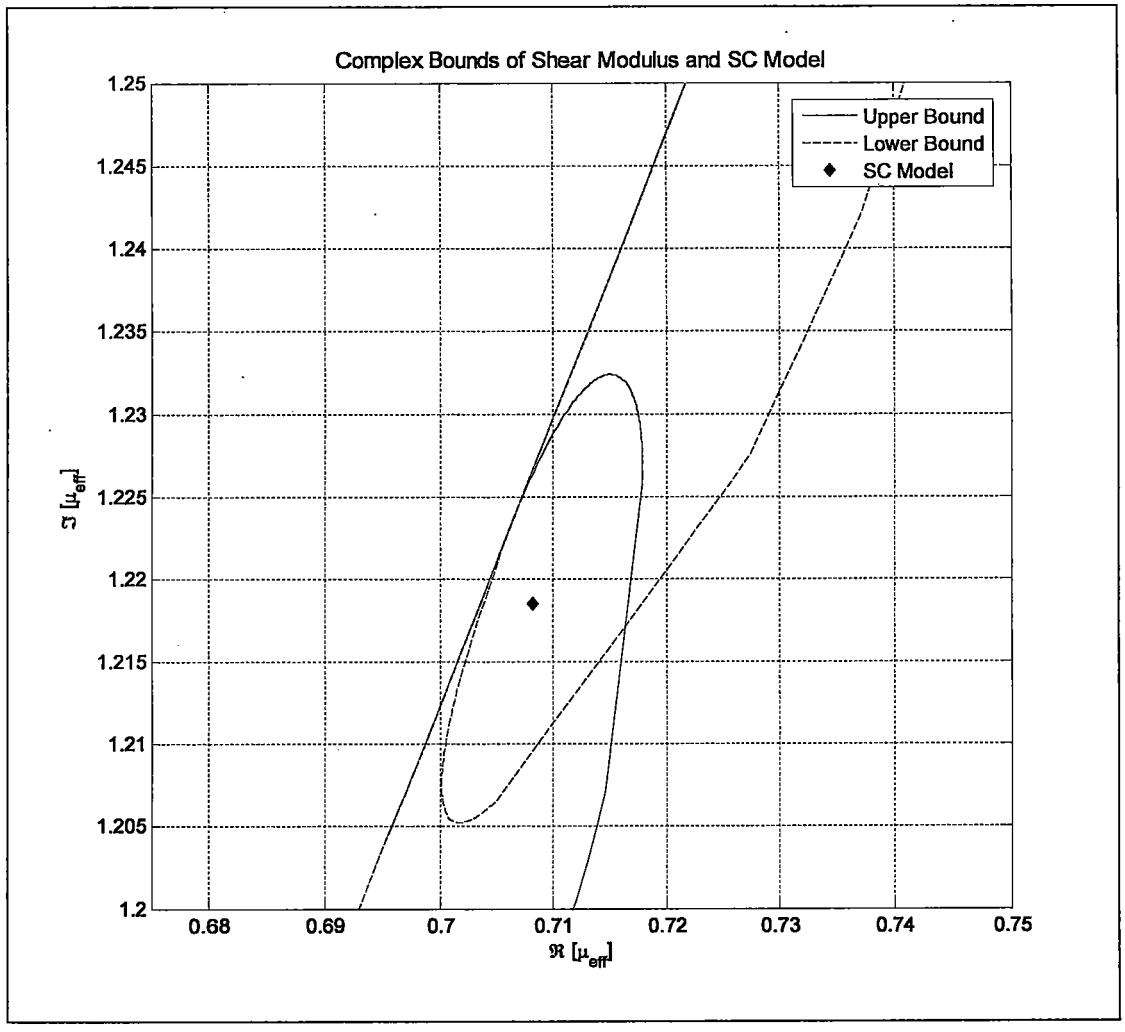

Figure R-4: Bornes du module de cisaillement dans le plan complexe depuis Milton et Berryman [71]. —— Borne supérieure; - - - Borne inférieure. Le modèle AC, ◆ , rentre dans les limites.

Comparaison avec l'expérience et les études paramétriques

Le principe de correspondance élastique-viscoélastique suggère que l'approximation du comportement d'un matériau composite viscoélastique par une méthode micromécanique dans le domaine fréquentiel quasi-statique corresponde à une approximation par l'énergie de déformation [75]. La validation de cette logique est extrêmement importante pour l'implémentation future du modèle AC quasi-statique dans le cadre de conception des matériaux amortissants. Il est pour cette raison que l'approximation par le modèle AC est toute d'abord comparée avec les données expérimentales et une modèle de dispersion acoustique de l'indice

d'affaiblissement acoustique (IAA) d'une dalle de matériau viscoélastique composite [76]. Les effets d'anisotropie, due aux inclusions enrobées ellipsoïdales orientées, sont le sujet de plusieurs études paramétriques. La première s'agit d'une étude sur l'IAA pour d'un matériau viscoélastique qui contient les renforcements oblates vides. Toutes ces inclusions oblates ont leurs axes majeurs orientés avec plan x_1-x_2 et on étudie l'IAA d'une dalle composite d'une épaisseur de 1 cm pour une onde incident qui se propage selon l'axe x_3. Figure R-5 montre que le modèle AC arrive à capter les effets d'anisotropie induite par inclusions isotropes mais ellipsoïdales et orientées.

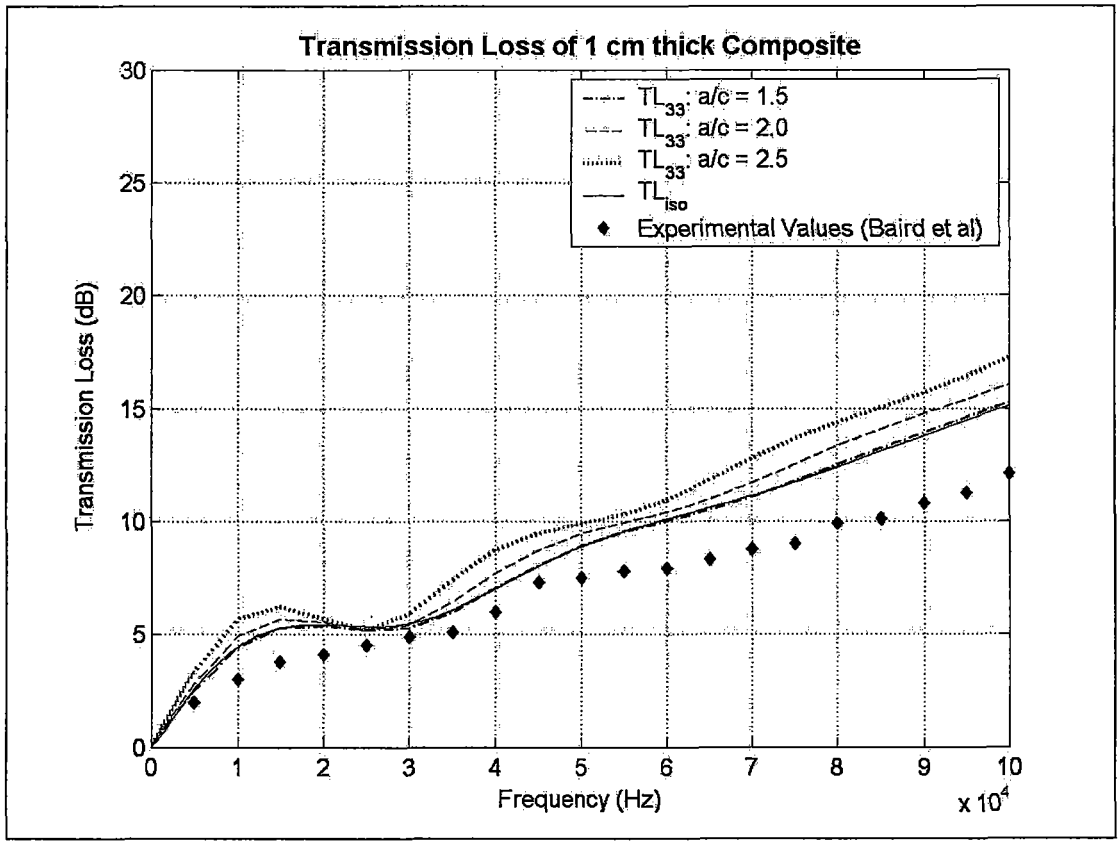

Figure R-5: IAA d'une dalle du matériau viscoélastique composite d'une épaisseur 1 cm. La matrice viscoélastique contient 13% des inclusions enrobées oblates. L'orientation des inclusions est telle que les axes longs sont perpendiculaires aux ondes incidentes. Etude paramétrique sur la variation du rapport des axes : —— $a/c=1$, —·· $a/c=1.5$, - - - $a/c=2$, ... $a/c=2.5$.

Dans le cadre d'anisotropie induit par les inclusions isotropes mais orientées le Figure R-6 considère le coefficient d'affaiblissement d'une onde plane, la partie imaginaire

du nombre d'onde complexe : $\hat{k} = \hat{k}' + i\hat{\alpha}$, en fonction d'angle de propagation de l'onde plan pour plusieurs formes d'inclusion enrobée. Les résultats de cette étude montre clairement que le modèle peut être applique aux problèmes d'homogénéisation à une grande gamme de matériau composites viscoélastique.

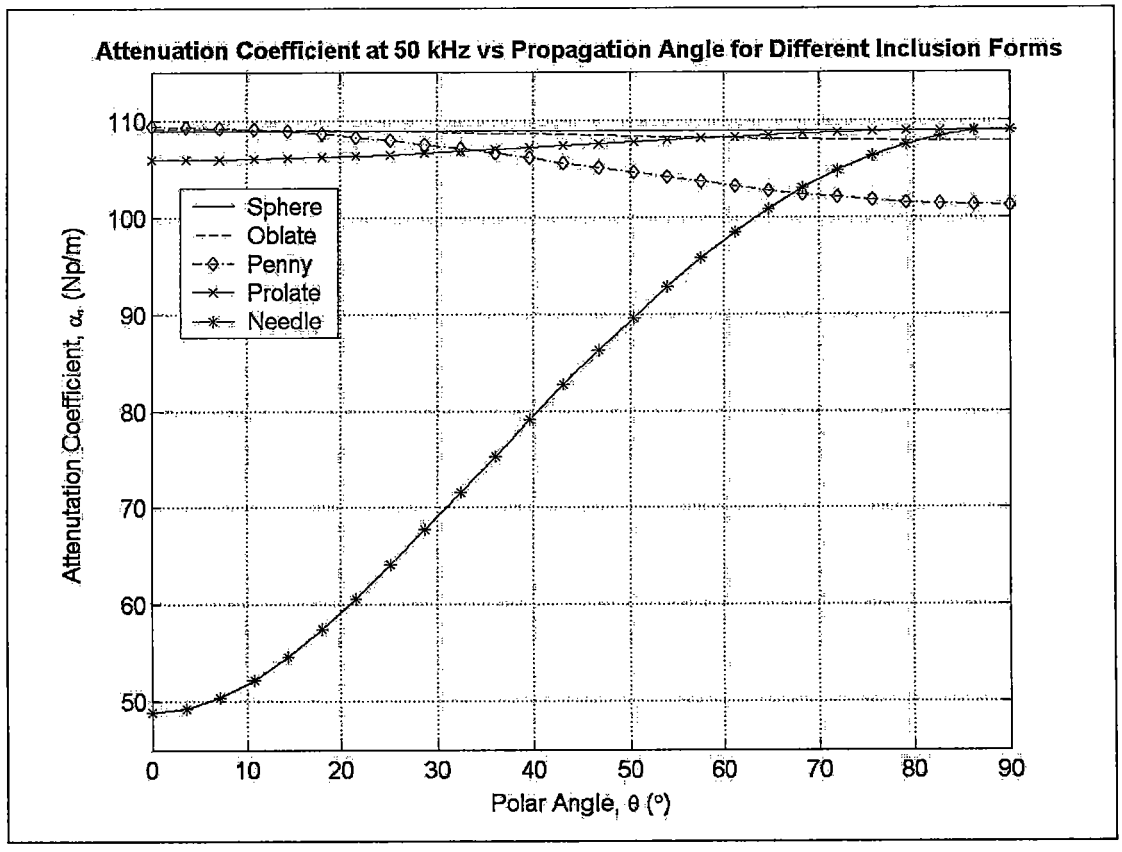

Figure R-6: Coefficient d'affaiblissement en fonction d'angle de propagation dans le plan x_1-x_3 dans un matériau composite viscoélastique avec 10% par volume d'inclusions de verre enrobée par Lucite ($\theta = 0$ représente l'axe x_3). La fréquence des ondes incidentes est 50 kHz.

Une faiblesse du modèle AC employée pour calculé les courbes de Figure R-5 et Figure R-6 est sa limitation aux applications avec les inclusions sphériques ou ellipsoïdales orientées. Une formulation DSCT rend le modèle AC plus robuste en permettant les variations d'orientation et de propriétés viscoélastique des inclusions enrobées. La formulation DSCT est validée avec plusieurs études et comparaisons différentes. Le premier étude compare les calcules AC DSCT avec ceux de Berryman [51] quand le matériau composite se comporte d'un manière isotrope à cause d'une orientation aléatoire d'inclusions ellipsoïdales. Puis la formulation DSCT est

sollicitée afin d'approximer la dépendance directionnelle des propriétés effectives en fonction de l'écart-type de la variation de l'orientation des inclusions ellipsoïdales. Une autre validation de la formulation DSCT est la comparaison du tenseur de rigidité effectif d'un schiste feuilletée possédant plusieurs matériaux différents et une orientation préférentielle de plaquettes d'argile. Les calcules du modèle AC DSCT montre un bon accord avec les données expérimentales de Jones et Wang [77] bien que la modèle micromécanique de Horby *et al* [78]. Une autre étude sur la formulation DSCT montre un bon accord avec les données expérimentales et modèle de dispersion multiple de Ledbetter and Datta [77] d'un composite SiC qui est approximé comme un matériau consistant de trois échelle distincte : sous-micron→meso→macro [79]. Finalement, le modèle AC avec une formulation DSCT est sollicité encore une fois pour approximer IAA d'un composite viscoélastique en prenant en compte un variation de l'épaisseur de l'enrobage des billes de verre creuses étudie par Baird *et al* [76]. Les résultats de ces calcules montrent une amélioration importante d'accord du modèle avec les donnée expérimentales, voire Figure R-7.

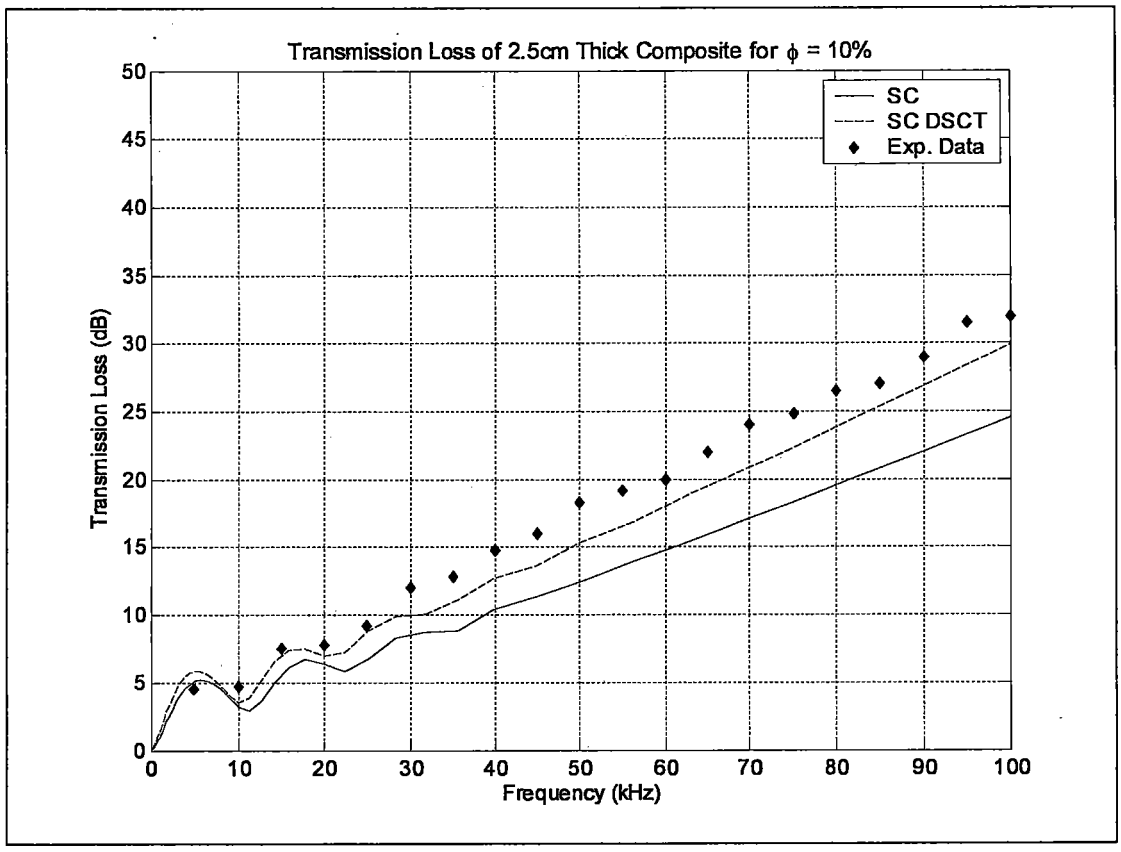

Figure R-7: IAA calculé avec le modèle AC et AC DSCT comparée avec les données expérimentales de Baird *et al* [76].

La dernière partie de Chapitre IV discute les problèmes numériques qui risque de se manifester en employant le modèle AC. Il existe certaines conditions qui rendre le modèle AC instable numériquement. La nature implicite de la solution au modèle AC est la racine de cette instabilité. La majorité de matériaux composites ne possèdent pas une composition de phases et géométrie d'inclusions enrobées qui suffit de rendre instable le modèle AC. Malheureusement, la composition et géométrie d'une grande partie des matériaux considérés par ce travail peuvent facilement rendre instable le modèle AC. La présence d'instabilité est surtout prononcée surtout quand le contraste des tenseurs de rigidité des inclusions et de la matrice est important et les inclusions sont plus souples que la matrice. Cette section discute les conditions clés qui mènent à l'instabilité et aussi plusieurs moyennes de surmonter le problème.

En dépit des complications numériques qui peuvent se manifester avec le modèle AC pour des inclusions enrobées, le Chapitre IV montre, avec les études paramétriques et comparaison avec l'expérience, le niveau de généralité et précision

du modèle AC quasi-statique. Le modèle approxime sûrement le comportement amortissant des composites viscoélastique particulaires. Ce modèle surpasse les modèles à base de dispersion acoustique dans le domaine fréquentiel quasi-statique comme il permet d'intégrer facilement des phases anisotropes aussi bien que les effet d'orientation des inclusions ellipsoïdales. La généralité augmentée du modèle micromécanique AC quasi-statique renforce l'idée de l'intégrer dans une stratégie de la conception des matériaux.

Chapitre V: Vers la conception des matériaux

Un aspect très important de l'approche émergente de la conception des matériaux est le développement des modèles mutli-échelles afin de fournir de l'information du comportement multi-échelle et multi-physique au processus de la conception [14]. Les deux chapitres précédents ont présentés et validés un modèle capable de passer de l'échelle microscopique au comportement macroscopique d'un matériau composite. Par contre, une approche complète de la conception des matériaux serait capable de faire le lien entre les échelles de longueur et temps très disparates (les échelles de longueurs entre atomistique et macroscopique et de temps entre pico-secondes et années). Les méthodes actuelles, et bien sûr le modèle présenté par le Chapitre III, n'est pas d'un tel niveau de complexité. Il est, donc, proposé d'approximer un comportement multi-échelle, en forme d'une plaque sandwich vibrante, avec une hiérarchie de modèles imbriqués, chacun capable de passer entre, au minimum, deux échelles différentes. Cette approche permette la sollicitation de l'ensemble des modèles, qui possède parfois un comportement très complexe dans l'espace de conception, afin de renseigner les stratégies de conception des matériaux amortissants [21].

Une méthode effective d'amortir les vibrations d'une plaque consiste en l'introduction d'une couche viscoélastique entre deux plaques fortement plus rigides que la couche viscoélastique. Cette géométrie force la couche intérieur à subir des

grands déplacements en cisaillement avec l'imposition d'un moment de flexion. Applications pour cette configuration se trouve dans l'industrie aérienne [2] et automobile [1, 5] à cause d'un comportement qui favorise l'isolation acoustique et thermale [80]. Parmi les éléments structuraux dans l'industrie automobile possédant une structure sandwich, on trouve le pare-brise. Celui-ci est l'objet d'étude de l'étude de cas de ce chapitre choisi pour illustrer une approche qui emploie une hiérarchie de modèles imbriqués. L'étude de cas du pare-brise présenté, illustré par le schéma du Figure R-8, consiste en une modèle qui comprendre quatre échelles : (*i*) la microstructure des matériaux constituants, (*ii*) les matériaux constituants (les plaques individuelles), (*iii*) l'élément structurelle (la plaque sandwich), et (*iv*) la structure (la plaque sandwich montée). Il est important de noter que même si la discussion de ce chapitre se centre autour du pare-brise, la démarche et l'analyse peut s'étendre facilement aux autres applications utilisant les plaques sandwich afin d'amortir l'énergie.

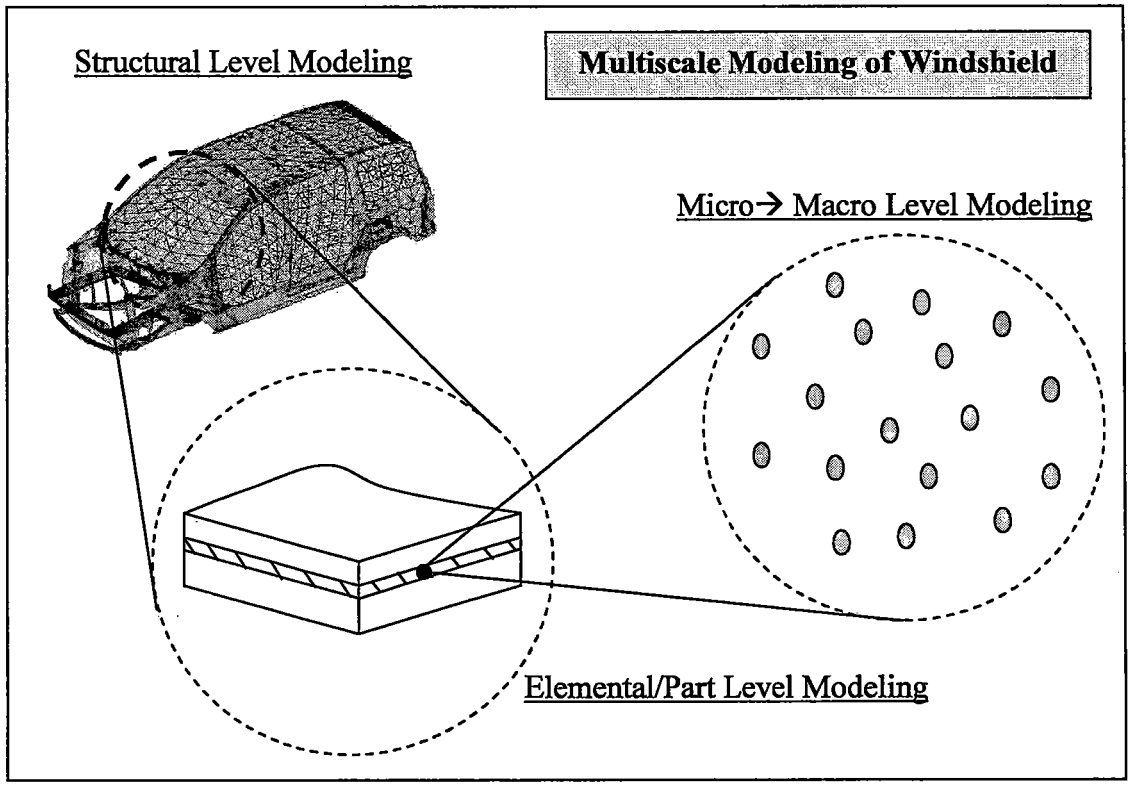

Figure R-8: L'approche de la modélisation multi-échelle d'un pare-brise.

La modélisation du comportement fréquentiel des plaques sandwichs est très développée. Une des premières contributions importantes est celle de Ross, Kerwin, et Ungar (RKU) [81]. Leur modèle utilise une sorte d'homogénéisation de la plaque tenant en compte le cisaillement de la couche viscoélastique suite à une onde de flexion. Le module de flexion effective rendu par ce modèle est complexe et dépende de la fréquence. Suite à leur contribution, la recherche sur le comportement des plaques sandwich s'est bien développée (voire des références exemples [82-87]). Malgré toute cette recherche approfondie, le modèle RKU est souvent employé aux premières étapes de l'étude d'une structure sandwich grâce à sa simplicité, sa précision, et son acceptation universelle. De plus, sa nature analytique le rendre efficace pour des études de sensibilité et pour l'intégration dans les calcules complexe. Pour ces raisons, le modèle RKU est utilisé dans ce travail afin d'approximé le comportement d'une plaque sandwich.

L'étude de cas présenté introduit quelques variables clés de l'espace de conception du comportement amortissant et fourni des informations de leur interaction et leur influence sur le comportement de la structure. L'analyse multi-structurale commence par une section concernant la modélisation de la plaque sandwich. La section met en évidence les effets de la géométrie et le comportement constitutif des matériaux constituants. Une étude de la sensibilité montre clairement que le moyen le plus efficace d'augmenter la capacité amortissante en gardant la rigidité d'une plaque sandwich est la croissance du facteur de perte du matériau viscoélastique en contraint. L'étude de la structure continue avec une analyse du comportement des poutres et plaques vibrantes encastrées aux limites dans un matériau viscoélastique. L'analyse des structures vibrantes consiste en une analyse modale d'après les modèles classiques qui intègre le module de flexion de la plaque sandwich, réalisé avec le modèle RKU. Figure R-9 montre le bon accord avec cette approche et un analyse par éléments finis, introduit par Daya et Potier-Ferry [83], d'un poutre cantilever. La figure montre la variation du facteur de perte du system, estimé par la méthode de la bande passante à trois dB, en fonction du facteur de perte

de la couche et les conditions limite viscoélastique. La différence entre les deux approches augmente avec la valeur du facteur de perte viscoélastique, mais l'approximation par les méthodes simplifiées n'est fiable que pour les facteurs de perte de la couche intérieure inférieures à 0.5 ($\eta_{VE} < 0.5$). L'accord entre ces deux approches justifie l'intégration du modèle RKU avec une formulation classique des plaques et poutres vibrantes pour une analyse des plaques sandwiches pour l'étude élémentaire de la conception des matériaux.

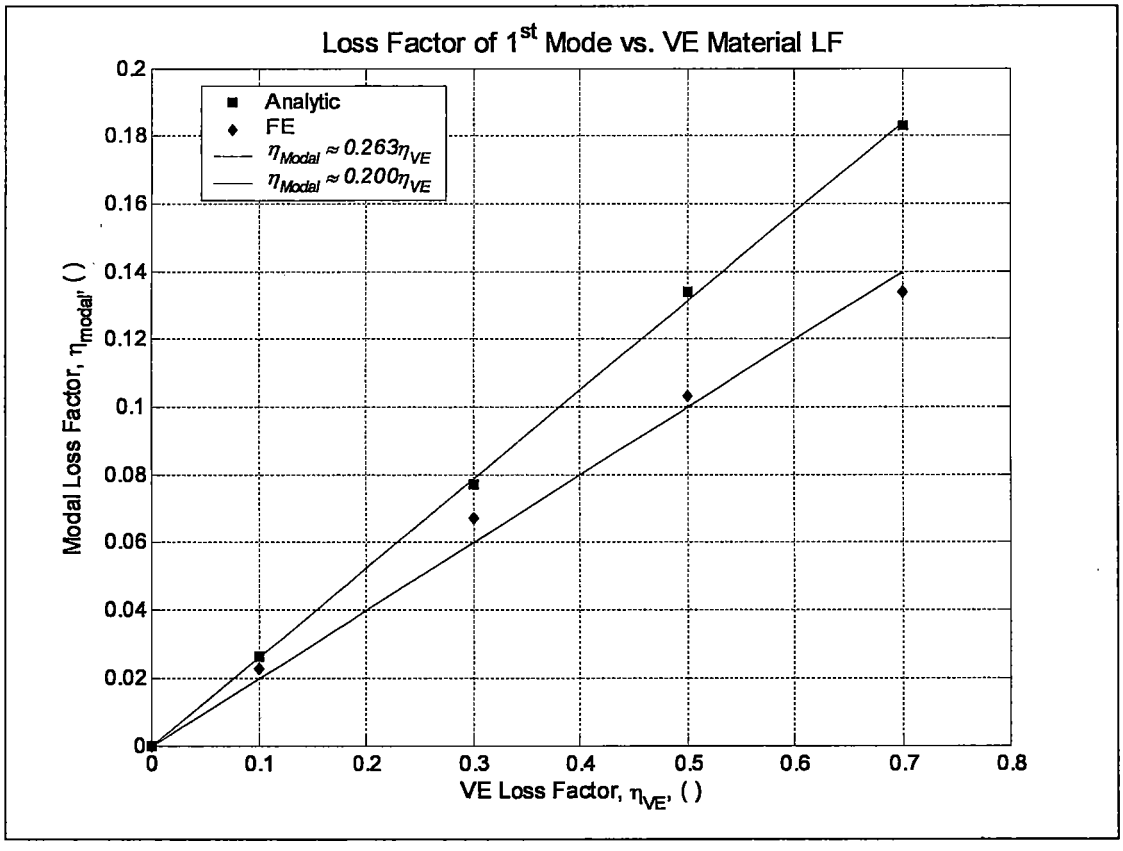

Figure R-9: Le facteur de perte du premier mode d'une poutre sandwiche encastrée dans un matériau viscoélastique. Résultats analytique par une hiérarchie de modèles comparé avec une analyse par éléments fini employant le modèle de Daya et Potier-Ferry [83].

Les résultats du Chapitre IV montrent que le modèle AC quasi-statique donne les bonnes approximations du comportement amortissant des composites viscoélastique. Le but de l'étude actuelle est le renseignement d'une stratégie de la conception des matériaux par le modèle AC. Il est, donc, intéressant d'étudier l'amortissement en fonction de la variation de la microstructure de la couche

viscoélastique d'un pare-brise. Il faut d'abord étudier l'influence de la microstructure sur le comportement de la plaque sandwiche. La Figure R-10 présente une mesure d'amortissement des ondes de flexion, $\hat{\alpha}^{flex}/\hat{k}'^{,flex}$, qui estime la fraction d'amplitude amorti par longueur d'onde [88]. La figure montre une forte augmentation de l'affaiblissement d'une onde de flexion propageant dans la plaque sandwiche, possédant les propriétés et la géométrie d'un pare-brise, en fonction de la faction volumique des vides de la couche viscoélastique (PVB).

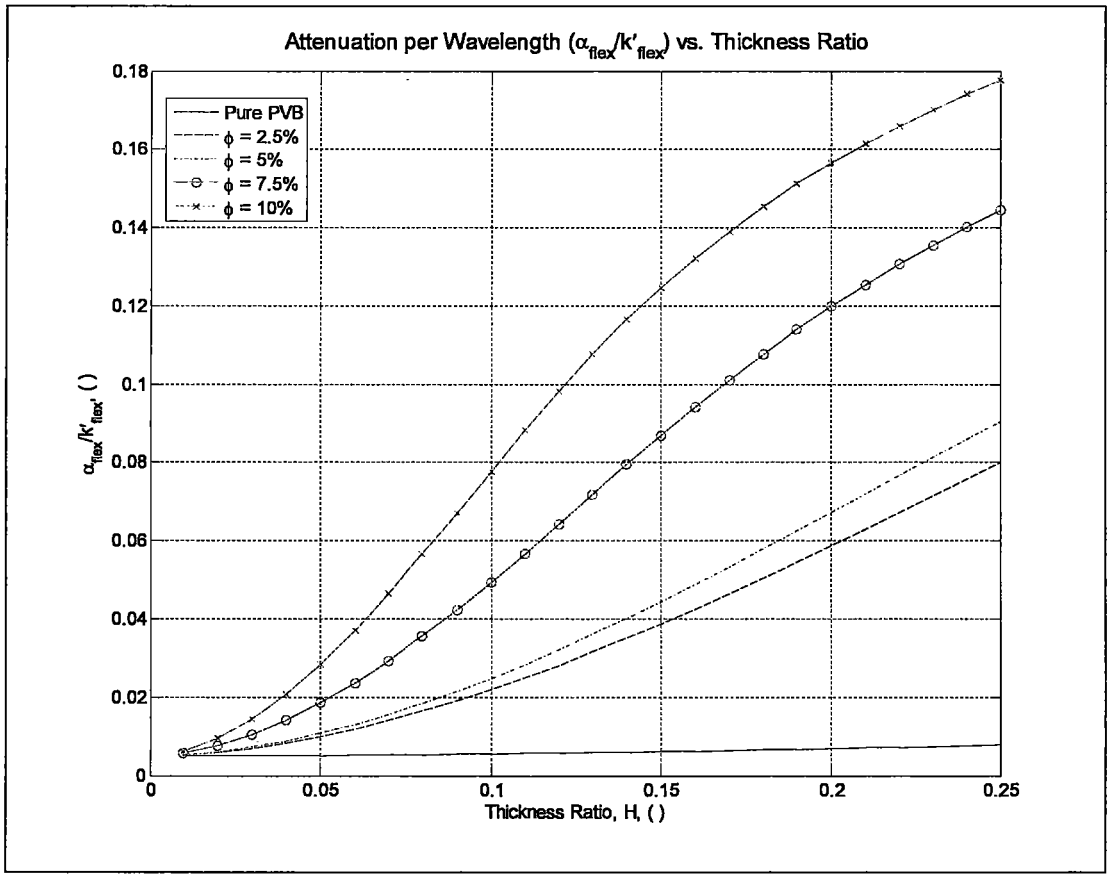

Figure R-10: La fraction d'amplitude d'une onde de flexion amorti par longueur d'onde dans une plaque sandwiche en fonction de la fraction volumique des vides dans la couche viscoélastique approximée par les modèles RKU et micromécanique AC.

La hiérarchie de modèles permet aussi d'illustrer la propagation des effets de la variation de la microstructure au passage de plusieurs échelles de longueurs. La Figure R-11 montre une augmentation quasi-quadratique du facteur de perte modale d'une plaque sandwich circulaire en fonction de la fraction volumique des vides de la

couche viscoélastique. L'augmentation du comportement amortissant observé à l'échelle de la structure n'est pas, malheureusement, très importante comme désiré, ceci peut être attribué aux matériaux traditionnels d'un pare-brise. La recherche actuelle suggère qu'il est fort possible que l'introduction des matériaux non-conventionnels comme hétérogénéité dans la couche viscoélastique puisse mener à augmenter la capacité amortissante à l'échelle structurelle.

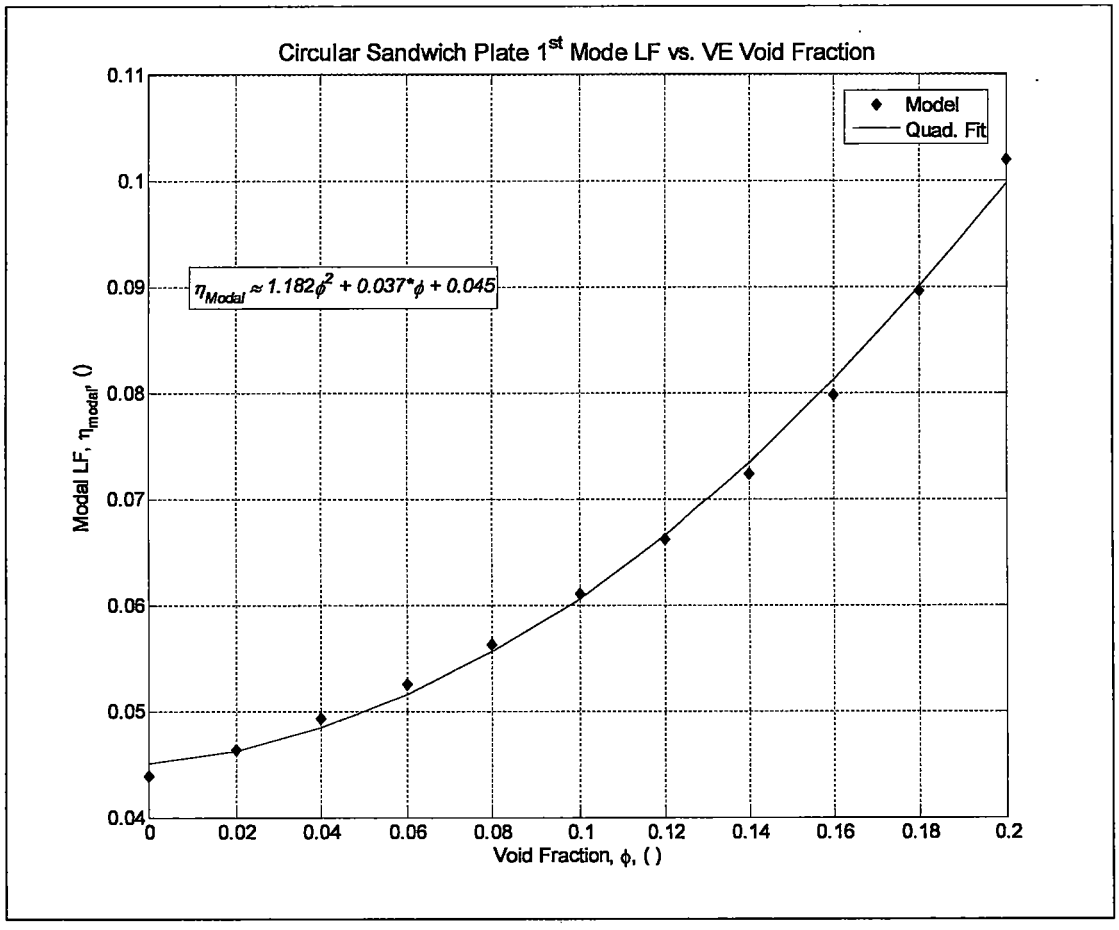

Figure R-11: La variation du facteur de perte du premier mode d'une plaque sandwiche circulaire en fonction de la fraction volumique des vides dans la couche viscoélastique, ϕ.

Un comportement non-conventionel qui mène à une hausse important de l'amortissement macroscopique s'appelle « la rigidité négative. » Les mécanismes d'instabilité de certains matériaux manifestent les grands déplacements suite à un petit chargement qui est bien approximé par une rigidité négative. Le travail de Lakes *et al* [9, 10, 12] montre clairement qu'un tel comportement entrain un croissance très

important de l'amortissement macroscopique. Une hausse significative en comportement amortissant se manifeste quand la valeur du module qui corresponde au chargement, par exemple $\hat{\mu}_I$, s'exprime en fonction du même module de la matrice, $\hat{\mu}_I$, par $\hat{\mu}_I \approx -1.1\hat{\mu}_M$ [9]. La Figure R-12 présente le comportement amortissante à l'échelle structurelle d'un pare-brise sandwich, dont la couche viscoélastique comprend des inclusions ayant une rigidité négative $\hat{\mu}_I \approx -1.1\hat{\mu}_{PVB}$, par approximation de l'IAA en fonction de la fréquence d'une onde plane incidente [89].

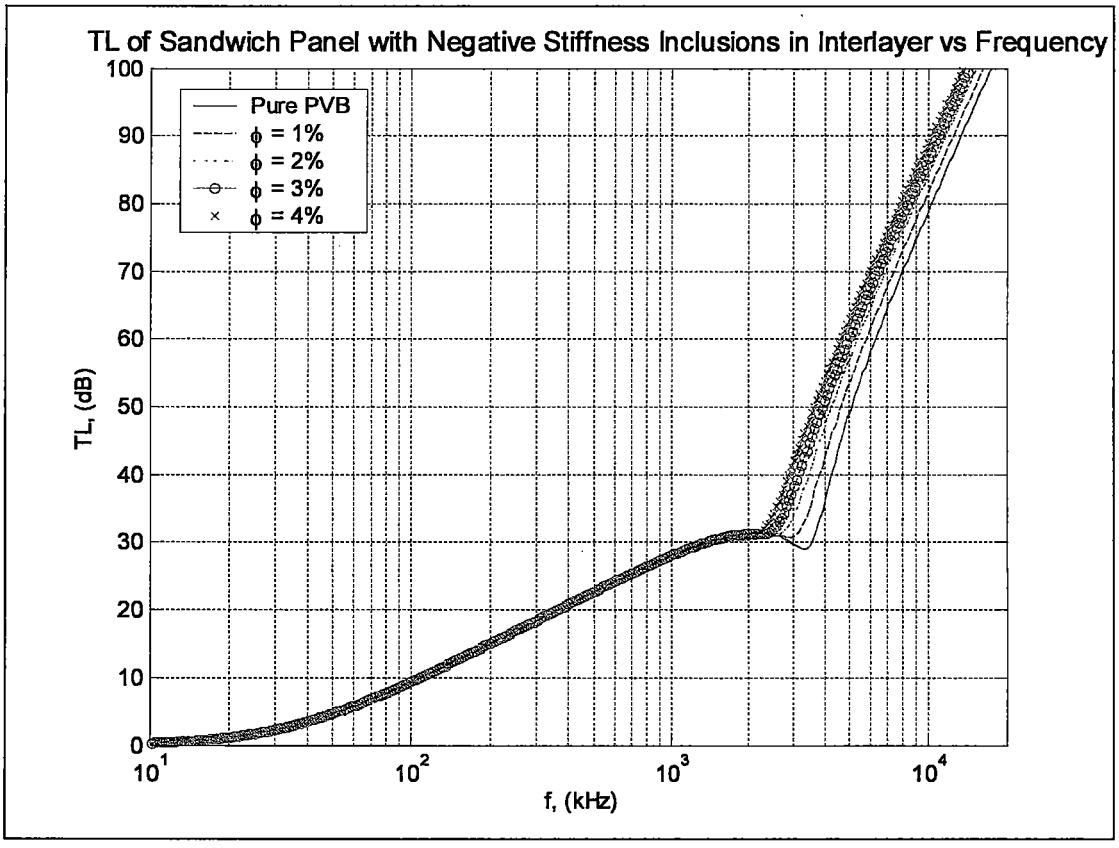

Figure R-12: L'approximation de l'IAA d'une pare-brise dont la couche PVB comprend les petites fractions volumique d'inclusions instables ($\mu_I = -1.1\mu_{PVB}$).

Les résultats montrent une croissance dramatique de la capacité de la structure pour dissipé de l'énergie à la fréquence coïncidente. Certainement, l'introduction des inhomogénéités de rigidité négative mène à une réduction en IAA à la fréquence coïncidente presque complète, même à faible fraction volumique des inclusions.

En dépite du faite que les courbes de la Figure R-12 représentent le comportement d'un matériau hypothétique, il est très intéressante de montrer que la méthodologie d'une hiérarchie de modèles imbriqués capte bien ce comportement non-conventionelle. Il met en évidence un niveau de control augmenté sur les variables dans l'espace de conception. Il montre aussi la fiabilité, la puissance, et surtout la flexibilité d'une telle stratégie pour renseigner la conception des matériaux. L'étude de cas présenté valide, surtout, l'intégration du modèle micromécanique AC dans une stratégie de la conception des matériaux et incite la recherche approfondie des microstructures qui mène aux effets structurels amortissants prononcés.

Chapitre VI: Conclusions et perspectives

Le chapitre final donne des conclusions générales de la thèse. Les résultats et contributions importants des modèles et méthodes présentées en chaque chapitre sont résumés et discutés. Ils donnent des perspectives sur le rôle du travaille présenté et suggère des avenues de recherche approfondi. Finalement, le chapitre se termine avec une discussion de l'importance de la modélisation multi-échelle et multi-fonctionelle des matériaux dans l'avenir de la conception des matériaux.

CHAPTER I

INTRODUCTION

1.1 Objective and motivation

The principal objective of this thesis is the derivation, development, and validation of a quasi-static self-consistent micromechanical model to facilitate the exploration and generation of design specifications for absorptive materials.

Throughout history humankind has created tools and structures to satisfy wants and needs. These structures are omnipresent in daily life and range in form and function from buildings, to cars, to computers, to airplanes. The success of any given structure depends entirely on a hierarchy of elements and the design of those elements. This hierarchy includes the structure as a whole, the individual structural elements, the components comprising each of those individual elements, the materials from which each component is fabricated, and finally the composition of those materials [90]. In other words, a structure can be viewed as a system which possesses elements that exist at multiple length scales. Behavior of the structure as a whole is governed by behavior at each individual length scale and by interactions between those length scales [14]. True engineering design must take this fact into account. It is clear, therefore, that successful design must consider not only the design of each element at its length scale, but also the complex interaction of the hierarchy of length scales [91]. This design philosophy can ideally be extended to include even the design of the materials.

Classic design methods require the selection of materials which conform to the needs of the preconceived whole [19]. This design methodology is well developed and well understood. Unfortunately, the limiting factor in design when applying this approach is very often the lack of available materials which meet the needs of the structure, thereby limiting the entire design processes [14, 15]. The intertwined fields of composite material design, manufacture, and modeling have developed in response to this lack of available materials and have greatly supplemented the design process. Though these fields address the lack of available materials, as currently implemented they still simply create materials to be selected from a list for subsequent design needs through the material selection approach. Such an approach, though very useful for many applications, ignores a more elegant solution which aims to create materials specifically conceived for the demands of a given application [21]. Such an approach not only creates materials for specific needs but also includes material creation in the design of the system as a whole, and is therefore usually called material by design [90].

Material by design, or simply material design, is a very active area of research. One well accepted approach to material design aims to extend a systems design to include the concurrent design of materials for specific high importance components [14, 21, 91]. This extension is very natural as materials themselves can easily be viewed as multiscale structures [90, 92]. Such a strategy ensures the function of the structure and gives ultimate control to the designer. The study of material design is, however, very new and requires considerable research before being a viable option for engineers. Detailed development and investigation of multiscale structures, which includes multiscale material models, is a key aspect of such research. These investigations yield a great deal of information and understanding about the effects of material structure on desired structural behavior [20, 22]. This information can then be used to inform material design strategies.

Material design is inherently a multiscale and multi-physics problem as the demands of a structure include thermal, electrical, and mechanical loading at all

length scales. One area of interest in many engineering domains is the dissipation of energy. Applications for materials with a high capacity to absorb acoustic and vibrational energy can be found in almost every industry. For example, high loss materials are often used as a filler in structural elements such as the fuselage of an aircraft [2] or the chassis of an automobile [1]. As filler, such materials simultaneously reinforce the structure and reduce vibrations and noise. Similar energy attenuation benefits are realized when these high loss materials are used in the form of coatings and layers. Coating treatments have been employed for noise abatement in plenum chambers and ducts [3], on vibrating structures [4], and in automobile windshields [5]. Furthermore, it is known that the damping capacity of materials can be increased by introducing heterogeneities [6] into the material, thereby creating a particulate composite material. Due to the large number of potential applications for lossy materials, constitutive modeling of viscoelastic composite materials is of great interest and has been for nearly half a century [7, 8]. Recent research suggesting the possibility of creating composites that exhibit extremely high damping [9-13] combined with advances in the design of materials [14, 15] has given renewed impetus to research in the modeling of viscoelastic composite materials. For this reason, this thesis concentrates on modeling particulate composites for damping applications and moves towards the implementation of the proposed model in a material by design scheme.

1.2 Hypothesis and strategy

The development of a quasi-static frequency domain self-consistent micromechanical model will provide a tool for the design of absorptive materials.

The first step in validating this hypothesis is the development of a robust quasi-static frequency domain self-consistent (SC) micromechanical model. This model must be capable of approximating the effective frequency dependent behavior of various complex particulate composite materials. Model inputs will be the material properties of each constituent phase and the inclusion shape and orientation. The desired model output is the effective frequency dependent tensors describing isotropic or anisotropic viscoelastic composite material behavior. Validation of the model will be accomplished through comparisons with theoretical bounds for complex composite media, accepted models, and experimental data and through parametric studies. To further validate this hypothesis, the SC model will be integrated into a simple multiscale structural model. The goal of this example is to observe trends, to compare simulated multiscale model behavior with experimental data and finite element approximations, and to study the effect of material microstructure on structural behavior.

1.3 Thesis overview

This thesis is divided into six chapters. The following chapter, Chapter II, summarizes the principles employed throughout the thesis and notes many important works from which considerable background has been gathered. Chapter II begins with a general discussion regarding energy dissipation in both homogeneous and heterogeneous materials and recalls measures of energy dissipation. A structural vibrations approach to energy dissipation is then discussed. The approach presented employs the relationship between energy dissipation and strain energy. After examining strain energy dissipation approximations the chapter then discusses acoustic scattering in particulate composites, its fundamental physical principles, and related modeling methods. This chapter terminates with a detailed bibliographical review of the two prominent research areas covered in this thesis: (*i*) homogenization

techniques for modeling effective particulate composite material behavior from both the static (micromechanical) and the dynamic (acoustic scattering) perspectives, and (*ii*) important developments in material by design research using a multiscale and multi-physics approach.

Chapter III derives a SC micromechanical model in the quasi-static frequency domain for a composite consisting of a viscoelastic host containing viscoelastic ellipsoidal coated inclusions. This is achieved by extending the static model of Cherkaoui *et al* [23, 24] to include the constitutive frequency dependence of the constituent phases. The derivation is posited on the elastic-viscoelastic correspondence principle and employs Green's formalisms and interfacial operators to arrive at a general frequency dependent homogenization model for particulate composites. The resulting quasi-static model is then generalized using dilute strain concentration tensor (DSCT) formulation. This generalization permits the homogenization of composites containing a large array of coated inclusions, inclusion orientation distributions, and coating thicknesses.

The purpose of Chapter IV is to validate the quasi-static SC model though comparisons with accepted analytic bounds, acoustic scattering based models, and static and acoustic experimental data. The chapter begins with an overview of the important contributions in bounding methods for complex valued effective material behavior. Three specific complex bounding techniques are introduced and approximations from the quasi-static SC model derived in Chapter III are shown to fall within those bounds. The model is then employed in several elementary studies concerning the particulate composite lossy behavior. The SC model is employed to approximate the isotropic composite material behavior of a viscoelastic material containing spherical hollow glass micro-spheres [93]. SC model results are used to calculate the transmission loss (TL) of a layer of this composite material submerged in water. These results are shown to agree with an acoustic scattering model proposed by Baird *et al* [76] and experimental TL data from the same authors. Oriented ellipsoidal coated inclusion effects are then examined via parametric studies of TL,

complex wavenumber, and complex sound speed for hypothetical materials created from the same constituent phases as those studied by Baird *et al* [76]. The next validation step is an illustration of SC DSCT model generality. The SC DSCT model is first used to approximate isotropic behavior resulting from a uniform distribution of ellipsoidal inclusions embedded in a host material. These results are compared with a model proposed by Berryman for a lossy rock-water suspension as a function of volume fraction [51]. This comparison validates the usage of the SC DSCT form to approximate the effects of varying ellipsoidal inclusion orientation on macroscopic composite material behavior. The next SC DSCT model check presents a parametric study of inclusion orientation distribution on macroscopic composite anisotropy. The SC DSCT model is compared with the experimentally obtained and theoretically approximated stiffness values of a composite shale material studied by Jones and Wang [77] and Hornby *et al* [78], respectively. The shale material studied by these researchers consisted of several different mineral phases embedded in preferentially oriented clay platelets. Effective stiffness tensor approximations provided by the SC DSCT model show good agreement with both experimental and theoretical values provided by these researchers. The SC DSCT model is then employed to approximate the behavior of a silicon carbide – aluminum composite material. Due to fabrication processes, the microstructure of this composite is best described as consisting of two distinct length scales: (*i*) sub-micron SiC particulates embedded in an Al matrix, and (*ii*) identically oriented mesoscopic Al particulates embedded in a SiC-Al composite. The effective behavior of this composite was approximated using the SC DSCT via a nested multiscale approach (sub-micron→meso→macro) and shows good agreement with both the multiple scattering model and experimental data provided by Ledbetter and Datta [79]. Finally, the SC DSCT model is validated by returning to the analysis of the particulate composite slab TL data provided by Baird *et al* [76]. The SC DSCT model is employed to approximate the effects of coating thickness variation on the observed TL. The result of this approximation shows large improvement in agreement with experimental data over the simple single-thickness approximation.

Chapter V investigates the feasibility of quasi-static SC model implementation as a tool for a material by design strategy. This is achieved by integrating a hierarchy of models which are valid on each length scale of a simple dynamic structure: a vibrating sandwich plate. This structural element is analogous to an automobile windshield and was chosen to show the practical implications of this approach. Modeling begins by discussing the relevant part and structure level models for a vibrating sandwich plate. Part level modeling consists of finding the effective sandwich plate bending modulus using the constrained layer damping model derived by Ross *et al* [81]. Analysis of sandwich plate behavior begins with parametric studies on the constituent material behavior and geometry of a sandwich plate to provide information about effective lossy sandwich plate behavior. Sensitivity analysis of the effective modulus yields information which can be applied to efficiently increase lossy plate behavior. This model is validated though comparison with experimental TL data from several different layered windshield samples. Next, models for a viscoelastically constrained beam and plate are employed to study the contributions of lossy plate and boundary condition behavior to the modal loss factor of a vibrating plate. The beam and plate models used for this study were derived using classic beam and plate theory. These models represent the structural level behavior of the simple multiscale example. The structure and part level models are then integrated and compared with finite element approximations of the modal loss factor for a viscoelastically constrained "cantilever" sandwich beam. Finally, SC model approximations of the behavior of a particulate composite constrained layer and/or boundary conditions are integrated into the part and structure level models to yield a nested hierarchy of behavioral models. The integration of these models permits the study of microstructural effects on the dissipation of structural vibrations. Voided viscoelastic materials are shown to increase the structural damping of a circular sandwich plate and the increases in modal loss factor is shown to increase quadratically as a function of void fraction. Windshield TL is then approximated by integrating part level and material homogenization models combined with the analytic

modified-mass law [89]. Voided interlayer materials yield TL improvements near coincidence, though they are marginal. A simple example of high loss composites employing negative stiffness inclusions [9, 10, 12], however, are shown to greatly improve TL behavior at coincidence. The results of this chapter are very encouraging and suggest that the quasi-static SC model can easily be implemented as tool in a material by design strategy.

The final chapter, Chapter VI, concludes and summarizes the important results and contributions from the models and methods presented in each chapter. This chapter also presents some perspectives on the role of the work presented in this thesis and suggests avenues for future research.

CHAPTER II

BIBLIOGRAPHIC REVIEW AND PRINCIPLES

2.1 Damping materials

Applications for materials with a high capacity to absorb acoustic and vibrational energy can be found in almost every industry. For example, high loss materials are often used as a filler in structural elements such as the fuselage of an aircraft [2] or the chassis of an automobile [1]. As filler, such materials simultaneously reinforce the structure and reduce vibrations and noise. Similar energy attenuation benefits are realized when these high loss materials are used in the form of coatings and layers. Coating treatments have been employed for noise abatement in plenum chambers and ducts [3], on vibrating structures [4], and in automobile windshields [5]. Furthermore, it is known that the damping capacity of materials can be increased by introducing heterogeneities [6] into the material, thereby creating a particulate composite material.

Due to the many different areas for application of high loss materials, constitutive modeling of viscoelastic composite materials has been [8, 27] and remains of high interest in many different engineering fields. This work derives, develops, validates, and explores a multiscale material model of lossy composite materials for future implementation in a material by design strategy. Such material modeling begins with a fundamental understanding of the physical processes that lead to damping behavior. This section, therefore, gives a brief overview of the mechanisms that lead to energy absorption, the mathematical tools used to

approximate lossy behavior, and the simplifying assumptions employed throughout this thesis.

In general, all materials that display damping behavior can be defined as viscoelastic materials [75]. Viscoelastic behavior is fundamentally due to the intrinsic absorption of dynamic strain energy in a material by conversion to heat. Crystallographic materials, such as metals, convert strain energy to heat through internal friction while energy absorption in polymeric materials is the result of molecular chain sliding and relaxation. In general, the stress in a viscoelastic material is dependent on imposed strain rate. This rate dependence translates to a stress response in the frequency domain that is called a relaxation spectrum. The relaxation spectrum of a viscoelastic material shows that the stress level is dependent on both the magnitude and frequency of the applied strain [94]. In most cases the stress-strain relationship in crystallographic materials is very weakly rate dependent and leads to a broadband damping response in the frequency domain. The magnitude of this broadband damping capacity is also very small and for these two reasons metals are seldom referred to in the context of viscoelastic behavior. Polymeric materials, on the other hand, display both high rate dependences and high losses and are therefore classified as viscoelastic. It is important to note, however, that all small strain behavior of real materials can be classified, to a certain degree, as viscoelastic [94].

A simple method to show the principles of viscoelastic material behavior is to discuss the time dependent behavior of a one-dimensional sample such as a bar. The phenomena that typify the viscoelastic response of a bar are creep and stress relaxation. Creep is the strain increase over time due to constant applied stress and stress relaxation is the decay of the stress level in a material when subjected to a constant strain [75]. These two phenomena are shown graphically in Figure 2-1 and Figure 2-2, respectively.

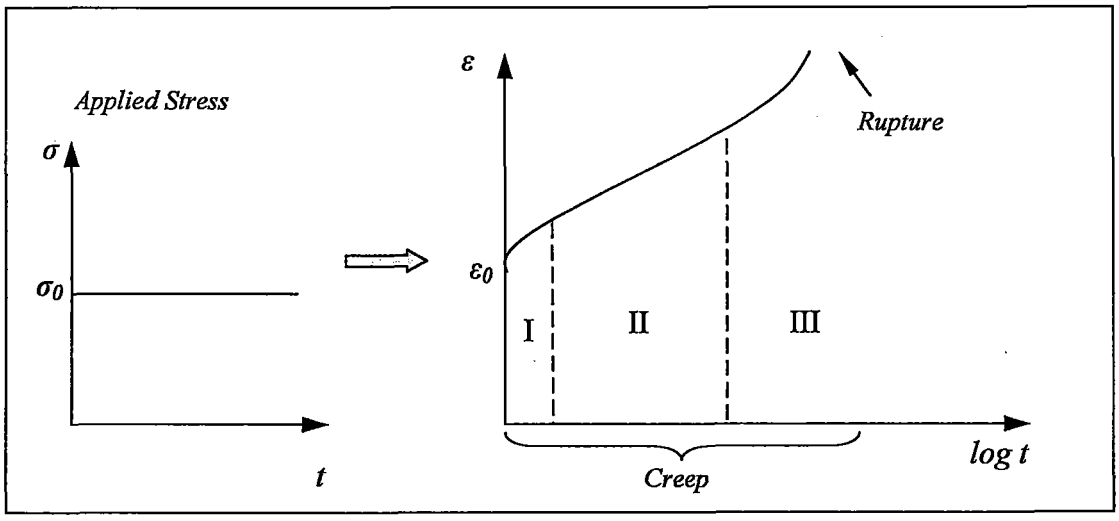

Figure 2-1: Evolution of the strain, ε, of a bar under constant stress, σ_0 (creep response). I, II, and III represent the three stages of creep. ε_0 is the value of the elastic strain.

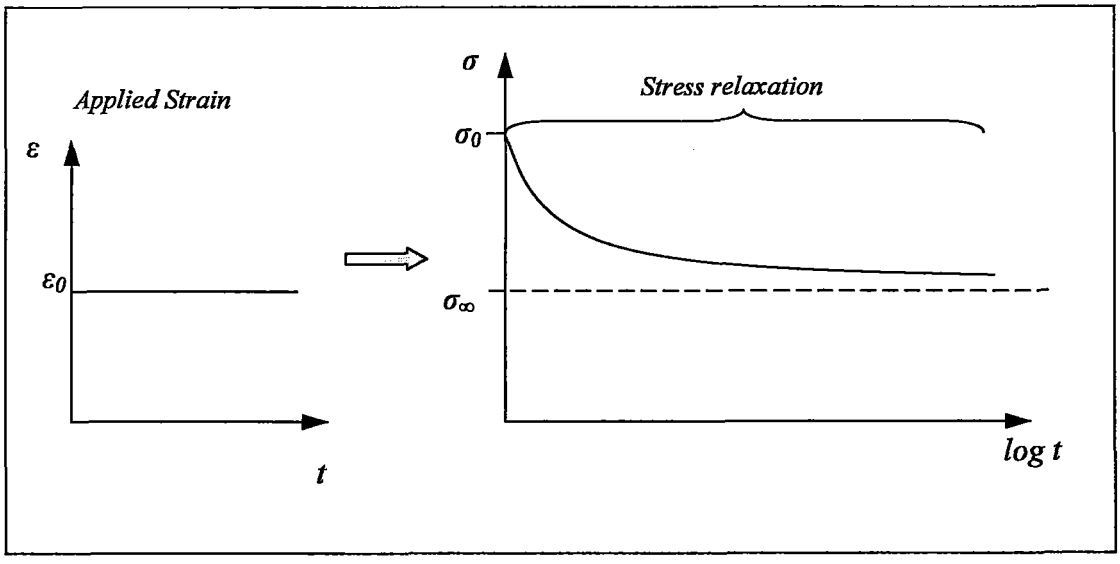

Figure 2-2: Stress relaxation, σ(t), in a bar under constant strain, ε_0. σ_0 is the value of the elastic stress and σ_∞ is the limiting value of σ(t) as $t \rightarrow \infty$.

The initial elastic response represents only an infinitesimally small fraction of the total response time in most materials and has therefore not been included in the figures above. It is also very important to stress that the viscoelastic response *is not* characterized by the whole of the responses illustrated above because they display both the elastic and plastic response of a material. Viscoelastic behavior involves only recoverable deformation and therefore is more conceptually related to elasticity. However viscous behavior, which is generally associated with inelastic deformation, must be used to describe the lossy component of viscoelastic materials. These two

figures clearly illustrate that the material response can be decomposed into two parts: (*i*) the elastic part and (*ii*) the viscous part [95]. Using this information, the moduli relating the time dependent stress or strain to the loading condition is written in the very general form of Equations (II.1.1) and (II.1.2) below.

$$\sigma(t) = \sigma_0 + \int_0^t E(t-\tau)\frac{d\varepsilon(\tau)}{d\tau}d\tau \qquad \text{(II.1.1)}$$

$$\varepsilon(t) = \varepsilon_0 + \int_0^t J(t-\tau)\frac{d\sigma(\tau)}{d\tau}d\tau \qquad \text{(II.1.2)}$$

In the above expressions, $E(t)$ is the relaxation modulus and $J(t)$ is the relaxation compliance of the material, $\sigma(t)$ and $\varepsilon(t)$ represent the total stress and strain of the material respectively at time t, σ_0 and ε_0 are the initial elastic stress and strain, and τ is the retarded time. The elastic values of stress and strain are given via the one dimensional Hooke's law as: $\sigma_0 = E_0\varepsilon_0$ and $\varepsilon_0 = \sigma_0/E_0 = J_0\sigma_0$. Expressions (II.1.1) and (II.1.2) show that the stress and strain at any given time is a function of both the initial elastic response and some value that evolves with time according to the integral on the right-hand side (RHS). This integral represents a material memory function that takes the loading history into account in the present value and is the source of the phase lag / hysteresis observed in viscoelastic materials when submitted to cyclic loading [94].

Noting that Equations (II.1.1) and (II.1.2) are mathematically analogous, the following analysis will be carried out for the stress relaxation case only. Given a time varying imposed strain, $\varepsilon(t)$, the stress at any time can be determined from Equation (II.1.3) below.

$$\sigma(t) = E^e(t)\varepsilon(t) + \int_0^t E^M(t-\tau)\frac{d\varepsilon(\tau)}{d\tau}d\tau \qquad \text{(II.1.3)}$$

In this expression, $E^e(t)$ represents the elastic part of the material response at time *t*, and $E^M(t)$ is the rate dependent material memory function. The elastic function represents the material stiffness at time *t* and the memory function is dependent on the mechanical loading history from time $t = 0$ to the present time, *t*. This formulation of the material behavior is called the Boltzmann equation which takes the relaxation of the material into account [6]. From this relationship it is easy to show that Equation (II.1.3) is the time domain representation of a *complex* Young's modulus in the frequency domain. The frequency dependent complex modulus is found by applying the Fourier transform to both sides of Equation (II.1.3). The integral in (II.1.3) represents the convolution of $E^M(t)$ with the applied strain rate, $d\varepsilon(t)/dt$. The application of the Fourier transform and some simplification will yield the following frequency dependent complex modulus representation of the time dependent behavior given in (II.1.3) [6, 75]:

$$\hat{\sigma}(\omega) = \hat{E}'(\omega)\left[1 - i\hat{\eta}_E(\omega)\right]\hat{\varepsilon}(\omega) \qquad \text{(II.1.4)}$$

where $\hat{\eta}_E(\omega)$ represents the Young's modulus loss factor defined as $\hat{\eta}_E(\omega) \equiv \hat{E}''(\omega)/\hat{E}'(\omega)$. The exact relationships between the variables $E^e(t)$, $E^M(t)$, $E'(t)$, and $E''(t)$ depend on the material model employed and therefore are not explicitly given here, see Christensen [96] for a more detailed analysis. It is important to note that the Euler's equation convention employed above is the '$e^{-i\omega t}$' convention shown in Equation (II.1.5). This convention is employed throughout this work.

$$e^{-i\varphi} = \cos(\varphi) - i\sin(\varphi) \tag{II.1.5}$$

Equation (II.1.4) can be written in the same form as its static equivalent. The ability to describe viscoelastic material behavior by substituting complex valued variables into classic behavioral laws in place or purely real variables is called the elastic–viscoelastic correspondence principle [75]. The corresponding one dimensional viscoelastic Hooke's law is given in (II.1.6).

$$\hat{\sigma}^*(\omega) = \hat{E}^*(\omega)\hat{\varepsilon}^*(\omega) \tag{II.1.6}$$

In the above expression the * indicates that the quantity is complex in general. The real part of the complex Young's modulus, $\hat{E}'(\omega)$, is called the storage modulus and represents the part of the material behavior that stores energy. The imaginary part, $\hat{E}''(\omega)$, is called the loss modulus, and describes material behavior that dissipates energy. This complex representation of the rate dependent lossy behavior of viscoelastic materials through complex moduli in the frequency domain greatly facilitates material behavior calculations. It is for this reason that the lossy behavior of a viscoelastic material is almost always represented in this simplified form and it has been shown to be applicable to micromechanical modeling [53, 97-99].

Now consider the case where $\varepsilon(t)$ is imposed and is, therefore, a purely real function of time. Equation (II.1.6) then simplifies to the following representation.

$$\begin{aligned} \sigma_0 e^{-i(\omega t-\varphi)} &= E_0 e^{i\varphi}\varepsilon_0 e^{-i\omega t} \\ \sigma_0 e^{i\varphi} &= E_0 e^{i\varphi}\varepsilon_0 \end{aligned} \tag{II.1.7}$$

Noting that the tangent of the loss angle, φ, given in Equation (II.1.7) is the equal to the Young's modulus loss factor, $\hat{\eta}_E$.

$$\hat{\eta}_E = \tan\varphi \tag{II.1.8}$$

All variables with a subscript "$_0$" in the above equations represent the magnitude of the corresponding variable [6].

It is important to recognize that representing viscoelastic behavior by employing the elastic-viscoelastic correspondence principle greatly simplifies mathematical models of the complex physical mechanisms leading to lossy behavior in any material. For example, when a time varying strain is imposed on a one-dimensional material sample the material immediately develops some stress depending on the strain rate and the specific material. The imposed deformation is completely recovered upon unloading, but the recovery path is not linear (as is evidenced from Equation(II.1.2)). Just after loading, the material relaxes leading to a stress reduction. The stress relaxation results in a phase lag between the imposed cyclic strain and the resulting cyclic stress. The phase lag, shown in Figure 2-3, is directly related to the loss factor of the material through relation (II.1.8). This lag corresponds to a hysteresis loop that is traced in the $\varepsilon(t) - \sigma(t)$ plane as a function of time. The area of this hysteresis loop is what quantifies the absorption of the strain energy by the viscoelastic material.

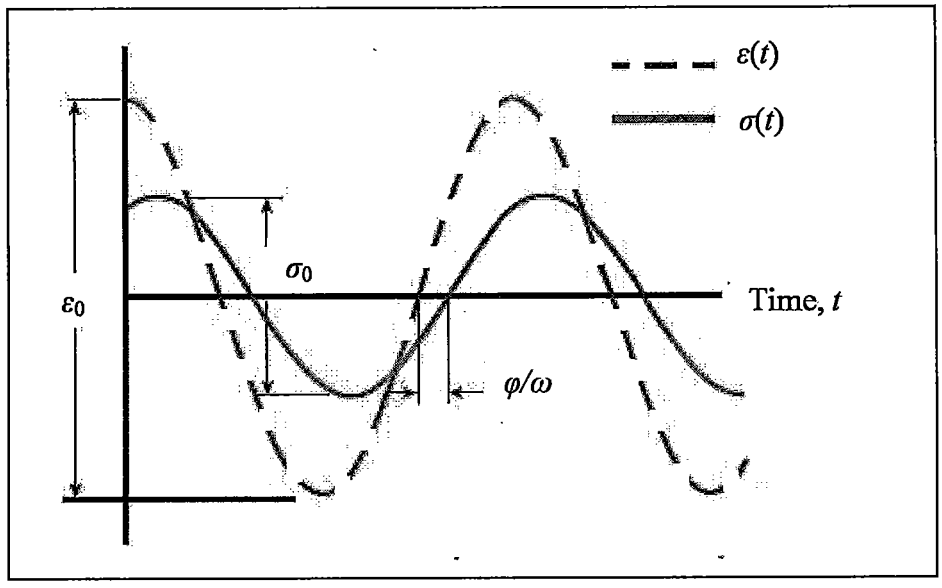

Figure 2-3: Time domain response of a one dimensional sample of viscoelastic material to an imposed cyclic strain.

Finally, it should be noted that the above simple demonstration only considered material behavior in extension, though an identical analysis could have been carried out for shear or volumetric behavior. It is therefore possible to extend the one dimensional relations given above to the more general case of viscoelastic anisotropy. As discussed above, due to the elastic-viscoelastic correspondence principle, extension of the constitutive laws of one dimensional viscoelastic behavior to behavior in three dimensions is almost trivial. Relations (II.1.9) and (II.1.10) give the constitutive viscoelastic material behavior laws for an anisotropic viscoelastic solid.

$$\hat{\sigma}^*_{ij}(\omega) = \hat{C}^*_{ijkl}(\omega)\hat{\varepsilon}^*_{kl}(\omega) \qquad \text{(II.1.9)}$$

with:

$$\hat{C}^*_{ijkl}(\omega) = \hat{C}'_{ijmn}(\omega)\left[I_{mnkl} - i\hat{\eta}_{mnkl}(\omega)\right] \qquad \text{(II.1.10)}$$

Where I_{ijkl} represents the fourth order identity tensor defined below.

$$I_{ijkl} = \tfrac{1}{2}\left(\delta_{ik}\delta_{jl} + \delta_{il}\delta_{jk}\right) \qquad \text{(II.1.11)}$$

Equation (II.1.9) is the general form of the elastic-viscoelastic correspondence principle. In this form, both the frequency dependent stiffness, $\hat{C}'_{ijkl}(\omega)$, and the loss factor, $\hat{\eta}_{ijkl}(\omega)$, can depend on direction. A large part of this thesis deals with the approximation of the frequency dependent complex stiffness tensor, $\hat{C}^*_{ijkl}(\omega)$, of viscoelastic particulate composites through micromechanical methods. The aim of this modeling is to validate a material model for future introduction into a material design strategy.

The following sections introduce two different approaches utilized to approximate the macroscopic damping behavior of a particulate composite. Section 2.1.1 presents the idea of approximating structural damping capacity through strain energy methods. This approach is wide spread in the field of structural vibrations, but the same rationale can also be applied, within certain limits, to composite material modeling. The strain energy approach approximates the damping capacity by calculating the ratio of the strain energy in lossy components to the total strain energy in the structure. Section 2.1.2 presents a completely different approach based on the physics of acoustic wave propagation. This methodology is based on the mechanisms of the reflection and mode conversion of waves incident on a material heterogeneity. These two approaches are based on very different physical concepts. Each approach merits study, however, since the physical mechanisms they describe are all present in the dynamic behavior of particulate composites.

2.1.1 Strain energy methods for approximating damping capacity

One well known method for approximating the damping capacity of structures with lossy components in the field of vibrations is called the strain energy method. This approach consists of calculating the ratio of two different measures of strain

energy. The numerator is the sum of the product of the strain energy, W_i, and material loss factor, η_i, of all lossy elements of the structure, and the denominator is simply the sum of the strain energy in every structural element [99]. Ungar and Kerwin introduced this approach which relationship (II.1.12) summarizes [16].

$$\eta_{tot} = \frac{\sum_{i=1}^{N} \eta_i W_i}{\sum_{i=1}^{N} W_i} \tag{II.1.12}$$

This relationship is a direct result of the complex modulus formulation employed in modeling viscoelastic materials. For the unidirectional loading case, the material's loss factor is related to the strain energy and the hysteresis area via the following relationship:

$$\eta = D/\pi\sigma_0\varepsilon_0 \tag{II.1.13}$$

Here D represents the hysteresis area and the denominator is the total strain energy of one cycle of loading. Given the definition of specific strain energy (energy per unit volume), $W \equiv \pi\sigma_0\varepsilon_0$, and by setting $N = 1$, Equation (II.1.12) reduces to the definition of the material loss factor for a single lossy element. Expression (II.1.12) generalizes this rationale to a system of N different elements potentially having N different damping capacities. The method described above is a simple, accurate, and very amenable to finite element (FE) calculations [97-99]. This approach is employed in many structural vibration applications where each element can easily be modeled as a continuous material having a distinct viscoelastic response [100]. The works of Ross *et al*[81], Soni [86], and Mead and Markus [85], are further examples of this approach and its application to the approximation of the damping capacity of multi-layered plates.

The method explained above is conceptually easy to understand and to apply at the structural level, especially though FE analysis, see the examples of Sun and Lu [101], Nashif [102], or McDaniel and Ginsberg [103]. Unfortunately, the case of particulate composites presents many difficulties to the application of this approach. The difficulty stems from the fact that the calculation of the strain distribution in each material phase is complicated by the shape, orientation, and distribution of the inclusion phases. However, since the approach has proven robust and accurate at a structural level, it is interesting to explore its potential for application to particulate composites which represent structures in a more general sense. To this end, a brief study of the strain energy of the composite sphere shown in Figure 2-4 is given. A sphere, with bulk and shear moduli of K and μ, respectively, has an outer radius b and is subject to an external pressure p_0 and boundary conditions (BC), χ, at $r = a$.

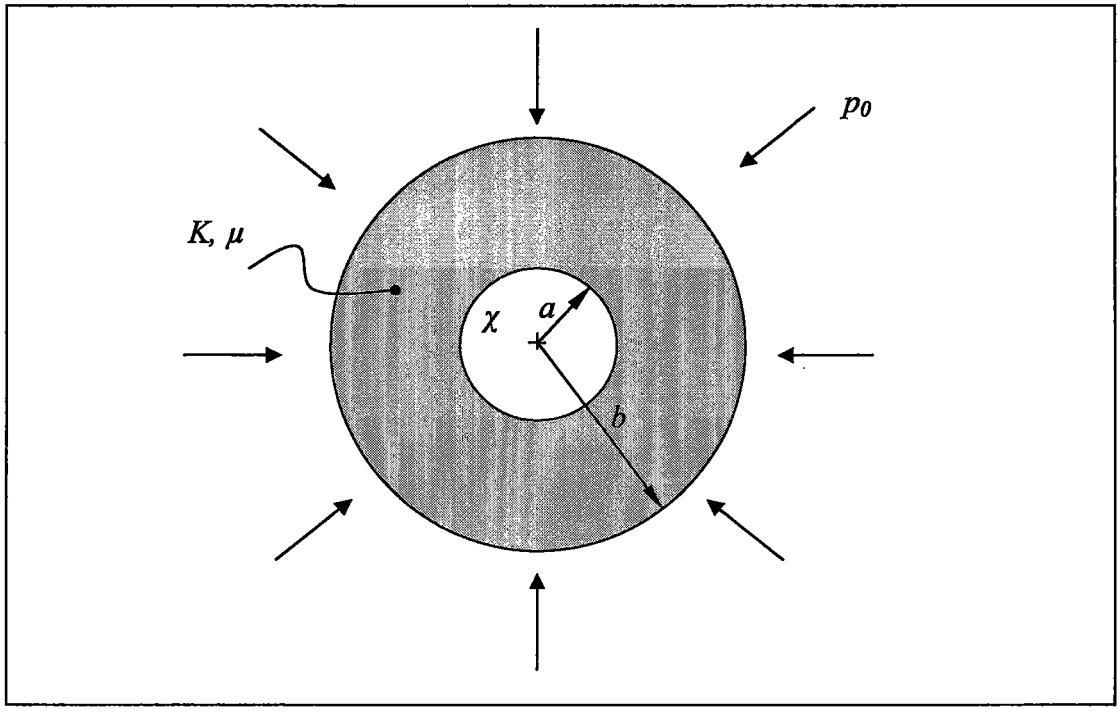

Figure 2-4: Composite sphere of inner and outer radii a and b respectively. The material has a bulk and shear moduli denoted as K and μ respectively. The boundary conditions at $r = a$ can be changed and are designated as χ.

When submitted to external loading, the strain energy in the material located between $r = a$ and $r = b$ is be calculated from expression (II.1.14) below [104].

$$W = \frac{1}{2}\int_V \varepsilon_{ij} C_{ijkl} \varepsilon_{kl} dV = \frac{1}{2}\int_V \sigma_{ij}\varepsilon_{ij} dV \qquad \text{(II.1.14)}$$

The following ratio is now defined in order to show the change in strain energy located between these two different radii due to different BC imposed at $r = a$:

$$R = \frac{\int_a^b \left[\sigma_{rr}^{CpS}(r)\varepsilon_{rr}^{CpS}(r) + \sigma_{\varphi\varphi}^{CpS}(r)\varepsilon_{\varphi\varphi}^{CpS}(r) + \sigma_{\theta\theta}^{CpS}(r)\varepsilon_{\theta\theta}^{CpS}(r)\right] r^2 dr}{\int_0^b \left[\sigma_{rr}^{CS}(r)\varepsilon_{rr}^{CS}(r) + \sigma_{\varphi\varphi}^{CS}(r)\varepsilon_{\varphi\varphi}^{CS}(r) + \sigma_{\theta\theta}^{CS}(r)\varepsilon_{\theta\theta}^{CS}(r)\right] r^2 dr} \qquad \text{(II.1.15)}$$

Where σ_{xx}^{CS} and ε_{xx}^{CS} represent the stress and strain in the x direction (either r, φ, or θ in the spherical coordinate system) of a continuous sphere and σ_{xx}^{CpS} and ε_{xx}^{CpS} are the same constants for the case of a composite sphere. When the loading is spherically symmetric (as is the case for an imposed external pressure) the stresses and strains in the material will only exhibit radial dependence. This dependence is derived by solving the Navier-Stokes equations whose results are given in Equations (II.1.16)(a)-(e) [104]. The values of coefficients α and β can then be determined from the BC at $r = a$ and the pressure, p_0, imposed at $r = b$.

$$\text{(a) } u_r(r) = \alpha r + \frac{1}{r^2}\beta \qquad \text{(d) } \sigma_{rr}(r) = 3K\alpha - 4\mu\beta\frac{1}{r^3}$$

$$\text{(b) } \varepsilon_{rr}(r) = \alpha - \frac{2}{r^3}\beta \qquad \text{(e) } \sigma_{\theta\theta}(r) = \sigma_{\varphi\varphi}(r) = 3K\alpha + 4\mu\beta\frac{1}{r^3} \qquad \text{(II.1.16)}$$

$$\text{(c) } \varepsilon_{\theta\theta}(r) = \varepsilon_{\varphi\varphi}(r) = \alpha + \frac{2}{r^3}\beta$$

The resulting relationship expressing the total strain energy for a continuous sphere ($a = 0$) is given below in Equation (II.1.17):

$$W^{CS} = \frac{2}{3}\pi\left(\frac{p_0^2 b^3}{3K}\right) \tag{II.1.17}$$

To show how the boundaries at $r = a$ affect the total strain energy in the composite sphere, the following cases will be investigated and compared: (*i*) rigid boundary conditions at $r = a$ ($u_r(a) = 0$), and (*ii*) pressure release boundary conditions at $r = a$ ($\sigma_{rr}(a) = 0$). The result of the evaluation of the ratio in Equation (II.1.15) for cases (*i*) and (*ii*) are given below in Equations (II.1.18) and (II.1.19) with corresponding plots in Figure 2-5 and Figure 2-6.

$$R^{i} = \frac{3\frac{K}{\mu}(1-f)}{4f - 3\frac{K}{\mu}} \tag{II.1.18}$$

$$R^{ii} = \frac{1}{(1-f)^2}\left\{1 - f\left[1 + \frac{1}{3}\ln(f)\right] + \frac{2(1+\nu)}{3(1-2\nu)} f(1-f)\right\} \tag{II.1.19}$$

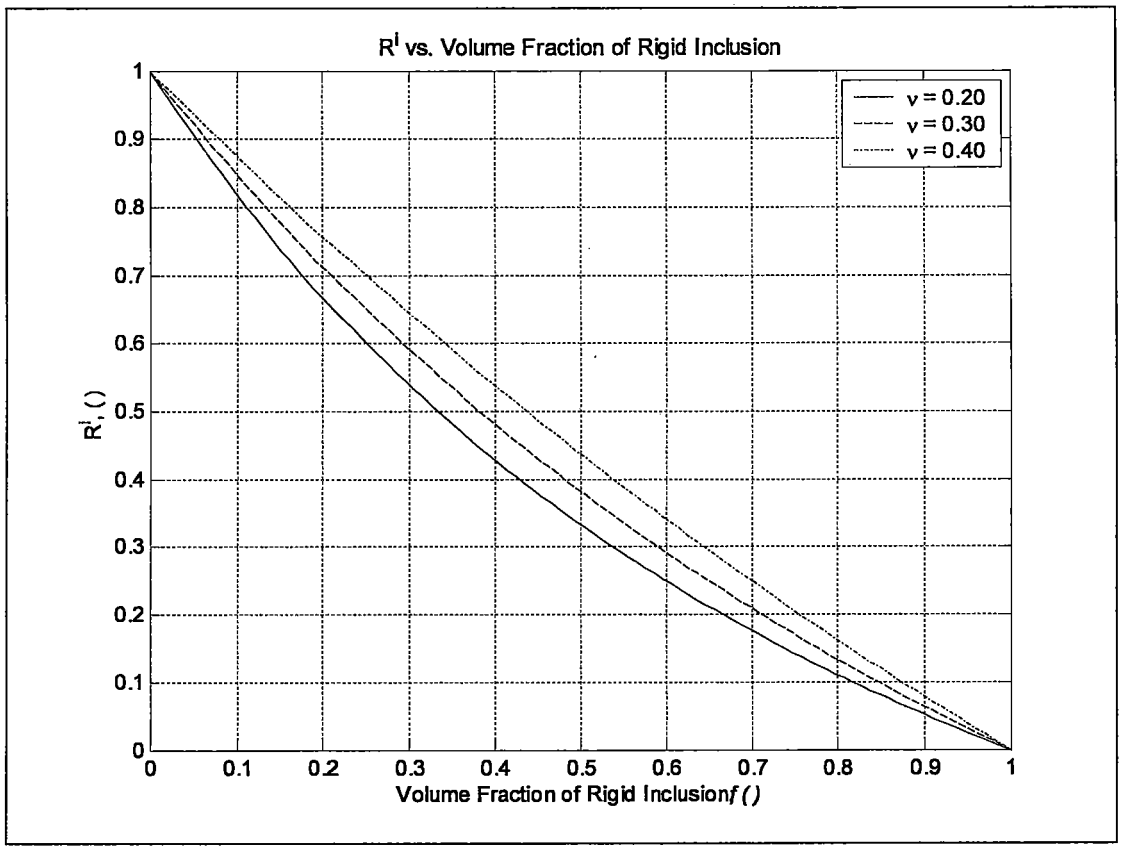

Figure 2-5: Ratio of strain energy in matrix material of composite sphere for three different values of Poisson's ratio with rigid BC at $r = a$ as a function of volume fraction, $f = a^3/b^3$.

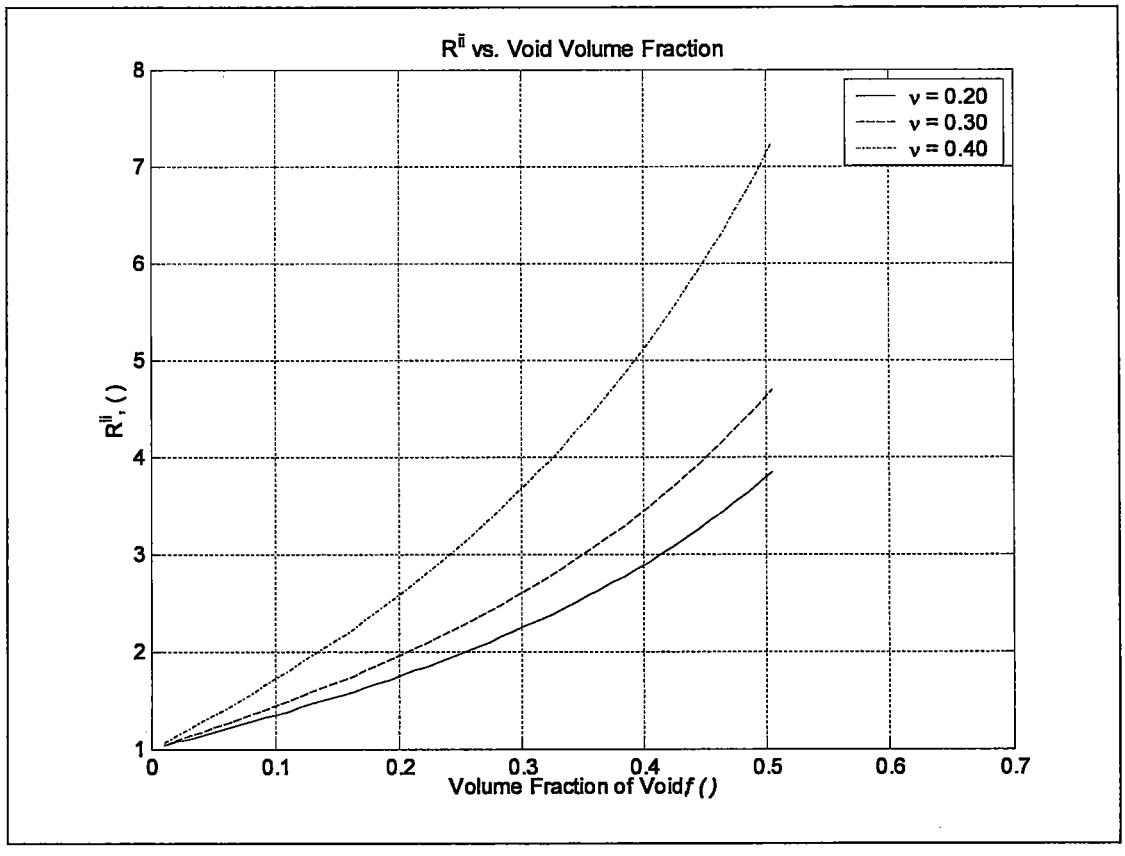

Figure 2-6: Ratio of strain energy in matrix material of composite sphere for three different values of Poisson's ratio with pressure release ($\sigma_{rr} = 0$) BC at $r = a$ as a function of volume fraction, $f = a^3/b^3$.

In Equations (II.1.18) and (II.1.19) f represents the volume fraction of the composite sphere occupied by the rigid inclusion or void, $f = a^3/b^3$, and v is the Poisson's ratio of the material occupying the space between $r = a$ and $r = b$. This simple illustration demonstrates how the presence of voids in a material quickly raises the total strain energy as a function of volume fraction. This strain energy rational to approximate damping capacity implies that if the matrix material is lossy, voiding the material greatly increases the composite material's capacity to dissipate energy for a given applied *stress*, represented in this case as p_0. Along the same lines of thought, if the voids were replaced with inclusions having a lower stiffness value than that of the matrix, the damping capacity of the composite would still be superior to a sphere consisting of the matrix material alone for the same applied *stress*. It is also obvious that rigid inclusions, or indeed inclusions that are stiffer than the matrix, diminish the strain energy present in the matrix material for a fixed applied *stress*. In the case where only the matrix is lossy, this would have a negative effect on the composite's damping capacity for the imposed *stress* case. It must be noted, however, that in wave propagation problems the effects of inertia and multiple scattering render this statement not necessarily true. Converse to the arguments above, if the composite sphere is loaded with a fixed *strain* imposed at $r = b$, rigid inclusions will increase the total strain energy present in the matrix material. For the imposed strain case all of the arguments given above for the voided sphere will be true for the sphere containing a rigid inclusion.

Unfortunately, for a true composite material, the calculation of the strain energy in each constituent phase is complicated by material stiffness contrasts and anisotropy along with inclusion shape and spatial orientation. Approximation of the overall loss factor of a particulate composite material through the strain energy method therefore becomes difficult. However, a micromechanical approach, which

relies on the calculation of the average strain field in each constituent phase of the composite, provides a practical means to approximate the damping capacity of particulate composites. A bibliographic review of the important contributions to micromechanics and the specific work of this thesis will be given in Section 2.2.

2.1.2 Acoustic scattering methods for approximating damping capacity

Acoustic wave absorption is the result of the four following physical mechanisms: (*i*) scattering by inhomogeneities, (*ii*) mode conversion at the interfaces of inhomogeneities, (*iii*) redirection, and (*iv*) intrinsic absorption by conversion to heat [6]. Figure 2-7 illustrates the dominant physical processes that occur when a plane wave impinges on an inhomogeneity in the form of a coated inclusion. The propagation of a harmonic longitudinal plane wave in the x_i direction is described by Equation (II.1.20) below.

$$\hat{p}_I\left(x_i,t\right)=\hat{A}e^{-i(\omega t-k_i x_i)} \tag{II.1.20}$$

$$k=\frac{2\pi}{\lambda}=\frac{\omega}{c} \tag{II.1.21}$$

In the above equations $\hat{A}$ represents the complex magnitude of the incident wave, k is the wavenumber calculated using Equation (II.1.21), ω is the angular frequency, λ is the wavelength (not the Lamé constant), and c is the sound speed in the material.

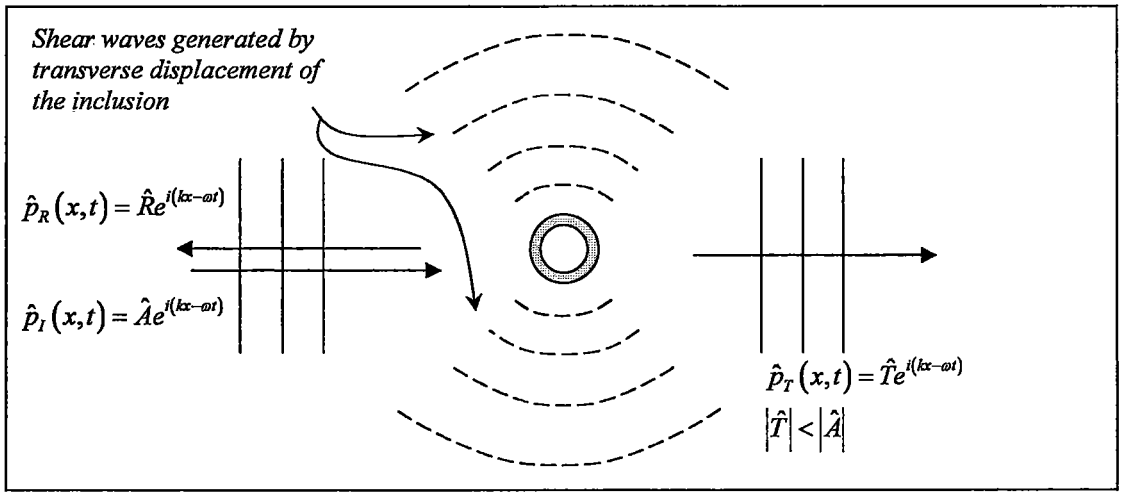

Figure 2-7: Illustration of the dominant physical mechanisms that take place when a longitudinal plane wave impinges on an material inhomogeneity.

Figure 2-7 illustrates the four mechanisms leading to energy dissipation. The first mechanism mentioned is scattering due to inhomogeneities. The incident wave is scattered when longitudinal and shear waves are generated due to reflection at the interface of the material discontinuity. These waves propagate out from the inhomogeneity in all directions with magnitudes that depends on the angle (measured with respect to the incident wave direction) and frequency of the incident wave [105]. Following scattering, the host material attenuates each new wave front and therefore it is in this manner that scattering leads to more efficient *absorption* of wave energy and not simply redirection of that energy. This process leads to an increased damping capacity of the heterogeneous material as a whole. It is the goal of wave scattering based models of composite materials to capture this physical behavior in order to quantify the effective material stiffness and damping properties.

In general, each time a plane wave encounters an impedance difference a portion of the incident energy is reflected and the rest is transmitted. A portion of the reflected energy propagates as plane waves and the remaining energy propagates in the form of different types of waves, a high percentage of which are shear waves. The amount of energy propagating in each wave depends on the specific material properties of the medium on each side of the interface and the angle of incidence [106]. This process of generating several types of waves due to the reflection of a

plane wave at a material inhomogeneity is known as mode conversion, and it leads to more efficient damping. One of the reasons mode conversion increases damping efficiency is difference in the wavelength of shear waves and longitudinal waves. The wavelength of shear waves is shorter than that of longitudinal waves in the same material for the same frequency. This difference in wavelength means that a shear wave will undergo more cycles when propagating the same distance as a longitudinal wave. Since lossy material absorb a given percentage of wave energy each cycle, this process leads to more energy absorption for the same distance traveled. The fact that most materials display a higher damping capacity in shear further increases the damping capacity when mode conversion occurs. Mode conversion also creates more wave fronts. Because each wave front propagates in the absorptive material, the net result is an increase in the total damping efficiency. Mode conversion also occurs when shear waves are also generated due to the transverse displacement of the heterogeneity in the direction of propagation. This displacement results from the stress gradient of the longitudinal wave. The gradient first pushes the inclusion to the right, using Figure 2-7 as reference, until the maximum stress level is reached, and then pulls it back to the left during rarefaction. It is obvious that this leads to shearing motion in the host material in directions that are not parallel to the propagation direction.

The way in which the redirection of wave energy leads to a reduction in energy should be clarified. For an ideal infinite lossless medium, the energy of a plane wave received at point *B* is the same as the energy when it was sent from point *A*. If an heterogeneity is placed in between these two points, part of the energy present at point *A* will never arrive at point *B* because of the reflection/scattering by the heterogeneity. The result for the lossless medium is that the total energy in the composite will remain unchanged. There will, however, be a decrease in the wave's amplitude at point *B*. The amplitude reduction due to the presence of an heterogeneity could be quantified with a measure called the Insertion Loss (IL) [3]. When the host material is lossy and many inhomogeneities are present, redirection

increases absorption by increasing the distance a single wave front travels due to multiple reflections. Since the absorption of energy is a function of the distance traveled, the final result is an increase in the damping capacity [6].

Finally, in all real materials acoustic wave absorption results from viscoelastic material behavior discussed at the beginning of this section. Lossy behavior is, in general, dependent on internal friction, molecular chain relaxation, and other physical phenomena that change mechanical energy into thermal energy which ultimately heats the material [75]. The capacity of a given material to damp a traveling wave is easily quantified for propagation in the host medium using Equation (II.1.20) through the complex wave number, $\hat{k}(\omega)$, defined in relation (II.1.22) [106].

$$\hat{k}_i^*(\omega) = \omega\sqrt{\frac{\rho}{\hat{C}_{ijkl}^*(\omega)n_j n_k p_l}} = \hat{k}_i'(\omega) + i\hat{\alpha}_i(\omega) \qquad \text{(II.1.22)}$$

In the above equation, ρ is the material density, $C_{ijkl}^*(\omega)$ is the complex frequency dependent stiffness described by relation (II.1.10), n_j and n_k are the normal directions as described by the Christoffel equation, $\left|C_{ijkl}^* n_j n_k - \rho c^2 \delta_{il}\right| = 0$ [106], δ_{il} is the Kronecker delta, p_l is the wave polarization describing the propagation direction, $\hat{k}_i'(\omega)$ is the real part of the wave number, and $\hat{\alpha}_i(\omega)$ is the attenuation coefficient. It is important to note that for realistic values of the loss factor ($0 \le \eta \le 1$) and if the real part of the elastic moduli remains constant, the attenuation coefficient is a monotonically increasing function of the host material loss factor. By inserting (II.1.22) into (II.1.20) it becomes obvious that the wave magnitude decays exponentially as a function of α_i and the distance traveled as shown in Equation (II.1.23).

$$\hat{p}_I(x_i, t) = \hat{A}e^{-\alpha_i x_i}e^{-i(\omega t - k_i' x_i)} \qquad \text{(II.1.23)}$$

The relationships presented thus far show why a homogenization scheme that correctly captures the mechanisms of scattering by finding a complex, frequency dependent, effective stiffness tensor, can yield insight into the design of lossy materials.

One problem with the method described in Section 2.1.1 is its limitation to the quasi-static case. The quasi-static domain is defined by the ratio of the incident wavelength to the descriptive inclusion dimension and is usually expressed via the non-dimensional quantity ka where a represents the largest inclusion dimension and k is the wavenumber. The quasi-static domain is limited to those frequencies that render $ka << 1$ [105].

Energy dissipation due to wave scattering by the presence of a material inhomogeneity is well approximated in the quasi-static domain by the strain energy in the near field of that inhomogeneity [6]. In this frequency range the "propagation" of the wave at the inclusion scale is well represented as a time varying but spatially uniform stress/strain field. At this scale the effects of wave scattering are very small compared to the stress/strain concentration in the neighborhood of the inclusion. Using this knowledge, a strain energy based approach delivers reliable particulate composite damping capacity approximations in the frequency domain by introducing the lossy, frequency dependent, constituent material behavior into static models [53]. In order for a model to be reliable for complex particulate composites careful consideration must be taken in modeling the strain field everywhere in the composite. This is the case for most mean field homogenization theories [25]. If, on the other hand, the frequency of the propagating waves is such that $ka \approx 1$ or even $ka \geq 1$, models based on mean stress/strain field theories are no longer valid. For these frequencies such models neglect the physical mechanisms of scattering [107] and, therefore, single or multiple scattering homogenization approaches must be employed. The model and experimental data presented in this thesis are limited to the quasi-static domain. However, in an effort to give a complete picture of the frequency dependent

behavior of particulate composites, a bibliographic review of the significant works in the area of scattering based homogenization techniques is presented in Section 2.3.

2.2 Micromechanical homogenization of particulate composites

The most precise approach to modeling the macroscopic behavior of complex materials would be one that takes its intrinsic multiscale structure into account. This type of multiscale approach requires knowledge of the physical behavior of the material at each scale as well as the nature of the interaction between scale levels. If a modeling approach captures the material behavior at each scale level of interest and the interaction mechanisms between scales, it is possible to approximate material behavior at all scales based on knowledge of the material's composition. The micromechanical approach is, by definition, a multiscale modeling approach. It assumes that two structural levels exist such that the effects of interfaces, heterogeneities, and other physical phenomena at the lower level can be taken into account at the upper level via an averaging approach. These structural levels are defined by length scales such that $l << L$ where l is the descriptive dimension at the lower length scale and L describes the upper length scale. This tacitly assumes that the upper length scale properties, referred to in this work as global or macroscopic, are the result of an average of the behavior of the lower length scales and therefore that no point to point interaction takes place between scales [27]. The idea behind this approach is illustrated by defining a Representative Volume Element (RVE). A RVE is the smallest material volume unit (element) whose effective behavior is assumed to represent the macroscopic behavior of the complex material. Selection of a RVE plays a large part in defining the limitations of any proposed micromechanical method [26]. A RVE example for a composite consisting of a matrix with identically oriented coated ellipsoidal inclusions is shown below in Figure 2-8. This RVE represents the self-consistent (SC) model introduced by Cherkaoui *et al* [23]. This RVE assumes

that the composite material behavior can be well approximated by writing the constitutive equations of a single coated inclusion embedded in the effective material, which has unknown material properties [23].

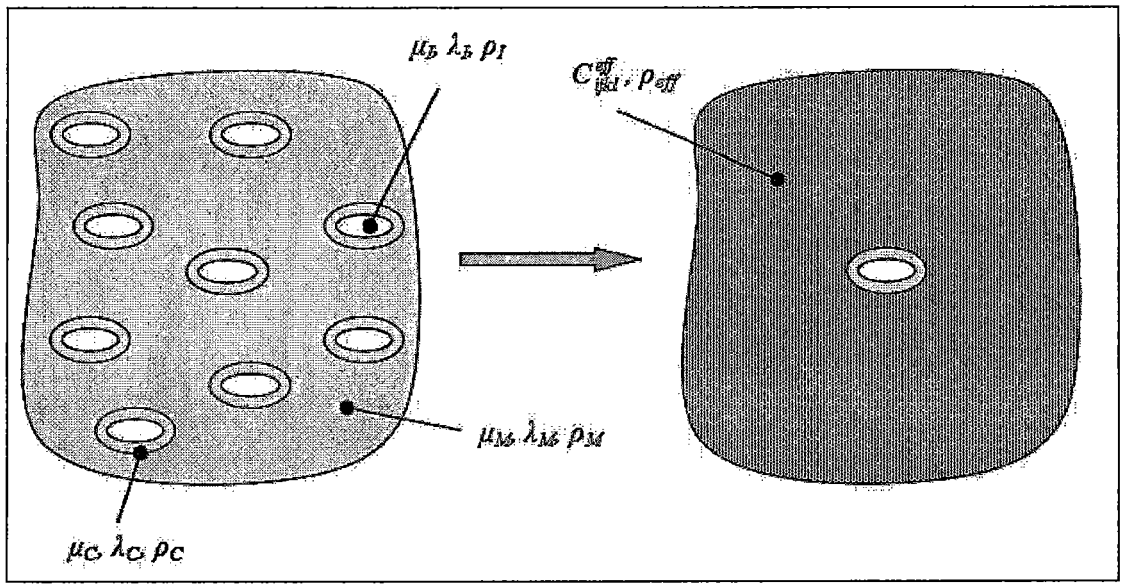

Figure 2-8: RVE for the SC model of Cherkaoui *et al* [23]. λ_x and μ_x represent the Lamé constants and ρ_x the density of material *x*. C^{eff}_{ijkl} is the effective stiffness tensor and *I, C,* and *M* specify respectively the inclusion, coating, and matrix.

Historically, all micromechanical mean field theories have been based entirely on the physical principles of continuum mechanics. The approach taken in this thesis will be no different. Since its inception nearly fifty years ago, micromechanics has become a well developed field of study which has been shown capable of addressing many different fields of science. The approach is even currently being adapted to approximate the behavior of nanomaterials (ex: [55-57]). The development of this field is the result of two distinct needs: (*i*) the need to approximate the macroscopic behavior (elastic, plastic, thermal, electromagnetic, etc.) of materials containing micro-scale heterogeneities (micro/μ → macro/M scale transition) and (*ii*) the need to localize macroscopically applied fields to inferior length scales (M→μ scale transition) [26, 27]. Indeed, the approximation of the macroscopic response of an inhomogeneous material, which is an average of the microscopic behavior, requires knowledge of the spatially varying microscopic fields [108].

A good example that illustrates this point is the model proposed by Song *et al* [109] to approximate the global response of a bi-phase composite material having inclusions that can undergo phase transformation. This model applies a SC homogenization approach to approximate the macroscopic elastic and thermal material properties. The first step homogenizes the material ($\mu \rightarrow M$) thereby approximating the effective macroscopic composite properties based on its composition and thermomechanical loading. At this point, the localization of the imposed loads to the microscopic level ($M \rightarrow \mu$) is performed in order to calculate thermomechanical phase equilibrium of the inclusions via local physical laws and localized loads. Given the change in the phase composition of the inclusion, which changes the elastic and thermal properties, another homogenization step is made. This process repeats itself during the entire loading history. The micromechanical approach thus gives information of not only of the macroscopic response, but also of the thermomechanical state of the inclusions at all times during the loading history.

The specific materials and behavior just discussed are much different than those discussed in this work. However, the above example clearly shows the capacity of micromechanical models to resolve multiscale problems and give material behavior information simultaneously at multiple length scales. Further, the example illustrates an important principle: the behavior of microscopic heterogeneities can have a significant influence on the macroscopic behavior of a material. It is for these reasons that the micromechanical modeling approach is a powerful tool that can be employed to analyze multiscale problems.

2.2.1 Pertinent micromechanical modeling developments

The micromechanical approach employed in this work is a mean field model for particulate composite materials. All mean field models are based, in one way or another, on the seminal work of Eshelby [108]. Eshelby's results marked a great

improvement over elementary techniques such as the work of Voigt [110], Reuss [111]. Voigt and Reuss used variational principles and strain energy which cannot take inclusion shape into account.

The micromechanical modeling approach initiated by Eshelby consists of two fundamental operations: (*i*) localization and (*ii*) homogenization [26, 27]. As previously stated, these operations require the existence of at least two length scales within the material. It also assumes that the effect of material behavior and structure at the microscopic particulate length scale has only an average effect on material behavior at the macroscopic scale and that macroscopically applied loads can be localized to the microscopic level [27]. Eshelby's results [108] provide the insight and mathematical tools to resolve the localization problem via the equivalent inclusion method which results in localization tensor now called Eshelby's tensor, S_{ijkl}. This capability to localize macroscopically applied mechanical loading to the microscopic level is fundamental to the approximation of volumetric average stress and strain fields in the heterogeneous material. This set of operations is called the homogenization step. Localization allows volume averaging since it permits the derivation of stress and strain fields as a function of position which depend not only on the applied load, but also inclusion forms, orientations, and properties [28-30].

Following Eshelby's fundamental contribution a large array of models, for example those of Kröner [31], Budiansky [32], Wu [28], and Mori and Tanaka [33] were developed. All of these models employ a similar equivalent inclusion approach. Zeller and Dederichs [34], however, improved on the equivalent inclusion method by introducing a Green's function formalism that permits the calculation of the stress and strain fields at every point in a heterogeneous material at the microscopic scale. Their approach is based on the idea that the material behavior of a particulate composite can be approximated on the local, or microscopic, scale via expressions of the form shown below.

$$\mathbf{X}(\mathbf{r}) = \mathbf{X}^0 + \delta\mathbf{X}(\mathbf{r}) \qquad \text{(II.2.1)}$$

In this expression, $\mathbf{X}(\mathbf{r})$ represents the material properties or fields of interest in the heterogeneous medium. The concept behind this approach is that the material properties and fields of interest are globally homogeneous, $\mathbf{X}^0$, with small perturbations due to microscopic heterogeneities scattered throughout the host material, $\delta\mathbf{X}(\mathbf{r})$. The field generated by these heterogeneities can be approximated at every point in the material using Green's tensors and thereby providing a good representation of the microscopic behavior. This approach was improved upon by Mura [35] and Willis [36] to include plastic deformation and generalized for the case of two disoriented ellipsoidal plastic inclusions by Berveiller *et al* [37]. Another important improvement over the equivalent inclusion method was the introduction of interfacial operators which relate the stress and strain state across the interface of dissimilar materials [38, 39].

The combination of these two mathematic techniques provides an extremely powerful modeling tool of the physical phenomena present at the microscopic length scale which, in turn, improves the volumetric average approximation required in the homogenization step. The SC coated inclusion model of Cherkaoui *et al* [23, 24, 40], which will be extended to account for frequency dependent viscoelastic constituent phases in this work, owes its accuracy to the fact that it is derived using these tools.

It has been previously stated that all micromechanical models require the selection of a RVE. Each individual model is then derived using constitutive laws and the appropriate mathematical tools (Green's functions and interfacial operators, for example) based on the composition of the specific RVE. A RVE for a material consisting of a matrix containing coated ellipsoidal inclusions is shown below in Figure 2-9.

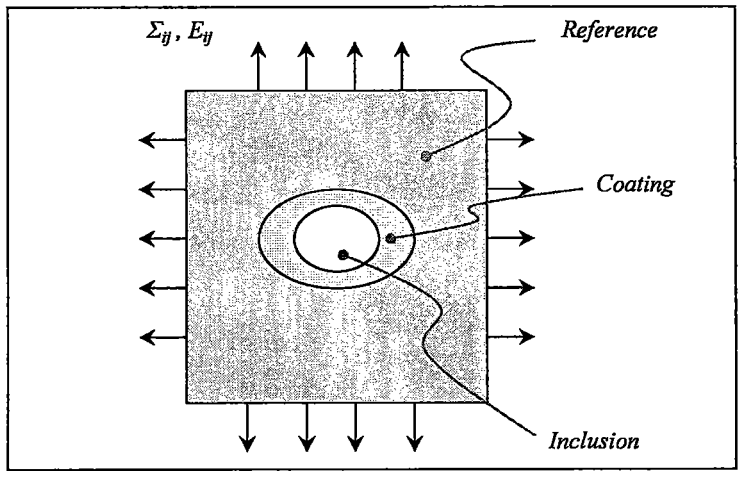

Figure 2-9: RVE of composite material consisting of a matrix containing coated ellipsoidal inclusions.

The Mori-Tanaka (MT) model, for example, assumes that the reference material of Figure 2-9 is the matrix material having elastic properties, $\mathbf{C}^M$, and the imposed global strain, E_{ij}, is that of the matrix, ε_{ij}^M [33]. This modeling approach is limited to the case of low inclusion volume fraction, f_I, as are many others due to the assumption that stress and strain fields of multiple inclusions do not interact [41]. In order to overcome this limitation, several approaches can be taken. One is a computationally expensive periodic array type of approach where the interaction of heterogeneities is directly taken into account [25]. A strong example of this approach is the explicit model proposed by Molinari and El Mouden [42] which applies Berveiller *et al*'s [37] paired inclusion Green's formalism and agrees well with established models and experiment for elevated volume fractions. Another approach is the SC approach which assumes that the reference material of Figure 2-9 is an effective material having unknown elastic properties, $\mathbf{C}^{eff}$ [41]. This approach was first proposed in the area of mechanics of materials by Kröner [31] to approximate the behavior of polycrystalline materials where the definition of a matrix is unclear. This approach was later improved upon by Budiansky [32], Hill [43, 44], and Berveiller and Zaoui [112], and finally generalized by Christensen and Lo [45].

The case of coated inclusions is of interest for several different reasons. One reason is to approximate the behavior of a bi-phase composite by assuming that the

material in the neighborhood of an inclusion, the "interphase," behaves differently than the matrix material. This is the aim of the model proposed by Jasiuk and Kouider [113]. Another, more obvious, reason for choosing a coated inclusion RVE is that the composite consists of a matrix containing coated inclusions. The model proposed by Cherkaoui *et al* [23, 24, 40] can be used for either aspect of the coated inclusion problem. Hervé and Zaoui [114] extended such an approach to model the *N*-layered coated inclusion case and Lipinski *et al* did so for the *N*-coated elliptical inclusion case [115]. Approximation of the dynamic behavior of such materials by employing the elastic-viscoelastic correspondence principle, in accordance with the works of Hashin [8, 63, 64] and Christensen [7], is the subject of this thesis. This will be done by extending the work of Cherkaoui *et al* [23, 24, 40] to the quasi-static domain and further refining the model.

2.3 Homogenization of particulate composites through acoustic scattering

Homogenization models for particulate composites based on the effects of wave scattering presented in Section 2.1.2 take two general forms: *i*) single scattering models and *ii*) multiple scattering models. Both approaches are based on resolution of the problem posed by finding the acoustic field resulting when a wave traveling in a host medium that encounters an heterogeneity. The difference between the two modeling approaches, as suggested by the naming convention, resides in the treatment of the interaction of waves reflected by the material discontinuity.

2.3.1 Single scattering models

The basis of all single scattering approaches is the assumption that inclusion concentration, usually referred to as scatterers, is low. This assumption allows the approximation of the entire acousticly induced displacement field in the composite as

a summation of the field scattered from each individual scatterer and that no interaction between these fields takes place. The first influential single scattering model of note was proposed by Ying and Truell [116] which resolves the emulsion problem: fluid inclusions embedded in a fluid host medium. Their model introduces the important basic ideas of material homogenization via scattering methods but lacks the complexity needed to resolve the problem presented by heterogeneous solids.

The seminal work of Chaban [46] was a major contribution to the single scattering approach. It introduced two important hypotheses. The first hypothesis is that the total displacement field, $\vec{u}_{tot}$, in the heterogeneous medium can be represented as the summation of the incident displacement field, $\vec{u}_{inc}$, and the scattered field due to each scatterer, $\vec{u}_{s,i}$. This approximation requires that there can be *no* interaction between the scattered fields of the inclusions. Mathematically, this hypothesis is expressed below in Equation (II.3.1).

$$\vec{u}_{tot}(\mathbf{x}) \approx \vec{u}_{inc}(\mathbf{x}) + \sum_{i=1}^{N} \vec{u}_{s,i}(\vec{\rho}_i); \quad \vec{\rho}_i = \mathbf{x} - \mathbf{x}_{s,i} \tag{II.3.1}$$

In the above expression, the observation point and scatterer location are represented by $\mathbf{x}$, and $\mathbf{x}_{s,i}$, respectively [47]. The second hypothesis is the assumption that the scattered displacement field due to an inclusion having a volume, V_0, and the effective medium material properties is equivalent to the field scattered by the same volume of composite material *if* the observation point is in the far-field [47, 49, 76, 117, 118]. Figure 2-10 shows a schematic of the "RVE" of the single scattering approach. One implication of the second hypothesis is that the center of each inclusion must be approximated as being located at the center of the scattering volume, V_0. This is mathematically expressed as: $\left|\mathbf{x} - \mathbf{x}_{s,i}\right| \approx \left|\mathbf{x} - \mathbf{x}_{V_0,center}\right|$.

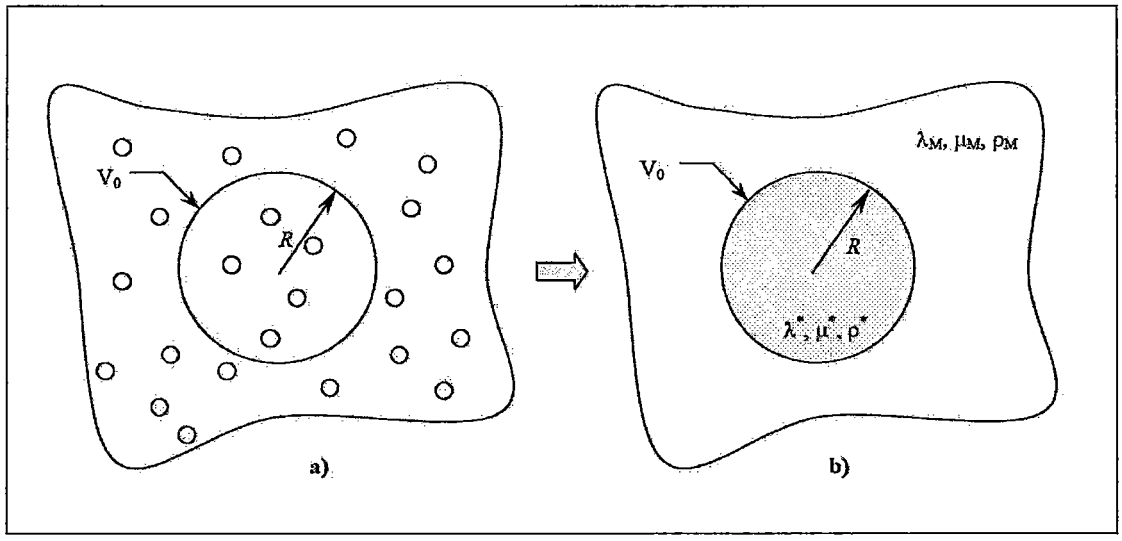

Figure 2-10: The composite material, (a), and the RVE, (b), for the single scattering approach introduced by Chaban [46].

To find the analytic solution to this problem, the equations of an incident plane wave must be decomposed as a summation of spherical waves that encounter an inclusion for the both case (a) and (b) illustrated above. The approximate solution is a series expansion with respect to *ka*, where higher order *ka* terms are truncated [76]. This truncation is only valid in the case where $ka<<1$ therefore corresponding to the quasi-static case discussed in Section 2.1. Finally, the expressions arising from the solutions of configurations (a) and (b) are set equal and it is then possible to resolve the system for the effective material properties of the heterogeneous material.

The result of all of these approximations, especially the first hypothesis, is that simple scattering models are only valid for low concentrations of inclusions, $\leq 10\%$ as a rule of thumb, and for $ka<<1$. This scattering regime is called Rayleigh scattering in honor of Lord Rayleigh [89]. However, several clever approaches have been found that provide a reliable approximation of the effective material behavior for an increased volume fraction; on the order of $\leq 30\%$ scatterer concentration. These approaches are called SC scattering models. Chaban's model incorporates the SC approximation by assuming that the scattered field from multiple non-interacting inclusions is equivalent to the field created by a single inclusion having effective material properties [46].

Another highly employed single scattering model was proposed by Kuster and Toksöz (KT) [47] which is based on the integral equations for the displacement field derived by Mal and Knopoff [119]. Their model has the capacity to approximate the effective behavior of a material containing spherical and spheroidal inclusions, but unfortunately has no dependence on the frequency outside of the frequency dependent matrix material. The absence of frequency dependence results from the fact that the model does not take into account inclusion resonant behavior. Though this model gives reasonable approximations for several areas of study, such as geophysics, the first resonance, which is related to monopole scattering, can have an important effect on the effective behavior of the material even in the quasi-static domain [118, 120, 121]. Gaunaurd and Überall (GU) included several higher order terms in the series expansion described previously in order to address this problem [49]. The idea of including resonant behavior is a result of their work with voided materials and bubbly liquids. For such materials experimental results showed a marked deviation from theoretical values calculated using KT methods which lack resonant scattering effects [48]. It is, however, important to note that for certain types of materials, those where the inclusion has a higher stiffness value than that of the matrix, the KT approach provides a good approximation in the quasi-static domain. For this case, the monopole resonance does not have a significant effect on the global behavior. Indeed, the SC model proposed by Berryman for bi-phased composites with spherical [122] or ellipsoidal [51] inclusions shows good agreement with the KT approximation.

The work presented in this thesis focuses on the behavior of composite materials in the quasi-static domain and, therefore, single scattering models are very relevant to this discussion. Among the multitude of single scattering models, some of the most relevant to this work are highlighted below. The model described by Kerr [118] is a GU-type SC single scattering model for bi-phase composites. This model was extended to the case of coated fluid inclusions by Baird *et al* [76] and its approximations have been compared with experimental values of Transmission Loss

(TL). The model of Anson and Chivers [123], also a GU-type single scattering model, deserves mention as it is probably the most complete scattering model describing isotropic composite behavior for a material consisting of a matrix containing spherical coated micro-inclusions. Their model can approximate the effective behavior of a composite material, a suspension, or an emulsion based on the elastic, viscous, and thermal properties of the constituent phases. Though it is a very complete model, its complexity is usually superfluous as the time scales for viscoelastic and thermal processes in viscoelastic composites are very different [76]. It is for this reason that the only scattering model considered in this work is that of Baird *et al* [76].

2.3.2 Multiple scattering models

Multiple scattering models are generally employed in order to overcome two specific limitations of single scattering approaches: (*i*) the inability to provide reliable approximations of the effective behavior of composites with high scattering concentrations, and (*ii*) the inability to model effective behavior at higher frequencies [121, 124]. The first significant contribution to the multiple scattering problem was that of Foldy [125]. Foldy's work introduced a multiple scattering formalism based on a set of truncated integral equations resulting from the fields of multiple point scatterers in an isotropic host material. Lax extended this formalism to the case of anisotropic scatterers by employing a correlation function for two particles [126]. These two contributions employ a complex wavenumber and depend on the frequency, the scatterer volume fraction, and the far-field forward scattering amplitude [121]. Waterman and Truell (WT) improved these models by adding the effect of far-field back-scattering [127]. Their approach is the basis of a large number of multiple scattering models. Models based on the WT approach include those of

Bose and Mal [128], Lloyd and Berry [129], Ledbetter and Datta [79], Lu and Liaw [29], and Aggelis *et al* [121].

Another very important contribution to the multiple scattering approach was contributed by Twersky [130-132]. Twersky developed a method that takes the interaction of inclusions into account via a pair correlation function. This was done in a series of papers, most importantly for the free space [130] and two dimensional [131] cases. The same methodology has since been employed by several authors, notably Varadan *et al* [124]. These authors designate relations (II.3.2) and (II.3.3) shown below as the total displacement field for the multiple scattering case. Varadan *et al* then employ the pair correlation function formalism of Twersky to relate these fields [124].

$$\vec{u}(\mathbf{x}) = \vec{u}_{inc}(\mathbf{x}) + \sum_{i=1}^{N} \vec{u}_{s,i}(\vec{\rho}_i); \quad \vec{\rho}_i = \mathbf{x} - \mathbf{x}_i \tag{II.3.2}$$

$$\vec{u}_{s,i}(\mathbf{x}) = \vec{u}_{inc}(\mathbf{x}) + \sum_{j=i}^{N} \vec{u}_{s,j}(\vec{\rho}_j); \quad a < |\vec{\rho}_j| < 2a \tag{II.3.3}$$

In the above equations a represents the descriptive dimension of the scattering heterogeneity.

The multiple scattering models introduced above provide a very realistic picture of the physical processes taking place at the inclusion scale. One notable drawback is that they are extremely mathematically complicated even for simple cases such as an isotropic matrix containing spherical inclusions. Despite their added complexity, several of these models, [124-126, 133, 134] for example, are still only valid at *low* volume fractions of scatterers and for spherical inclusions. Further, implementation of these models for non-spherical scatterers or anisotropic phases becomes even more complicated, if not impossible. Though methods exist to overcome these problems (see Anson and Chivers [135], Aggelis *et al* [121], or Yang [136] for example), these approaches are generally more important for applications

outside the quasi-static domain represented by $ka \approx 1$ or $ka>1$ [124] and for this reason are not considered in this work.

2.4 Material by design

Classic system and structure design require material selection for each material component. Material selection depends on the foreseen physical demands: elastic, thermal, electric, etc [137, 138]. Unfortunately, the limiting factor in design is often material behavior of the components. A clear example of material limiting design is the microprocessor. Microprocessor performance depends on the thermal properties of the material from which it is fabricated. By assuming that the material properties cannot be changed, excellent solutions have been found to resolve the problem as a heat transfer problem. A more elegant solution, however, would be the design of a material uniquely created for the multifunctional needs of the microprocessor. This latter approach is known as *Inductive Design*, an approach studied in detail by Olsen [15, 90] and illustrated in Figure 2-11.

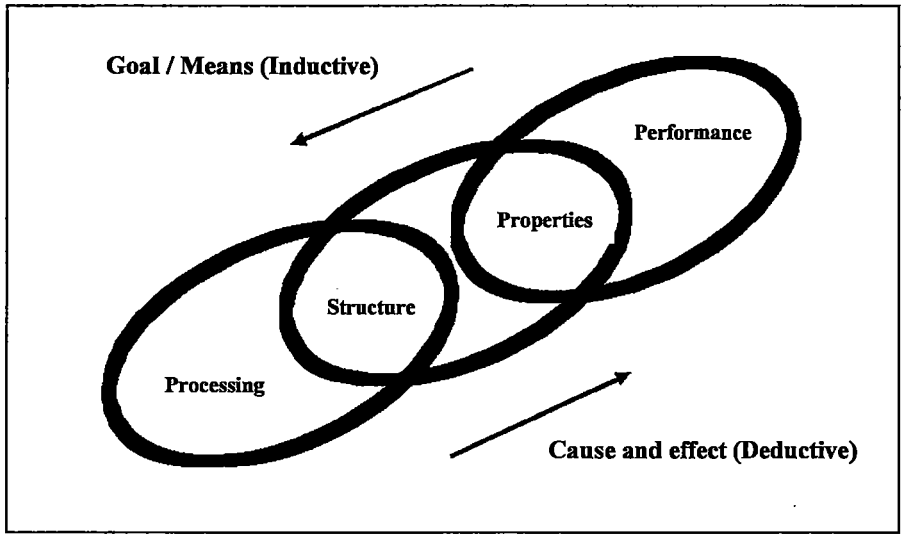

Figure 2-11: Schematic representation of the two approaches to design, taken from Olsen [15, 90].

The concept of inductive design requires the ability to design materials according to the needs of a structure; design for manufacture and not the classic idea of manufacture for design. The idea of material design is not entirely new (see, for example, Cohen's discussion on the reciprocity of structure and properties of a material [139] or Smith's work on hierarchical structure of materials [92]), however the scientific community still does not truly design materials [20]. Material design is a very active research area which is currently dominated by strategies that extend system design, which is normally limited to the component level, to include materials [14]. Several strong examples of the implementation of this methodology exist, notably those of Seepersad *et al* on the multifunctional and multiphysics design of cellular structures [91], Olsen *et al* concerning the design of high strength steels [140], and Stupp and Braun on the design of biomaterials, ceramics, and semi-conductors [141]. Implementing this methodology requires collaboration between many different areas of research and development from economic analysis to the modeling of macroscopic behavior of materials based on micro and molecular structure [14], see Figure 2-12.

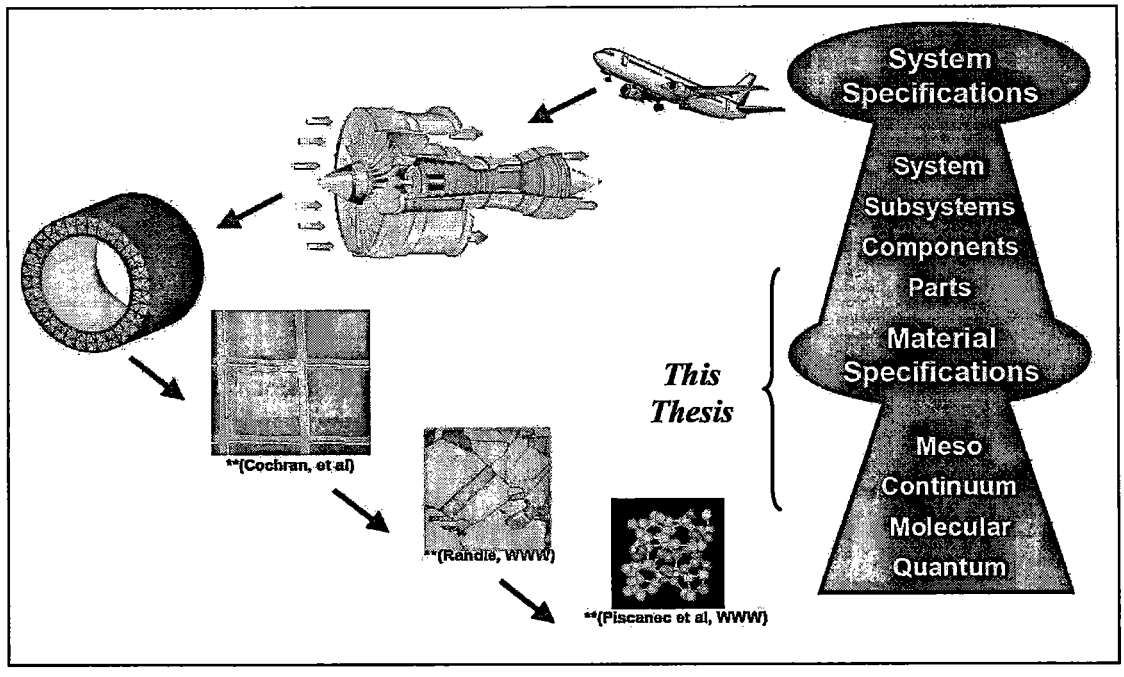

Figure 2-12: Schematic of complete system design, including the design of materials. Figure from Seepersad [20], Cochran [142], Randle [143], and Piscanec [144].

The work of this thesis does not try to put in place such an overreaching strategy, but rather to improve an existing micromechanical model for damping applications. The model is then cast as a tool for the material by design framework described above for applications where damping is an important aspect.

CHAPTER III

MICROMECHANICAL MODELING OF VISCOELASTIC COMPOSITES CONTAINING COATED INCLUSIONS

3.1 Introduction

The previous chapter introduced the self-consistent homogenization technique and examples were given in the static (ex: Cherkaoui *et al* [23, 40]) and quasi-static (ex: Gaunaurd and Überall (GU) [48, 49] and Kuster and Toksöz (KT) [47]) domains. Both methodologies approximate macroscopic behavior by modeling physical processes at the microscopic scale and then applying averaging techniques to arrive at homogeneous material approximations of the particulate composite macroscopic behavior. The GU approach (which was employed by Kerr [118], Baird *et al* [76], and Anson and Chivers [123, 135]) is based on elastic wave propagation in heterogeneous media and is limited to the case where the wavelength of the incident wave, λ, is much larger than the inclusion's descriptive dimension, a. The same frequency dependent restriction on the wavelength also applies to the KT approach. These quasi-static scattering approaches have been shown to be applicable across a large range of length scales, from geophysics [47] to ultrasonics [76]. Further, the GU approach has the added advantage of taking inclusion resonant behavior into account, which is often important even in the quasi-static domain [48, 49, 76]. Implementing scattering based models is, unfortunately, extremely difficult or even impossible when inclusions are non-spherical and/or constituent phases are anisotropic. This restriction greatly limits scattering model application for the wide

range of existing particulate composites. The micromechanical approach, on the other hand, is not limited by the complexities presented by material anisotropy or non-spherical inclusions.

As discussed in Chapter II, the elastic-viscoelastic correspondence principle [63, 75] and strain energy arguments [16] suggest that macroscopic lossy behavior of particulate viscoelastic composites will be well approximated through micromechanical methods. It is with this rationale that the micromechanical model of Cherkaoui *et al* [23] will be extended to the quasi-static regime in an effort to approximate the macroscopic lossy behavior of particulate viscoelastic composites as a function of frequency. This chapter aims to introduce and develop the self-consistent micromechanical approach in the quasi-static domain for a composite material consisting of a homogeneous matrix containing coated ellipsoidal inclusions.

3.2 Derivation of quasi-static three phase self-consistent model

In general, micromechanical methods are based on two distinct steps: (*i*) localization, which determines the relationship between the microscopic (local) fields and the macroscopic (global) loading, and (*ii*) homogenization, which employs averaging techniques to approximate macroscopic behavior [26]. Sections 3.2.1 – 3.2.3 of this chapter show the derivation of the average strain fields in the viscoelastic inclusion and coating materials by employing the integral equation, Green's formalism, and interfacial operators by adopting the work of Cherkaoui *et al* [23, 24] to the quasi-static domain. This is the localization step. Section 3.2.4 then applies a self-consistent scheme to find the viscoelastic particulate composite's frequency dependent effective stiffness tensors via the relationships derived in Sections 3.2.1 – 3.2.3. This is the homogenization step. Finally, the quasi-static form of the model presented by Cherkaoui *et al* will be generalized using dilute strain concentration tensors in Section 3.3.

The localization step is essentially based on the equivalent inclusion method introduced by Eshelby [108]. Eshelby's approach is modified in the present work by solving an integral equation for the displacement field at every point in an infinite homogeneous reference medium rather than by directly employing the equivalent inclusion method. The integral equation employed in this work is the result of a Green's function relating the stiffness contrast between the reference medium and a *coated* inclusion to the displacement field at each point in space [34, 37, 145]. This integral equation will be coupled with interfacial operators to modify the solution to the simpler problem of an inclusion in an infinite host medium and thereby find the solution for a coated inclusion embedded in an infinite host [38, 39].

The first requirement for the derivation of the integral equation is the definition of an elementary unit which is assumed to represent the particulate composite studied. This unit is called the representative volume element (RVE) [26]. The RVE chosen to describe the material presently studied consists of a host material containing two concentric ellipsoidal inclusions (see Figure 3-1). The two ellipsoids represent the inclusion, I, and its coating, C [23]. In this work the coating thickness is assumed to be sufficiently thin to permit the approximation of the strain field in the coating as uniform in directions normal to the inclusion's surface. This assumption allows calculation of the average strain field in the coating via interfacial operators. These operators are applied to the strain field in the inclusion, which is assumed to be uniform in accordance with Eshelby [23, 108]. It is important to point out that the thin coating approximation simplifies the following model but limits its applicability. Fortunately, the methodology employed can be extended to the more general case of a multi-coated inclusion that does not require the thin coating approximation which is covered elsewhere, [146].

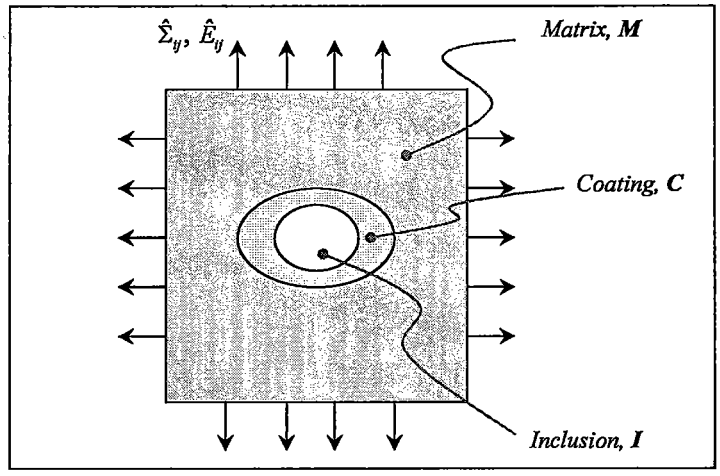

Figure 3-1: Topology of a coated inclusion embedded in a limitless matrix. Σ_{ij} and E_{ij} represent the macroscopically applied stresses and strains, respectively.

The following quasi-static self-consistent model derivation for a heterogeneous viscoelastic material closely follows Cherkaoui's derivation of the static analogue [147]. The following derivation is important, however, because it employs the elastic-viscoelastic correspondence principle introduced in the previous chapter and follows the rationale of Hashin [8, 63] and Christensen [7]. The derivation will detail the physical principles captured by the model and explicitly state limitations for its application.

The topology of the present coated inclusion problem consists of an inclusion phase occupying a volume, V_I, whose frequency dependent mechanical behavior is described by the viscoelastic stiffness tensor, $\hat{\mathbf{C}}^I$. Surrounding this inclusion phase is a thin coating of another material whose viscoelastic behavior described by the tensor $\hat{\mathbf{C}}^C$ and that occupies a volume, V_C. The coated inclusion is embedded in a host material described by the viscoelastic stiffness tensor, $\hat{\mathbf{C}}^0$. The following derivation assumes that the viscoelastic stiffness tensor of *each* material is frequency dependent. The frequency dependent behavior can be approximated by material models (Kelvin-Voigt, Zener, etc) or from curve fits of experimental data (Havriliak-Negami [148], etc). For this model the exact representation of the frequency dependence is not important, it is only important to note that the model derivation does not make any restriction on the constituent material viscoelastic behavior.

At this point, several notation conventions need to be mentioned. First, tensor quantities will be denoted either with index notation or in bold, for example: $\hat{C}_{ijkl} \Leftrightarrow \hat{\mathbf{C}}$. These two representations are interchangeable and will appear throughout this thesis corresponding to the required clarity for the mathematical operations employed. The next commonly employed convention is the representation of complex frequency dependent quantities through any of the equivalent expressions shown in Equation (III.2.1).

$$\hat{X} \Leftrightarrow \hat{X}(\omega) = X^R(\omega) - iX^I(\omega) = X^R(\omega)\left[1 - i\eta_X(\omega)\right] = \left|X(\omega)\right| e^{i\varphi(\omega)} \quad \text{(III.2.1)}$$

Where $\hat{X}(\omega)$ represents any complex variable in the frequency domain and ω is the frequency. The complex quantity consists of real, $X^R(\omega)$, and imaginary, $X^I(\omega)$, parts and has a loss factor and loss angle denoted by $\eta_X(\omega)$ and $\varphi(\omega)$ respectively. The final convention employed is the "e^{-ix}" Euler's equation: $e^{-ix} = \cos(x) - i\sin(x)$.

This derivation is further limited to the case of viscoelasticity and small perturbation theory. The interfaces matrix-coating and coating-inclusion interfaces are assumed to be perfect, thus ensuring continuity of traction and displacement across these boundaries [23]. One of the most limiting hypotheses for the application of this theory in the frequency domain is the small perturbation approximation [63]. This approximation assumes that inertial effects within the composite are negligible and, therefore, that the equilibrium equation (in the absence of body forces) reduces to the following:

$$\hat{\sigma}_{ij,j} - \rho \frac{\partial^2 \hat{u}_i}{\partial t^2} = 0 \;\Rightarrow\; \hat{\sigma}_{ij,j} = 0 \qquad \text{(III.2.2)}$$

It is this approximation that limits micromechanical methods to the quasi-static, $ka << 1$, domain and can lead to large error when inertial terms are important as those terms can lead to inclusion resonances and other important dynamic effects. Despite this limitation, the micromechanical approach provides a very accurate approximation of the frequency dependent lossy behavior of viscoelastic particulate composites when applied in the correct frequency range. This enhanced modeling freedom makes the quasi-static micromechanical approach very interesting for application in a material by design stratagem.

3.2.1 Localization and the integral equation

Zeller and Dederichs proposed modeling the composite material shown in Figure 3-1 as a *homogeneous* material whose elastic behavior varies spatially [34]. Taking this approach, the local behavior is dictated by the constitutive laws at each point is space. Elastic-viscoelastic correspondence allows the expression of the constitutive viscoelastic material behavior at each point in space through the viscoelastic form of Hooke's law: $\hat{\sigma}_{ij}(\mathbf{r}) = \hat{C}_{ijkl}(\mathbf{r})\hat{\varepsilon}_{kl}(\mathbf{r})$. The form proposed by Zeller and Dederichs implies that local material properties can be approximated as spatially dependent variations about the properties of the reference material which are independent of position. The mathematical expression of their approach is shown in Equation (III.2.3) for the viscoelastic stiffness tensor [37].

$$\hat{\mathbf{C}}(\mathbf{r}) = \hat{\mathbf{C}}^0 + \delta\hat{\mathbf{C}}(\mathbf{r}) \quad \text{with} \quad \mathbf{r} \in V \qquad \text{(III.2.3)}$$

In the above equation $\hat{\mathbf{C}}^0$ represents the viscoelastic stiffness tensor of the reference material which is constant for all $\mathbf{r}$, $\delta\hat{\mathbf{C}}(\mathbf{r})$ denotes the spatially dependent viscoelastic stiffness tensor variation, and V represents the volume of the

homogeneous medium. It is now assumed that there exists some displacement field, $\hat{u}_i^d = \hat{E}_{ij}\hat{x}_j$ imposed on the external surface of the reference medium, S, where $\hat{x}_j \in S$ and $\hat{E}_{ij}$ is the macroscopically imposed strain. The localization step begins by writing the equations for the stress and strain fields at every point in the homogenous medium [147]. These relations will be derived from the local expression for equilibrium, Equation (III.2.2), the local constitutive law, Equation (III.2.3), and by assuming that the contrast of the viscoelastic stiffness tensors of the constituent materials can be approximated with a locally compatible strain field, $\hat{\varepsilon}_{ij}(\mathbf{r})$ [34, 37]. The local constitutive law is first substituted into the local equilibrium equation yielding:

$$\left(\hat{C}_{ijkl}(\mathbf{r})\hat{u}_{k,l}(\mathbf{r})\right)_{,j} = 0 \qquad \text{(III.2.4)}$$

where $\hat{u}_k(\mathbf{r})$ is the local compatible displacement field in the composite material at every point in V. For the case of small perturbations, this displacement field is related to the strain field with the classic relation: $\hat{\varepsilon}_{ij}(\mathbf{r}) = \frac{1}{2}\left[\hat{u}_{i,j}(\mathbf{r}) + \hat{u}_{j,i}(\mathbf{r})\right]$ [104]. Now, when Equation (III.2.3) is inserted into the form of the equilibrium Equation (III.2.4) giving:

$$\hat{C}^0_{ijkl}\hat{u}_{k,lj}(\mathbf{r}) = \left[-\delta\hat{C}_{ijkl}(\mathbf{r})\hat{\varepsilon}_{kl}(\mathbf{r})\right]_{,j} \qquad \text{(III.2.5)}$$

Careful inspection of expression (III.2.5) indicates that the left-hand side (LHS) represents a distribution of fictitious volume forces which depend on the local viscoelastic stiffness [34]. Equation (III.2.5) can therefore be re-written as follows:

$$\hat{f}_i(\mathbf{r}) = \left[\delta\hat{C}_{ijkl}(\mathbf{r})\hat{\varepsilon}_{kl}(\mathbf{r})\right]_{,j} \tag{III.2.6}$$

This form of the equilibrium equation implies that the differential equation given in Equation (III.2.5) can be solved by employing Green's functions. This is done through the second order Green's tensor, $\hat{G}^0_{km}(\mathbf{r}-\mathbf{r}')$, where the superscript *0* denotes that the resulting solution propagates the effect of the volume force distribution through the reference medium. In this case, Green's tensor calculates the displacement in the k direction at the point $\mathbf{r}$ due to a time varying force, $f_i(t) = \mathbb{R}\mathrm{e}\left\{\hat{f}_i e^{-i\omega t}\right\}$, acting in the m direction and located at the point $\mathbf{r}'$.

The second order Green's tensor $\hat{G}^0_{km}(\mathbf{r}-\mathbf{r}')$ is found by solving the differential Equation (III.2.7):

$$\hat{C}^0_{ijkl}\hat{G}^0_{km,lj}(\mathbf{r}-\mathbf{r}') + \delta_{im}\delta(\mathbf{r}-\mathbf{r}')\delta(\omega-\omega') = 0 \tag{III.2.7}$$

for the boundary conditions on the external surface, S, of the homogeneous medium [37]. In the above, δ_{im} is the Kronecker delta, $\delta(\omega-\omega')$ is the frequency domain Dirac delta function, and $\delta(\mathbf{r}-\mathbf{r}')$ is the three dimensional Dirac delta function [37]. By modifying the work of Berveiller *et al* [37] to take the time variation of the distributed body forces into account, it can be shown that the solution to Equation (III.2.5) is given by the two integral equivalent equations below.

$$\hat{u}_m(\mathbf{r}) = \hat{u}^0_m(\mathbf{r}) + \int_{-\infty}^{\infty}\int_V \hat{G}^0_{im}(\mathbf{r}-\mathbf{r}')\hat{f}_i(\mathbf{r}')d\mathbf{r}'d\omega' \tag{III.2.8}$$

$$\hat{u}_m(\mathbf{r}) = \hat{u}^0_m(\mathbf{r}) + \int_{-\infty}^{\infty}\int_V \hat{G}^0_{im}(\mathbf{r}-\mathbf{r}')\left[\delta\hat{C}_{ijkl}(\mathbf{r}')\hat{\varepsilon}_{kl}(\mathbf{r}')\right]_{,j'} d\mathbf{r}'d\omega' \tag{III.2.9}$$

Integrating (III.2.9) by parts yields the following displacement field:

$$\hat{u}_m(\mathbf{r}) = \hat{u}_m^0(\mathbf{r}) - \int_{-\infty}^{\infty}\int_V \hat{G}_{im,j'}^0(\mathbf{r}-\mathbf{r}')\left[\delta\hat{C}_{ijkl}(\mathbf{r}')\hat{\varepsilon}_{kl}(\mathbf{r}')\right]d\mathbf{r}'d\omega' \qquad \text{(III.2.10)}$$

Recall the following property of the Green's tensor.

$$\hat{G}_{im,j'}^0 = \frac{\partial\hat{G}_{im}^0(\mathbf{r}-\mathbf{r}')}{\partial x_j'} = -\frac{\partial\hat{G}_{im}^0(\mathbf{r}-\mathbf{r}')}{\partial x_j} = -\hat{G}_{im,j}^0 \qquad \text{(III.2.11)}$$

And lastly, the simplified integral equation (III.2.12) expressing the strain field in the medium results from evoking the small strain approximation and the integral property of the Dirac delta function, $g(\omega) = \int_{-\infty}^{\infty} g(\omega')\delta(\omega-\omega')d\omega'$ [34, 145]:

$$\hat{\varepsilon}_{ij}(\mathbf{r}) = \hat{E}_{ij} - \int_V \hat{\Gamma}_{ijkl}^0(\mathbf{r}-\mathbf{r}')\delta\hat{C}_{klmn}(\mathbf{r}')\hat{\varepsilon}_{mn}(\mathbf{r}')d\mathbf{r}' \qquad \text{(III.2.12)}$$

In the above expression, $\hat{E}_{ij}$ represents the uniform macroscopic strain field of the medium which has *no spatial dependence*, and $\hat{\Gamma}_{ijkl}^0(\mathbf{r}-\mathbf{r}')$ is known as the modified Green's tensor. The modified Green's tensor is related to the previously introduced second order Green's tensor through expression (III.2.13).

$$\hat{\Gamma}_{ijkl}^0 = -\frac{1}{2}\left[\hat{G}_{ki,jl}^0(\mathbf{r}-\mathbf{r}') + \hat{G}_{kj,il}^0(\mathbf{r}-\mathbf{r}')\right] \qquad \text{(III.2.13)}$$

Relation (III.2.12) specifically shows that the strain field at the macroscopic length scale can be approximated by averaging the effects of material variations within the

volume, V. This reinforces Christensen's statement that multiscale modeling requires the effects of discontinuities at the microscopic length scale to have only an average effect on the macroscopic behavior [27].

It is now useful to define the spatial variation of the viscoelastic constants. For the topology shown in Figure 3-1, this variation can be mathematically expressed using the Heaviside step function $\theta(\mathbf{r})$ [149].

$$\delta\hat{\mathbf{C}}(\mathbf{r}) = \left(\hat{\mathbf{C}}^{I} - \hat{\mathbf{C}}^{0}\right)\theta^{I}(\mathbf{r}) + \left(\hat{\mathbf{C}}^{C} - \hat{\mathbf{C}}^{0}\right)\left[\theta^{2}(\mathbf{r}) - \theta^{I}(\mathbf{r})\right] \qquad \text{(III.2.14)}$$

Where the Heaviside step functions of the inclusion, $\theta^{I}(\mathbf{r})$, and composite inclusion (defined as the inclusion plus the coating), $\theta^{2}(\mathbf{r})$, are defined as:

$$\theta^{I}(\mathbf{r}) = \begin{cases} 1 & \text{if } \mathbf{r} \in V_{I} \\ 0 & \text{if } \mathbf{r} \notin V_{I} \end{cases}$$

$$\theta^{2}(\mathbf{r}) = \begin{cases} 1 & \text{if } \mathbf{r} \in V_{2} \\ 0 & \text{if } \mathbf{r} \notin V_{2} \end{cases} \qquad \text{(III.2.15)}$$

where V_I designates the inclusion volume and V_2 designates the volume of the composite inclusion. Equation (III.2.14) can then be expressed in a more compact form by introducing viscoelastic stiffness contrast tensors and the Heaviside step function variation, $\delta\theta^{I}(\mathbf{r})$ [24, 40].

$$\delta\hat{\mathbf{C}}(\mathbf{r}) = \Delta\hat{\mathbf{C}}^{I0}\theta^{I}(\mathbf{r}) + \Delta\hat{\mathbf{C}}^{C0}\delta\theta^{I}(\mathbf{r}) \qquad \text{(III.2.16)}$$

In the relation above, $\Delta\hat{C}^{XY}$ represents the difference, or contrast, between the viscoelastic stiffness tensor of materials X and Y, $\Delta\hat{\mathbf{C}}^{XY} = \hat{\mathbf{C}}^{X} - \hat{\mathbf{C}}^{Y}$. The variation

$\delta\theta^I(\mathbf{r})$ is defined by the upper expression in Equation (III.2.17). The lower relationship only hold true when the inclusion coating is thin.

$$\begin{aligned}\delta\theta^I(\mathbf{r}) &= \theta(x_i, a_i + \Delta a_i) - \theta^I(x_i, a_i) \\ &\approx \sum_i \frac{\partial\theta^I}{\partial a_i}\Delta a_i\end{aligned} \tag{III.2.17}$$

Cherkaoui *et al* [24], have further shown that for the thin coating case, $\delta\theta^I(\mathbf{r})$ can be approximated by Equation (III.2.18).

$$\delta\theta^I(\mathbf{r}) \approx p\sum_i \frac{\Delta a_i}{a_i}\frac{x_i^2}{a_i^2}\delta(S_I) \tag{III.2.18}$$

In the above expression, x_i are the coordinates of a point on the inclusion surface, a_i is the radius of the ellipsoidal inclusion, Δa_i is the inclusion coating thickness along the x_i direction, $\delta(S_I)$ is the Dirac delta distribution for the surface of the inclusion, S_I, and p is the perpendicular distance from the inclusion center to the tangent plane of the surface at the point x_i. The distance p can be calculated for any point on the surface S_I using Equation (III.2.19) [24].

$$p^{-1} = \sqrt{\frac{x_1^2}{a_1^4} + \frac{x_2^2}{a_2^4} + \frac{x_3^2}{a_3^4}} \tag{III.2.19}$$

Equations (III.2.18) and (III.2.16) can now be inserted into Equation (III.2.12) to yield an expression for strain at every point in the homogenous medium. The resulting volume integral can be simplified by employing the following property of the Dirac delta distribution: $\int_V g(\mathbf{r})\delta(S)d\mathbf{r} = \int_S g(\mathbf{r})dS$.

$$\hat{\varepsilon}_{ij}(\mathbf{r}) = \hat{E}_{ij} - \int_{V_I} \hat{\Gamma}^0_{ijkl}(\mathbf{r}-\mathbf{r}')\Delta\hat{C}^{I0}_{klmn}\hat{\varepsilon}_{mn}(\mathbf{r}')d\mathbf{r}'$$
$$-\sum_{\alpha}\int_{S_I^+} \hat{\Gamma}^0_{ijkl}(\mathbf{r}-\mathbf{r}^+)\Delta\hat{C}^{C0}_{klmn}\hat{\varepsilon}_{mn}(\mathbf{r}^+)p\frac{\Delta a_\alpha}{a_\alpha}\frac{x_\alpha^2}{a_\alpha^2}dS \qquad \text{(III.2.20)}$$

Here, S_I^+ is the external surface of the inclusion, $\mathbf{r}^+$ is a point on the coating side of the inclusion – coating interface, and the components of $\varepsilon_{mn}(\mathbf{r}^+)$ describe the strain field inside the coating at a point very close to the inclusion – coating interface. Equation (III.2.20) is quite complicated and would be difficult to resolve in its present form. Fortunately, it is possible to find a relationship between the field $\varepsilon_{mn}(\mathbf{r}^+)$ and the strain field in the inclusion, which is assumed to be uniform in accordance with Eshelby's results [108]. This is done by employing interfacial operators [147], which are the subject of the following section.

3.2.2 Interfacial operators

The stress and strain fields in the coating material can be very complicated in general. This problem is exacerbated by the material discontinuity that exists at the coating – inclusion and coating – reference material interfaces. This material discontinuity leads to jumps in the stress and strain fields across material interfaces. In order to approximate the stress and strain state in the coating material, this section first makes simplifying hypothesis that *the stress and strain fields are uniform through the coating thickness in directions normal to the inclusion surface*. This is a reasonable approximation for a *thin* coating which is the case when $\Delta a_i/a_i << 1$. Care must be taken, however, when this no longer holds true. By assuming that the coating is thin, the interfacial operators studied by Walpole [38] and Hill [39] will be employed in the following sections to relate the stress and strain fields in the inclusion to those in the coating material.

Interfacial operators are convenient mathematical tools which calculate the stress or strain jump across a material interface. These operators are derived by writing the equations for the continuity of displacement and traction across the material interface. This derivation begins with the general case of two solid phases, A and B, with viscoelastic constants $\hat{\mathbf{C}}^A$ and $\hat{\mathbf{C}}^B$ separated by a surface with unit normal, $\vec{n}$ as shown in Figure 3-2.

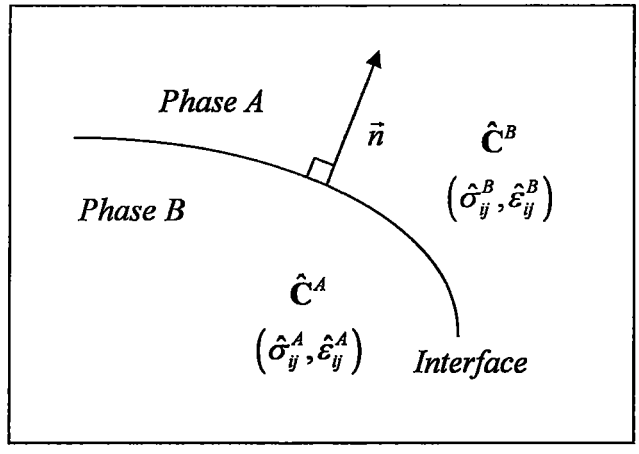

Figure 3-2 : Schematic of the interface of two viscoelastic solids used in the derivation of interfacial operators.

The interfacial operator derived below assumes that the bond between materials A and B is perfect. This assumption leads to two requirements on the mechanical behavior across the material interface: (*i*) continuity of displacement, $\hat{\vec{u}}$, and (*ii*) continuity of traction, $\hat{\sigma}_{ij}n_j$. These two mechanical behaviors are mathematically represented with Equations (III.2.21) and (III.2.22), respectively [147].

$$[\hat{u}_i] \equiv \hat{u}_i^A - \hat{u}_i^B = \vec{0} \qquad \text{(III.2.21)}$$

$$[\hat{\sigma}_{ij}]n_j \equiv (\hat{\sigma}_{ij}^A - \hat{\sigma}_{ij}^B)n_j = \vec{0} \qquad \text{(III.2.22)}$$

where n_j represent the components of the unit normal vector of the interface. The values of the normal vector are determined from Equation (III.2.23) when this interface is assumed to be a closed surface in the form of and ellipsoid.

$$n_i = \frac{x_i}{a_i^2} p \tag{III.2.23}$$

The continuity of displacement requirement given in expression (III.2.21), allows the calculation of displacement gradient jump at each point, $\mathbf{r}(x_i)$, on the interface as follows. It is first noted that $d\vec{u}_i = u_{i,j} dx_j$, yielding the following from Equation (III.2.21):

$$\left[\hat{u}_{i,j}\right] dx_j = \left(\hat{u}_{i,j}^A - \hat{u}_{i,j}^B\right) dx_j = 0 \tag{III.2.24}$$

Given that dx_j denotes the direction tangent to the surface and that $n_j dx_j = 0$ by definition, (III.2.24) is equivalent to the following expression [24]:

$$\left[\hat{u}_{i,j}\right] \equiv \hat{u}_{i,j}^A - \hat{u}_{i,j}^B = \hat{\lambda}_i n_j \tag{III.2.25}$$

In the above expression, $\hat{\lambda}_i$ represents the complex time varying displacement gradient jump across the interface. Noting that the gradient field is symmetric with respect to indices i and j, Equation (III.2.25) is altered to give the strain jump across the material interface, denoted as $\left[\hat{\varepsilon}_{ij}\right]$.

$$\left[\hat{\varepsilon}_{ij}\right] = \hat{\varepsilon}_{ij}^A - \hat{\varepsilon}_{ij}^B = \frac{1}{2}\left(\hat{\lambda}_i n_j + \hat{\lambda}_j n_i\right) \tag{III.2.26}$$

Now, continuity of traction and constitutive behavior gives the following statement.

$$\hat{\sigma}_{ij}^{A} n_j = \hat{\sigma}_{ij}^{B} n_j \quad \Rightarrow \quad \hat{C}_{ijkl}^{A} \hat{\varepsilon}_{kl}^{A} n_j = \hat{C}_{ijkl}^{B} \hat{\varepsilon}_{kl}^{B} n_j \tag{III.2.27}$$

In this form, the expression of continuity of traction permits the elimination of one of the strain fields in Equation (III.2.26). For example, if phase B is assumed to be the reference material, $\hat{\varepsilon}_{ij}^{A}$ can be eliminated leaving:

$$\begin{gathered} \hat{C}_{ijkl}^{B} \hat{\varepsilon}_{kl}^{B} n_j = \hat{C}_{ijkl}^{A} \left(\varepsilon_{kl}^{B} + \hat{\lambda}_k n_l \right) n_j \\ \Downarrow \\ \left(\hat{C}_{ijkl}^{B} - \hat{C}_{ijkl}^{A} \right) \hat{\varepsilon}_{kl}^{B} n_j = \hat{C}_{ijkl}^{A} n_l n_j \hat{\lambda}_k \end{gathered} \tag{III.2.28}$$

The right-hand side (RHS) of the lower expression in Equation (III.2.28) is Christoffel's matrix for material A, $\hat{K}_{ik}^{A}$, defined as $\hat{K}_{ik}^{A} = \hat{C}_{ijkl}^{A} n_l n_j$, multiplied by the complex magnitude of the strain jump across the interface, $\hat{\lambda}_k$. From this expression, the magnitude of the strain jump can be calculated from knowledge of the viscoelastic stiffness tensors of each material, the outward unit normal of the surface, and the strain field in the reference material via in Equation (III.2.29).

$$\hat{\lambda}_i = \left(\hat{K}_{ik}^{A} \right)^{-1} n_l \left(\hat{C}_{klmn}^{B} - \hat{C}_{klmn}^{A} \right) \hat{\varepsilon}_{mn}^{B} \tag{III.2.29}$$

Using the above expression, the strain jump is re-written as:

$$\hat{\varepsilon}_{ij}^{A} - \hat{\varepsilon}_{ij}^{B} = \hat{\bar{P}}_{ijkl}^{A} \left(\hat{C}_{klmn}^{B} - \hat{C}_{klmn}^{A} \right) \hat{\varepsilon}_{ij}^{B} \tag{III.2.30}$$

where the interfacial operator, $\hat{\bar{P}}_{ijkl}^{A}$, follows directly from the substitution of Equation (III.2.29) into (III.2.26). The interfacial operator is defined in Equation (III.2.31)

[40]. Note that the interfacial operator is only dependent on the constituent material properties and the outward unit normal of the interface.

$$\hat{\bar{P}}^A_{ijkl} \equiv \frac{1}{2}\left[\left(\hat{K}^A_{ik}\right)^{-1} n_j n_l + \left(\hat{K}^A_{jk}\right)^{-1} n_i n_l\right]$$
$$\Downarrow \qquad \text{(III.2.31)}$$
$$\hat{P}^A_{ijkl} \equiv \frac{1}{4}\left[\left(\hat{K}^A_{ik}\right)^{-1} n_j n_l + \left(\hat{K}^A_{jk}\right)^{-1} n_i n_l + \left(\hat{K}^A_{il}\right)^{-1} n_j n_k + \left(\hat{K}^A_{jl}\right)^{-1} n_i n_k\right]$$

The expressions above lead to the following general expressions relating the strain field in phase A to that in phase B.

$$\hat{\varepsilon}^A_{ij} \doteq \left[\hat{P}^A_{ijkl}\left(\hat{C}^B_{klmn} - \hat{C}^A_{klmn}\right) + I_{ijmn}\right]\hat{\varepsilon}^B_{mn}$$
$$\text{(III.2.32)}$$
$$\hat{\varepsilon}^B_{ij} = \left[\hat{P}^B_{ijkl}\left(\hat{C}^A_{klmn} - \hat{C}^B_{klmn}\right) + I_{ijmn}\right]\hat{\varepsilon}^A_{mn}$$

Where the fourth order identity tensor, I_{ijkl}, is defined as $I_{ijkl} = (1/2)\left(\delta_{ik}\delta_{jl} + \delta_{il}\delta_{jk}\right)$ and δ_{ij} is the Kronecker delta. Interfacial operators have several important mathematical properties which have been detailed by Hill [39]. For the purposes of this work, however, they are simply employed to calculate discontinuities of the stress and strain fields across a material interface.

3.2.2.1 Application to local strain fields

The interfacial operators developed above can be used to simplify Equation (III.2.20) which describes the local strain field in the homogeneous medium. This simplification occurs when the strain field in the coating is related to the strain field in the inclusion by applying interfacial operators. These operators permit the calculation

of the strain field at the inclusion-coating interface on the coating side, $\hat{\varepsilon}_{ij}\left(\mathbf{r}^{+}\right)$, from the strain field the same interface on the inclusion side, $\hat{\varepsilon}_{ij}\left(\mathbf{r}^{-}\right)$. This strain jump calculation does not require any simplifying assumptions about the strain fields in either medium. $\hat{\varepsilon}_{ij}\left(\mathbf{r}^{+}\right)$ is calculated by adding the strain jump across the interface, using equations in the form of (III.2.32), to the strain field on the inclusion side of the interface. This operation is shown mathematically in Equation (III.2.33).

$$\hat{\varepsilon}_{ij}\left(\mathbf{r}^{+}\right)=\hat{\varepsilon}_{ij}\left(\mathbf{r}^{-}\right)+\hat{P}^{C}_{ijkl}\Delta\hat{C}^{IC}_{lkmn}\hat{\varepsilon}_{mn}\left(\mathbf{r}^{-}\right) \qquad \text{(III.2.33)}$$

Here $\Delta\hat{\mathbf{C}}^{IC}$ is a tensor representing the contrast between the viscoelastic stiffness of the inclusion, *I*, and the coating, *C*. Eshelby showed that the strain field in the inclusion, being on the smallest length scale, can be accurately approximated as uniform in space. The best approximation of that uniform strain value is a volumetric average [108]. Applying this logic to the current problem gives Equation (III.2.34).

$$\hat{\varepsilon}^{I}_{ij}\equiv\frac{1}{V_I}\int_{V_I}\hat{\varepsilon}_{ij}\left(\mathbf{r}\right)d\mathbf{r} \quad \mathbf{r}\in V_I \;\Rightarrow\; \hat{\varepsilon}^{I}_{ij}\equiv\hat{\varepsilon}\left(\mathbf{r}^{-}\right) \qquad \text{(III.2.34)}$$

Equation (III.2.33) then simplifies to (III.2.35).

$$\hat{\varepsilon}_{ij}\left(\mathbf{r}^{+}\right)=\hat{\varepsilon}^{I}_{ij}+\hat{P}^{C}_{ijkl}\Delta\hat{C}^{IC}_{lkmn}\hat{\varepsilon}^{I}_{ij} \qquad \text{(III.2.35)}$$

Finally, the expression above for $\hat{\varepsilon}_{ij}\left(\mathbf{r}^{+}\right)$ is substituted into the integral equation. The resulting expression for local strain field in the homogenous medium with spatially varying viscoelastic constants simplifies to Equation (III.2.36) [24]:

$$\hat{\varepsilon}_{ij}(\mathbf{r}) = \hat{E}_{ij} - \int_{V_I} \hat{\Gamma}^0_{ijkl}(\mathbf{r}-\mathbf{r}')\Delta\hat{C}^{I0}_{klmn}\hat{\varepsilon}^I_{mn}d\mathbf{r}'$$
$$-\sum_{\alpha}\int_{S_I^+}\hat{\Gamma}^0_{ijkl}(\mathbf{r}-\mathbf{r}^+)\Delta\hat{C}^{C0}_{klmn}\hat{\varepsilon}^I_{mn}p\frac{\Delta a_\alpha}{a_\alpha}\frac{x_\alpha^2}{a_\alpha^2}dS \qquad \text{(III.2.36)}$$
$$-\sum_{\alpha}\int_{S_I^+}\hat{\Gamma}^0_{ijkl}(\mathbf{r}-\mathbf{r}^+)\Delta\hat{C}^{C0}_{klmn}\hat{P}^C_{mnpq}\Delta C^{IC}_{pqrs}\hat{\varepsilon}^I_{rs}p\frac{\Delta a_\alpha}{a_\alpha}\frac{x_\alpha^2}{a_\alpha^2}dS$$

It is important to point out that the above integral equation only depends on the average strain field in the inclusion, the viscoelastic stiffness of the constituent materials, and the geometry of the coated inclusion. When carrying out the homogenization step, only the average strain field in each phase will be required. Given that the stiffness tensor, $\hat{\mathbf{C}}(\mathbf{r})$, is piece-wise uniform, it is possible to calculate the macroscopic average strain from Equation (III.2.36). The strain localization tensor for the average strain in the inclusion and coating materials can be then found from the resulting expression for the macroscopic strain [24]. This is the subject of the next two sections.

3.2.3 Localization: Average strain fields in the inclusion and coating

The derivation of the integral equation in Sections 3.2.1 and 3.2.2, which used techniques introduced by Zeller and Dederichs [34], Hill [39], and Walpole [38], emphasizes one of the most basic requirements of multiscale modeling given by Christensen [27]. The requirement is that inhomogeneities, representing the smallest length scale, only have an average effect on the behavior observed at the macroscopic scale. Following this logic, the integral equation representation (III.2.36) describing the local strain field will now be used to approximate the effective behavior of the heterogeneous medium at the macroscopic scale by calculating the volumetric average of $\hat{\varepsilon}_{ij}(\mathbf{r})$.

The volume average of the complex strains in the inclusion and coating, $\hat{\varepsilon}_{ij}^{I}$ and $\hat{\varepsilon}_{ij}^{C}$ respectively, must first be defined.

$$\hat{\varepsilon}_{ij}^{I} = \frac{1}{V_I}\int_{V_I}\hat{\varepsilon}_{ij}(\mathbf{r})d\mathbf{r}$$

$$\hat{\varepsilon}_{ij}^{C} = \frac{1}{V_C}\int_{V_C}\hat{\varepsilon}_{ij}(\mathbf{r})d\mathbf{r} \tag{III.2.37}$$

The volume average of Equation (III.2.36) with respect to the inclusion gives [24]:

$$\begin{aligned}\hat{\varepsilon}_{ij}^{I} = \hat{E}_{ij} &- \frac{1}{V_I}\int_{V_I}\int_{V_I}\hat{\Gamma}_{ijkl}^{0}(\mathbf{r}-\mathbf{r}')\Delta\hat{C}_{klmn}^{I0}\hat{\varepsilon}_{mn}^{I}d\mathbf{r}'d\mathbf{r} \\ &- \frac{1}{V_I}\sum_{\alpha}\int_{S_I^+}\left\{\int_{V_I}\hat{\Gamma}_{ijkl}^{0}(\mathbf{r}-\mathbf{r}^+)d\mathbf{r}\right\}\Delta\hat{C}_{klmn}^{C0}\hat{\varepsilon}_{mn}^{I}p\frac{\Delta a_\alpha}{a_\alpha}\frac{x_\alpha^2}{a_\alpha^2}dS \\ &- \frac{1}{V_I}\sum_{\alpha}\int_{S_I^+}\left\{\int_{V_I}\hat{\Gamma}_{ijkl}^{0}(\mathbf{r}-\mathbf{r}^+)d\mathbf{r}\right\}\Delta\hat{C}_{klmn}^{C0}\hat{P}_{mnpq}^{C}\Delta C_{pqrs}^{IC}\hat{\varepsilon}_{rs}^{I}p\frac{\Delta a_\alpha}{a_\alpha}\frac{x_\alpha^2}{a_\alpha^2}dS\end{aligned} \tag{III.2.38}$$

It is now necessary to employ the simplifying assumption that the strain field in the coating is uniform through its thickness in directions normal to the inclusion surface. By noting that $\hat{\varepsilon}_{ij}^{C}$ is equal to $\hat{\varepsilon}_{ij}(\mathbf{r}^+)$, the average strain field in the coating can calculated from Equation (III.2.35). This expression illustrates that for a thinly coated inclusion, the strain field in the coating only depends on the inclusion normal, the average strain in the inclusion, and the constituent material properties of the inclusion and coating.

$$\hat{\varepsilon}_{ij}^{C} = \hat{\varepsilon}_{ij}^{I} + \frac{1}{V_C}\left\{\int_{V_C}\hat{P}_{ijkl}^{C}d\mathbf{r}\right\}\Delta\hat{C}_{klmn}^{IC}\hat{\varepsilon}_{mn}^{I} \tag{III.2.39}$$

Future equation treatment is simplified by defining the following tensor which denotes the volume average of the modified Green's tensor.

$$\hat{T}^{I}_{ijkl}\left(\hat{\mathbf{C}}^{0}\right)=\int_{V_I}\hat{\Gamma}^{0}_{ijkl}\left(\mathbf{r}-\mathbf{r}'\right)d\mathbf{r}' \quad \text{si } \mathbf{r}\in V_I \tag{III.2.40}$$

This tensor is related to Eshelby's tensor, **S**, as shown below [37, 108]:

$$\hat{\mathbf{S}}=\hat{\mathbf{T}}^{I}\left(\mathbf{C}^{0}\right):\hat{\mathbf{C}}^{0} \tag{III.2.41}$$

Using interfacial operators, $\int_{V_I}\hat{\Gamma}^{0}_{ijkl}\left(\mathbf{r}^{+}-\mathbf{r}\right)d\mathbf{r}$ is related to the relationship given in (III.2.40) as follows [24]:

$$\int_{V_I}\hat{\Gamma}^{0}_{ijkl}\left(\mathbf{r}^{+}-\mathbf{r}\right)d\mathbf{r}=\hat{T}^{I}_{ijkl}\left(\hat{\mathbf{C}}^{0}\right)-\hat{P}^{0}_{ijkl} \tag{III.2.42}$$

Substituting Equation (III.2.42) into the expression for the average strain field of the inclusion, (III.2.38), eliminates the volume integral inside the summation and the surface integral. The resulting expression is still complicated by terms containing the projection, p, and interfacial operators, $\hat{\mathbf{P}}^{*}$, where * represents either the inclusion, the coating, or the reference material. Fortunately, Equations (III.2.38) and (III.2.39) are greatly simplified through further application of the thin coating assumption and Equation (III.2.42). The result is two expressions relating the average macroscopic strain field to the average inclusion and coating strain fields, the viscoelastic material properties of each constituent phase, and the coated inclusion geometry.

It is first shown that the volume of the coating is related to an integral on the entire representative volume, V, through the Heaviside functions given in Equation (III.2.15).

$$V_C = \int_{V_C} d\mathbf{r} = \int_V \left[\theta^2(\mathbf{r}) - \theta^I(\mathbf{r})\right] d\mathbf{r} \qquad \text{(III.2.43)}$$

The Heaviside step function variation, $\delta\theta^I(\mathbf{r})$, definition given by relation (III.2.18) is therefore related to the coating volume as shown in Equation (III.2.44) when the coating is assumed to be thin.

$$V_C \approx \int_V \sum_i p \frac{\Delta a_i}{a_i} \frac{x_i^2}{a_i^2} \delta(S_I) d\mathbf{r} = \sum_i \int_{S_I} p \frac{\Delta a_i}{a_i} \frac{x_i^2}{a_i^2} dS \qquad \text{(III.2.44)}$$

The far RHS of the expression above partially simplifies expression (III.2.38) describing the average strain in the inclusion. However, the expression is still complicated by the surface integral of the interfacial operators. This problem will be addressed in the following analysis. Equation (III.2.40) is first integrated with respect to the coating volume, V_C, and rearranged giving (III.2.45) [24].

$$\int_{V_C} \hat{P}^*_{ijkl} d\mathbf{r} = V_C \hat{T}^I_{ijkl}\left(\hat{\mathbf{C}}^*\right) - \int_{V_C} \int_{V_I} \hat{\Gamma}^*_{ijkl}\left(\mathbf{r}^+ - \mathbf{r}\right) d\mathbf{r}^+ d\mathbf{r} \qquad \text{(III.2.45)}$$

Noting that $V_C = V_2 - V_I$, the term on the right above can be decomposed as follows:

$$\int_{V_C} \int_{V_I} \hat{\Gamma}^*_{ijkl}\left(\mathbf{r}^+ - \mathbf{r}\right) d\mathbf{r}^+ d\mathbf{r} = \int_{V_2} \int_{V_I} \hat{\Gamma}^*_{ijkl}\left(\mathbf{r}^+ - \mathbf{r}\right) d\mathbf{r}^+ d\mathbf{r} - \int_{V_I} \int_{V_I} \hat{\Gamma}^*_{ijkl}\left(\mathbf{r} - \mathbf{r}'\right) d\mathbf{r} d\mathbf{r}' \qquad \text{(III.2.46)}$$

Generalizing Equation (III.2.40) yields the two following expressions [23]:

$$\hat{T}^{2}_{ijkl}\left(\hat{\mathbf{C}}^{*}\right)=\int_{V_2}\hat{\Gamma}^{*}_{ijkl}\left(\mathbf{r}-\mathbf{r}'\right)d\mathbf{r}' \quad \text{si } \mathbf{r}\in V_2$$

$$\hat{T}^{I}_{ijkl}\left(\hat{\mathbf{C}}^{*}\right)=\int_{V_I}\hat{\Gamma}^{*}_{ijkl}\left(\mathbf{r}-\mathbf{r}'\right)d\mathbf{r}' \quad \text{si } \mathbf{r}\in V_I \tag{III.2.47}$$

Application of Equation (III.2.47) simplifies the two terms on the RHS of (III.2.46) to the two following expressions relating the inclusion volume and the modified Green's function integral.

$$V_I\hat{T}^{2}_{ijkl}\left(\hat{\mathbf{C}}^{*}\right)=\int_{V_2}\int_{V_I}\hat{\Gamma}^{*}_{ijkl}\left(\mathbf{r}-\mathbf{r}'\right)d\mathbf{r}^{+}d\mathbf{r}$$

$$V_I\hat{T}^{I}_{ijkl}\left(\hat{\mathbf{C}}^{*}\right)=\int_{V_I}\int_{V_I}\hat{\Gamma}^{*}_{ijkl}\left(\mathbf{r}-\mathbf{r}'\right)d\mathbf{r}'d\mathbf{r} \tag{III.2.48}$$

Substituting these relations into Equation (III.2.46) gives [24]:

$$\int_{V_C}\int_{V_I}\hat{\Gamma}^{*}_{ijkl}\left(\mathbf{r}^{+}-\mathbf{r}\right)d\mathbf{r}^{+}d\mathbf{r}=V_I\left(\hat{T}^{2}_{ijkl}\left(\hat{\mathbf{C}}^{*}\right)-\hat{T}^{I}_{ijkl}\left(\hat{\mathbf{C}}^{*}\right)\right) \tag{III.2.49}$$

Inserting (III.2.49) into Equation (III.2.45) gives the following relationship describing the volume integral of the interfacial operator in the coating.

$$\int_{V_C}\hat{P}^{*}_{ijkl}d\mathbf{r}=V_C\hat{T}^{I}_{ijkl}\left(\hat{\mathbf{C}}^{*}\right)-V_I\left(\hat{T}^{2}_{ijkl}\left(\hat{\mathbf{C}}^{*}\right)-\hat{T}^{I}_{ijkl}\left(\hat{\mathbf{C}}^{*}\right)\right) \tag{III.2.50}$$

The integral of the interfacial operator, $\hat{\mathbf{P}}^{*}$, on V_C is related to an integral over the entire the representative volume, V, as shown in upper expression of Equation (III.2.51). The lower expression is simply a re-statement of Equation (III.2.50).

$$\int_{V_C} \hat{P}^*_{ijkl} d\mathbf{r} = \int_V \hat{P}^*_{ijkl} \delta\theta^I(\mathbf{r}) d\mathbf{r} = \sum_\alpha \int_{S_I} \hat{P}^*_{ijkl} p \frac{\Delta a_\alpha}{a_\alpha} \frac{x_\alpha^2}{a_\alpha^2} dS$$
$$= V_C \hat{T}^I_{ijkl}\left(\hat{\mathbf{C}}^*\right) - V_I\left[\hat{T}^2_{ijkl}\left(\hat{\mathbf{C}}^*\right) - \hat{T}^I_{ijkl}\left(\hat{\mathbf{C}}^*\right)\right] \tag{III.2.51}$$

Using all of the above expressions, it is finally possible to express the average strain fields as a function of tensors $\hat{\mathbf{T}}^I\left(\hat{\mathbf{C}}^*\right)$ and $\hat{\mathbf{T}}^2\left(\hat{\mathbf{C}}^*\right)$, the geometry of the coated inclusion, and the viscoelastic stiffness tensors of the constituent materials. This is done by substituting Equations (III.2.44) and (III.2.51) into integral equations (III.2.38) and (III.2.39). The resulting expressions for the average strain field in the inclusion and coating are given in Equations (III.2.52) and (III.2.53), respectively.

$$\begin{aligned}\hat{\varepsilon}^I_{ij} = \hat{E}_{ij} &- \hat{T}^2_{ijkl}\left(\hat{\mathbf{C}}^0\right)\Delta\hat{C}^{I0}_{klmn}\hat{\varepsilon}^I_{mn} \\ &- \frac{V_C}{V_I}\hat{T}^I_{ijkl}\left(\hat{\mathbf{C}}^0\right)\Delta\hat{C}^{C0}_{klmn}\hat{T}^I_{mnpq}\left(\hat{\mathbf{C}}^C\right)\Delta\hat{C}^{IC}_{pqrs}\hat{\varepsilon}^I_{rs} \\ &- \frac{V_C}{V_I}\left[\hat{T}^I_{ijkl}\left(\hat{\mathbf{C}}^C\right) - \hat{T}^I_{ijkl}\left(\hat{\mathbf{C}}^0\right)\right]\Delta\hat{C}^{IC}_{klmn}\hat{\varepsilon}^I_{mn} \\ &+ \left[I_{ijmn} + \hat{T}^I_{ijkl}\left(\hat{\mathbf{C}}^0\right)\Delta\hat{C}^{C0}_{klmn}\right]\left[\hat{T}^2_{mnpq}\left(\hat{\mathbf{C}}^C\right) - \hat{T}^I_{mnpq}\left(\hat{\mathbf{C}}^C\right)\right]\Delta\hat{C}^{IC}_{pqrs}\hat{\varepsilon}^I_{rs}\end{aligned} \tag{III.2.52}$$

$$\hat{\varepsilon}^C_{ij} = \hat{\varepsilon}^I_{ij} + \left[\hat{T}^I_{ijkl}\left(\hat{\mathbf{C}}^C\right) - \frac{V_I}{V_C}\left\{\hat{T}^2_{ijkl}\left(\hat{\mathbf{C}}^C\right) - \hat{T}^I_{ijkl}\left(\hat{\mathbf{C}}^C\right)\right\}\right]\Delta\hat{C}^{IC}_{klmn}\hat{\varepsilon}^I_{mn} \tag{III.2.53}$$

Several important aspects of the integral of the modified Green's tensor must be highlighted at this point. First, $\hat{\mathbf{T}}^2\left(\hat{\mathbf{C}}^*\right)$ is calculated on the volume V_2 which represents the combined volume of the inclusion and coating. This volume is assumed to be ellipsoidal in shape and the volume integral is dependent on the ratio of its axes, $(a_i + \Delta a_i)/(a_j + \Delta a_j)$. Likewise, $\hat{\mathbf{T}}^I\left(\hat{\mathbf{C}}^*\right)$, is calculated on the volume V_I

and depends on the ratio a_i/a_j [147]. For the specific case where $\Delta a_i/a_i = \Delta a_j/a_j$, the following results [23]:

$$\frac{a_i + \Delta a_i}{a_i + \Delta a_i} = \frac{a_i\left(1 + \Delta a_i / a_i\right)}{a_j\left(1 + \Delta a_j / a_j\right)} = \frac{a_i}{a_j} \tag{III.2.54}$$

Therefore, when the ratio of the coating thickness to the inclusion axis is the same in all directions and the coating is thin the following will always be true: $\hat{\mathbf{T}}^2\left(\hat{\mathbf{C}}^*\right) = \hat{\mathbf{T}}^I\left(\hat{\mathbf{C}}^*\right)$. The remainder of this work is based on the above assumption, which further simplifies relations (III.2.52) and (III.2.53) to Equations (III.2.55) and (III.2.56).

$$\begin{aligned}\hat{\varepsilon}^I_{ij} = \hat{E}_{ij} &- \hat{T}^I_{ijkl}\left(\hat{\mathbf{C}}^0\right)\Delta\hat{C}^{I0}_{klmn}\hat{\varepsilon}^I_{mn} \\ &- \frac{V_C}{V_I}\hat{T}^I_{ijkl}\left(\hat{\mathbf{C}}^0\right)\Delta\hat{C}^{C0}_{klmn}\hat{T}^I_{mnpq}\left(\hat{\mathbf{C}}^C\right)\Delta\hat{C}^{IC}_{pqrs}\hat{\varepsilon}^I_{rs} \\ &- \frac{V_C}{V_I}\left[\hat{T}^I_{ijkl}\left(\hat{\mathbf{C}}^C\right) - \hat{T}^I_{ijkl}\left(\hat{\mathbf{C}}^0\right)\right]\Delta\hat{C}^{IC}_{klmn}\hat{\varepsilon}^I_{mn}\end{aligned} \tag{III.2.55}$$

$$\hat{\varepsilon}^C_{ij} = \hat{\varepsilon}^I_{ij} + \hat{T}^I_{ijkl}\left(\hat{\mathbf{C}}^C\right)\Delta\hat{C}^{IC}_{klmn}\hat{\varepsilon}^I_{mn} \tag{III.2.56}$$

Equations (III.2.55) and (III.2.56) are used in the following section to find the strain localization tensors, $\hat{\mathbf{A}}^I$ and $\hat{\mathbf{A}}^C$. These strain localization tensors ultimately permit the calculation of the effective viscoelastic stiffness tensor of the composite material. It is important to note that calculating $\hat{\mathbf{T}}^I\left(\hat{\mathbf{C}}^*\right)$ for the general case is not trivial [26, 37, 41]. The three different methods exist to numerically approximating this tensor. They are: (*i*) Fourier transforms, (*ii*) potential functions, and (*iii*) direct implementation using Eshelby's results [147]. The simplest of these methods,

implementation of Eshelby's results, can only be used when the host material is isotropic. The Fourier transform technique, which is described in detail in Appendix A, has been employed in this work. Further discussion on the numerical approximation of this tensor during SC model implementation is addressed in Section 4.4.

3.2.4 Homogenization and the self-consistent approximation

The integral equations derived above provide a means to calculate the local strain fields given the loading conditions imposed at the RVE boundary. It is possible to use these expressions and averaging operations to approximate the macroscopic behavior of a viscoelastic particulate composite in the dilute case. Unfortunately, the assumptions implicit with the Green's function formulation employed to derive the integral equation do not take into account inclusion interaction. If inclusion volume fraction is elevated it is necessary to account for these interactions. Several different approaches exist to approximate this interaction and the method employed in this work is the self-consistent method. The SC model is derived by defining the RVE as shown below in Figure 3-3. It assumes that the reference material is the effective material, an assumption that indirectly takes inclusion interaction into account [43]. The resulting SC model is an *implicit* set of tensor equations whose solution is the effective viscoelastic stiffness tensor of the composite.

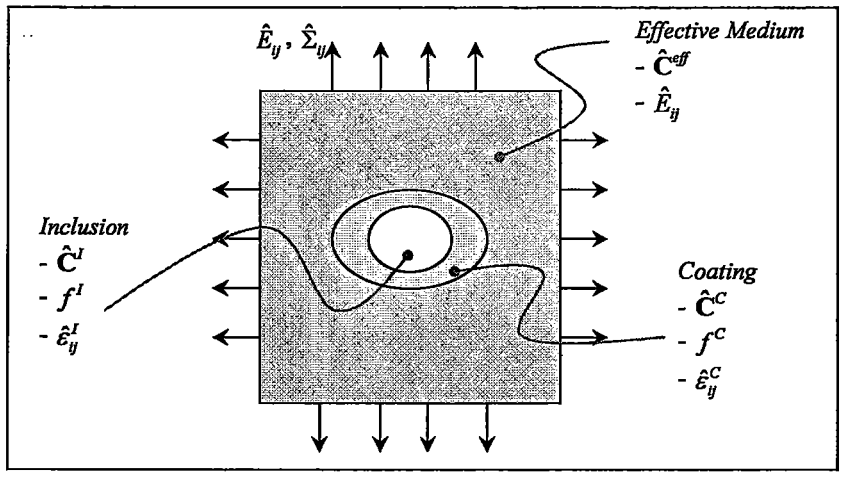

Figure 3-3: The SC model RVE consists of a coated inclusion surrounded by the homogeneous effective medium. The inclusion and coating are fully described by their viscoelastic properties $\hat{\mathbf{C}}^{I}$ and $\hat{\mathbf{C}}^{C}$, an average strain field $\hat{\varepsilon}_{ij}^{I}$ and $\hat{\varepsilon}_{ij}^{C}$, and volume fractions f^{I} and f^{C}, respectively. The effective medium is submitted to macroscopic stress and strain fields, $\hat{\Sigma}_{ij}$ and $\hat{E}_{ij}$, and has viscoelastic stiffness tensor $\hat{\mathbf{C}}^{eff}$.

The first homogenization step defines the volumetric composition of the composite material. The total volume of the particulate composite is decomposed into portions that are occupied by the inclusion, V_I, coating, V_C, and matrix, V_M, according to $V = V_M + V_I + V_C$. This equation yields the volume fraction relation below.

$$f^{M} + f^{I} + f^{C} = 1 \qquad \text{(III.2.57)}$$

Here f^{X} is the volume fraction of phase X and is related to the total volume fraction of the composites by $f^{X} = V^{X}/V$.

The uniform stress and strain fields of the composite, $\hat{\Sigma}_{ij}$ and $\hat{E}_{ij}$, must be defined in terms of their local analogues, $\hat{\sigma}_{ij}(\mathbf{r})$ and $\hat{\varepsilon}_{ij}(\mathbf{r})$. The classic approach defines the macroscopic fields as the volumetric average of the local fields defined by (III.2.58) and (III.2.59) [26].

$$\hat{E}_{ij} = \frac{1}{V}\int_{V} \hat{\varepsilon}_{ij}(\mathbf{r})\,d\mathbf{r} \qquad \text{(III.2.58)}$$

$$\hat{\Sigma}_{ij} = \frac{1}{V}\int_V \hat{\sigma}_{ij}(\mathbf{r})\,d\mathbf{r} \tag{III.2.59}$$

Homogenization begins by relating the macroscopic stress and strain to each other through Hooke's law for viscoelastic solids using the elastic-viscoelastic correspondence principle.

$$\hat{\Sigma}_{ij} = \hat{C}^{eff}_{ijkl}\hat{E}_{kl} \tag{III.2.60}$$

In the above equation, $\hat{\mathbf{C}}^{eff}$ denotes the effective viscoelastic stiffness tensor of the composite. The concept of a strain localization tensor, $\hat{\mathbf{A}}(\mathbf{r})$, is now introduced. This tensor relates the macroscopic strain field to the local strain field as shown below in Equation (III.2.61) [35, 41].

$$\hat{\varepsilon}_{ij}(\mathbf{r}) = \hat{A}_{ijkl}(\mathbf{r})\hat{E}_{kl} \tag{III.2.61}$$

The average macroscopic strain and stress are then found through application of Equations (III.2.57) – (III.2.59) [26].

$$\hat{E}_{ij} = f^M\hat{\varepsilon}^M_{ij} + f^I\hat{\varepsilon}^I_{ij} + f^C\hat{\varepsilon}^C_{ij} \tag{III.2.62}$$

$$\hat{\Sigma}_{ij} = f^M\hat{\sigma}^M_{ij} + f^I\hat{\sigma}^I_{ij} + f^C\hat{\sigma}^C_{ij} \tag{III.2.63}$$

The two following relations result from application of Equation (III.2.61). These expressions relate the macroscopic strain field and the average strain in the inclusion and coating materials.

$$\hat{\varepsilon}_{ij}^{I} = \hat{A}_{ijkl}^{I}\hat{E}_{ij} \tag{III.2.64}$$

$$\hat{\varepsilon}_{ij}^{C} = \hat{A}_{ijkl}^{C}\hat{E}_{ij} \tag{III.2.65}$$

It is also important to recalling the constitutive laws for each material phase:

$$\hat{\sigma}_{ij}^{I} = \hat{C}_{ijkl}^{I}\hat{\varepsilon}_{kl}^{I} \tag{III.2.66}$$

$$\hat{\sigma}_{ij}^{C} = \hat{C}_{ijkl}^{C}\hat{\varepsilon}_{kl}^{C} \tag{III.2.67}$$

$$\hat{\sigma}_{ij}^{M} = \hat{C}_{ijkl}^{M}\hat{\varepsilon}_{kl}^{M} \tag{III.2.68}$$

The simple relationship between the average local stress field in material X and the macroscopic strain field, (III.2.69), results from the substitution of relations in the form of Equations (III.2.64) and (III.2.65) into the constitutive law equations [26].

$$\hat{\sigma}_{ij}^{X} = \hat{C}_{ijkl}^{X}\hat{A}_{klmn}^{X}\hat{E}_{mn} \tag{III.2.69}$$

The average strain field in the matrix is found by inserting Equations (III.2.64) and (III.2.65) into relation (III.2.62). The stress field in the matrix is then given through application of Equation (III.2.68) [24]. The results of these operations are given below in expressions (III.2.70) and (III.2.71), respectively.

$$\hat{\varepsilon}_{ij}^{M} = \frac{1}{f^{M}}\left(I_{ijkl} - f^{I}\hat{A}_{ijkl}^{I} - f^{C}\hat{A}_{ijkl}^{C}\right)\hat{E}_{kl} \tag{III.2.70}$$

$$\hat{\sigma}_{ij}^{M} = \frac{1}{f^{M}} \hat{C}_{ijkl}^{M} \left(I_{klmn} - f^{I} \hat{A}_{klmn}^{I} - f^{C} \hat{A}_{klmn}^{C} \right) \hat{E}_{mn} \qquad \text{(III.2.71)}$$

The average stress in the matrix material can also be found by combining Equation (III.2.63) and stress localization equations in the form of (III.2.69) as shown in (III.2.72).

$$\hat{\sigma}_{ij}^{M} = \frac{1}{f^{M}} \left(\hat{C}_{ijmn}^{eff} - f^{I} \hat{C}_{ijkl}^{I} \hat{A}_{klmn}^{I} - f^{C} \hat{C}_{ijkl}^{C} \hat{A}_{klmn}^{C} \right) \hat{E}_{mn} \qquad \text{(III.2.72)}$$

The effective viscoelastic stiffness tensor of the particulate composite is finally found by equating relations (III.2.71) and (III.2.72) and solving for $\hat{\mathbf{C}}^{eff}$ [24].

$$\boxed{\hat{\mathbf{C}}^{eff} = \hat{\mathbf{C}}^{M} + f^{I} \left(\hat{\mathbf{C}}^{I} - \hat{\mathbf{C}}^{M} \right) : \hat{\mathbf{A}}^{I} + f^{C} \left(\hat{\mathbf{C}}^{C} - \hat{\mathbf{C}}^{M} \right) : \hat{\mathbf{A}}^{C}} \qquad \text{(III.2.73)}$$

The strain localization tensors, $\hat{\mathbf{A}}^{I}$ and $\hat{\mathbf{A}}^{C}$, must be found to complete this model. These tensors are dependent on the volumetric composition of the composite, the geometry of the coated inclusions, the constituent material properties, and the *effective* material properties [23]. Expressions for these terms must be found via the integral equations derived in the previously. This is done by re-arranging (III.2.55) and (III.2.56) as shown below in Equation (III.2.74).

$$\hat{E}_{ij} = \left(\hat{A}_{ijkl}^{X} \right)^{-1} \hat{\varepsilon}_{kl}^{X} \qquad \text{(III.2.74)}$$

Here X represents the inclusion, I, or the coating, C. After re-arranging these expressions into the above form, the model is rendered self-consistent by setting the effective material properties equal to the reference material ($\hat{\mathbf{C}}^{0} = \hat{\mathbf{C}}^{eff}$) in keeping

with the RVE given in Figure 3-3. The resulting strain localization equations are given in Equations (III.2.75) and (III.2.76).

$$\boxed{\begin{aligned}\left(\hat{\mathbf{A}}^{I}\right)^{-1} &= \mathbf{I}_4 + \hat{\mathbf{T}}^{I}\left(\hat{\mathbf{C}}^{eff}\right):\Delta\hat{\mathbf{C}}^{C} + \frac{f_C}{f_I}\hat{\mathbf{T}}^{I}\left(\hat{\mathbf{C}}^{eff}\right):\Delta\hat{\mathbf{C}}^{C}:\hat{\mathbf{T}}^{I}\left(\hat{\mathbf{C}}^{C}\right):\Delta\hat{\mathbf{C}}^{IC} \\ &+ \frac{f_C}{f_I}\left[\hat{\mathbf{T}}^{I}\left(\hat{\mathbf{C}}^{C}\right) - \hat{\mathbf{T}}^{I}\left(\hat{\mathbf{C}}^{eff}\right)\right]:\Delta\hat{\mathbf{C}}^{IC}\end{aligned}} \quad \text{(III.2.75)}$$

$$\boxed{\hat{\mathbf{A}}^{C} = \left(\mathbf{I}_4 + \hat{\mathbf{T}}^{I}\left(\hat{\mathbf{C}}^{C}\right):\Delta\hat{\mathbf{C}}^{IC}\right):\hat{\mathbf{A}}^{I}} \quad \text{(III.2.76)}$$

One further term of interest is the strain localization tensor for the matrix material. This can be useful in several applications such strain energy studies.

$$\hat{\mathbf{A}}^{M} = \frac{1}{1-\varphi}\left[\mathbf{I}_4 - f^{I}\hat{\mathbf{A}}^{I} - f^{C}\hat{\mathbf{A}}^{C}\right] \quad \text{(III.2.77)}$$

The contrast tensors are again defined as $\Delta\hat{\mathbf{C}}^{X} = \hat{\mathbf{C}}^{X} - \hat{\mathbf{C}}^{eff}$ where X represents the inclusion or coating, $\mathbf{I}_4$ is the fourth order identity tensor, and φ is the volume fraction of the composite inclusion: $\varphi = f^{I} + f^{C}$. Equations (III.2.73), (III.2.75), and (III.2.76) constitute Cherkaoui's general SC micromechanical model extended to the quasi-static frequency domain through application of the elastic-viscoelastic correspondence principle.

3.3 Generalization using Dilute Strain Concentration Tensors

True particulate composite material composition can vary widely based on number of constituent materials, coated inclusion geometry combinations, and inherent fabrication and property variations. Unfortunately, the model derived in

Section 3.2 is limited in the types of composites that can be treated. The form of Equations (III.2.73), (III.2.75), and (III.2.76) only allow approximation of the effective material behavior for the simple case of a composite material consisting of three material phases: matrix, inclusion, and coating, where the coated inclusions have identical shapes and orientation in space [52]. This limitation is a direct result of the derivation of the strain localization tensors and, more specifically, the integral equation approximation. The SC model can be generalized to include the effects of multiple types of coated inclusion materials, variations of coating thickness, multiple coated inclusion geometries, and variations in coated inclusion orientation. This level of generality is achievable through the application of dilute strain concentration tensors (DSCT) [52]. Recently, models employing DSCT formulation to approximate the effective behavior of polymers containing nano-tubes have illustrated the generality of this approach [55-57]. These applications have shown that micromechanical models formulated with DSCT formulation accurately approximate nanotube shape and orientation distribution effects on the global behavior of the composite. The DSCT approach applied in this work expands the RVE to include all of the different coated inclusion variations. This change of RVE will lead to a SC model that is analogous to the one derived in Section 3.2. Because the SC DSCT approach assumes that the reference material surrounds each coated inclusion, it is easy to visualize the expanded RVE employed in this section as a summation of N different sub-RVE's as shown below in Figure 3-4.

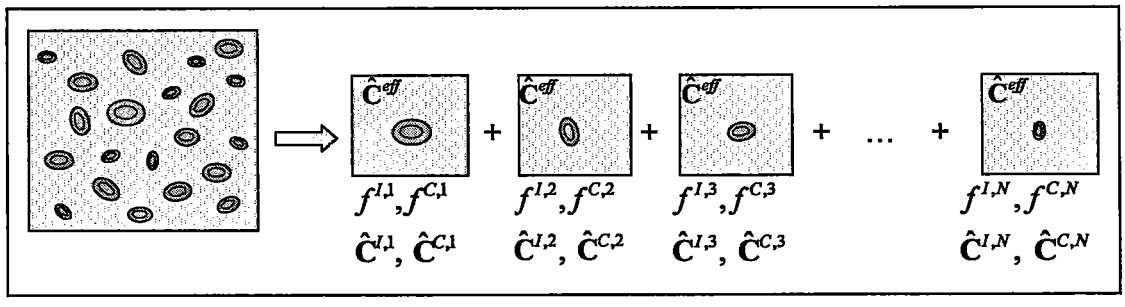

Figure 3-4: Schematic representation of DSCT formulation of the SC model as the sum of N different RVE's corresponding to each coated inclusion family.

The RVE representation in Figure 3-4 schematically shows the SC DSCT approach. In what follows, all coated inclusions that have identical material type, spatial orientation, and shape are referred to as a coated inclusion family. The entire composite consists of N different coated inclusion families chosen to represent the nature of the material. Each family is assumed to be surrounded by the effective material and to occupy a volume fraction, $\varphi^{\varsigma} = f^{I,\varsigma} + f^{C,\varsigma}$. DSCT formulation assumes that the effects of each coated inclusion family can be superimposed in order to arrive at a reasonable approximation of the effective behavior of the particulate composite. The DSCT approach also assumes that the descriptive dimension of all coated inclusion families is of the same order of magnitude and, like all micromechanical approaches, that this dimension is much smaller than the macroscopic length scale [27]. DSCT formulation, as all other micromechanical approaches, is limited to total low volume fraction inclusions unless inclusion interaction is taken into account in some way [57]. In the following sections, the derivation presented in Sections 3.2.1 – 3.2.4 is adapted for a composite containing coated inclusion families thereby deriving a SC DSCT model analogous to Equations (III.2.73), (III.2.75), and (III.2.76). The generality of this SC DSCT model allows accurate viscoelastic composite material homogenization for materials containing coated inclusions with a wide range of material properties, spatial orientations, and shapes. For the sake of brevity, the following "derivation" is not a detailed repetition of all equations in Sections 3.2.1 – 3.2.4, but rather a summary of the prior derivation adapted to the multiple coated inclusion case.

3.3.1 Localization and the integral equation

Derivation of the SC DSCT model requires several changes to the previous derivation to ensure the accurate localization. First, differences in the topology of the RVE must be addressed. The single coated inclusion RVE shown in Figure 3-1

represents only a single *family* of coated inclusions when applying DSCT. In the DSCT approach, an RVE such as the one shown in Figure 3-5 will consist of N different sub-RVE's each of which are analogous to the RVE shown in Figure 3-1.

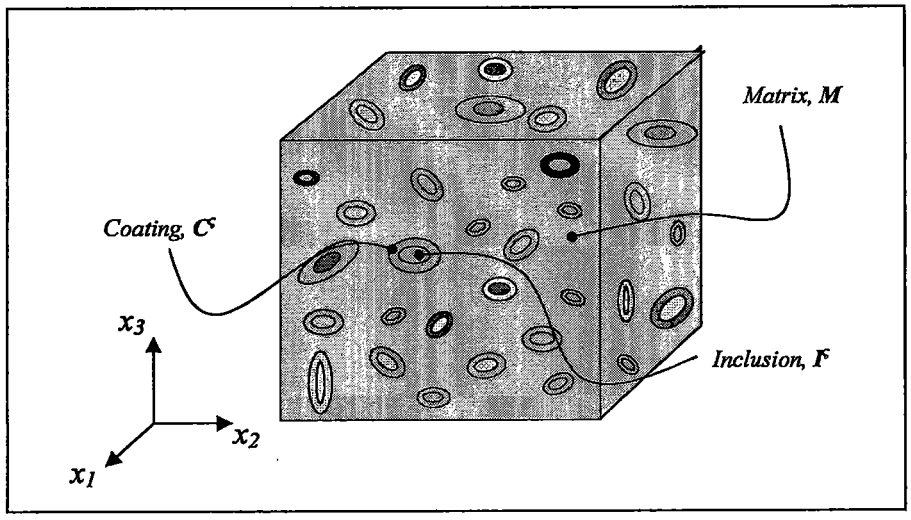

Figure 3-5: Topology of a particulate viscoelastic composite with N coated inclusion families.

The topology of the above RVE corresponds to N coated inclusion families where each family, ς, is represented with a single inclusion of volume, $V_{I,\varsigma}$, and viscoelastic stiffness, $\hat{\mathbf{C}}^{I,\varsigma}$, and is coated with another material having a volume, $V_{C,\varsigma}$, and viscoelastic stiffness, $\hat{\mathbf{C}}^{C,\varsigma}$. Each family is also assumed to have a unique ellipsoidal shape characterized by major axes, a_i^ς, aligned with the *local* coordinate system, $\tilde{\mathbf{x}}^\varsigma$. Euler angles ϑ^ς, ϕ^ς, and ψ^ς relate the *local* coordinate system to the *global* coordinates using the "x" convention (see Appendix B) [149]. As in the previous section, all coated inclusions are embedded in the reference material with viscoelastic stiffness, $\hat{\mathbf{C}}^0$.

It is now possible to start the derivation of the SC DSCT model beginning with the expression for the local behavior of the composite material. The viscoelastic stiffness tensor of the heterogeneous material can again be expressed as a

homogeneous material having spatially varying viscoelastic properties. For the RVE shown in Figure 3-5 this variation is expressed identically to Equation (III.2.3).

$$\hat{\mathbf{C}}(\mathbf{r}) = \hat{\mathbf{C}}^0 + \delta\hat{\mathbf{C}}(\mathbf{r}) \quad \text{with} \quad \mathbf{r} \in V \tag{III.3.1}$$

$\hat{\mathbf{C}}^0$ represents the spatially uniform viscoelastic stiffness tensor of the reference material and V is the RVE volume. Unlike the previous derivation, however, the spatial variation tensor, $\delta\hat{\mathbf{C}}(\mathbf{r})$, must be modified to approximate the influence of N different coated inclusion families. Equation (III.2.14) is therefore generalized to the form shown below.

$$\begin{aligned}
\delta\hat{\mathbf{C}}(\mathbf{r}) &= \left(\hat{\mathbf{C}}^{I,1} - \hat{\mathbf{C}}^0\right)\theta^{I,1}(\mathbf{r}) + \left(\hat{\mathbf{C}}^{C,1} - \hat{\mathbf{C}}^0\right)\left[\theta^{2,1}(\mathbf{r}) - \theta^{I,1}(\mathbf{r})\right] \\
&\quad + \left(\hat{\mathbf{C}}^{I,2} - \hat{\mathbf{C}}^0\right)\theta^{I,2}(\mathbf{r}) + \left(\hat{\mathbf{C}}^{C,2} - \hat{\mathbf{C}}^0\right)\left[\theta^{2,2}(\mathbf{r}) - \theta^{I,2}(\mathbf{r})\right] \\
&\quad \vdots \\
&\quad + \left(\hat{\mathbf{C}}^{I,N} - \hat{\mathbf{C}}^0\right)\theta^{I,N}(\mathbf{r}) + \left(\hat{\mathbf{C}}^{C,N} - \hat{\mathbf{C}}^0\right)\left[\theta^{2,N}(\mathbf{r}) - \theta^{I,N}(\mathbf{r})\right] \\
&= \sum_{\varsigma=1}^{N}\left(\Delta\hat{\mathbf{C}}^{I0,\varsigma}\theta^{I,\varsigma}(\mathbf{r}) + \Delta\hat{\mathbf{C}}^{C0,\varsigma}\delta\theta^{I,\varsigma}(\mathbf{r})\right)
\end{aligned} \tag{III.3.2}$$

In Equation (III.3.2) the shorthand viscoelastic contrast tensors, $\Delta\hat{\mathbf{C}}^{X0,\varsigma} = \hat{\mathbf{C}}^{X,\varsigma} - \hat{\mathbf{C}}^0$, denote the contrast between the ςth coating or inclusion and the reference material. The Heaviside step functions $\theta^{I,\varsigma}(\mathbf{r})$, $\theta^{2,\varsigma}(\mathbf{r})$, and $\delta\theta^{I,\varsigma}(\mathbf{r})$ defined below are generalizations of Equations (III.2.15) and (III.2.17):

$$\theta^{1,\varsigma}(\mathbf{r}) = \begin{cases} 1 & \text{if } \mathbf{r} \in V_{1,\varsigma} \\ 0 & \text{if } \mathbf{r} \notin V_{1,\varsigma} \end{cases}$$

$$\theta^{2,\varsigma}(\mathbf{r}) = \begin{cases} 1 & \text{if } \mathbf{r} \in V_{2,\varsigma} \\ 0 & \text{if } \mathbf{r} \notin V_{2,\varsigma} \end{cases}$$

$$\delta\theta^{1,\varsigma}(\mathbf{r}) = \theta^{2,\varsigma}(\mathbf{r}) - \theta^{1,\varsigma}(\mathbf{r}) \tag{III.3.3}$$

It is important to note that the form of Equations (III.3.2) and (III.3.3) assumes that all viscoelastic stiffness tensors and Heaviside step functions are expressed with respect to the global coordinate system. This fact requires the rotation of each quantity from their local coordinate system to the global coordinate system.

The derivation of the SC DSCT model can now be taken up from the modified equilibrium equation given in Equations (III.2.5) and (III.2.6). These equations will be used to derive the N different modified Green's tensors which take the shape, orientation, and stiffness contrast of each family into account. Equation (III.3.4) below gives the equilibrium equation for the N coated inclusion families.

$$\begin{aligned} \hat{C}^{0}_{ijkl}\hat{u}_{k,lj}(\mathbf{r}) &= \left[-\delta\hat{C}_{ijkl}(\mathbf{r})\hat{\varepsilon}_{kl}(\mathbf{r})\right]_{,j} = \hat{f}_i(\mathbf{r}) \\ &= \sum_{\varsigma=1}^{N} -\left[\left\{\Delta C^{I0,\varsigma}_{ijkl}\theta^{I,\varsigma}(\mathbf{r}) + \Delta C^{C0,\varsigma}_{ijkl}\left(\theta^{2,\varsigma}(\mathbf{r}) - \theta^{I,\varsigma}(\mathbf{r})\right)\right\}\hat{\varepsilon}_{kl}(\mathbf{r})\right]_{,j} \\ &= \sum_{\varsigma=1}^{N} \hat{f}_i^{\varsigma}(\mathbf{r}) \end{aligned} \tag{III.3.4}$$

For the N coated inclusion family case, it is obvious that the distribution of fictitious forces is the result of the summation of N distributions, each described by Equation (III.2.6). The Green's tensor solution to this differential equation, therefore, must be represented as the sum of N Green's tensors, $\hat{G}^{0,\varsigma}_{km}\left(\mathbf{r}-\mathbf{r}'^{,\varsigma}\right)$, which is permitted due to the superposition properties of the Green's functions. Each individual Green's tensor is a function that calculates the displacement in the k direction at the point $\mathbf{r}$ when a time varying unit force due to the inhomogeneity of the ςth family of coated

inclusions, $\hat{f}_i^{\varsigma}(\mathbf{r})$, is applied at the point $\mathbf{r}'^{,\varsigma}$ in the m direction. Equation (III.2.7) must therefore be changed to the following form.

$$\hat{C}_{ijkl}^{0}\hat{G}_{km,lj}^{0,\varsigma}\left(\mathbf{r}-\mathbf{r}'^{,\varsigma}\right)+\delta_{im}\delta\left(\mathbf{r}-\mathbf{r}'^{,\varsigma}\right)\delta\left(\omega-\omega'\right)=0 \qquad \text{(III.3.5)}$$

Given this expression, which is analogous to (III.2.7), the resultant integral equation for the displacement field becomes a summation of N integrals with Green's tensor kernals representing each coated inclusion family as shown below in Equation (III.3.6):

$$\hat{u}_m(\mathbf{r})=\hat{u}_m^0(\mathbf{r})-\sum_{\varsigma=1}^{N}\int_{-\infty}^{\infty}\int_V \hat{G}_{im,j'}^{0,\varsigma}\left(\mathbf{r}-\mathbf{r}'^{,\varsigma}\right)\left[\delta\hat{C}_{ijkl}\left(\mathbf{r}'^{,\varsigma}\right)\hat{\varepsilon}_{kl}^{\varsigma}\left(\mathbf{r}'^{,\varsigma}\right)\right]d\mathbf{r}'^{,\varsigma}\,d\omega' \quad \text{(III.3.6)}$$

Where $\hat{\varepsilon}_{kl}^{\varsigma}(\mathbf{r})$ represents the compatible strain at the point $\mathbf{r}$ due to the ςth family of coated inclusions. The integral equation (III.3.7)describing the strain field at every point in the homogenous material is found by applying the properties of the Dirac delta function for the frequency integral and the small strain approximation.

$$\hat{\varepsilon}_{ij}(\mathbf{r})=\hat{E}_{ij}-\sum_{\varsigma=1}^{N}\int_V \hat{\Gamma}_{ijkl}^{0,\varsigma}\left(\mathbf{r}-\mathbf{r}'^{,\varsigma}\right)\delta\hat{C}_{klmn}\left(\mathbf{r}'^{,\varsigma}\right)\hat{\varepsilon}_{mn}^{\varsigma}\left(\mathbf{r}'^{,\varsigma}\right)d\mathbf{r}'^{,\varsigma} \qquad \text{(III.3.7)}$$

The modified Green's tensor for each coated inclusion family, $\hat{\Gamma}_{ijkl}^{0,\varsigma}$, given in (III.3.7) is expressed below in relation (III.3.8).

$$\hat{\Gamma}_{ijkl}^{0,\varsigma}=-\frac{1}{2}\left[\hat{G}_{ki,jl}^{0,\varsigma}\left(\mathbf{r}-\mathbf{r}'^{,\varsigma}\right)+\hat{G}_{kj,il}^{0,\varsigma}\left(\mathbf{r}-\mathbf{r}'^{,\varsigma}\right)\right] \qquad \text{(III.3.8)}$$

It is again important to note that in the present form, all of the terms in the above equations are defined with respect to the global coordinate system, **x**. The interfacial operators described in Sections 3.2.2 and 3.2.3 can now be employed to simplify the Equation (III.3.7),. These operations are greatly simplified when working in the local coordinate system, $\tilde{\mathbf{x}}^{\varsigma}$, and then rotating the result to the global reference system. Indeed, the entire interfacial operator derivation given in Section 3.2.2 is identical for each coated inclusion family with respect to their local coordinate system. Equations leading to SC model generalization through DSCT formulation are found in the following section by simply restating the important results in local coordinates. In the following paragraphs all variables represented as $\tilde{X}^{\varsigma}$ represent the variable X^{ς} with respect to the local coordinates of the ςth coated inclusion family.

3.3.2 Interfacial operators and average strain fields of coated inclusion families

The interfacial operators derived in Section 3.2.2 are general expressions that only assume that the reference coordinates of phases A and B are identical. Because of this, no re-derivation is necessary for the multiple coated inclusions problem. However, for the sake of simplicity in the following analysis, Equations (III.2.31) and (III.2.32) are re-stated here clearly delineating the variables as being referenced to the local coordinates.

$$\hat{\tilde{P}}^{A}_{ijkl} \equiv \frac{1}{4}\left[\left(\hat{\tilde{K}}^{A}_{ik}\right)^{-1}\tilde{n}_j\tilde{n}_l + \left(\hat{\tilde{K}}^{A}_{jk}\right)^{-1}\tilde{n}_i\tilde{n}_l + \left(\hat{\tilde{K}}^{A}_{il}\right)^{-1}\tilde{n}_j\tilde{n}_k + \left(\hat{\tilde{K}}^{A}_{jl}\right)^{-1}\tilde{n}_i\tilde{n}_k\right] \quad \text{(III.3.9)}$$

and

$$\hat{\tilde{\varepsilon}}_{ij}^{A} = \left[\hat{\tilde{P}}_{ijkl}^{A} \left(\hat{\tilde{C}}_{klmn}^{B} - \hat{\tilde{C}}_{klmn}^{A} \right) + I_{ijmn} \right] \hat{\tilde{\varepsilon}}_{mn}^{B}$$

$$\hat{\tilde{\varepsilon}}_{ij}^{B} = \left[\hat{\tilde{P}}_{ijkl}^{B} \left(\hat{\tilde{C}}_{klmn}^{A} - \hat{\tilde{C}}_{klmn}^{B} \right) + I_{ijmn} \right] \hat{\tilde{\varepsilon}}_{mn}^{A} \qquad \text{(III.3.10)}$$

Here $\hat{\tilde{K}}_{ik}^{\chi}$ represents Christoffel's matrix for material χ with respect to the local coordinates and is defined by $\hat{\tilde{K}}_{ik}^{\chi} = \hat{\tilde{C}}_{ijkl}^{\chi} \tilde{n}_l \tilde{n}_j$.

In order to apply the interfacial operators in the local coordinate system it is first necessary to return to Equation (III.3.4). More specifically, the Heaviside step function variation, $\delta\theta^{I,\varsigma}(\mathbf{r})$, and viscoelastic contrast tensors must be specified for application with respect to the local coordinates. The Heaviside step function variation is expressed in local coordinates with Equation (III.3.11), the analogue to expression (III.2.18).

$$\delta\tilde{\theta}^{I,\varsigma}(\tilde{\mathbf{r}}) \approx \tilde{p}^{\varsigma} \sum_{\alpha} \frac{\Delta\tilde{a}_{\alpha}^{\varsigma}}{\tilde{a}_{\alpha}^{\varsigma}} \frac{\left(\tilde{x}_{\alpha}^{\varsigma}\right)^2}{\left(\tilde{a}_{\alpha}^{\varsigma}\right)^2} \delta\left(\tilde{S}_{I,\varsigma}\right) \qquad \text{(III.3.11)}$$

Here $\tilde{p}^{\varsigma}$ is the perpendicular distance from the center of the ςth coated inclusion to its tangent plane at the point $\tilde{\mathbf{x}}^{\varsigma}$, $\tilde{a}_{\alpha}^{\varsigma}$ represents the αth major axes, and $\tilde{S}_{I,\varsigma}$ the surface of the inclusion of the ςth coated inclusion family. The perpendicular distance, $\tilde{p}^{\varsigma}$, is found by applying Equation (III.2.19) in the local system. Equations (III.3.2) and (III.3.11) are then combined to yield an expression for the ςth variation in viscoelastic constants (III.3.12).

$$\delta\hat{\tilde{\mathbf{C}}}^{\varsigma}(\mathbf{r}) = \left(\hat{\tilde{\mathbf{C}}}^{I,\varsigma} - \hat{\tilde{\mathbf{C}}}^{0}\right)\tilde{\theta}^{I}(\mathbf{r}) + \left(\hat{\tilde{\mathbf{C}}}^{C,\varsigma} - \hat{\tilde{\mathbf{C}}}^{0}\right)\tilde{p}^{\varsigma} \sum_{\alpha} \frac{\Delta\tilde{a}_{\alpha}^{\varsigma}}{\tilde{a}_{\alpha}^{\varsigma}} \frac{\left(\tilde{x}_{\alpha}^{\varsigma}\right)^2}{\left(\tilde{a}_{\alpha}^{\varsigma}\right)^2} \delta\left(\tilde{S}_{I,\varsigma}\right) \qquad \text{(III.3.12)}$$

It is important to stress that the calculation of this variation requires the rotation of the *reference* material to the local coordinates. Equation (III.3.13) below results from the insertion of (III.3.12) into the integral equation (III.3.7) and application of the appropriate rotation matrices.

$$\hat{\varepsilon}_{ij}(\mathbf{r}) = \hat{E}_{ij} - \sum_{\varsigma=1}^{N} R_{ir}^{\varsigma} R_{js}^{\varsigma} \int_{\tilde{V}_{I,\varsigma}} \hat{\tilde{\Gamma}}_{rskl}^{0,\varsigma}\left(\tilde{\mathbf{r}} - \tilde{\mathbf{r}}'^{,\varsigma}\right) \Delta\hat{\tilde{C}}_{klmn}^{I0,\varsigma} \hat{\tilde{\varepsilon}}_{mn}\left(\tilde{\mathbf{r}}'^{,\varsigma}\right) d\tilde{\mathbf{r}}'^{,\varsigma}$$
$$- \sum_{\varsigma=1}^{N} R_{ir}^{\varsigma} R_{js}^{\varsigma} \left[\sum_{\alpha} \int_{\tilde{S}_{I,\varsigma}^{+}} \hat{\tilde{\Gamma}}_{rskl}^{0,\varsigma}\left(\tilde{\mathbf{r}} - \tilde{\mathbf{r}}^{+,\varsigma}\right) \Delta\hat{\tilde{C}}_{klmn}^{C0,\varsigma} \hat{\tilde{\varepsilon}}_{mn}\left(\tilde{\mathbf{r}}^{+,\varsigma}\right) \tilde{p}^{\varsigma} \frac{\Delta\tilde{a}_{\alpha}^{\varsigma}}{\tilde{a}_{\alpha}^{\varsigma}} \frac{\left(\tilde{x}_{\alpha}^{\varsigma}\right)^2}{\left(\tilde{a}_{\alpha}^{\varsigma}\right)^2} dS \right] \qquad \text{(III.3.13)}$$

Where R_{ij}^{ς} is the rotation matrix determined from the Euler angles of the ςth coated inclusion family using relations given in Appendix B. The modified Green's tensor in the local coordinate system is determined through the evaluation of Equation (III.3.5) when the reference material and all spatial variables have been rotated to the local reference frame.

It is now possible to calculate the average strain in the inclusion and coating of each coated inclusion family. The strain jump between inclusion and coating materials must first be found through application of the interfacial operators given above. Using this information, the equation describing the strain at a position just outside the ςth coated inclusion can be calculated via the local equivalent of Equation (III.2.35) given below.

$$\hat{\tilde{\varepsilon}}_{ij}\left(\tilde{\mathbf{r}}^{+}\right) = \hat{\tilde{\varepsilon}}_{ij}^{I} + \hat{\tilde{P}}_{ijkl}^{C} \Delta\hat{\tilde{C}}_{lkmn}^{IC} \hat{\tilde{\varepsilon}}_{ij}^{I} \qquad \text{(III.3.14)}$$

The average strain in each phase is then calculated using the classic equations shown in (III.3.15):

$$\hat{\tilde{\varepsilon}}_{ij}^{I,\varsigma} = \frac{1}{V_{I,\varsigma}} \int_{V_{I,\varsigma}} \hat{\tilde{\varepsilon}}_{ij}(\tilde{\mathbf{r}}) d\tilde{\mathbf{r}}$$

$$\hat{\tilde{\varepsilon}}_{ij}^{C,\varsigma} = \frac{1}{V_{C,\varsigma}} \int_{V_{C,\varsigma}} \hat{\tilde{\varepsilon}}_{ij}(\tilde{\mathbf{r}}) d\tilde{\mathbf{r}} \tag{III.3.15}$$

Using these expressions, the integral equation given in (III.3.13) simplifies to give the average strain in the inclusion and coating of each family with respect to the local coordinates via the two following equations.

$$\begin{aligned}\hat{\tilde{\varepsilon}}_{ij}^{I,\varsigma} = \hat{\tilde{E}}_{ij} &- \frac{1}{V_{I,\varsigma}} \int_{\tilde{V}_{I,\varsigma}} \int_{\tilde{V}_{I,\varsigma}} \hat{\tilde{\Gamma}}_{ijkl}^{0,\varsigma}\left(\tilde{\mathbf{r}} - \tilde{\mathbf{r}}'^{,\varsigma}\right) \Delta\hat{\tilde{C}}_{klmn}^{I0,\varsigma} \hat{\tilde{\varepsilon}}_{mn}^{I,\varsigma} d\tilde{\mathbf{r}}'^{,\varsigma} d\tilde{\mathbf{r}} \\ &- \frac{1}{V_{I,\varsigma}} \sum_{\alpha} \int_{\tilde{S}_{I,\varsigma}^{+}} \left\{ \int_{\tilde{V}_{I,\varsigma}} \hat{\tilde{\Gamma}}_{ijkl}^{0,\varsigma}\left(\tilde{\mathbf{r}} - \tilde{\mathbf{r}}^{+,\varsigma}\right) d\tilde{\mathbf{r}} \right\} \Delta\hat{\tilde{C}}_{klmn}^{C0,\varsigma} \hat{\tilde{\varepsilon}}_{mn}^{I,\varsigma} \tilde{p}^{\varsigma} \frac{\Delta\tilde{a}_{\alpha}^{\varsigma}}{\tilde{a}_{\alpha}^{\varsigma}} \frac{\left(\tilde{x}_{\alpha}^{\varsigma}\right)^2}{\left(\tilde{a}_{\alpha}^{\varsigma}\right)^2} d\tilde{S} \\ &- \frac{1}{V_{I,\varsigma}} \sum_{\alpha} \int_{\tilde{S}_{I,\varsigma}^{+}} \left\{ \int_{\tilde{V}_{I,\varsigma}} \hat{\tilde{\Gamma}}_{ijkl}^{0,\varsigma}\left(\tilde{\mathbf{r}} - \tilde{\mathbf{r}}^{+,\varsigma}\right) d\tilde{\mathbf{r}} \right\} \Delta\hat{\tilde{C}}_{klmn}^{C0,\varsigma} \hat{\tilde{P}}_{mnpq}^{C,\varsigma} \Delta\hat{\tilde{C}}_{pqrs}^{IC,\varsigma} \hat{\tilde{\varepsilon}}_{rs}^{I,\varsigma} \tilde{p}^{\varsigma} \frac{\Delta\tilde{a}_{\alpha}^{\varsigma}}{\tilde{a}_{\alpha}^{\varsigma}} \frac{\left(\tilde{x}_{\alpha}^{\varsigma}\right)^2}{\left(\tilde{a}_{\alpha}^{\varsigma}\right)^2} d\tilde{S}\end{aligned} \tag{III.3.16}$$

$$\hat{\tilde{\varepsilon}}_{ij}^{C,\varsigma} = \hat{\tilde{\varepsilon}}_{ij}^{I,\varsigma} + \frac{1}{V_{C,\varsigma}} \left\{ \int_{\tilde{V}_{C,\varsigma}} \hat{\tilde{P}}_{ijkl}^{C,\varsigma} d\tilde{\mathbf{r}} \right\} \Delta\hat{\tilde{C}}_{klmn}^{IC,\varsigma} \hat{\tilde{\varepsilon}}_{mn}^{I,\varsigma} \tag{III.3.17}$$

It is now necessary to define the volume integral of the modified Green's tensor. In accordance with Equation (III.2.47), this integral is defined for each family of coated inclusions using the following equation.

$$\hat{\tilde{T}}_{ijkl}^{\chi,\varsigma}\left(\hat{\tilde{\mathbf{C}}}^{*}\right) = \int_{\tilde{V}_{\chi,\varsigma}} \hat{\tilde{\Gamma}}_{ijkl}^{*,\varsigma}\left(\tilde{\mathbf{r}} - \tilde{\mathbf{r}}'^{,\varsigma}\right) d\tilde{\mathbf{r}}'^{,\varsigma} \quad \text{if } \tilde{\mathbf{r}} \in \tilde{V}_{\chi,\varsigma} \tag{III.3.18}$$

Where $V_{\chi\varsigma}$ represents the inclusion or composite inclusion volume and * represents either the inclusion, the coating, or the reference material. Because the coating is

assumed to be thin for each family, Equations (III.2.43) and (III.2.44) can be combined and re-stated for each family as follows:

$$V_{C,\varsigma} = \int_{V_{C,\varsigma}} \left[\theta^{2,\varsigma}(\mathbf{r}) - \theta^{I,\varsigma}(\mathbf{r})\right] d\mathbf{r}$$
$$\approx \int_{\tilde{V}} \sum_{\alpha} \tilde{p}^{\varsigma} \frac{\Delta\tilde{a}_{\alpha}^{\varsigma}}{\tilde{a}_{\alpha}^{\varsigma}} \frac{\left(\tilde{x}_{\alpha}^{\varsigma}\right)^2}{\left(\tilde{a}_{\alpha}^{\varsigma}\right)^2} \delta\left(\tilde{S}_I\right) d\tilde{\mathbf{r}} = \sum_{i} \int_{\tilde{S}_I} \tilde{p}^{\varsigma} \frac{\Delta\tilde{a}_{\alpha}^{\varsigma}}{\tilde{a}_{\alpha}^{\varsigma}} \frac{\left(\tilde{x}_{\alpha}^{\varsigma}\right)^2}{\left(\tilde{a}_{\alpha}^{\varsigma}\right)^2} d\tilde{S} \qquad \text{(III.3.19)}$$

The derivation of equations equivalent to (III.2.45)-(III.2.51) with respect to the local coordinates of the ςth coated inclusion family is identical to the analysis carried out in Section 3.2.3. Expressions (III.3.21) and (III.3.22) which relate the inclusion and coating volumes to the integral of the modified Green's tensor by employing the interfacial operator property described by (III.3.20) are given here for continuity and clarity.

$$\int_{\tilde{V}_C} \hat{\tilde{P}}_{ijkl}^{*} d\tilde{\mathbf{r}} = V_C \hat{\tilde{T}}_{ijkl}^{I}\left(\hat{\tilde{\mathbf{C}}}^{*}\right) - \int_{\tilde{V}_C}\int_{\tilde{V}_I} \hat{\tilde{\Gamma}}_{ijkl}^{*}\left(\tilde{\mathbf{r}}^{+} - \tilde{\mathbf{r}}\right) d\tilde{\mathbf{r}}^{+} d\tilde{\mathbf{r}} \qquad \text{(III.3.20)}$$

$$\int_{\tilde{V}_C}\int_{\tilde{V}_I} \hat{\tilde{\Gamma}}_{ijkl}^{*,\varsigma}\left(\tilde{\mathbf{r}}^{+} - \tilde{\mathbf{r}}\right) d\tilde{\mathbf{r}}^{+} d\tilde{\mathbf{r}} = V_{I,\varsigma}\left(\hat{\tilde{T}}_{ijkl}^{2,\varsigma}\left(\hat{\tilde{\mathbf{C}}}^{*,\varsigma}\right) - \hat{\tilde{T}}_{ijkl}^{I,\varsigma}\left(\hat{\tilde{\mathbf{C}}}^{*,\varsigma}\right)\right) \qquad \text{(III.3.21)}$$

$$\int_{\tilde{V}_{C,\varsigma}} \hat{\tilde{P}}_{ijkl}^{*,\varsigma} d\tilde{\mathbf{r}} = \int_{\tilde{V}} \hat{\tilde{P}}_{ijkl}^{*,\varsigma} \delta\theta^{I,\varsigma}(\tilde{\mathbf{r}}) d\tilde{\mathbf{r}} = \sum_{\alpha} \int_{\tilde{S}_{I,\varsigma}} \hat{\tilde{P}}_{ijkl}^{*,\varsigma} \tilde{p}^{\varsigma} \frac{\Delta\tilde{a}_{\alpha}^{\varsigma}}{\tilde{a}_{\alpha}^{\varsigma}} \frac{\left(\tilde{x}_{\alpha}^{\varsigma}\right)^2}{\left(\tilde{a}_{\alpha}^{\varsigma}\right)^2} d\tilde{S}$$
$$= V_{C,\varsigma} \hat{\tilde{T}}_{ijkl}^{I,\varsigma}\left(\hat{\tilde{\mathbf{C}}}^{*,\varsigma}\right) - V_{I,\varsigma}\left[\hat{\tilde{T}}_{ijkl}^{2,\varsigma}\left(\hat{\tilde{\mathbf{C}}}^{*,\varsigma}\right) - \hat{\tilde{T}}_{ijkl}^{I,\varsigma}\left(\hat{\tilde{\mathbf{C}}}^{*,\varsigma}\right)\right] \qquad \text{(III.3.22)}$$

Now assume $\Delta a_i / a_i = \Delta a_j / a_j$ and insert the above expressions into Equations (III.3.16) and (III.3.17). This yields Equations (III.3.23) and (III.3.24) for the average inclusion and coating strain for the ςth coated inclusion family.

$$\hat{\tilde{\varepsilon}}_{ij}^{I,\varsigma} = \tilde{E}_{ij} - \hat{\tilde{T}}_{ijkl}^{I,\varsigma}\left(\hat{\tilde{\mathbf{C}}}^{0}\right)\Delta\hat{\tilde{C}}_{klmn}^{I0,\varsigma}\hat{\tilde{\varepsilon}}_{mn}^{I,\varsigma}$$
$$-\frac{V_{C,\varsigma}}{V_{I,\varsigma}}\hat{\tilde{T}}_{ijkl}^{I,\varsigma}\left(\hat{\tilde{\mathbf{C}}}^{0}\right)\Delta\hat{\tilde{C}}_{klmn}^{C0,\varsigma}\hat{\tilde{T}}_{mnpq}^{I,\varsigma}\left(\hat{\tilde{\mathbf{C}}}^{C,\varsigma}\right)\Delta\hat{\tilde{C}}_{pqrs}^{IC,\varsigma}\hat{\tilde{\varepsilon}}_{rs}^{I,\varsigma} \qquad \text{(III.3.23)}$$
$$-\frac{V_{C,\varsigma}}{V_{I,\varsigma}}\left[\hat{\tilde{T}}_{ijkl}^{I,\varsigma}\left(\hat{\tilde{\mathbf{C}}}^{C,\varsigma}\right) - \hat{\tilde{T}}_{ijkl}^{I,\varsigma}\left(\hat{\tilde{\mathbf{C}}}^{0}\right)\right]\Delta\hat{\tilde{C}}_{klmn}^{IC,\varsigma}\hat{\tilde{\varepsilon}}_{mn}^{I,\varsigma}$$

$$\hat{\tilde{\varepsilon}}_{ij}^{C,\varsigma} = \hat{\tilde{\varepsilon}}_{ij}^{I,\varsigma} + \hat{\tilde{T}}_{ijkl}^{I,\varsigma}\left(\hat{\tilde{\mathbf{C}}}^{C,\varsigma}\right)\Delta\hat{\tilde{C}}_{klmn}^{IC,\varsigma}\hat{\tilde{\varepsilon}}_{mn}^{I,\varsigma} \qquad \text{(III.3.24)}$$

It is now possible to employ these expressions in the homogenization step and derive the SC model generalized using DSCT.

3.3.3 Homogenization and effective material properties

The next step in the derivation of the SC DSCT model must begin with a discussion of the RVE. The simplest visualization of the RVE for SC model DSCT formulation has been given in Figure 3-4. This representation breaks the true RVE into N different RVE's, each representing a coated inclusion family. Each of these individual RVE's are identical to the one presented in Figure 3-3. The ςth RVE consists of a single inclusion having viscoelastic properties $\hat{\mathbf{C}}^{I,\varsigma}$ which occupies a fraction of the total volume, $f^{I,\varsigma}$, and is coated by a different material with viscoelastic constants $\hat{\mathbf{C}}^{C,\varsigma}$ which occupies a fraction of the total volume, $f^{C,\varsigma}$. The coated inclusion is embedded in the effective homogeneous medium with viscoelastic rigidity tensor $\hat{\mathbf{C}}^{eff}$. The entire RVE is assumed to be subjected to a time varying macroscopic strain represented by $\hat{E}_{ij}$. Further, as in Section 3.2.4, the following identity is noted for the sum of the volume fractions of all phases.

$$f^M + \sum_{\varsigma=1}^{N}\left(f^{I,\varsigma} + f^{C,\varsigma}\right) = 1 \qquad \text{(III.3.25)}$$

The macroscopic strain and stress definitions given in Equations (III.2.62) and (III.2.63) are modified for the N coated inclusion family case as shown below.

$$\hat{E}_{ij} = \frac{1}{V}\int_V \hat{\varepsilon}_{ij}(\mathbf{r})d\mathbf{r} = f^M \hat{\varepsilon}_{ij}^M + \sum_{\varsigma=1}^{N}\left(f^{I,\varsigma}\hat{\varepsilon}_{ij}^{I,\varsigma} + f^{C,\varsigma}\hat{\varepsilon}_{ij}^{C,\varsigma}\right) \qquad \text{(III.3.26)}$$

$$\hat{\Sigma}_{ij} = \frac{1}{V}\int_V \hat{\sigma}_{ij}(\mathbf{r})d\mathbf{r} = f^M \hat{\sigma}_{ij}^M + \sum_{\varsigma=1}^{N}\left(f^{I,\varsigma}\hat{\sigma}_{ij}^{I,\varsigma} + f^{C,\varsigma}\hat{\sigma}_{ij}^{C,\varsigma}\right) \qquad \text{(III.3.27)}$$

Where the strain and stress values on the RHS of the above equations denote the average value in their respective phase.

The N strain localization tensors for each phase are always defined via the general expression (III.2.61). Equations relating the average strain in the inclusion and coating phase of each family are therefore given as:

$$\hat{\varepsilon}_{ij}^{I,\varsigma} = \hat{A}_{ijkl}^{I,\varsigma}\hat{E}_{ij} \qquad \text{(III.3.28)}$$

$$\hat{\varepsilon}_{ij}^{C,\varsigma} = \hat{A}_{ijkl}^{C,\varsigma}\hat{E}_{ij} \qquad \text{(III.3.29)}$$

It is now possible to express the average strain and stress fields in the matrix material. To do so, Equation (III.3.26) and the strain localization relations above are employed to give the following expression for the average strain in the matrix.

$$\hat{\varepsilon}_{ij}^M = \frac{1}{f^M}\left[I_{ijkl} - \sum_{\varsigma=1}^{N}\left(f^{I,\varsigma}\hat{A}_{ijkl}^{I,\varsigma} + f^{C,\varsigma}\hat{A}_{ijkl}^{C,\varsigma}\right)\right]\hat{E}_{kl} \qquad \text{(III.3.30)}$$

Then by using the local constitutive law, the average stress in the matrix is:

$$\hat{\sigma}_{ij}^{M} = \frac{1}{f^{M}} \hat{C}_{ijkl}^{M} \left[I_{klmn} - \sum_{\varsigma=1}^{N} \left(f^{I,\varsigma} \hat{A}_{klmn}^{I,\varsigma} + f^{C,\varsigma} \hat{A}_{klmn}^{C,\varsigma} \right) \right] \hat{E}_{mn} \qquad \text{(III.3.31)}$$

The average stress in the matrix can also be deduced from the combination of Equation (III.3.27), the local constitutive laws, and the strain localization equations of the form of equation (III.3.28). This combination yields the following expression for the average stress in the matrix material.

$$\hat{\sigma}_{ij}^{M} = \frac{1}{f^{M}} \left[\hat{C}_{ijmn}^{eff} - \sum_{\varsigma=1}^{N} \left(f^{I,\varsigma} \hat{C}_{ijkl}^{I,\varsigma} \hat{A}_{klmn}^{I,\varsigma} + f^{C,\varsigma} \hat{C}_{ijkl}^{C,\varsigma} \hat{A}_{klmn}^{C,\varsigma} \right) \right] \hat{E}_{mn} \qquad \text{(III.3.32)}$$

Setting equations (III.3.31) and (III.3.32) equal and solving for the effective viscoelastic stiffness tensor yields Equation (III.3.33).

$$\boxed{\hat{\mathbf{C}}^{eff} = \hat{\mathbf{C}}^{M} + \sum_{\varsigma=1}^{N} \left[f^{I,\varsigma} \left(\hat{\mathbf{C}}^{I,\varsigma} - \hat{\mathbf{C}}^{M} \right) : \hat{\mathbf{A}}^{I,\varsigma} + f^{C,\varsigma} \left(\hat{\mathbf{C}}^{C,\varsigma} - \hat{\mathbf{C}}^{M} \right) : \hat{\mathbf{A}}^{C,\varsigma} \right]} \qquad \text{(III.3.33)}$$

Equation (III.3.33), coupled with the strain localization tensors that follow, is the DSCT form of the SC model. This represents a more general form of the quasi-static SC model given in Section 3.2 and further generalizes the model originally derived by Cherkaoui *et al* [23].

The strain localization tensors for each phase are derived by rearranging Equations (III.3.23) and (III.3.24) into the form:

$$\hat{E}_{ij} = \left(\hat{A}_{ijkl}^{X,\varsigma} \right)^{-1} \hat{\varepsilon}_{kl}^{X,\varsigma} \qquad \text{(III.3.34)}$$

In this expression X can represent either the inclusion or the coating in each family.

It is important to note that the strain localization tensors of each coated inclusion family are derived from Equations (III.3.23) and (III.3.24). For this reason they are defined with respect to the local coordinate system of the ςth coated inclusion family. It is therefore necessary to rotate the strain localization tensor quantities given in Equations (III.3.35) and (III.3.36) to the global coordinates before substituting them into Equation (III.3.33) to evaluate the effective properties.

$$\boxed{\begin{aligned}\left(\hat{\tilde{\mathbf{A}}}^{I,\varsigma}\right)^{-1} &= \mathbf{I}_4 + \hat{\tilde{\mathbf{T}}}^{I,\varsigma}\left(\hat{\tilde{\mathbf{C}}}^{eff}\right) : \Delta\hat{\tilde{\mathbf{C}}}^{C,\varsigma} \\ &+ \frac{f_{C,\varsigma}}{f_{I,\varsigma}}\hat{\tilde{\mathbf{T}}}^{I,\varsigma}\left(\hat{\tilde{\mathbf{C}}}^{eff}\right) : \Delta\hat{\tilde{\mathbf{C}}}^{C,\varsigma} : \hat{\tilde{\mathbf{T}}}^{I,\varsigma}\left(\hat{\tilde{\mathbf{C}}}^{C,\varsigma}\right) : \Delta\hat{\tilde{\mathbf{C}}}^{IC,\varsigma} \\ &+ \frac{f_{C,\varsigma}}{f_{I,\varsigma}}\left[\hat{\tilde{\mathbf{T}}}^{I,\varsigma}\left(\hat{\tilde{\mathbf{C}}}^{C,\varsigma}\right) - \hat{\tilde{\mathbf{T}}}^{I,\varsigma}\left(\hat{\tilde{\mathbf{C}}}^{eff}\right)\right] : \Delta\hat{\tilde{\mathbf{C}}}^{IC,\varsigma}\end{aligned}} \qquad \text{(III.3.35)}$$

$$\boxed{\hat{\tilde{\mathbf{A}}}^{C,\varsigma} = \left(\mathbf{I}_4 + \hat{\tilde{\mathbf{T}}}^{I,\varsigma}\left(\hat{\tilde{\mathbf{C}}}^{C,\varsigma}\right) : \Delta\hat{\tilde{\mathbf{C}}}^{IC,\varsigma}\right) : \hat{\tilde{\mathbf{A}}}^{I,\varsigma}} \qquad \text{(III.3.36)}$$

In the above expressions $\Delta\hat{\mathbf{C}}^{X,\varsigma} = \hat{\mathbf{C}}^{X,\varsigma} - \hat{\mathbf{C}}^{eff}$ is the contrast tensor between material X and the effective material where X represents either the inclusion or coating, and $\mathbf{I}_4$ is the fourth order identity tensor. The local expressions of the strain localization tensors given above are then rotated to the global system according to the Euler angles of the ςth coated inclusion family as follows:

$$\hat{A}^{X,\varsigma}_{ijkl} = R^{\varsigma}_{im}R^{\varsigma}_{jn}R^{\varsigma}_{kp}R^{\varsigma}_{lq}\hat{\tilde{A}}^{X,\varsigma}_{nmpq} \qquad \text{(III.3.37)}$$

Finally, as for the identical coated inclusions case presented in Section 3.2.4, it is possible to calculate strain localization tensor for the matrix material. The expression for the SC mode DSCT formulation is given below in Equation (III.3.38).

$$\hat{\mathbf{A}}^{M} = \frac{1}{1-\varphi}\left[\mathbf{I}_4 - \sum_{\varsigma=1}^{N}\left(f^{I,\varsigma}\hat{\mathbf{A}}^{I,\varsigma} + f^{C,\varsigma}\hat{\mathbf{A}}^{C,\varsigma}\right)\right] \qquad \text{(III.3.38)}$$

Where φ is the total volume fraction of all coated inclusion families given by (III.3.39).

$$\varphi = \sum_{\varsigma=1}^{N}\left(f^{I,\varsigma} + f^{C,\varsigma}\right) \qquad \text{(III.3.39)}$$

Equations (III.3.33), (III.3.35), and (III.3.36) constitute a generalized form of the quasi-static SC micromechanical model developed in Section 3.2 using DSCT. This generalized form of the SC model permits approximation of the effective elastic or viscoelastic properties for a wide variety of particulate composites. Indeed, the attractiveness of this SC model formulation is its ability to approximate the effective behavior of a wide variety of particulate composites including lossy composites. It presents an improvement in the static domain over the model as introduced by Cherkaoui *et al* [23, 24], and a vast improvement in the quasi-static domain for the approximation of lossy behavior over the scattering based models.

Before employing this model in a material by design strategy, however, it is first necessary to verify its accuracy and robustness. The aim of the following chapter is to validate this model derived above in the quasi-static regime through two different methods. First, the model will be compared to established bounds in the complex domain. This will ensure that the formulation of the model does not violate energy restrictions. Second, the model will be validated by comparing SC approximations against experimental data taken from the literature in both the static and quasi-static domain. Following this validation, Chapter V will then present an elementary multiscale material by design example which employs the quasi-static this SC model.

CHAPTER IV

VALIDATION AND APPLICATION OF THE SELF-CONSISTENT MODEL IN THE QUASI-STATIC DOMAIN

4.1 Overview

The aim of this chapter is the validation and application of the SC model in the quasi-static regime. This will be accomplished in two steps. The first step is the comparison of the SC model with existing bounds for complex composite media. This section begins with an introduction of complex bounding methods available in the literature. Following a detailed introduction, the SC is used to approximate the effective complex behavior of several different hypothetical composite media and the results are compared to accepted bounds. Agreement with existing bounds insures that the derived SC model does not violate basic physical laws. The second part of the SC model validation is done via parametric studies and comparison with experiment. To begin, the general SC model is employed to carry out parametric studies of the effective lossy behavior of viscoelastic composite materials containing oriented ellipsoidal inclusions. The transmission loss (TL) of a slab of a viscoelastic composite is calculated from the effective material behavior approximated using the general SC model. These results are then compared to experimental data and the SC single scattering model of Baird, Kerr, and Townend (BKT) [76]. Following this analysis, SC DSCT model approximations are compared with experimental data for viscoelastic composite materials having varying orders of anisotropy, multiple inclusion types, multiple length scales, and varying coating thicknesses. All of the

above steps validate the use of the SC model in the quasi-static domain and indicate the robustness of the DSCT formulation. Finally, the last section of this chapter discusses several numerical difficulties encountered during SC model implementation and the solution paths employed.

4.2 Complex bounds and the self-consistent model

In order to properly frame the use of the SC model for quasi-static wave propagation problems, the issue of bounds must be addressed. Insight into the validity and optimality of any mean field model can be established by investigating the effective properties calculated with the model and comparing the results to well-established bounds [150]. Comparison with bounds has a two fold purpose. Bounds on the effective behavior of composite materials describe the limits of possible effective material properties due to minimal and maximal energy restrictions. They are dependent on constituent material properties and the volume fractions of each phase. Disagreement with bounds invalidates a material model as it implies a violation of physical laws during model derivation. Verification that a proposed effective medium theory (EMT) falls within accepted bounds is, therefore, a first order model check. The second purpose for comparison with bounds is to check composite material optimality. Bounds provide information concerning the optimality of effective material behavior because they are derived from upper and lower energy restrictions. For this reason, proximity to an upper or lower bound gives a measure of how nearly optimal the phase composition, inclusion geometry, inclusion orientation, or any combination of these factors renders the effective behavior of the composite [67].

Bounding techniques for purely elastic materials, meaning that no losses occur and all material properties are modeled as *real*, are well known; see, for example, Hashin & Shtrikman [58], Walpole [59], Hill [60, 61], and for a detailed summary see

Hashin [62]. It is well known that the *n*-phase SC model falls within accepted bounds in the purely elastic case [43]. There has been comparatively little work done regarding the bounds of composites containing constituent phases with complex material properties. The subject of bounding the effective complex moduli of multiphase composites has been addressed in several papers starting with Hashin [8, 63, 64], Christensen [7], and Roscoe [65, 66]. Hashin's work proposes a method for calculating the effective complex moduli as a function in the frequency domain for elementary composites and only briefly mentions bounds which are restricted to very simple material mixtures. Christenson discusses the bounding problem, but restricts the discussion to the application of Hashin-Shtrikman (HS) bounds for a bi-phase viscoelastic matrix material containing either voids or rigid inclusions. Christenson's approach is simply the application of HS bounds to the real and imaginary parts of the effective moduli separately. Roscoe takes a similar approach to bounding effective viscoelastic behavior by applying the Voigt and Reuss bounds separately to the real and imaginary parts of a viscoelastic composite; the simplest and least restrictive complex bounding technique in the literature. These bounds were derived from variational principles expressing minimal and maximal strain energy in the viscoelastic composite, but the interaction of the real and imaginary parts was not considered. Recent developments in bounding the effective behavior of complex composites are based on the variational techniques of Cherkaev and Gibiansky [67] (see also Milton [68] and Miller [69]) which couple contributions from the real and imaginary parts of the constitutive phases on the expressions for overall energy. Results based on this approach are detailed in a series of related papers: Gibiansky & Milton [70], Milton & Berryman [71], Gibiansky & Lakes [72, 73], and Gibiansky & Torquato [74]. Many of the works referenced above were introduced for bounding the effective behavior of any complex composite medium which includes such material properties as effective electrical conductivity, magnetic permeability, or viscoelastic moduli. The methods derived by the above authors bound the effective bulk and/or shear moduli of *bi-phase* viscoelastic composite in zones prescribed by

arcs in the complex plane. These arcs are functions of the complex moduli and volume fractions of the constituent phases. The variational approaches of the above authors are more restrictive than those proposed by Roscoe, Hashin, or Christensen because they relate the complex bounds of the effective moduli to the real *and* imaginary parts of the constituent phases. For the elastic case, all of these approaches reduce to the Hashin-Shtrikman bounds for an isotropic bi-phase composite.

All of the bounding methods introduced above have limitations, especially when applied to composites containing coated ellipsoidal inclusions. The most relevant restrictions concerning this application are the number of constituent phases and composite anisotropy. Applying bounds derived for purely elastic composites to the real and imaginary parts of a viscoelastic composite separately, as proposed by Roscoe [65, 66] and Christenson [7], does not limit the resultant bounds to any specific number of constituent phases. Unfortunately, the Reuss [111], Voigt [110], and HS [58] bounds require the constituent phases and the composite material to be isotropic. More importantly, the interaction between the real and imaginary parts, which are related by the principle of causality [151, 152], is neglected. More restrictive bounds have been introduced by Cherkaev and Gibiansky are derived from variational methods do take storage and loss moduli interactions into account. Unfortunately, these bounds are restricted to bi-phase composites and also require both constituent and effective materials be isotropic. Though these methods are limited in terms of the number of phases and material anisotropy, they are the most developed bounds to be found in published literature. The three most tractable approaches available, those of Roscoe [65, 66], Milton and Berryman [71], and Gibiansky and Lakes [72], are summarized and plotted together with SC model estimates in the following section.

4.2.1 Complex shear and bulk modulus bounds proposed by Roscoe

The upper and lower bounds derived by Roscoe for a viscoelastic composite reduce to the application of Voigt and Reuss bounds separately to the real and imaginary parts of the composite [12]. These bounds provide the least restrictive limits of possible effective viscoelastic properties and can be calculated as a function of either inclusion volume fraction or frequency. Though these bounds are not restrictive they represent a good starting point for the validation of the SC model in the quasi-static domain.

The equations used to derive bounds proposed by Roscoe are analogous statements of the potential energy equations which are the basis of the extremum principles used to find the bounds for elastic composites, see Voigt [110] and Reuss [111]. The result of this analysis in the complex domain, see Appendix C, yields the bounds described by Equations (IV.2.1) and (IV.2.2) which are the weighted harmonic average and weighted average of the constituent phase properties, respectively.

$$\mu_{RL}^{*} = \left(\sum_r \frac{f_r}{\mu_r^{*}} \right)^{-1} \qquad \kappa_{RL}^{*} = \left(\sum_r \frac{f_r}{\kappa_r^{*}} \right)^{-1} \tag{IV.2.1}$$

$$\mu_{RU}^{*} = \sum_r f_r \mu_r^{*} \qquad \kappa_{RU}^{*} = \sum_r f_r \kappa_r^{*} \tag{IV.2.2}$$

In the above relationships, *RL* and *RU* denote the lower and upper bounds derived by Roscoe and are analogous to the Reuss and Voigt bounds, respectively. It is now important to note that due to energy considerations the following is true:

$$\begin{aligned} \mu_{RU}^{*} &\geq \mu_{eff}^{*} \quad \kappa_{RU}^{*} \geq \kappa_{eff}^{*} \\ j_{RL}^{*} &\geq j_{eff}^{*} \quad l_{RL}^{*} \geq l_{eff}^{*} \end{aligned} \tag{IV.2.3}$$

An important aspect of these bounds is their lack of restrictions with respect to the frequency inspected, the total number of constituent viscoelastic phases, r, or the total volume fraction, φ. This logic leads to the following restrictions on the possible values for the effective viscoelastic moduli:

$$\mu_{RL}^{'''}(\omega,\varphi) \le \mu_{eff}^{'''}(\omega,\varphi) \le \mu_{RU}^{'''}(\omega,\varphi)$$
$$\kappa_{RL}^{'''}(\omega,\varphi) \le \kappa_{eff}^{'''}(\omega,\varphi) \le \kappa_{RU}^{'''}(\omega,\varphi) \qquad \text{(IV.2.4)}$$

where ω is the frequency of interest. It is also useful to note that $f_{matrix} = 1 - \varphi$.

At this stage the quasi-static SC model is compared to these elementary complex bounds. This is achieved through two different comparisons. The approximations from the quasi-static SC model are first compared to the upper and lower bounds for a fixed frequency while the coated inclusion volume fraction is varied from 0 to 1 for a hypothetical viscoelastic composite created from the materials studied by Baird *et al* [76]. The frequency dependent SC model approximation of a viscoelastic composite with a fixed volume fraction is then compared the same bounds. The constituent material properties employed in these studies are listed in Table 4-1. The two composite materials containg identical coated inclusion phases of varying volume fractions, but are distinguishable by their polymer matrix properties. The matrix materials of these two composite materials, composite *1* and composite *2*, are decribed as "soft" and "stiff", respectively.

Table 4-1: Constituent material properties of the viscoelastic composites studied by Baird *et al* [76].

		Composite 1	*Composite 2*
Bulk modulus of matrix (Pa):	K^M	3×10^9	3×10^9
Density of matrix (kg/m^3):	ρ^M	935	1090
Dynamic shear modulus coefficients:	A_0	5.93978	6.675 69
	A_1	2.6618×10^{-1}	3.954×10^{-2}
	A_2	-3.613×10^{-2}	9.39×10^{-3}
	A_3	4.1×10^{-3}	3.85×10^{-3}
Dynamic loss factor coefficients:	B_0	5.251×10^{-2}	9.792×10^{-2}

		Composite 1	*Composite 2*
	B_1	1.9374×10^{-1}	5.9×10^{-4}
	B_2	-6.209×10^{-2}	6.89×10^{-2}
	B_3	8.19×10^{-3}	-9.25×10^{-3}
Bulk Modulus of coating (Pa):	K^C	2.1×10^9	2.1×10^9
Density of coating (kg/m^3):	ρ^C	1700	1700
Shear modulus of coating (Pa):	μ^C	1.26×10^9	1.26×10^9
Loss factor of coating:	η^C	0.1	0.1
Bulk modulus of air at 1 atm (Pa):	K^I	1.4×10^5	1.4×10^5
Density of air at 1 atm (kg/m^3):	ρ^I	1.28	1.28
Average coating fraction:	ε	$2.5 \text{ e } 10^{-2}$	$2.5 \text{ e } 10^{-2}$
Average outer shell radius:	b	5×10^{-5}	5×10^{-5}

The frequency dependent shear modulus of the matrix materials detailed in the above table is approximated through Equations (IV.2.5) – (IV.2.7) and by applying the following relationships.

$$\log \mu_M^R = A_0 + A_1 \log f + A_2 (\log f)^2 + A_3 (\log f)^3 \qquad \text{(IV.2.5)}$$

$$\delta_M = B_0 + B_1 \log f + B_2 (\log f)^2 + B_3 (\log f)^3 \qquad \text{(IV.2.6)}$$

$$\mu_M(f) = \mu_M^R (1 - i \tan \delta_M) \qquad \text{(IV.2.7)}$$

It is important to point out that f in these equations represents the frequency of interest and not the volume fraction. These equations and coefficients were found by fitting experimental data obtained from a Dynamic Mechanical Thermal Analyzer (DMTA) [76].

The results of the two studies comparing the quasi-static SC model approximation to the elementary bounds proposed by Roscoe are given below in Figure 4-1 through Figure 4-4. The matrix material is the "soft" material given in Table 4-1.

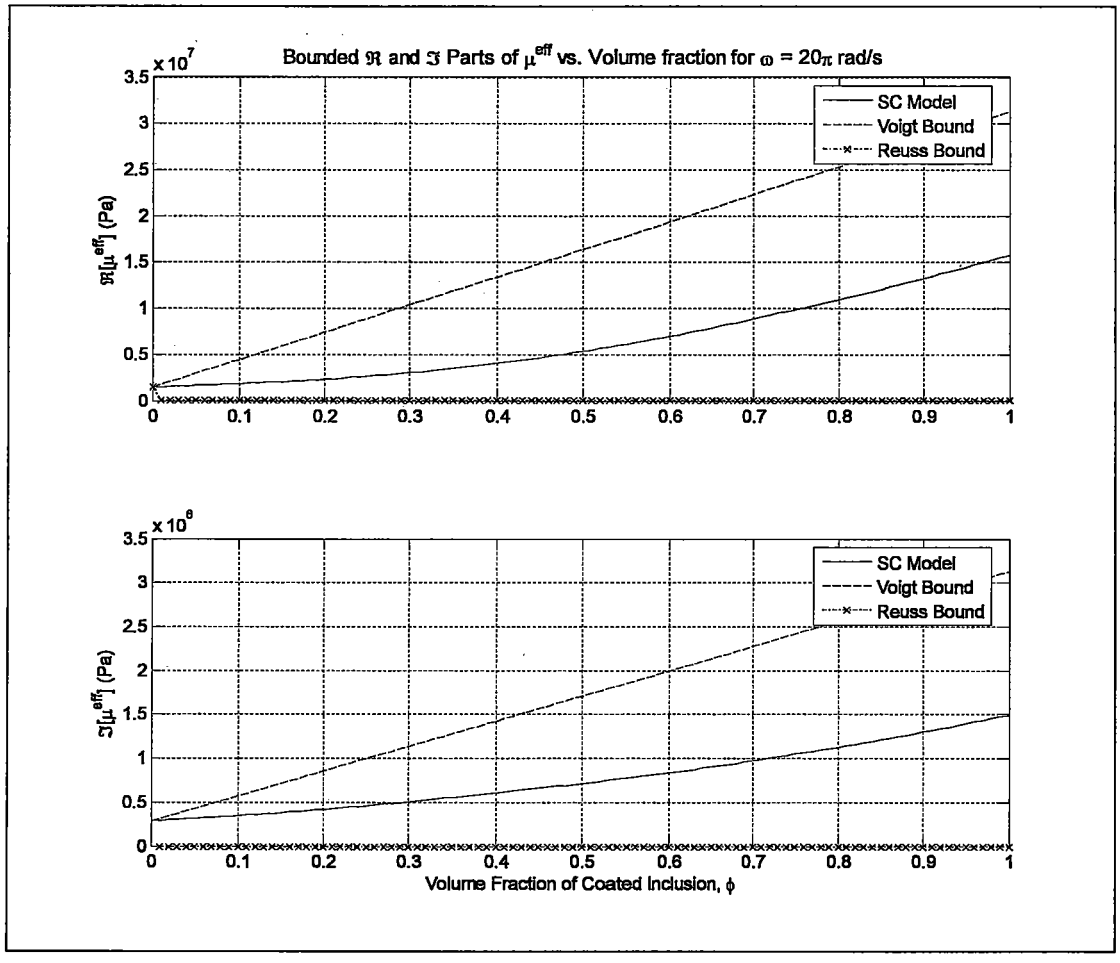

Figure 4-1: Real and imaginary parts of the effective shear modulus as function of coated inclusion volume fraction for a fixed frequency. SC model approximation shown with the upper and lower bounds proposed by Roscoe. (Lower bound of imaginary part is zero everywhere).

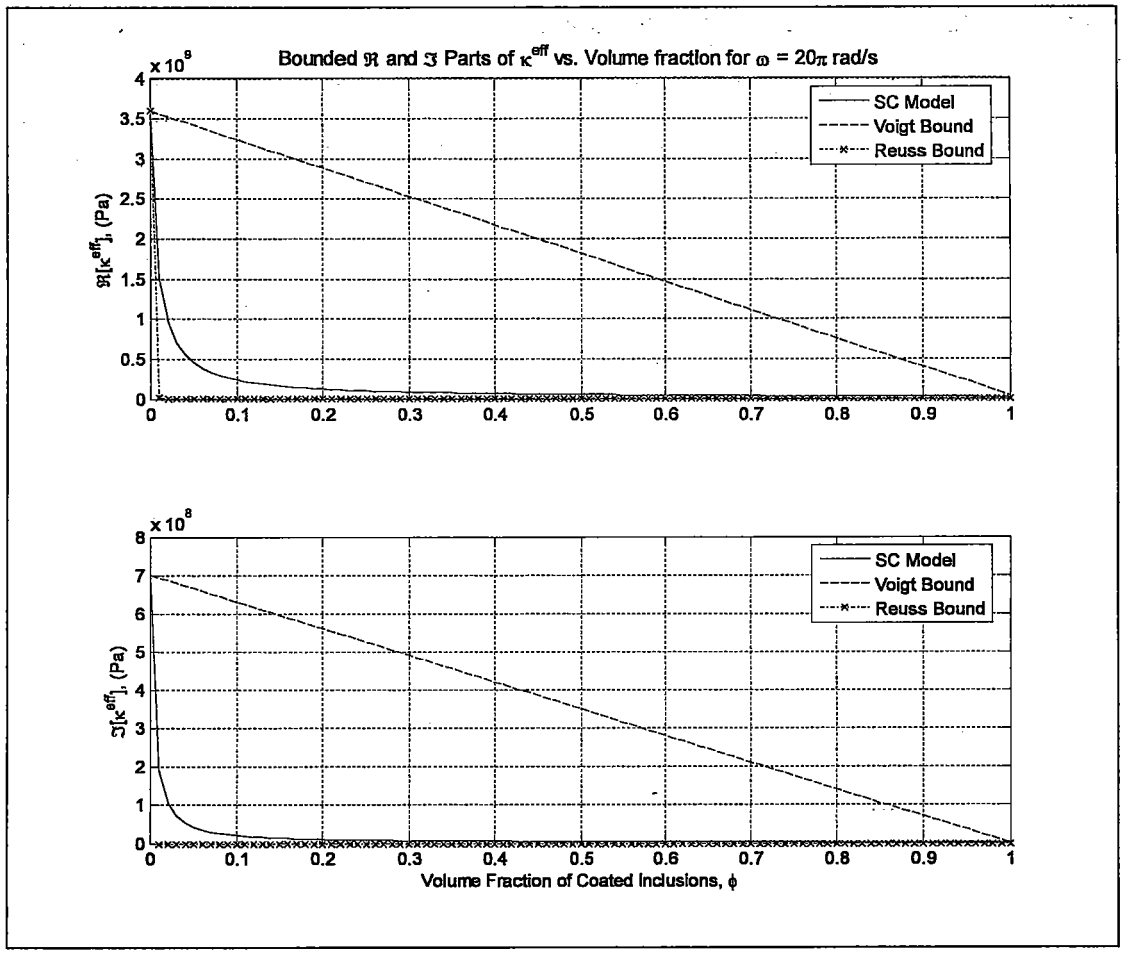

Figure 4-2: Real and imaginary parts of the effective bulk modulus as a function of coated inclusion volume fraction for a fixed frequency. SC model approximation shown with the upper and lower bounds proposed by Roscoe. (Lower bound of imaginary part is zero everywhere).

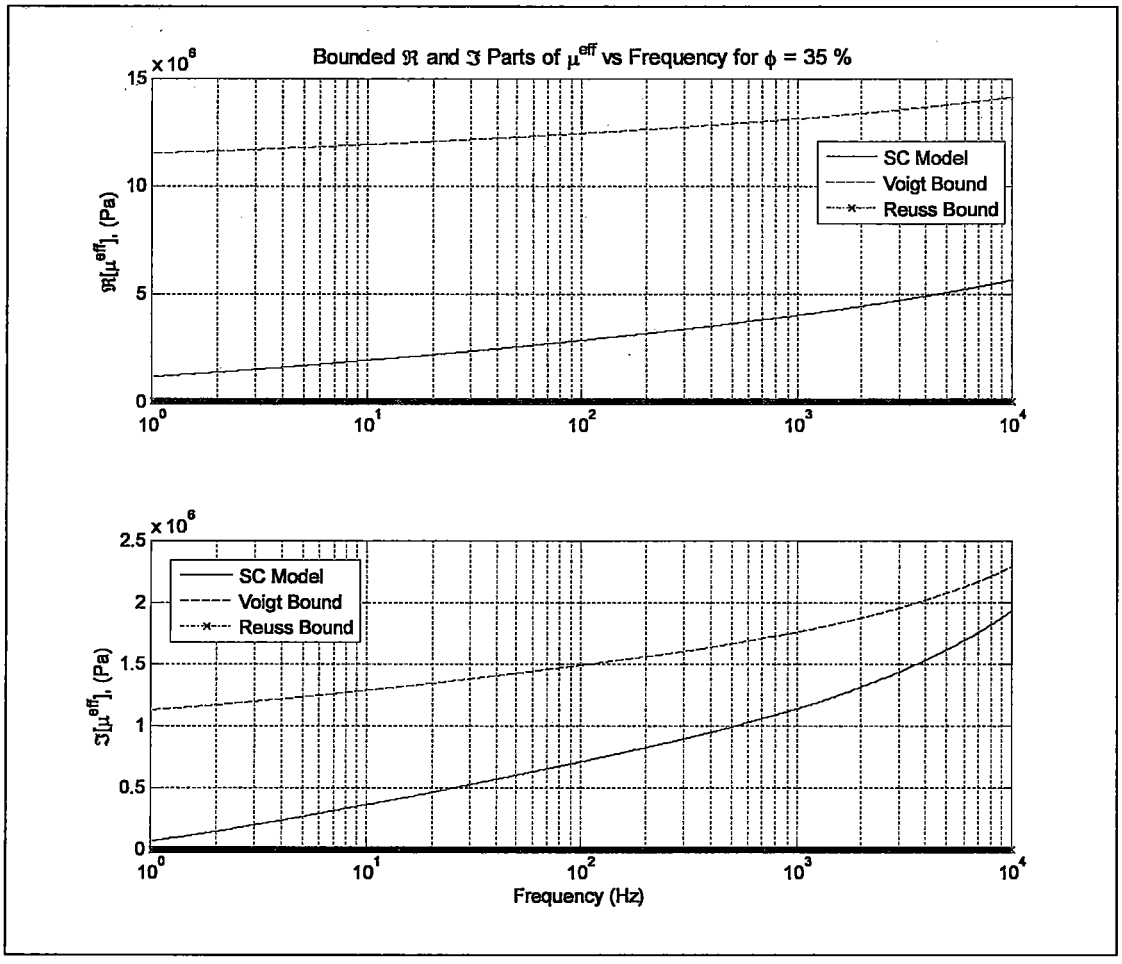

Figure 4-3: Real and imaginary parts of the effective shear modulus as a function of frequency for a fixed coated inclusion volume fraction. SC model approximation shown with the upper and lower bounds proposed by Roscoe. (Lower bound of imaginary part is zero everywhere).

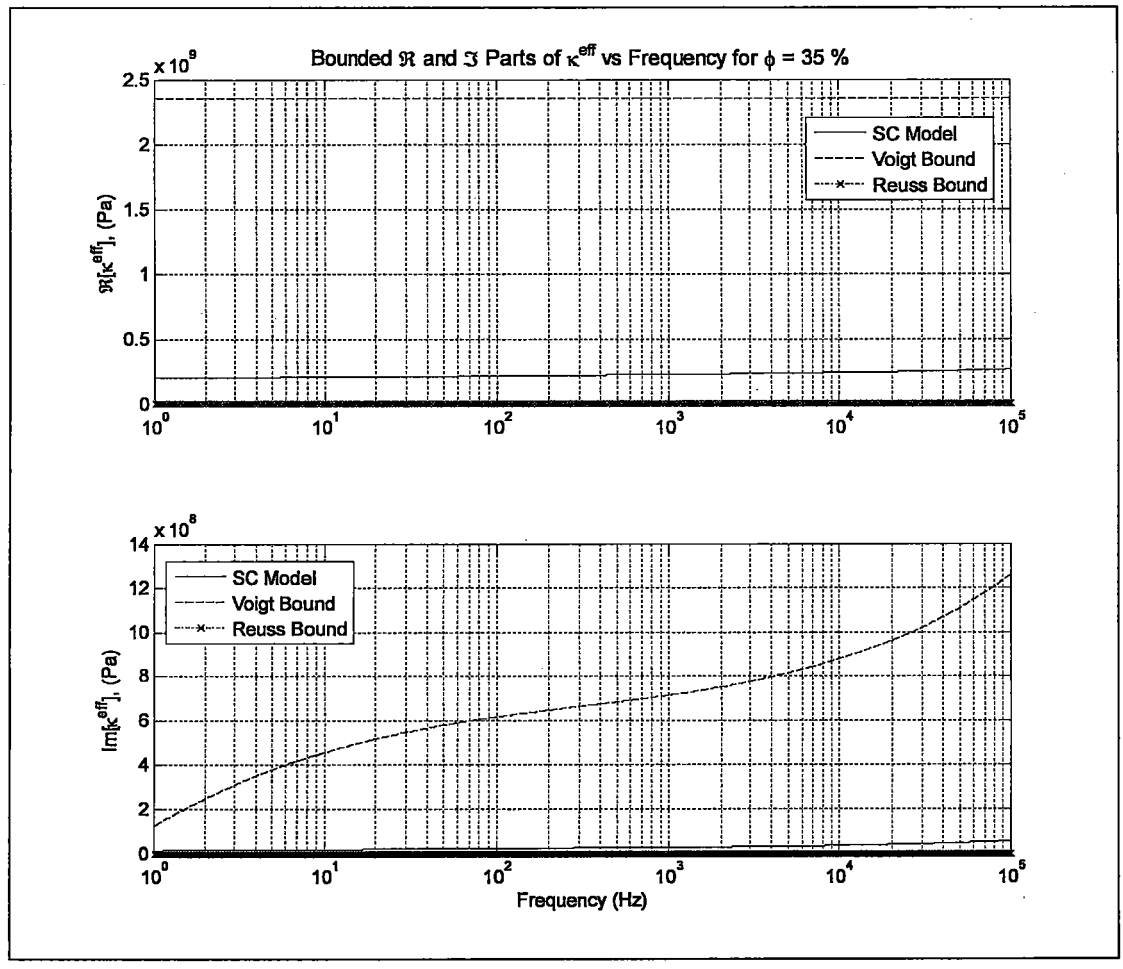

Figure 4-4: Real and imaginary parts of the effective bulk modulus as a function of frequency for a fixed coated inclusion volume fraction. SC model approximation shown with the upper and lower bounds proposed by Roscoe. (Lower bound of imaginary part is zero everywhere).

The above plots show that the SC model approximation falls within the complex bounds derived by Roscoe for viscoelastic composites as a function of both frequency and coated inclusion volume fraction. Though this study is far from exhaustive and not a direct proof, the plots suggest that no physical laws have been violated during the derivation of the quasi-static model. These observations are encouraging. However, since these bounds are the least restrictive, it is prudent to compare the SC model against more restrictive bounds. The restrictive bounds chosen to further validate the quasi-static SC model are the shear and bulk bounds for bi-phase viscoelastic composites derived by Milton and Berryman [71] and Gibiansky and Lakes [72], respectively.

4.2.2 Complex bounds using variational and translational techniques

The two bounding techniques described in this section stem from the complementary works of Milton [68] and Cherkaev and Gibiansky [67]. The objective of their work was to simplify the algebraic calculations required to find the bounds for complex valued effective material properties resulting from heterogeneous media. This is done via a fractional-linear *Y*-transformation [74]. These methods were derived for any complex valued material property whose fields are dissipative and time varying. The resulting bounds can therefore be applied to physical properties as disparate as electrical conductivity and viscoelasticity. Using complex valued expressions of Hooke's law and strain energy density, Cherkaev and Gibiansky [67] formulated four different min-max variational principles. These principles lead to rigorous bounds for the effective viscoelastic moduli of a bi-phase composite material. This approach inspects a bi-phase viscoelastic composite at a fixed inclusion volume fraction and prescribes a zone in the complex modulus plane which bounds the set of permissible values describing effective material behavior. Their results yield coupled bounds. Coupled bounds restrict the effective complex valued moduli based on functions of both the real *and* imaginary parts of the constituent phase moduli. Gibiansky and Lakes employed this approach to find the bounds on the effective viscoelastic bulk modulus [72]. Those bounds are defined by four arcs that intercept each other at two points in the complex plane. The outer-most of those four arcs define the limits of permissible effective complex bulk modulus values of a bi-phase viscoelastic composite. The approach derived by Milton and Berryman [71] to find bounds on the effective shear modulus is similar in its derivation and also based wholly on the work of Cherkaev and Gibiansky [67] and Milton [68]. Both of these bounding approaches, which are summarized in Appendix C, are restricted to the following cases: (*i*) bi-phase viscoelastic composites, (*ii*) isotropic behavior of both the composite and constituent phases, and (*iii*) calculation of bounds for a *single* frequency and a *single* volume fraction. These restrictions limit

quasi-static SC model validation. The third restriction is the most limiting for the inspection of a wide range of material compositions and exciting frequencies. These restrictions illustrate why these methods do not easily lend themselves to inspect the validity of an effective medium theory as a function of either volume fraction or frequency. Bounds based on these variational techniques are, however, the most rigorous available. Therefore, despite these limitations, it is valuable to check SC model approximations against these bounds. The following sub-sections employ the bounds described in Appendix C and plot the bounds together with the quasi-static SC approximation. This analysis provides further validation of the SC model in the quasi-static frequency domain.

4.2.2.1 Complex bounds on the bulk modulus of bi-phase media

The bounds for the bulk modulus derived by Gibiansky and Lakes [72] are defined for a bi-phase viscoelastic composite material. The composite's composition is defined by a phase *1* which occupies volume fraction f and its complex bulk and shear moduli are represented as κ_1 and μ_1, respectively. Conversely, phase *2* occupies a volume fraction $(1-f)$ and its bulk and shear moduli are represented as κ_2 and μ_2, respectively. The effective complex valued bulk modulus of the isotropic viscoelastic composite will be constrained to a "lens-shaped" region in the complex bulk modulus plane that is bounded by the outer-most pair of four circular arcs each of which correspond to the four min-max variational principles proposed by Cherkaev and Gibiansky [67] and Milton [68]. To illustrate their bounds, Gibiansky and Lakes presented a hypothetical viscoelastic composite material whose composition and constituent material properties are defined by the values given in Figure 4-5 below. Figure 4-5 shows that the bi-phase isotropic SC model falls within the bulk modulus bounds calculated by the relations above.

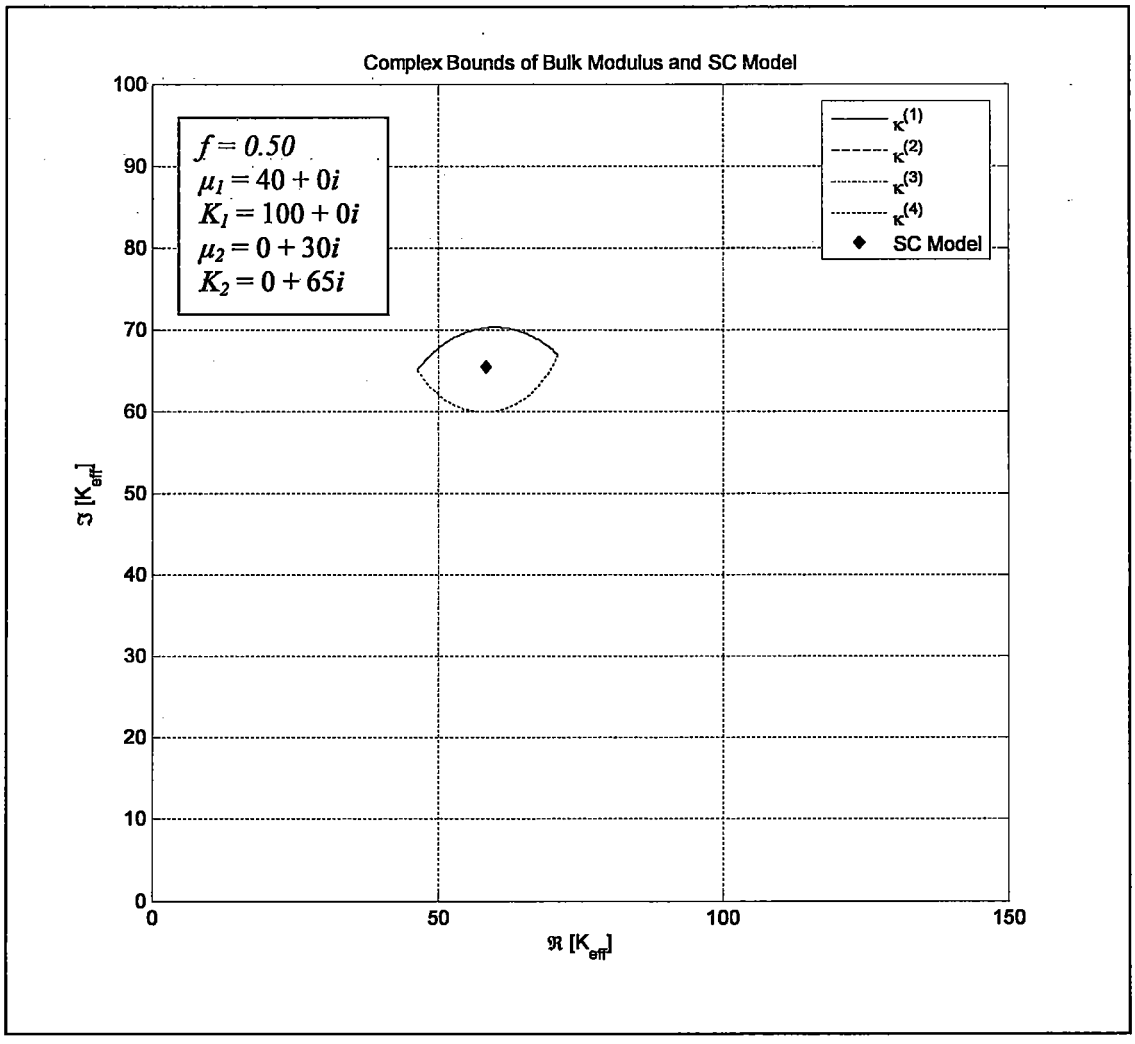

Figure 4-5: Bounds in the complex bulk modulus plane calculated from reference [72] and SC model approximation, ◆, of same composite. Bounds are delineated by four, sometimes overlapping, lines: $\kappa^{(1\text{-}4)}$.

4.2.2.2 Complex bounds on the shear modulus of bi-phase media

The bounds on the effective complex shear modulus derived by Milton and Berryman [71] are also based on the four variational principles and the *Y*-transform introduced by Cherkaev and Gibiansky [67] and Milton [68]. Their results yield arcs in the complex modulus plane which define the limits of permissible effective complex shear modulus values of a bi-phase viscoelastic composite. The bounds are best described by an algorithm in reference [71] which is summarized in Appendix C for convenience. It must be noted that difficulties can arise in calculating these bounds because some factors may be driven to infinity while the final result is always

finite. Further, these bounds are sometimes not completely closed, and tangent lines must be drawn to close the bounds. These complications make the process arduous and less than ideal for an exhaustive evaluation of model validity as a function of frequency or volume fraction, or both. Despite these difficulties, the comparison of the quasi-static SC model and these bounds given in Figure 4-6 shows good agreement and further suggests that the application of the SC model in the quasi-static regime is valid.

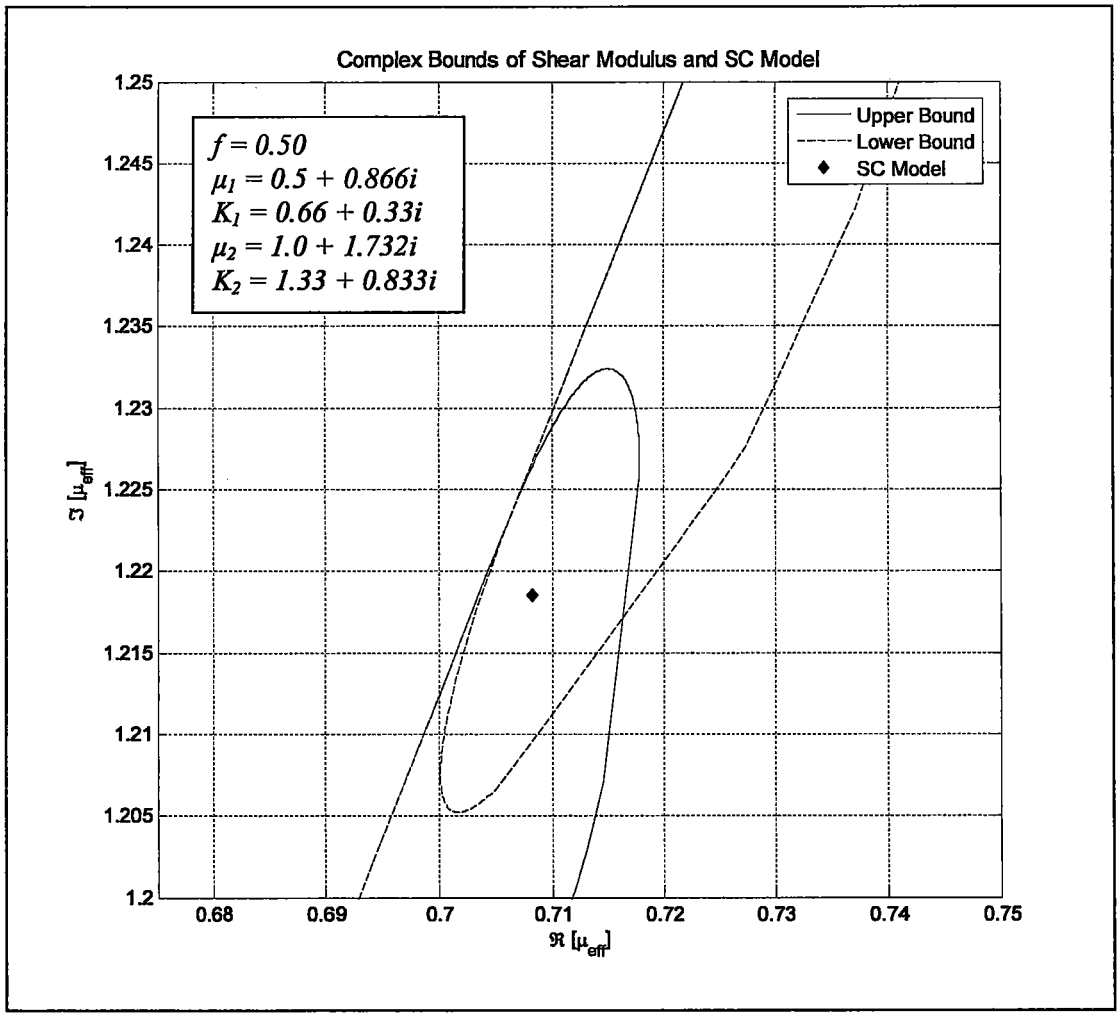

Figure 4-6: Bounds on the complex effective shear modulus given in reference [71]. —— Upper bound; - - - Lower bound. Calculated SC model point, ◆ , is shown to fall within ellipsoidal bounded area.

4.3 Validation of the general SC model in the quasi-static domain

The previous section described a fundamental check of the quasi-static SC modeling approach. The SC model was shown to fall within accepted complex bounds thus proving that no physical laws were violated in the derivation of the model. The SC model derived in Chapter III is therefore a valid effective medium theory for applications in the quasi-static frequency domain. Model validation against complex bounds is very important but it yields little information about the precision and versatility of the SC model. The remainder of present section investigates the SC model for more specific information about its capacity to model the effective behavior of various viscoelastic composite materials. This information is gathered through two methods: comparison with experiment and parametric studies. Specifically, the SC model precision is investigated by comparing model results with experimental data while the versatility is validated though a series of parametric studies. These two approaches provide a clear picture of SC model precision and its adaptability to model many different types of viscoelastic composites.

4.3.1 Elementary validation of quasi-static SC model

The fundamentals detailed in Chapter II indicate that the effective lossy behavior of a viscoelastic composite in the quasi-static domain is intimately related to the strain energy in its lossy components. To illustrate this point, the increase in strain energy in the "matrix" material of a voided composite sphere was given as an example. The present section generalizes the voided sphere concept to the case of an isotropic voided viscoelastic material. The following elementary parametric studies show trends of the effective behavior of the voided viscoelastic material as calculated by the SC model. The relationship of interest is between the composite's macroscopic lossy behavior and the void fraction. The goal of this simple study is to provide a first order validation of the quasi-static SC model by showing that the trends calculated with the SC model are in accordance with expectations.

The viscoelastic composite studied is a hypothetical material resulting from the introduction of spherical voids in a matrix of the "soft" polymer matrix material studied by Baird *et al* [76]. The properties of the matrix, together with all other material properties which are important for the following examples, were given by Baird *et al* and have been repeated in Table 4-1.

The fundamentals of the frequency dependent behavior of voided viscoelastic materials is well understood, see, for example, Jarzynski [6]. The three following trends are expected: (*i*) a decrease in the elastic moduli of the material, $\mathbf{C}_v$, with increasing void fraction, φ, (*ii*) an increased damping capacity with increasing frequency, and (*iii*) an increased damping capacity with increasing void fraction. The first trend is the result of removing material and thereby weakening the resistance of the whole to deformation. Figure 4-7 clearly shows that the SC model correctly approximates this trend across all frequencies inspected.

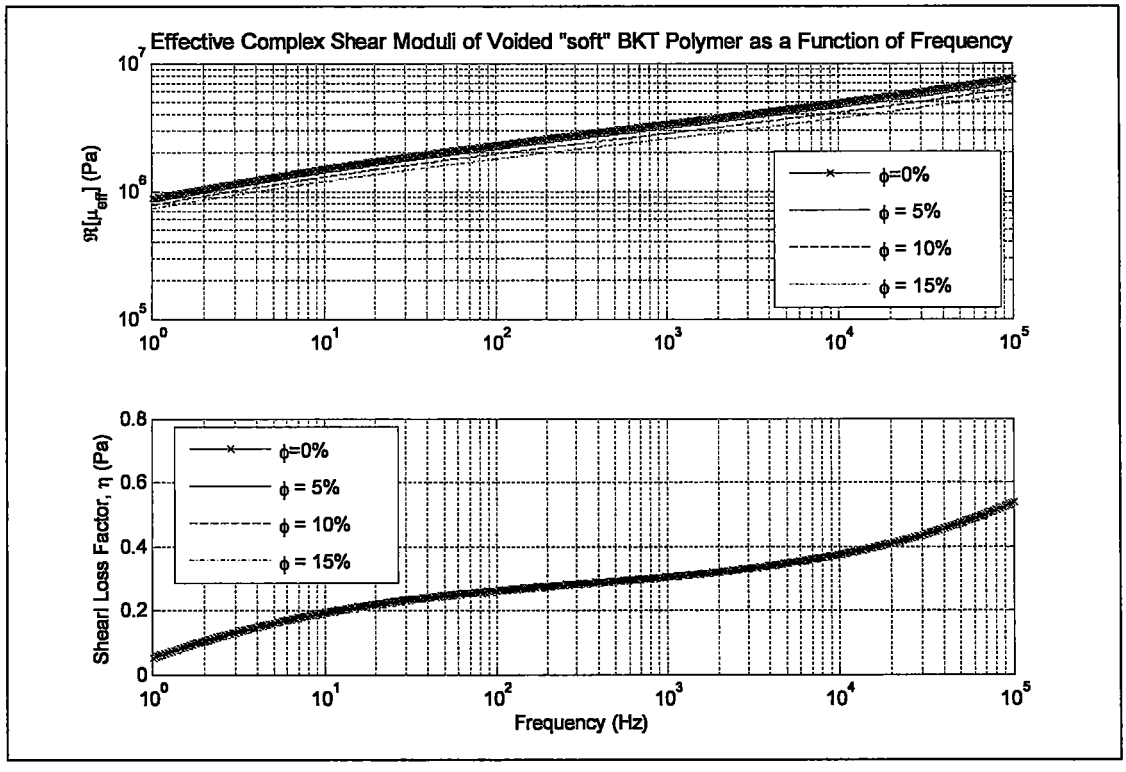

Figure 4-7: Effective complex shear modulus of a voided viscoelastic material as a function of frequency. The pure matrix response is shown together with three differnent values of void fraction.

The second trend, an increase in damping capacity with increasing frequency, is the result of contributions from both wave scattering and constitutive viscoelastic material behavior. The scattering contribution is described as follows. As frequency increases, the relative void size increases with respect to incident wavelengths. This is equivalent to stating that the non-dimensional number *ka* increases. This "increase" in void size leads to more efficient reflection, re-direction, and mode conversion by voids thereby creating more wave-fronts which are subsequently attenuated by the viscoelastic host material. The ultimate result is an increase in the absorptive quality of the material[1]. The contribution from constitutive viscoelastic material behavior results from an increase in the characteristic phase lag between the load and the resulting strain with increasing frequency. The result is an increased hysteresis loop area in stress-strain space (see Section 2.1.1). It is very important to note that this behavior is *not the case for all viscoelastic materials at all frequencies* [153]. Typical characteristics of the frequency dependant complex shear modulus are shown in Figure 4-8. This figure shows that both the storage and loss modulus have a strong frequency dependence and that the damping capacity of a viscoelastic material increases monotonically as a function of frequency for $0 < f < f_{crit}$. However, for the materials and frequency ranges studied in these examples, the damping capacity will increase monotonically as a function of frequency. It is also important to stress that increases in lossy behavior with increasing frequency observed in the *quasi-static* frequency domain are dominated by the constitutive behavior of the viscoelastic behavior and that scattering contributions have a minimal contribution. The ability of the SC model to correctly capture this behavior regardless of the void fraction is shown in Figure 4-10.

---

[1] Incidentally, this argument is the same used by Lord Rayleigh to explain why the sky is blue. Blue light, having the shortest wavelength in the visible spectrum, is more efficiently scattered by particles in the air and is therefore more visible. His fundamental work in the area of wave scattering is also the reason that low *ka* scattering is called Rayleigh scattering and that the limit of $ka << 1$ is called the Rayleigh limit.

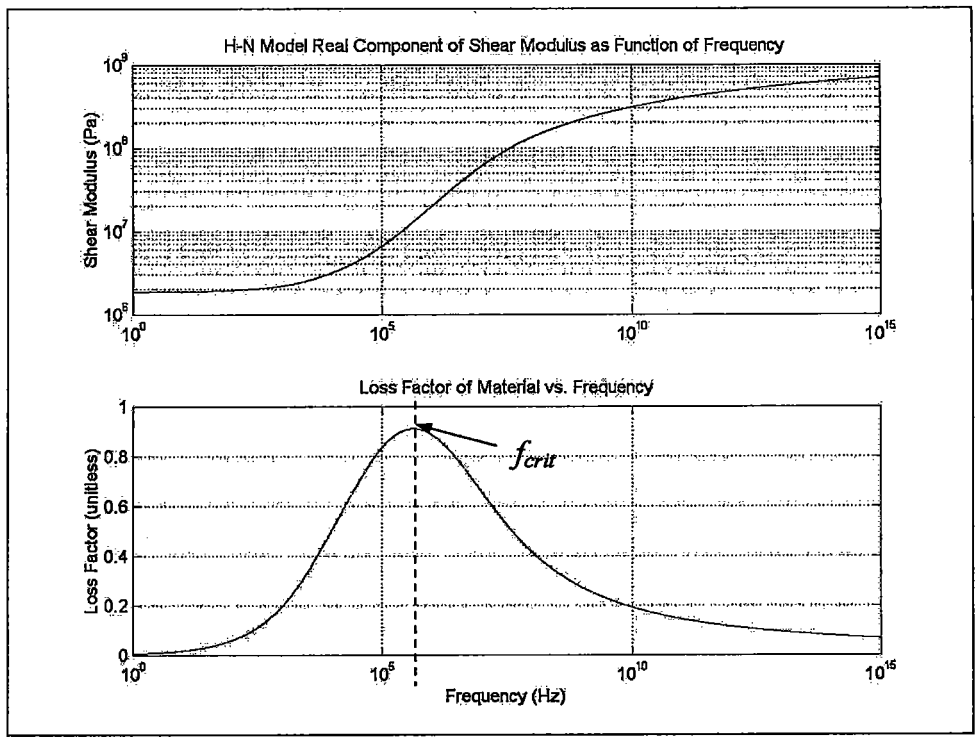

Figure 4-8: General characteristics of the frequency dependent shear modulus of viscoelastic. The modulus is approximated by the Havriliak-Negami model [148]. Damping capacity of the viscoelastic material is a monotonically increasing function of frequency for $0 < f < f_{crit}$.

The third trend, an increase in damping capacity with increasing void fraction, is the result of both wave scattering and viscoelastic material strain energy contributions. Increasing material void fraction results in more efficient wave scattering at each frequency of interest because the scattering volume is increased. Increasing material void fraction at a fixed frequency, therefore, is analogous to the effect of increasing frequency for a fixed void fraction which was explained in the previous paragraph. The increase in damping capacity with increasing void fraction can also be explained using strain energy arguments. The time varying specific strain energy, defined as the strain energy per unit volume, in any material is calculated from either of the two expressions given in Equation (IV.3.1).

$$\hat{w} = \frac{1}{2}\hat{\sigma}_{ij}\hat{\varepsilon}_{ij} = \begin{cases} (1/2)\hat{\sigma}_{ij}\hat{J}_{ijkl}\hat{\sigma}_{kl} \\ (1/2)\hat{\varepsilon}_{ij}\hat{C}_{ijkl}\hat{\varepsilon}_{kl} \end{cases} \qquad \text{(IV.3.1)}$$

In the above equation $\hat{w}$ represents the specific strain energy, $\hat{\sigma}_{ij}$ the applied stress, $\hat{\varepsilon}_{ij}$ the strain, and $\hat{\mathbf{J}}$ is the compliance tensor which is the inverse of the stiffness tensor, $\hat{\mathbf{C}}$. It is noted that the strain and stress fields *are not independent* of each other and the selction of the strain energy relationship can therefore be made for simplicity depending whether the material is loaded with a known stress or know displacement (strain). For a propagating wave of known magnitude the strain energy should be calculated with the relation $2\hat{w} = \hat{\sigma}_{ij}\hat{J}_{ijkl}\hat{\sigma}_{kl}$. As previously stated, increasing the void fraction of any material leads to a decrease in the elastic constants and conversely to an *increase* in the compliance of the effective material. It is clear from this expression that for a given applied stress level an increase in the magnitude of the material compliance translates to an increase in the specific strain energy in the effective material. Further, since voids cannot carry any load, this increase in strain energy is concentrated in the viscoelastic host material. Chapter II illustrated that an increase in strain energy of lossy materials leads to an increase in the total energy absorbed. Figure 4-9 illustrates the ability of the SC model to correctly approximate this expected physical behavior. The plot shows the ratio of the specific strain energy in the voided material to that in a homogeneous material for the same applied shear stress, τ. The plot clearly shows that the SC model correctly captures the increase in specific strain energy as the void fraction is increased for all frequencies.

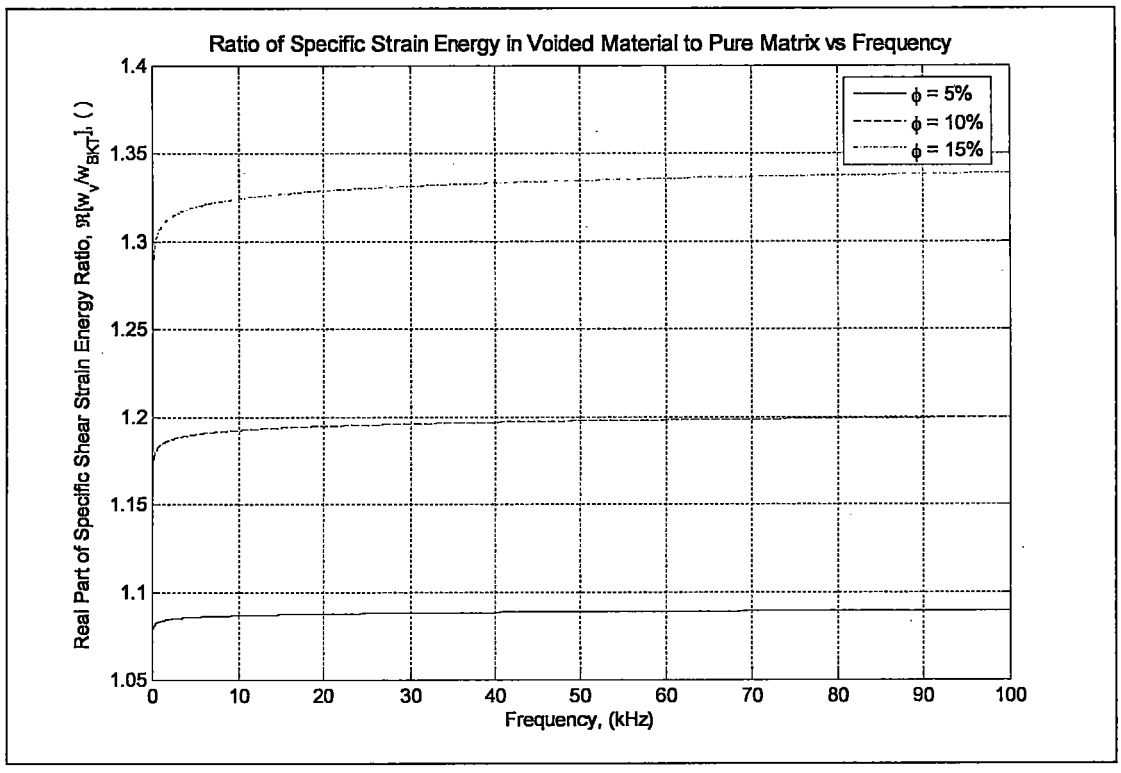

Figure 4-9: Increase in the specific strain energy of voided composites due to pure shear loading. The ratio shown is the ratio of the specific strain energy in a voided composite to the strain energy in a homogeneous material submitted to the same shear stress.

The result of the increased strain energy present in the viscoelastic matrix material shown in Figure 4-9 is an increase in the macroscopic damping capacity of the composite. Evidence of this increased damping capacity is best captured through parametric studies of the longitudinal and shear wave attenuation coefficients. The attenuation coefficient is the imaginary part of the complex wave number and is a measure of the decay rate for a wave propagating in a medium with lossy properties. Recalling equations (II.1.20) and (II.1.21), the longitudinal and shear wave attenuation coefficients for propagation in the voided polymer given here are found from the two expressions below.

$$\hat{k}_\mu^* = \omega\sqrt{\frac{\rho}{\hat{\mu}^{eff}}} = \hat{k}_\mu' + i\hat{\alpha}_\mu \quad \Rightarrow \quad \hat{p}_\mu(x,t) = \hat{A}e^{-\hat{\alpha}_\mu x}e^{-i\left(\omega t - \hat{k}_\mu' x\right)}$$

$$\hat{k}_L = \omega\sqrt{\frac{\rho}{\hat{\lambda}^{eff} + 2\hat{\mu}^{eff}}} = \hat{k}_L' + i\hat{\alpha}_L \quad \Rightarrow \quad \hat{p}_L(x,t) = \hat{B}e^{-\hat{\alpha}_L x}e^{-i\left(\omega t - \hat{k}_L' x\right)} \tag{IV.3.2}$$

These equations show that an increase in the magnitude of the attenuation coefficient leads directly to an increase in the attenuation of the propagating wave. Figure 4-10 illustrates that the SC model captures the increased damping capacity of a voided polymer with increasing void fraction and increasing frequency.

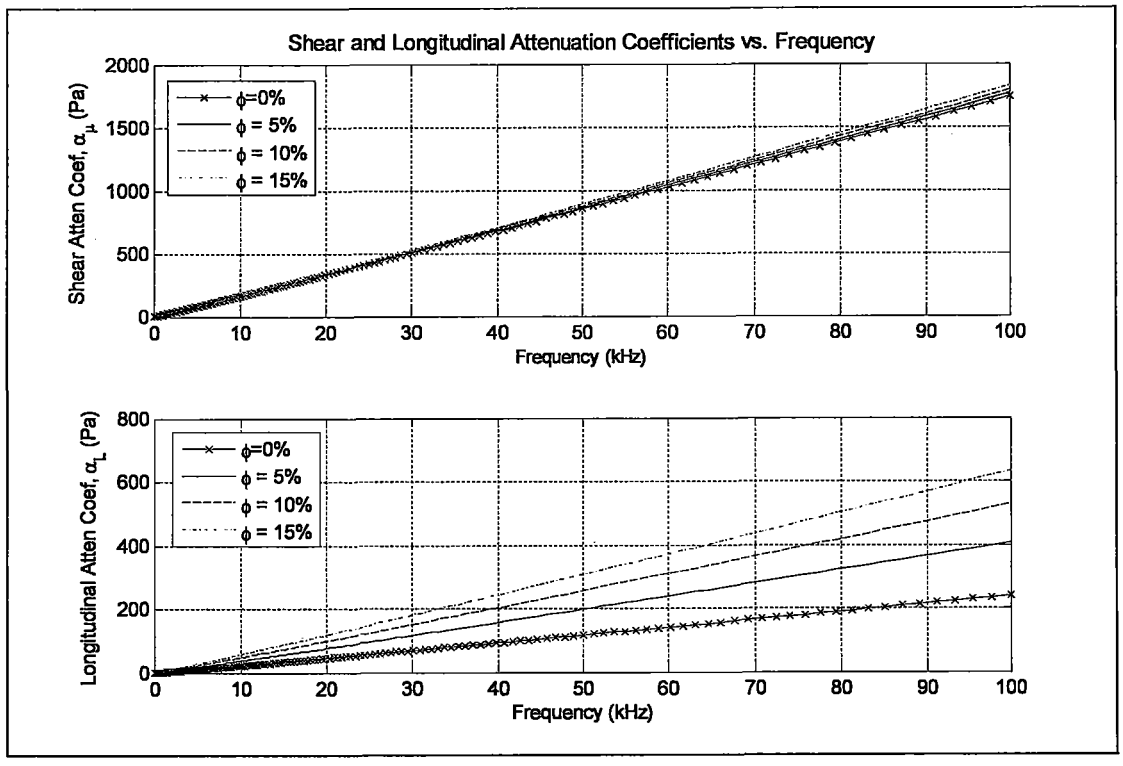

Figure 4-10: Attenuation coefficients for shear and longitudinal wave propagation in a pure polymer compared with the effective behavior of three different voided composites approximated by the SC model.

One very important observation about Figure 4-7 and Figure 4-10 is that the increase in lossy behavior is the result of material softening caused by removing material. The softening is best indicated by an increase in the magnitude of the compliance tensor. For an imposed stress, σ, (which is the case for classic propagating wave) the strain energy increases in the lossy matrix and, as a direct result, the overall damping capacity of the material is increased. This is further illustrated by examining Figure 4-11 which shows the increase in the inverse of the shear and longitudinal moduli as a function of void fraction.

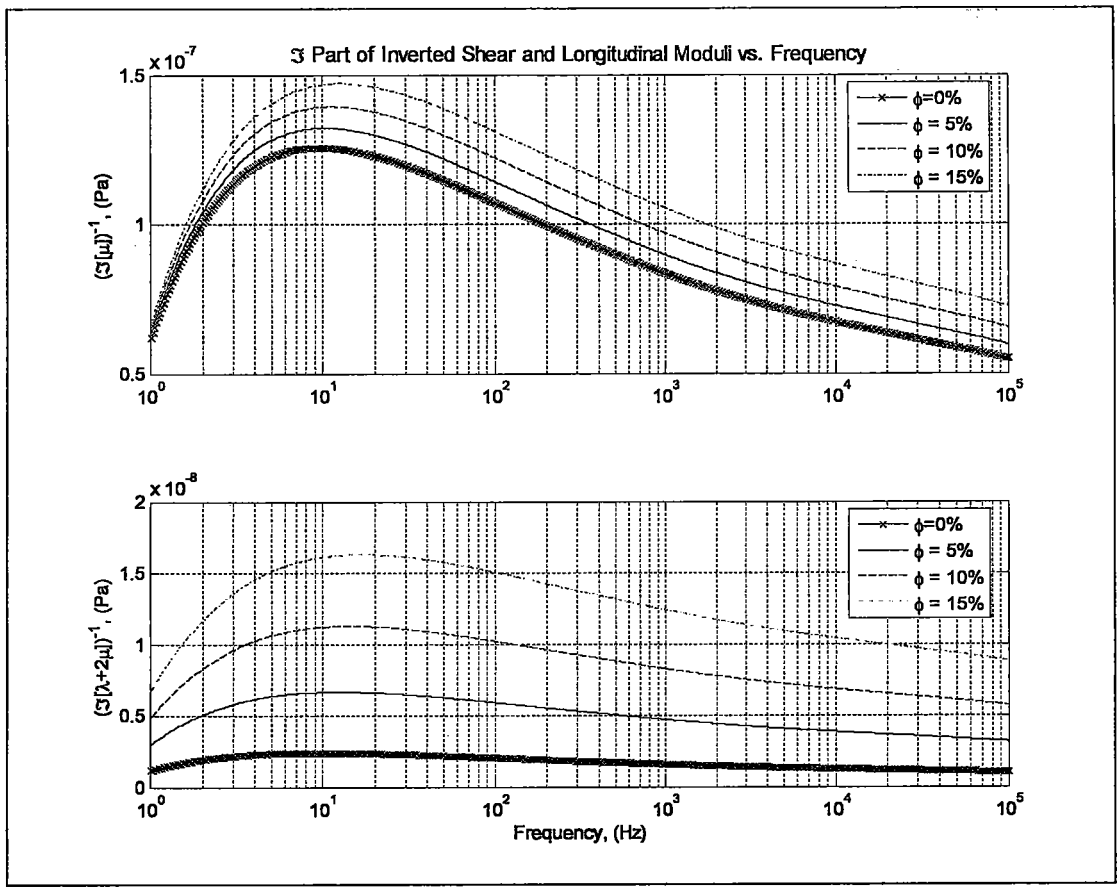

Figure 4-11: The imaginary part of the inverted shear and longitudinal moduli of a pure polymer compared with the effective behavior of three different voided composites as approximated by the SC model.

It is also important to specify that material softening increases lossy behavior for the case presented above because the imposed loading is stress controlled. However, the opposite is true when the prescribed loading is an imposed time-varying strain. An increase in the overall lossy behavior of a viscoelastic composite results from the *reinforcement* of a lossy host when loading is strain controlled since the specific strain energy is computed from $2\hat{w} = \hat{\varepsilon}_{ij}\hat{C}_{ijkl}\hat{\varepsilon}_{kl}$ in that case. *The true measure of the absolute damping capacity of a composite material is therefore not its stiffness tensor loss factor, but rather the magnitude of the imaginary part of the tensor directly related to the loading condition.* If the real part of the stiffness tensor is constant, an increased stiffness loss factor is a sufficient measure of composite damping capacity. For wave propagation in complex composites, however, the most

accurate measure of damping capacity is the imaginary part of the effective compliance tensor and related terms. The following section presents a measure related to the compliance of a composite material, the Transmission Loss (TL). Estimates of the effective complex moduli for a composite consisting of a viscoelastic matrix containing coated micro-inclusions are compared with experimental data from Baird *et al* [76]. Parametric studies on inclusion geometry and orientation are also given.

4.3.2 Comparison of modeling results with experimental TL data: Oriented ellipsoidal inclusions

The following quasi-static SC model verification is a sound isolation application. SC model estimates of the effective complex moduli of a viscoelastic composite are used to calculate the TL of a material layer as a function of frequency. The SC estimates of the TL are compared to experimental data and the low *ka* scattering model of Baird *et al* [76]. Following this comparison, parametric studies of the inclusion geometry effects on the spatial dependence of composite material lossy properties are presented in order to explore SC model strengths.

The following analysis details how the TL of a slab of viscoelastic composite material is calculated from the effective material properties. TL is a measure of the sound isolation provided by an obstruction between a sound source and receiver. Specifically, TL is the ratio of the incident wave energy to the energy transmitted through an obstruction, in this case the composite material layer [3]. Assume that a submerged composite material layer is subjected to a normally incident plane wave. The magnitude of the incident, reflected, and transmitted pressures can be calculated by requiring continuity of pressure and velocity at the two water-composite interfaces represented by $x_3 = 0$ and $x_3 = L$ in Figure 4-12.

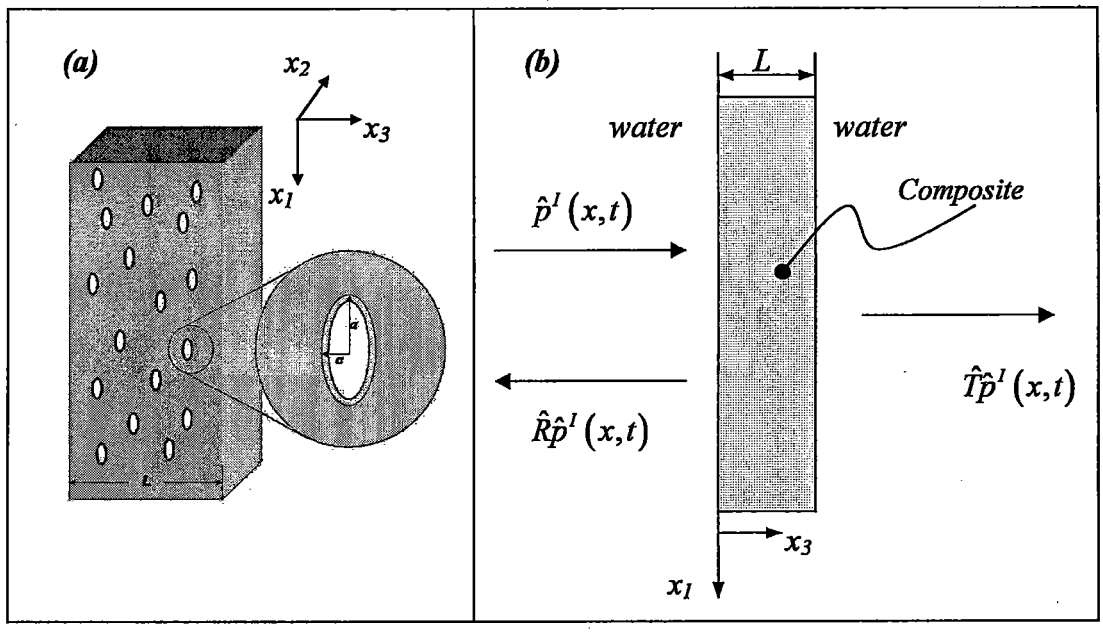

Figure 4-12: (a) Representation of a viscoelastic matrix slab containing identically oriented ellipsoidal inclusions. (b) Incident, reflected, and transmitted plane-wave visualization used to calculate the TL of the composite material layer.

In the figure above, $\hat{p}^I$ is the magnitude of the incident pressure, $\hat{R}$ is the reflection coefficient, $\hat{T}$ is the transmission coefficient, L is the thickness of the composite, and a and c represent the major and minor axes of the oriented oblate coated inclusions.

Consider an isotropic fluid medium described by a mass density ρ and sound speed c_s in which an acoustic plane wave of the form $e^{i(\hat{k}x_3-\omega t)}$ is normally incident on an infinitely long slab of thickness L, as shown in Figure 4-12b. The composite is composed of a viscoelastic matrix material described by the complex Lamé constants, $\hat{\lambda}_M$ and $\hat{\mu}_M$, a density ρ_M and contains coated ellipsoidal inclusions. This initial study considers the orthotropic case of a slab containing oblate spheroidal inclusions all oriented such that their minor axes are along the x_3 direction of propagation. The inclusions are defined by their Lamé constants $\hat{\lambda}_I$ and $\hat{\mu}_I$ and a density ρ_I, and the coating by $\hat{\lambda}_C$ and $\hat{\mu}_C$ and density ρ_C. The coating has a thickness Δa where $\Delta a/a$ is assumed to be much less than unity. It is further assumed that $\Delta a/a = \Delta c/c$. For plane

wave transmission in the x_3 direction through a composite material slab submerged in water, the TL, in decibels, is defined in terms of the transmission coefficient $\hat{T}$ by Equations (IV.3.3) – (IV.3.7) [105] :

$$TL = -10\log_{10}(\hat{T}\hat{T}^*) \tag{IV.3.3}$$

$$\hat{T} = 2\left[2\cos(\hat{k}_{33}^{eff}L) - i\left(\frac{\hat{Z}_{33}^{eff}}{(\rho c_s)^{water}} + \frac{(\rho c_s)^{water}}{\hat{Z}_{33}^{eff}}\right)\sin(\hat{k}_{33}^{eff}L)\right]^{-1} \tag{IV.3.4}$$

The effective wavenumber of the composite material in the x_3 direction is given by

$$\hat{k}_{33}^{eff} = \omega\sqrt{\frac{\rho^{eff}}{\hat{M}^{eff}}} = \hat{k}_{33}^{\prime eff} + i\hat{\alpha}_{33}^{eff} \tag{IV.3.5}$$

and the effective density and impedance of the composite are, respectively,

$$\rho^{eff} = \rho^M - \phi\left[\rho^M - \rho^C\left(3\frac{\Delta a}{a}\right) - \rho^I\left(1 - 3\frac{\Delta a}{a}\right)\right] \tag{IV.3.6}$$

and

$$\hat{Z}_{33}^{eff} = \rho^{eff}\hat{c}_{33}^{eff} = \sqrt{\hat{M}^{eff}\rho^{eff}} \tag{IV.3.7}$$

In the above equations, $\hat{M}^{eff} = \hat{C}_{33}^{eff}$ is the complex plane wave modulus of the material in the direction of wave propagation, $\hat{c}_{33}^{eff}$ is the longitudinal phase velocity in the x_3 direction, $\hat{\alpha}_{33}^{eff}$ is the longitudinal wave amplitude attenuation coefficient in the x_3 direction, ϕ is the volume fraction of coated inclusions, $(\rho c_s)^{water}$ is the specific

acoustic impedance of water known to be 1.5×10^6 Rayl, and the asterisk denotes the complex conjugate.

It was previously shown that micromechanical models can be used to approximate the global dynamic behavior of isotropic three phase lossy composites in the low frequency, or quasi-static, regime [53]. In that study, viscoelastic composite materials were created by introducing various volume fractions of spherical ($a/c = a/b = 1$) coated inclusions into the "stiff" matrix material whose properties are given in Table 4-1. The TL resulting from layers of these viscoelastic composite materials were measured for frequencies ranging from 0 to 100 kHz by Baird *et al* [76]. TL estimates were calculated using the low *ka* limit scattering model introduced by Baird *et al* (BKT) and the coated inclusion SC model derived in Chapter III. The results have been reproduced in Figure 4-13. These plots replicate Figures 2 – 6 of reference [76] but add SC model estimates. Two facts are readily apparent from inspection of these plots. First, the quasi-static SC model is shown to have good agreement with the low frequency scattering model. Second, the SC model provides accurate estimates of frequency dependent lossy behavior as a function of both the frequency and the coated inclusion volume fraction.

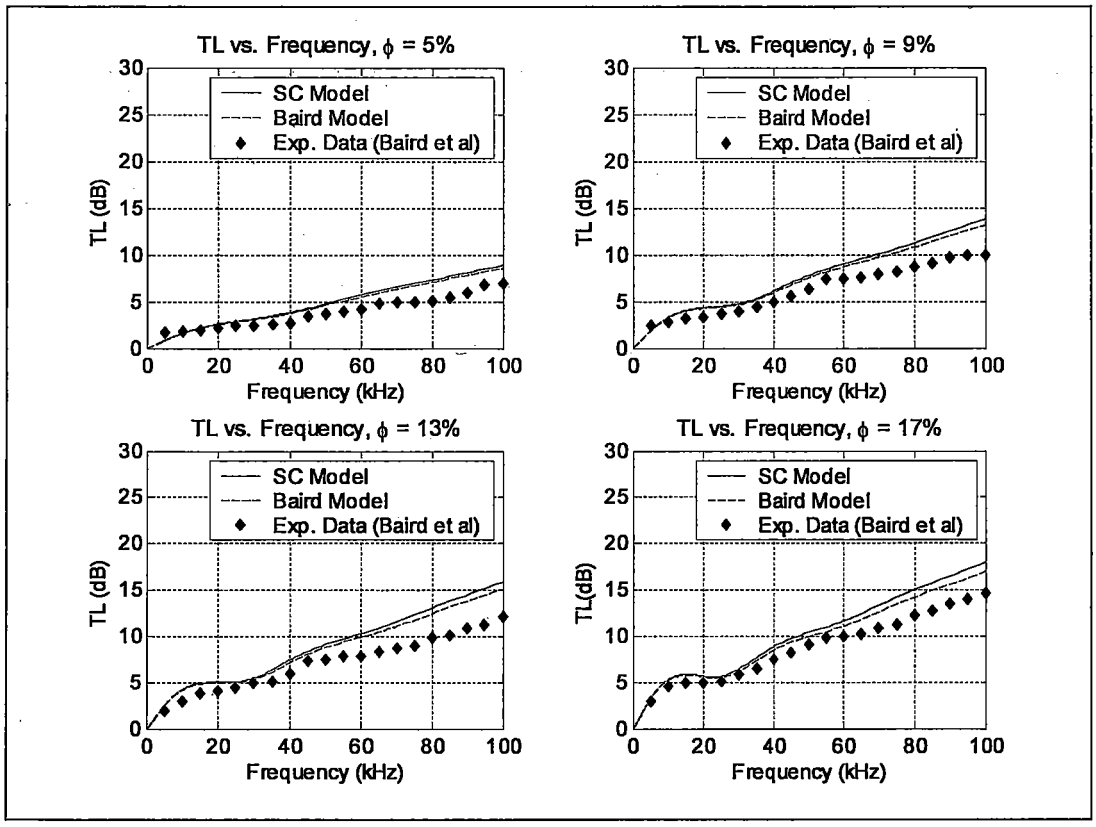

Figure 4-13: SC and BKT model estimates of TL for a 1 cm thick slab of viscoelastic composite submerged in water. Experimental data taken by Baird *et al* [76].

Quasi-static SC model precision results from the fact that it accurately approximates the mechanisms dominating the response of a particulate composite material to time-varying loading. Namely, the micromechanical approach takes small strains in the neighborhood of an inclusion into account using the well-developed homogenization techniques of strain localization and volume averaging. This approach therefore accounts for losses occurring during wave propagation in a direct manner by calculating strain rather than through asymptotic scattering approximations. This approach has the added advantage of being easily amenable to the modeling of anisotropic composite material behavior resulting from preferentially oriented non-spherical inclusions or anisotropic constituent phases.

The next section employs the SC model to approximate sound transmission through a viscoelastic composite slab containing a fixed volume fraction of coated oblate inclusions in order to observe the effect of varying aspect ratios. The constituent materials are the same as those employed by Baird *et al* [76] for the case

of a stiff matrix. Figure 4-14 plots the TL as a function of frequency for a fixed coated inclusion volume fraction calculated using the SC model for identically oriented inclusions as shown in Figure 4-12(a).

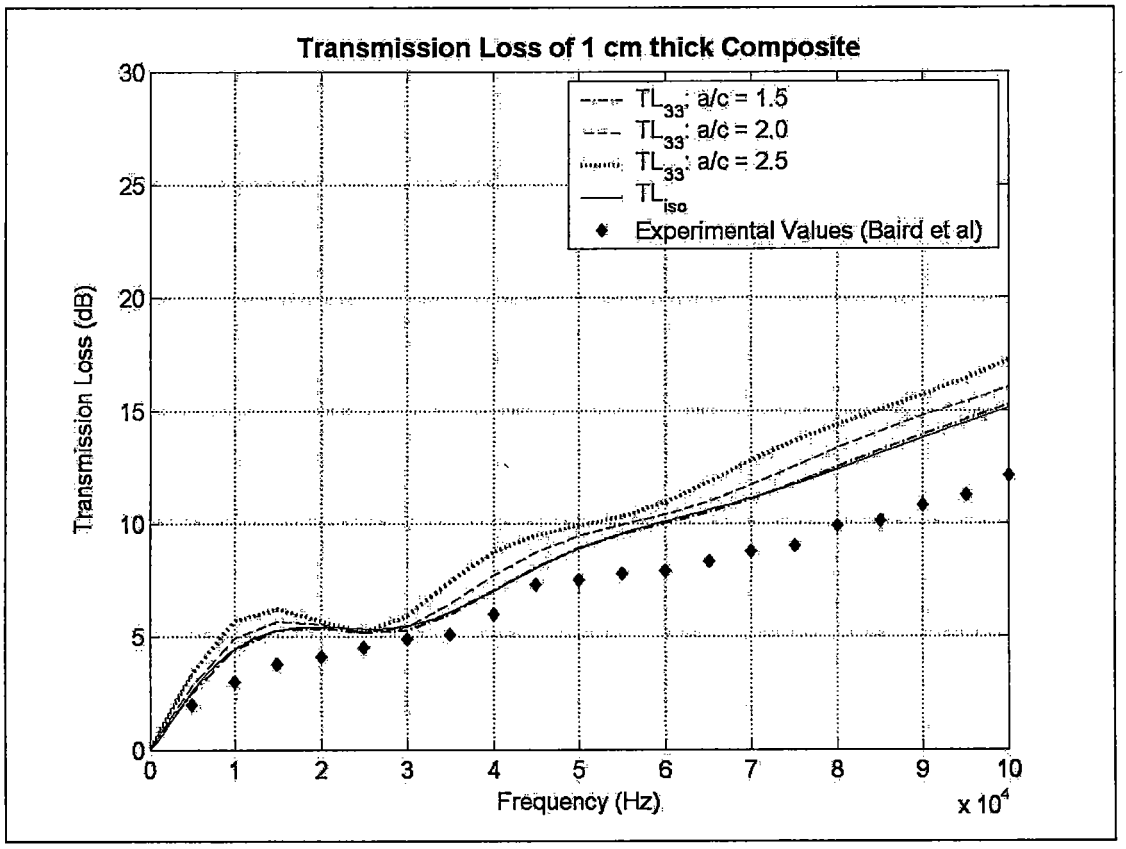

Figure 4-14: Transmission loss of 1 cm thick slab of composite material oriented as shown in Figure 4-12(a) and containing 13% by volume of oblate coated inclusions of varying aspect ratios. —— $a/c = 1$, —.- $a/c = 1.5$, - - - $a/c = 2$, ... $a/c = 2.5$.

Oscillations in TL observed at the lower frequencies are the result of thickness resonances. Maximum transmission, i.e., minimum TL, occurs at the half-wavelength resonances while maximum transmission losses occur at the odd quarter wavelength resonances. It is observed that increasing the aspect ratio *a/c* results in a small increase in TL (less than 2 dB in the 0 to 100 kHz range) because of the increased shear strain in the neighborhood of the inclusion caused by its form. In other words, for the same traveling compressional stress wave field, more deformation occurs in the neighborhood of the oblate inclusions as compared to the spherical inclusions. Thus more mode conversion to shear occurs, inducing increased losses. This trend is

also confirmed by plotting the attenuation coefficient, $\hat{\alpha}^{eff}$, of the longitudinal wave number as a function of the angle in the x_1-x_3 plane, as shown in Figure 4-16. The angle is the polar angle, here denoted as θ, in spherical coordinates. The plot shows the attenuation coefficient for a longitudinal wave traveling in the direction, **n**, defined as $\mathbf{n} = \langle \sin\theta\cos\varphi\,\hat{\mathbf{i}}, \sin\theta\sin\varphi\,\hat{\mathbf{j}}, \cos\theta\,\hat{\mathbf{k}} \rangle$ where φ is the azimuthal angle, in an infinite medium containing oriented ellipsoidal inclusions oriented as shown in Figure 4-15.

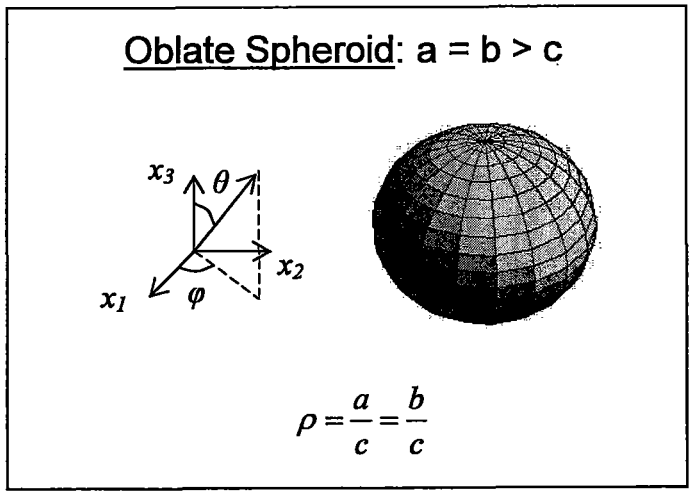

Figure 4-15: Geometry of oblate spheroids and their orientation with respect to the global coordinate system.

It is in this way that the influence of changing the orientation of inclusions with respect to the coordinate system shown in Figure 4-12a is studied. It is interesting to note that changing the incident direction, **n**, as described above is equivalent to fixing the incident direction of the plane wave and rotating the oblate inclusions about the x_2-axis. The attenuation coefficient in the x_1-x_3 plane ($\varphi = 0$) as a function of polar angle is calculated from Equation (IV.3.8).

$$\hat{\alpha}^2(\theta) = \hat{\alpha}_{11}^2 \sin^2\theta + \hat{\alpha}_{33}^2 \cos^2\theta \qquad \text{(IV.3.8)}$$

Figure 4-16 shows that both the attenuation coefficient (in Np/m) and the anisotropy factor, defined as $(\hat{\alpha}_{11} - \hat{\alpha}_{33})/\hat{\alpha}_{33}$, increase as the aspect ratio increases. One interesting point is that as the polar angle increases, the attenuation coefficient is also seen to increase. Here it is noted that there are competing factors which tend to increase or decrease the lossy behavior with respect to the polar angle. These competing factors are the effective shearing area of the inclusions, which depends on inclusion form, and the increase or decrease in effective material stiffness of the composite due to coated-inclusion properties. For the case shown in Figure 4-16, the oblate form of the inclusions increases the shearing area parallel to the propagation direction. This tends to increase the lossy properties of the composite and results in an increase in the composite material's damping capacity, described here by the attenuation coefficient, as a function of polar angle.

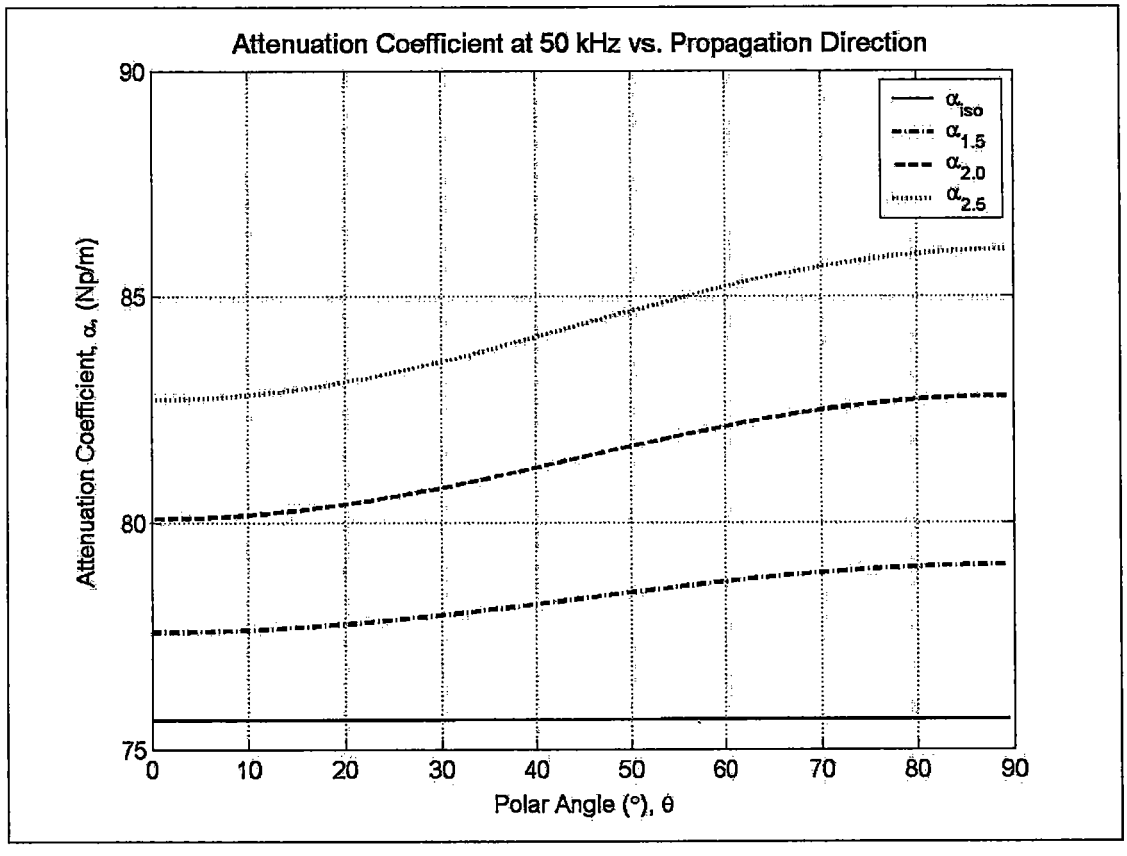

Figure 4-16: Attenuation coefficient as a function of angle in the x_1-x_3 plane of material containing oblate ellipsoidal inclusions of varying aspect ratios ($\theta = 0$ coincides with x_3-axis). The volume fraction of inclusions is 13% and the frequency of the incident wave is 50 kHz. —— $a/c = 1$, —.— $a/c = 1.5$, - - - $a/c = 2$, ... $a/c = 2.5$.

In the example given below, that of prolate and penny shaped Lucite inclusions, the opposite trend is observed as the inclusion and coating material properties lead to an overall increase in stiffness which will dominate the increase in shearing area related to inclusion geometry. Staying with the oblate inclusion example, Figure 4-17 plots the real and imaginary parts of the complex wave speed in the x_3 -direction as a function of frequency for aspect ratios a/c = 1, 1.5, 2.0, and 2.5, again for a fixed volume fraction $\phi = 0.13$. The results show another aspect of the change in inclusion form, specifically that for a fixed frequency, the real part of the phase velocity decreases with increasing aspect ratio. This corresponds to a relative softening of the composite in the x_3-direction as the aspect ratio increases. The softening, a result of oblate inclusion geometry, increases the specific strain energy in the neighborhood of the inclusion for the same imposed stress levels. At the same time, for single frequency, the absolute value of the imaginary part of the phase velocity also decreases with increasing aspect ratio. This decrease in the imaginary part is proportionally less than the decrease of the real part and therefore corresponds to an increase in attenuation in the x_3-direction for the oblate geometry. Otherwise stated: the magnitude of the imaginary part of the inverted plane wave modulus along x_3 increases with increasing aspect ratio. As discussed in Section 4.3.1, this causes an increase in the specific strain energy for a fixed value of imposed stress, thereby increasing the absorptive qualities of the composite along x_3.

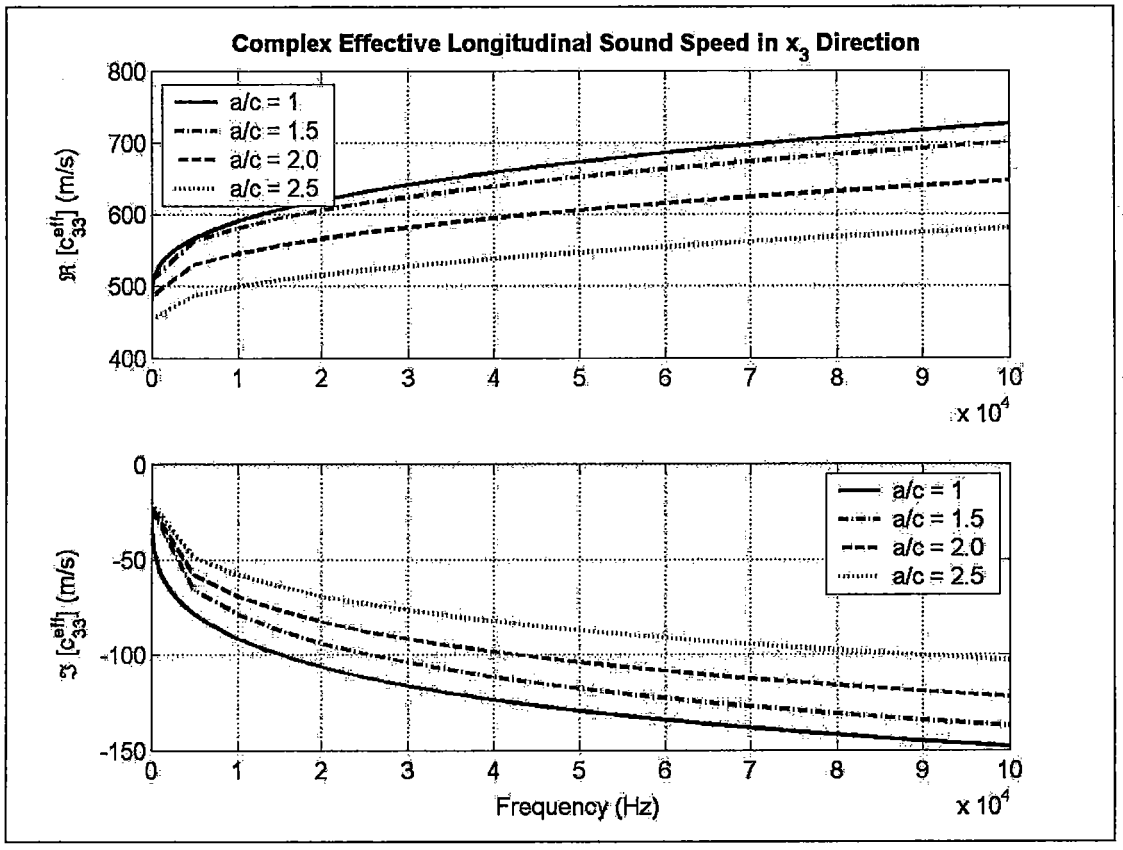

Figure 4-17: Real and imaginary parts of effective complex longitudinal wave speed in x_3-direction as function of frequency for a volume fraction inclusions of 13%. —— $a/c=1$, —·— $a/c=1.5$, - - - $a/c=2$, ... $a/c=2.5$.

The above discussion is for a specific case of a viscoelastic matrix containing oblate coated inclusions. The SC model is more general, however, and can be used to study the effects of prolate, needle shaped, and penny shaped inclusions (along with any variation of these forms). In what follows, the SC model is applied to the case of composite material composed of the same "stiff" viscoelastic matrix material containing inclusion and coating materials with the properties given in Table 4-2. This parametric study investigates the effects of such geometries on the overall damping properties of the composite.

Table 4-2: Material properties of coating and inclusion for material modeled in Figure 4-18.

	μ (GPa)	ν	ρ (kg/m^3)
Coating	1.40	0.40	1200
Inclusion	28.5	0.23	2300

To display the SC model's capabilities, five types of inclusions are considered: spherical, oblate, prolate, penny-shaped, and needle-shaped ellipsoids. Table 4-3 gives the minor radius ratios, *a/b* and *a/c*, for each of these cases.

Table 4-3: Minor radius ratios for composite modeled in Figure 4-18.

	Sphere	*Oblate*	*Penny*	*Prolate*	*Needle*
a/b	1	1	1	1	1
a/c	1	3	10	$\frac{1}{3}$	$\frac{1}{10}$

Figure 4-18 shows the variation of the calculated attenuation coefficient in the $x_1 - x_3$ plane as a function of polar angle. Minimum attenuation observed coincides with propagation along the x_3-axis ($\theta = 0$) for a composite containing needle shaped inclusions aligned with this axis. For the same composite, attenuation increases monotonically with increasing angle between incident plane wave and the long-axis of the needle shape inclusions. This plot also shows that attenuation diminishes for propagation along the x_1-axis (and therefore, by symmetry, the x_2-axis) of a composite containing penny-shaped inclusions whose large radii (a and b) are aligned with the x_1-x_2 plane. It was previously mentioned that this decreasing attenuation is the result of increased stiffness in the direction that coinciding with the long major axes when the composite inclusion has a higher stiffness value than the matrix. For the present material studied, this affect dominates the increase in shearing area due to inclusion geometry. Using the specific strain energy argument, the increase in composite material stiffness in certain directions decreases the strain specific energy for stress wave of fixed magnitude propagating in the same direction. This reasoning also explains why the attenuation coefficient anisotropy factor of the oblate and penny shaped inclusions is higher than for the needle shaped inclusions. The oblate form of those inclusions renders the increase in shearing area increasingly influential with respect to the reinforcement it imparts to the composite. For the oblate and penny-shaped inclusions the increase in stiffness still dominates but the effects are reduced

because the shearing area is significantly higher in this form of inclusion (compared to the needle-shape).

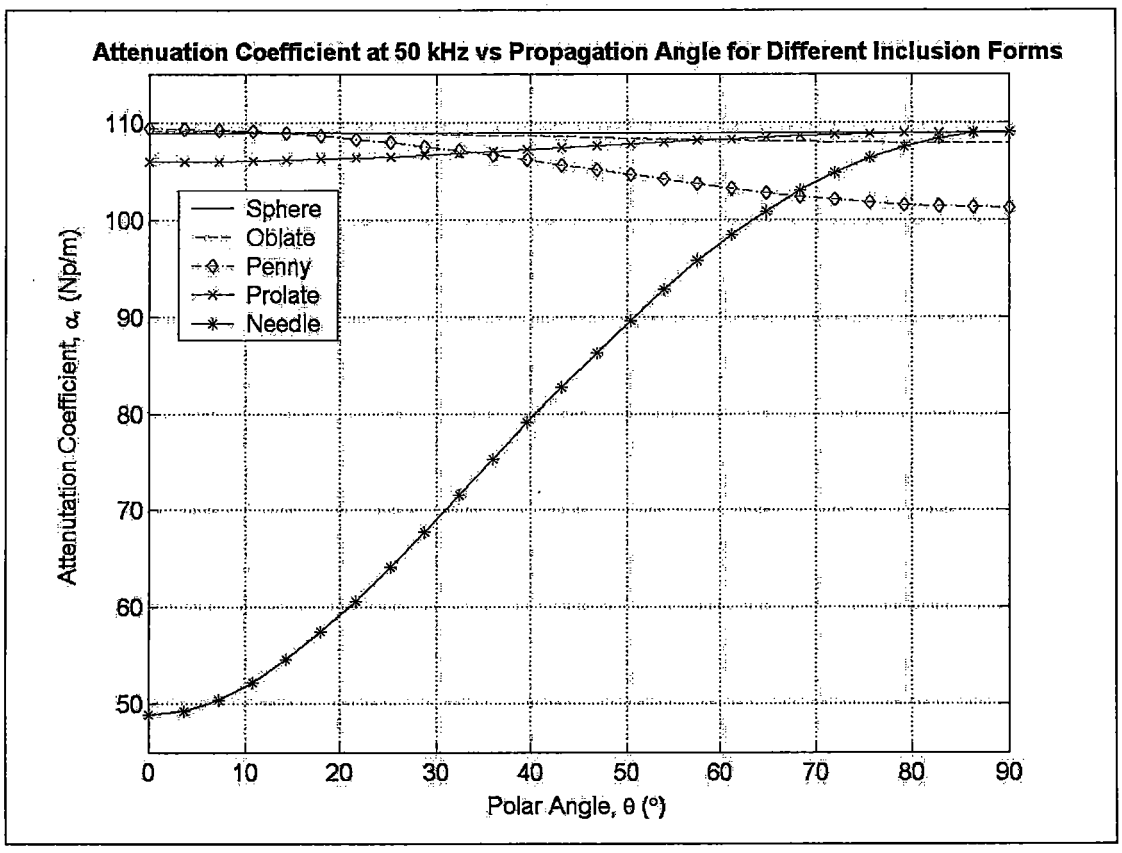

Figure 4-18: Attenuation coefficient as a function of angle in the x_1-x_3 plane for a composite consisting of a viscoelastic matrix with Lucite coated glass ellipsoidal inclusions of different forms ($\theta = 0$ coincides with x_3-axis). The volume fraction of inclusions is 10% and the frequency of the incident wave is 50 kHz.

As expected, the composite containing spherical inclusions has a constant attenuation regardless of propagation direction, and the oblate and prolate inclusion cases fall somewhere between the limits of the penny-shape and needle-shape inclusions, respectively. One point of interest is that the attenuation coefficient for propagation along the x_3 axis for materials containing both oblate and penny-shaped inclusions is slightly superior to that of the material containing spherical inclusions. An explanation of this behavior is that the shape of the inclusion leads to stronger mode conversion at the boundaries resulting from stress concentrations related to the inclusion form.

At this point it is interesting to point out that all of the factors discussed above give a few guidelines for the design of composite materials having a desired lossy behavior. First, if inclusions are softer than the matrix material, increased inclusion aspect ratios lead to increased damping capacity in all directions as compared to the same inclusion volume fraction of spherical inclusions. The highest losses will be observed in directions perpendicular to the outward normals of increased shear areas. This is illustrated with the oblate inclusion case shown in Figure 4-16. Secondly, if stiffness is required in one direction while high losses are desired in an orthogonal direction, high modulus needle shaped inclusions are an ideal solution (see Figure 4-18). This type of inclusion leads to low losses and high reinforcement along the longest inclusion minor axis but maintains lossy behavior nearly identical to spherical inclusions, which is double the attenuation observed along the longest axis, for propagation in all directions perpendicular to that axis. Using these two cases as guidelines and the quasi-static general SC model for design, numerous types of materials of varying lossy behavior can be conceived relatively easily.

The present section explored some of the strengths of the general SC model in the quasi-static domain. The SC model used for these calculations is limited to a single inclusion form, set of material properties, and spatial orientation. Reformulation of the SC model using dilute strain concentration tensors (DSCT) permits the approximation of the behavior of many different types of viscoelastic composite materials with relative ease. It is the purpose of the following section to show the level of generality achievable through application of the SC DSCT model derived in Section 3.3.

4.3.3 Identical coated inclusions with a known orientational distribution

The most common application of dilute strain concentration tensors cited in literature is the approximation of the globally isotropic material properties of

composites containing identical non-spherical inclusions having a uniform orientation distribution. The generality of Equation (III.3.33), however, permits the homogenization of composites containing non-spherical inclusions with a preferential orientation distribution just as easily as for the case of a uniform distribution. This is done by taking the approach discussed below. First the orientational average or a fourth order tensor quantity is defined in the following equation [56].

$$\{B_{ijkl}\} = \frac{1}{\alpha}\int_{\Omega} p(\Omega) a_{im} a_{jn} a_{kp} a_{lq} B_{nmpq} d\Omega \qquad \text{(IV.3.9)}$$

In this expression, α is an integration factor, a_{ij} is the rotation matrix determined by the appropriate Euler angles, θ, φ, and ψ, **B** is a fourth order tensor defined with respect to its local coordinate system, $\{\mathbf{B}\}$ is the orientational average of the same tensor with respect to the global coordinate system, Ω is the orientational space defined by the Euler angles, and $p(\Omega)$ is the orientation distribution function. It is now useful to define a normalized distribution function, $n(\Omega)$:

$$n(\Omega) = \frac{p(\Omega)}{\alpha} = \frac{p(\Omega)}{\int_{\Omega} p(\Omega) d\Omega} \qquad \text{(IV.3.10)}$$

Equation (IV.3.10) defines a distribution which has the desirable property that its integral over the entire orientation space is unity. Substituting Eq. (IV.3.10) into Eq. (IV.3.9) yields:

$$\{B_{ijkl}\} = \int_{\Omega} n(\Omega) a_{im} a_{jn} a_{kp} a_{lq} B_{nmpq} d\Omega \qquad \text{(IV.3.11)}$$

Now, in order to find the effective properties of a composite containing ellipsoidal inclusions with a known orientation distribution and a known inclusion and coating

volume fraction (f^I and f^C, respectively), it is helpful to define the following tensor quantity.

$$\hat{\mathbf{C}}^{loc} = f^I\left(\hat{\mathbf{C}}^I - \hat{\mathbf{C}}^M\right):\hat{\mathbf{A}}^I + f^C\left(\hat{\mathbf{C}}^C - \hat{\mathbf{C}}^M\right):\hat{\mathbf{A}}^C \qquad \text{(IV.3.12)}$$

$\hat{\mathbf{C}}^{loc}$ is simply the last two terms of Equation (III.2.73) and is calculated by the SC model with respect to the local coordinate system for the family of inclusions having the same orientation in space. Then, when all coated inclusions in the composite are assumed to have identical shape and material properties, the effective material properties of the composite can be found by taking the orientational average of $\hat{\mathbf{C}}^{loc}$ and adding it to the matrix stiffness tensor, $\hat{\mathbf{C}}^M$, as follows:

$$\hat{C}^{eff}_{ijkl} = \hat{C}^M_{ijkl} + \sum_{\theta}\sum_{\phi}\sum_{\psi} n(\theta,\phi,\psi)\, a_{im}a_{jn}a_{kp}a_{lq}\hat{C}^{loc}_{nmpq}\Delta\theta\Delta\phi\Delta\psi \qquad \text{(IV.3.13)}$$

Equation (IV.3.13) is a general expression that permits the calculation of the effective properties of a composite consisting of identical oriented coated inclusions such as those studied by Haberman *et al* [50], randomly oriented inclusions such as for the composites studied by Berryman [51], and for any known preferential orientation distribution such as can be observed in shale material studied by Hornby *et al* [78] by selection of the appropriate orientation distribution. Equation (IV.3.12) for $\hat{\mathbf{C}}^{loc}$ is not, in general, an analytical expression and therefore the evaluation of the integral is approximated by a summation in Equation (IV.3.13).

4.3.3.1 Approximation of globally isotropic properties

The section presents an initial verification of the generalized SC model using concentration tensors. The verification is simply a check on the agreement between

the SC DSCT model and Berryman's model [51] for the case of ellipsoidal inclusions having a uniform orientation distribution. The effective compressional and shear wave speeds in the materials studied by Berryman have been reproduced for the prolate and oblate inclusion cases (see Figures 5b, c and 6b, c of reference [51]) in Figure 4-19 and Figure 4-20, respectively. The materials studied are suspensions of either prolate ($a/b = a/c = 10$) or oblate ($a/b = 1;\ a/c = 10$) rock particles in water. The rock material is assumed to have the bulk and shear moduli $K_r = 44.9(1\text{-}0.004i)$ GPa and $\mu_r = 37.9\ GPa$, respectively and a density of $\rho_r = 2700\ kg/m^3$ while the same properties for water are $K_w = 2.18\ GPa$, $\mu_w = 1\text{-}i682\ Pa$, and $\rho_w = 1000\ kg/m^3$. The shear modulus of water is assumed to be lossy in accord with Berryman's paper and a very small (but non-zero) value is assigned to the real part in order to avoid singularity problems with calculation of the strain localization tensor, $\hat{\mathbf{A}}^1$, in the SC DSCT model.

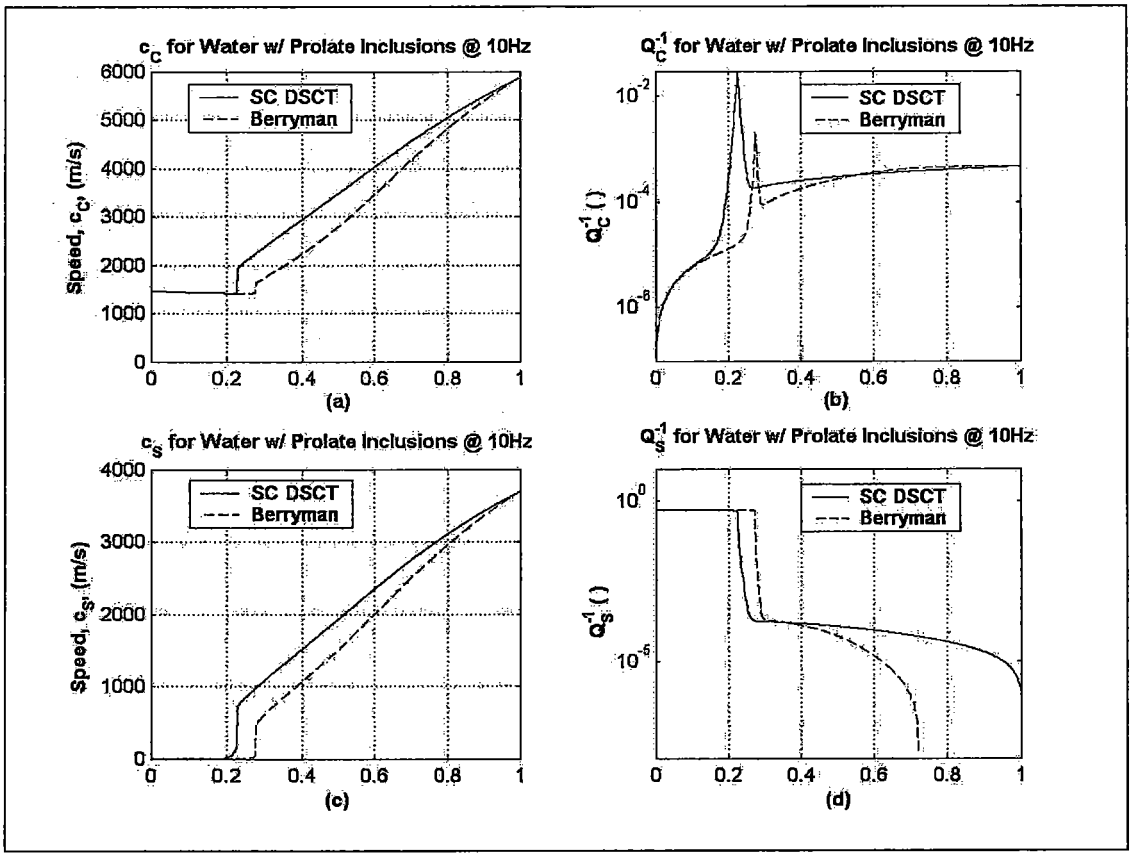

Figure 4-19: Compressional and shear wave speeds and Q^{-1} values as a function of volume fraction calculated using the SC DSCT model and Berryman's model [51] for the case of prolate rock inclusions in water where a/b = a/c = 10.

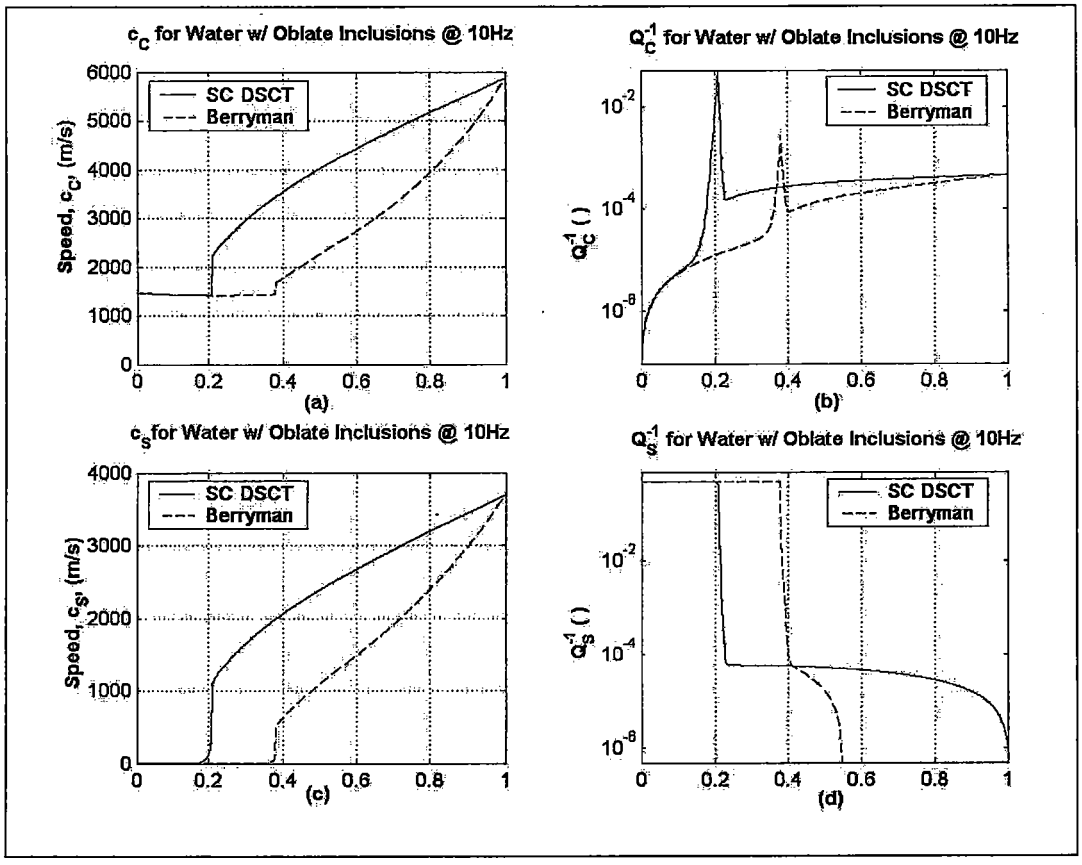

Figure 4-20: Compressional and shear wave speeds and Q^{-1} values as a function of volume fraction calculated using the SC DSCT model and Berryman's model [51] for the case of oblate rock inclusions in water where a/b = 1 and a/c = 10.

These plots illustrate that the behavior modeled by the SC DSCT model and Berryman's model (which were reproduced for reference using the equations (32) and (33) along with the appendix of reference [51]) is qualitatively similar though there are some significant quantitative differences. Firstly, the real parts of both the compressional and shear wave speeds (c_C and c_S respectively) are nearly constant as a function of volume fraction up to a certain concentration where the effect of the rock inclusions begins to have a marked effect on the global behavior and a sharp increase in both wave speeds is observed. It is important to point out that the sharp increases in effective sound speed observed at specific model dependent concentration levels have a physical significance and that the apparent jump (or discontinuity) is due to the numerical evaluation. The sharp increase in sound speed is directly related to the fact that the elastic constants of the constituent phases differ by several orders of magnitude. When the matrix material is significantly softer than that of the inclusion,

many models will predict a similar sharp increase in the effective elastic constants at some level of concentration. This occurs at some concentration level that represents the point at which the reinforcement of the stiffer phase becomes important and, because the high contrast between the materials is high, the result is a sharp increase in effective elastic properties as a function of volume fraction. Berryman refers to this concentration as the "threshold of rigidity" and gives an excellent discussion of the physics of the modeled behavior in Section V of reference [122] in terms of different modeling approaches. Physically it is obvious that regardless of the abruptness of this transition, there can never be a true jump in material properties as a function of the volume fraction of constituent materials. Indeed, the magnitude of the observed "jump" decreases as the step size used for evaluation decreases leaving instead a very steep slope which is exacerbated by the implicit nature of the self-consistent model [122]. Smaller concentration steps have not been employed in order to reduce calculation time and because this behavior can be explained in terms of physical phenomena and the modeling approach. It is important to note that the specific volume fraction corresponding to the threshold of rigidity varies depending on the inclusion aspect ratio and the elastic contrast of the constituents for both the SC DSCT model and Berryman's model.

The threshold of rigidity discussed above coincides with another observation, the presence of a singularity in the values of $\hat{Q}_c^{-1}$ associated with the compressional wave number for the same rock concentration value. $\hat{Q}_c^{-1}$ is related to the damping quality of the composite and calculated from the expression $\hat{k}_{c,s} = \hat{k}'_{c,s} + i/2\hat{Q}_{c,s}$, where $\hat{k}_{c,s}$ is the complex compressional or shear wave number of the effective material, indeed $\hat{Q}_{c,s}^{-1} = 2\hat{\alpha}_{c,s}$. Importantly, both the micromechanical SC DSCT model and Berryman's model show this result. For the case of prolate inclusions, the SC DSCT formulation shows the singularity at $\approx 23\%$ rock, whereas Berryman's model displays this singularity at a concentration of $\approx 30\%$ and for the case of oblate inclusions these

values are ≈21% using SC DSCT and ≈38% using Berryman's model. Though the location of the singularity in the SC DSCT model is different from that modeled by Berryman, the behavior, as described at length by Berryman [122], is non-physical in both cases and is due uniquely to SC modeling's implicit solution formulation for composites consisting of materials with such high contrast between elastic constants. Here it is stressed, as was pointed out by Berryman [122], that the lossy component of the effective wave speeds are over predicted near this singularity and that this is a weakness of the SC modeling approach for high contrast composites. More importantly, the trends of the DSCT formulation for the SC coated inclusion model agree well with Berryman's accepted model. Indeed Berryman's SC relations were derived by using the orientational averages of Wu's "*T*-matrix" formulation [28] (which is based on Eshelby's solution) for the case of a uniform distribution of orientation of ellipsoidal inclusions. The two approaches are therefore quite similar, with Berryman's formulation falling closer to the lower bound and the SC DSCT being nearer the upper bound. The large quantitative difference between the two models is due this fact coupled with the high contrast of constituent materials for this particular case. The qualitative agreement with Berryman's approach is pointed out here as a validation the DSCT formulation for implementation in the quasi-static regime when a composite material has a complex microstructure and yet displays globally isotropic behavior because the identical inclusions have a random orientation distribution.

At this point it is informative to show that the DSCT formulation can just as easily be used allow an increased degree of flexibility in modeling particulate composites that are globally anisotropic as a result of inherent material anisotropy, preferential orientation of ellipsoidal inclusions, or both. The advantage of the SC DSCT model is that modeling of such materials, which are globally anisotropic, is treated in the exact same manner as discussed above, and therefore no additional modeling complexity is added for homogenization of such composites. This is a marked improvement over Berryman's approach, which is limited to globally

isotropic materials, or the SC model, which is limited to either spherical or identically oriented inclusions. One further improvement that can be made by using the current model, since it is valid for coated inclusions, is the implementation of the generalized SC (GSC) model for the case of bi-phase composites. The GSC model, which was introduced by Christensen and Lo [45], assumes that the inclusion phase is surrounded directly by the matrix material and that entire coated inclusion is then embedded in an effective medium of unknown properties. This modification to the SC model has been shown to yield better results than the SC, Mori-Tanaka, and differential methods for increased volume fractions [154].

4.3.3.2 Approximation of globally anisotropic properties

DSCT formulation easily lends itself to computations of the effective material properties for composite materials consisting of inclusions having non-spherical geometries with a preferential orientation (neither aligned nor randomly oriented). Such microstructures can be observed in geologic materials, such as the shales studied by Hornby *et al* [78], or in fabricated materials due to manufacturing processes. This section presents a parametric study of the attenuation coefficient as a function of propagation angle in a composite consisting of prolate inclusions in a lossy matrix in order to illustrate the capability of the SC DSCT model to capture these effects.

Consider a hypothetical material consisting of a polymer matrix having the properties of the "soft" polymer characterized by Baird *et al* [76] which is assumed to be incompressible at all frequencies and containing prolate glass inclusions ($a/b = a/c = 5$, $\mu_{glass} = 28.5\ GPa$, $\upsilon_{glass} = 0.23\ GPa$, $\rho_{glass} = 2300\ kg/m^3$). The inclusions are assumed to have an axis-symmetric preferential orientation along the x_1-axis where the level of preference is fully described by a Gaussian distribution of solid azimuthal angle, θ, having an assumed standard deviation, σ_θ (see Figure 4-21).

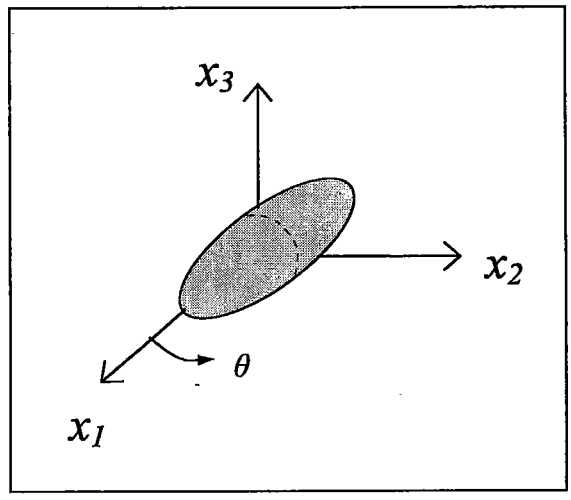

Figure 4-21: Orientation of prolate glass inclusions. θ is the azimuthal angle.

The complete orientation distribution, $n(\Omega)$, given in Equation (IV.3.10) is then defined using the normalized Gaussian distribution for the azimuthal angle, $n_{gauss}(\theta)$, as follows:

$$n(\Omega_{ij}) = n_{gauss}(\theta_i) n_{gauss}(\theta_j)$$

$$\text{where: } \theta_{i,j} \in \left[\frac{-\pi}{2}, \frac{\pi}{2}\right] \qquad \text{(IV.3.14)}$$

It is important to note that the comma in Equation (IV.3.14) *does not* denote the spatial derivative. This normalized distribution function can then be employed directly in Equation (IV.3.13) to approximate the effective properties of a material having inclusions of assumed orientational preference. This was done for a composite consisting of 10% by volume glass inclusions at a frequency of 25 kHz for five different values of σ_θ ranging from 0° (all inclusions aligned along the x_1-axis) to ∞° (uniform distribution yielding a globally isotropic composite). The results of the parametric study are given below in Figure 4-22.

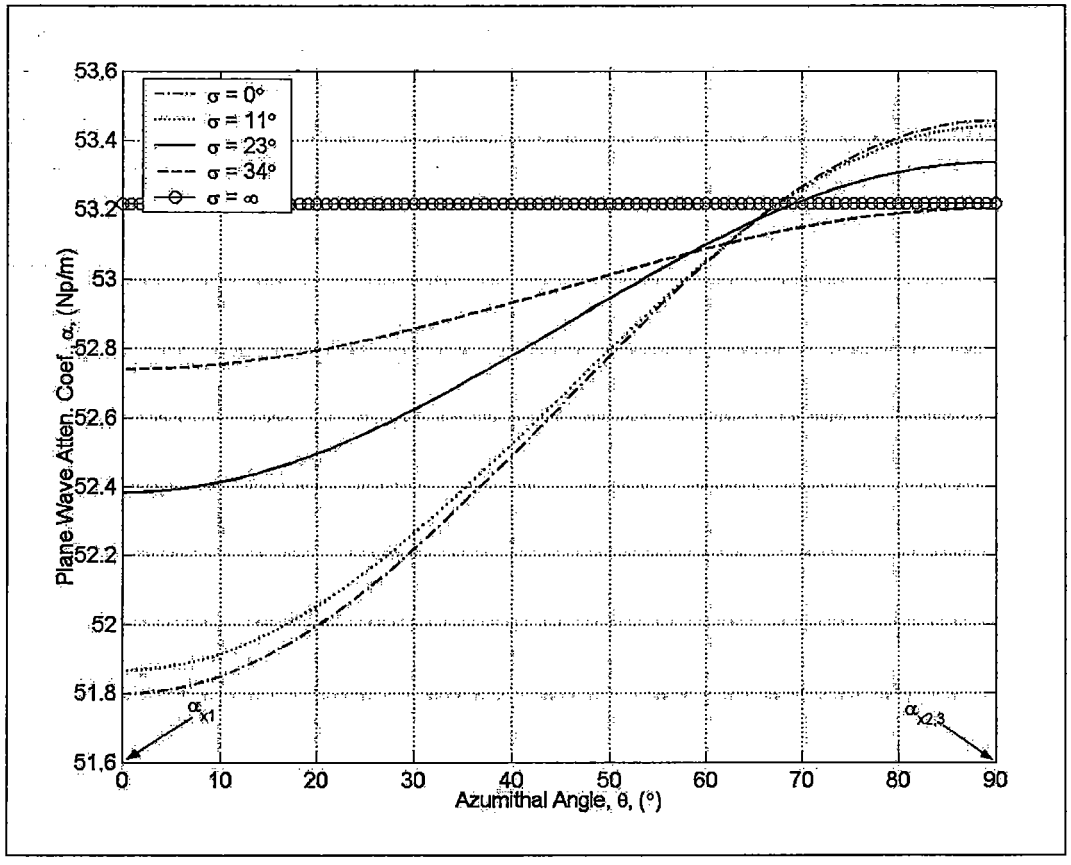

Figure 4-22: Variation of attenuation coefficient as a function of azimuthal angle for glass/polymer composite with varying degrees of anisotropy. Volume fraction of prolate inclusions $\varphi = 10\%$, $a/b = a/c = 5$, frequency inspected $f = 25$ kHz.

Two intuitive checks are immediately obvious from the inspection of Figure 4-22. First, the magnitude of anisotropy factor, defined here as $(\hat{\alpha}_3 - \hat{\alpha}_1)/\hat{\alpha}_3$, decreases with increasing σ_θ from the case of aligned prolate inclusions ($\sigma_\theta = 0$) up to the limit of $\sigma_\theta = \infty$ where the composite is isotropic and similar to the materials studied in the previous section. Second, the minimum attenuation coefficient calculated is for propagation along the x_1-axis for the case of identically oriented glass inclusions aligned with the x_1-axis. This yields minimal attenuation because of the high-stiffness and non-lossy material behavior of the inclusions. Several other interesting points can be observed about these calculations. An interesting feature of this plot is that for highly preferential orientation distributions one observes a slightly higher value of $\hat{\alpha}$ in directions orthogonal to the x_1-axis over the uniform distribution case. This is due to the increase in strain energy brought about by stress concentration at inclusion ends

for plane wave incidence perpendicular to the major inclusion axis. Though this effect is small, it is an interesting result of orientational preference. It also illustrates the effects that can be captured by the quasi-static SC DSCT model that relate stress concentration due different inclusion geometries and orientation distributions to the macroscopic damping capacity of a viscoelastic composite. This parametric study clearly shows the capability of the SC DSCT model to capture the variation of anisotropy depending on orientational preference of like inclusions. Since, either as a natural occurrence or due to inherent variability in processing techniques, very few real materials have identically oriented particulate inclusions this additional flexibility is very useful. Indeed, the case study below shows a potential application of this specific capability.

4.3.3.3 Comparison with experiment

The effective elastic constants of the shale material studied by the Hornby *et al* [78] are approximated here using the SC DSCT model as a case study. The shale can be broadly described as a composite material consisting of a load bearing water-filled porous clay containing three distinct "spherical" mineral inclusion phases (quartz, feldspar, and pyrite) of different concentrations (see Figure 4-23). For a more detailed description of the composition of the material see reference [78].

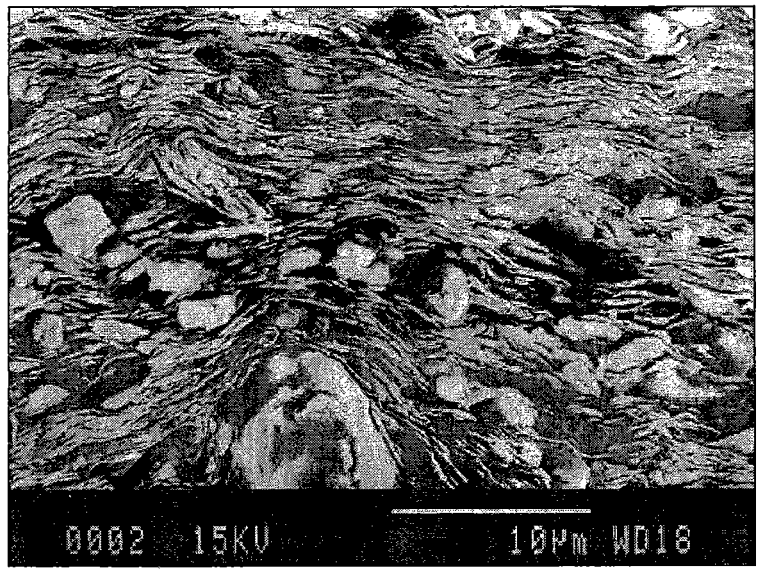

Figure 4-23: Micrograph of shale studied by Horby *et al* [78] (image from reference).

The porous clay itself is best described by fully-connected oblate clay platelets with a preferential orientation distribution (axis-symmetric about the x_3-axis) arranged such that ~11% porosity remains. For modeling purposes, it is assumed that the water-filled pores can conversely be considered as oblate inclusions ($a/b = 1$, $a/c = 20$) with preferential orientation (axis-symmetric about the x_3-axis) in an otherwise continuous isotropic clay matrix of known properties given in reference [78]. The material properties used here are summarized in Table 1 and were taken from various sources (Mavko *et al* [155] and Merkel *et al* [156],) since not all constituent phase properties were specified in reference [78].

Table 4-4: Material properties of the constituent phases of shale studied by Hornby et al. Material data taken from various sources: clay [78], quartz and feldspar [155], pyrite [156].

	K (GPa)	*μ (GPa)*	*ρ (kg/m³)*	*φ (%)*
Clay	22.9	10.6	1826	---
Water	2.2	1×10^{-6}	1000	11
Quartz	36.4	45.0	2640	53
Feldspar	75.6	25.6	2630	11
Pyrite	103.7	109	5015	9

Hornby *et al*'s approximation of the effective properties of shale studied was done in three different homogenization steps. First, the effective fluid-clay composite was approximated as a transversely isotropic clay medium with 11% oblate water-filled

pores. An orientational average was then taken of this medium by employing the spatial distribution of pore orientation (approximated from micrographs of the shale) yielding the effective properties of the fluid-clay matrix. Finally, the spherical mineral phases were added to this effective fluid-clay composite to get an approximation of the effective components of the stiffness tensor. For approximation of the global effective properties of this shale material the SC DSCT model yields the most accurate results when the modeling is done in two separate steps. First, a transversely isotropic matrix fluid porous clay medium is approximated using techniques described in Section 4.3.3.2 above. The pores are assumed to have an orientation distribution similar to that given in Equation (IV.3.14), but for the case of oblate inclusions the axis of symmetry is the x_3-axis and the angular variations are for the solid polar angle, φ (see Figure 4-15). The standard deviation of angular variation was assume to be $\sigma_\varphi = 30^\circ$ in accordance with the histogram show in Fig. 9 of reference [78]. This effective medium was then used as the matrix to which the three spherical mineral phases were added. The results of this modeling approach are given in Table 4-5.

Table 4-5: Experimental data and results of effective stiffness coefficients of shale (GPa) for various modeling techniques. DSCT = Dilute strain concentration tensor; SC = Self-Consistent; GSC = Generalized Self-Consistent.

	Observed (GPa)	*Hornby et al (GPa)*	*SC DSCT (GPa)*	*GSC DSCT (GPa)*
C_{11}	34.3 ± 1.4	34.7	29.8	30.0
C_{22}	34.3 ± 1.4	34.7	29.8	30.0
C_{33}	22.7 ± 0.9	22.2	18.7	20.0
C_{44}	5.4 ± 0.8	6.0	4.7	4.8
C_{55}	5.4 ± 0.8	6.0	4.7	4.8
C_{66}	10.6 ± 1.6	10.8	8.3	8.4
C_{12}	*Not reported*	*Not reported*	12.3	12.4
C_{13}	10.7 ± 5.4	11.5	14.7	14.7
C_{23}	10.7 ± 5.4	11.5	14.7	14.7

The results of the SC DSCT model are in good agreement with the properties observed by Jones and Wang [77] and modeled by Hornby *et al* [78].

Approximations have been run using both the SC DSCT model as well as the GSC model with DSCT formulation. Both of these techniques underestimate all of the observed values of the components of the stiffness tensor except C_{13} and C_{23} with the GSC model showing improved agreement with experimental values as would be expected. The experimental error on the mean value of components C_{13} and C_{23} is very high however, and so comparison of the model with the experimental values is mostly for qualitative purposes. Indeed, the SC DSCT model predicts the effective values of all stiffness coefficients to within 10% of the lower limit of the experimentally observed values and the anisotropic behavior of the composite shale due to the preferentially oriented oblate pores is well captured by the DSCT formulation. With regards to the accuracy of the SC DSCT and GSC model approximations with respect to the approach of Hornby *et al*, several points musts be raised. First of all, the agreement of the two models is highly dependent on the values used for the moduli of the constituent mineral phases. Due to the fact that these values were not given in the reference, this could be one source of disagreement between the results given here and those arrived at by Horby *et al.* It is also important to note that the agreement with the experimental data is partially dependent on the modulus in question. The SC DSCT and GSC models show better agreement with the values of the shear moduli whereas the approach Hornby *et al* obviously approximates the plane wave moduli (C_{11}, C_{22}, and C_{33}) more accurately. Most importantly, the application of the SC DSCT model to approximate the effective properties of this material with good qualitative and quantitative agreement between model and experiment is a strong example of the generality of the DSCT approach.

4.3.4 Sub-micron → Micro → Macro Modeling

Another area where the SC DSCT model can be show to be applicable is in the area of multiscale modeling. Many complex materials are most accurately modeled

as having behavior that can be modeled on several scales. The main problem presented by these materials is the ability to tie behavior on multiple scales together in a manner that yields a complete picture of the material behavior at the scale of interest based on its multiscale composition. Indeed the micromechanical approach is, by definition, a type of multiscale modeling. The materials modeled above, however, have been for the simple case of two separate scales. In the following case the influence of the material properties and geometry of one or multiple types inclusions on the same length scale is homogenized in order to approximate the behavior of the composite on a larger length scale. For multiscale modeling purposes, it is, in general, assumed that there exist several length scales such that the effect of inhomogeneities and interfaces at an inferior scale can be taken into account at the next highest length scale through some type of averaging technique. This tacitly assumes that the behavior at lower level length scales only have an effect on the next highest level in some average way and that no point-to-point interactions are important between length scales [27]. For the cases presented above, for example, the effect of inclusions (whose interaction at their respective length scale is indirectly taken into account via the self-consistent scheme) on the global homogeneous behavior is done through an averaging scheme that involves finding the proper DSCT. For composites consisting of more than two scales, homogenization techniques analogous to the DSCT describe above must be developed between each length scale and the next highest length scale, starting with the smallest scale to be considered and increasing until the effective global behavior is approximated. This is a very interesting problem that applies to nano-composites and many naturally occurring materials displaying structural hierarchy. The approach requires the ability to model inhomogeneities and interfaces on the local level (at their respective length scale) with respect to the surrounding medium and then to use this information to model the global behavior (see, for example, Spearot *et al* [157]). Problems of this kind are very difficult due to the complexity of models at very small length scales, and are beyond the scope of this work. Here the emphasis is simply on showing that the SC DSCT

model can be used when the effect of multiple scales must be taken into account. To do so, the results of the SC DSCT model of a silicon carbide–aluminum (SiC-Al) composite material presented by Ledbetter and Datta are shown together with the experimental and theoretical results presented in the reference [79].

4.3.4.1 Comparison with experiment

The material studied by Ledbetter and Datta is a bi-phase material with complex microstructure due to manufacturing processes. Modeling this material requires a scale transition between three different length scales. The smallest length scale is that of prolate ($a/b = a/c = 3$) SiC inclusions with a uniform orientation distribution embedded in an aluminum matrix. These prolate inclusions have sub-micron descriptive lengths (~250-750 nm) and are non-uniformly distributed within the aluminum host (see Figure 4-24a). The distribution of the SiC particles within the aluminum host is such that identically oriented oblate islands ($a/b = 1$, $a/c = 3$) of pure aluminum with descriptive lengths of ~2-4 μm remain. These pure aluminum islands are surrounded by a "sea" of high volume fraction SiC–Al composite. The length scale associated with the Al islands is an intermediate scale, which is referred to as the meso-scale, between the sub-micron (nano) scale and the macroscopic scale. The total volume fraction of SiC in the composite was experimentally determined to be 30%, but, because of the non-uniformity of the spatial distribution, the concentration level of SiC particles in the "sea" is approximated as being 50% [79]. For modeling purposes, the important material properties of SiC and Al were given as: $K_{SiC} = 223.4\ GPa$, $\mu_{SiC} = 188.1\ GPa$, $\rho_{SiC} = 3160\ kg/m^3$, $K_{Al} = 74.9\ GPa$, $\mu_{Al} = 26.7\ GPa$, and $\rho_{Al} = 2700\ kg/m^3$.

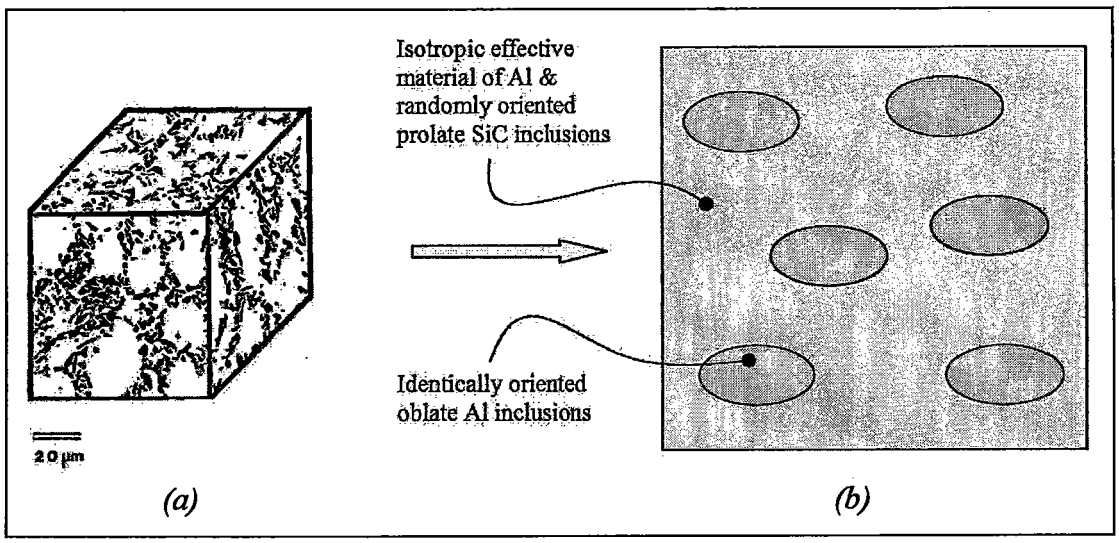

Figure 4-24: Composite material studied by Ledbetter and Datta (image taken from reference [79]). The material consists of a non-uniform distribution of sub-micron prolate SiC particles in an aluminum matrix. (a) Micrograph of material, SiC particles are dark areas, (b) Schematic of modeling approach employed.

Ledbetter and Datta proposed a multiple scattering model which is valid for ellipsoidal inclusions having either uniform or identically oriented orientation distribution to approximate the effective material properties of this composite which gives good results [79]. Their model illustrates the difficulty involved in developing scattering-based models for approximation of the effective properties of composites displaying complex microstructure. The modeling was done in two steps (see Figure 4-24b) the first of which involves approximating the "sea" as a homogeneous isotropic medium resulting from the 50-50 mix of SiC prolate inclusions having a uniform orientation distribution and the aluminum matrix. This isotropic medium is then idealized as the matrix material of the global composite material which has identically oriented (aligned with the x_1-x_2 plane) oblate Al inclusions with a volume fraction of 40%. The implementation of the SC DSCT model is done in an identical manner. First the sub-micron→meso transition is made by employing the DSCT formulation given in Section 4.3.3.1 to find a globally isotropic medium which acts as the matrix for a meso→macro scale transition modeling step. The meso→macro step is done by employing the basic SC model given in Equations (III.2.73), (III.2.75), and (III.2.76) where the matrix found in the previous step is assumed to contain 40%

oblate Al inclusions aligned with the x_1-x_2 plane. The results of this modeling approach are tabulated in Table 4-6 together with the theoretical and experimental values given by Ledbetter and Datta [79], the DSCT GSC, and the DSCT Mori-Tanaka (MT) model results.

Table 4-6: Observed and calculated values of the coefficients of the stiffness tensor (GPa) for Al-SiC composite of Ledbetter and Datta [79]. (DSCT = Dilute strain concentration tensor; GSC = Generalized Self-Consistent; MT = Mori-Tanaka; LD = Ledbetter and Datta).

	Observed	*SC DSCT*	*GSC DSCT*	*MT DSCT*	*LD*
C_{11}	165.9	172.9	170.8	240.9	172.7
C_{22}	165.1	172.9	170.8	240.9	172.7
C_{33}	148.3	161.7	160.7	118.7	148.0
C_{44}	43.3	47.9	47.3	42.9	42.9
C_{55}	43.4	47.9	47.3	42.9	42.9
C_{66}	48.7	51.7	50.6	51.3	51.3
C_{12}	68.5	69.2	69.1	99.1	70.1
C_{13}	62.2	69.1	69.0	67.9	67.7
C_{23}	62.2	69.1	69.0	67.9	67.7

The DSCT GSC and DSCT MT models were run for comparison purposes. For this particular composite, the MT model seems to greatly over-estimate the effective material properties and approximates too high of a degree of anisotropy. This is not unexpected, as the MT is known to overestimate effective material properties when the matrix material is more stiff than the inclusion phase [158, 159]. As observed in the previous section, the DSCT GSC model again shows improved agreement with the experimental values as compared to the SC DSCT model. The capability of the three-phase coated-inclusion SC model of Cherkaoui to be extended to a GSC scheme is indeed one of the strengths which was also noted Section 4.3.3.3 that is stressed. The results indicate that the SC DSCT and GSC models both over-estimate the measured material properties and show a lower degree of anisotropy than that observed; the difference in the values of C_{12} and C_{23} is negligible and the contrast between C_{44} and C_{66} is not as marked as is the actual material or the LD model. Nevertheless, the theoretical transverse isotropy, $C_{66}^{theory} = \left(C_{11}^{SC} - C_{12}^{SC}\right)/2$, shows only a 0.5% difference between the SC DSCT model and theoretical values of C_{66}. The

model is therefore shown to be giving consistent results. Here it must be noted that the LD model yields a better approximation of the observed effective properties of the SiC-Al composite than the SC DSCT model. The improved agreement more than likely stems from the fact that the LD model is derived from multiple scattering considerations and therefore is able to directly take into account high volume fractions whereas the SC formulation implicitly approximates such behavior. As the volume fraction increases, the error involved in the implicit scheme will increase and therefore leads to the SC model's lower precision approximation. It is important, however, to stress that the generality of the SC DSCT model for applications to composite materials of very different constituent phases, geometries, and orientational preferences as displayed here and in the examples above is a great advantage over models such as that proposed by Ledbetter and Datta which are restricted to heterogeneities with identical orientations or a uniform orientation distribution.

4.3.5 Distribution of coating thicknesses

The last validation of the SC DSCT model is an example of how it can be extended to capture the effect of the variation in coating thickness observed in real materials. Previous sections showed that the SC model gives very good approximations of the lossy behavior of a viscoelastic material containing hollow microspheres by comparing calculated values of TL to experimental values. One of the assumptions of that formulation is that all coated inclusions are identical. Though the effect of the relative inclusions size with respect to other inclusions can be assumed to have a negligible effect on the global properties since they are all on the same length scale and must be several orders of magnitude smaller than the wavelength of the incident wave in the host material, the distribution of coating thickness can still have a non-negligible effect. This is due to the fact that the contrast in material properties between the inclusion (which is a void) and coating (a

glassy material) is significant. Indeed, the model proposed by Baird *et al* [76], included a modification for what they called a "size effect." Though the appellation of their model as capturing a "size-effect" is a misnomer as only the variation in coating thickness is taken into account, their model shows improved agreement with TL data for a 2.5 cm thick slab of viscoelastic composite. Here the SC model is modified by using the concept of DSCT to take into account a variation in coating thickness. This is done by recognizing that each family of composite inclusions that have the same coating thickness can be modeled as representing a family of inclusions with slightly different material properties. The homogenization scheme is then represented similarly to that shown in Figure 3-4, where the coating thickness of the inclusions is varied from family to family and there is no orientational effect because of the inclusions are spherical.

In order to cast the tensor relations for the effective moduli of the composite for a variation of coating thickness an approach similar to that outlined by Baird *et al* is employed. First, the coating fraction, $\gamma_{i,j}$, is defined which quantifies the percentage of the composite inclusion volume which is coating for a family of spherical coated inclusions with inner radius a_i and outer radius b_j. Here, the subscripts on γ do not denote a tensor quantity but simply the coating fraction for different values of inner and outer radii, likewise the comma does not denote a spatial derivative. For this idealized family of spherical composite inclusions, the coating fraction can then be expressed as a function of the radii as shown below.

$$\gamma_{i,j} = 1 - \left(\frac{a_i}{b_j}\right)^3 \qquad \text{(IV.3.15)}$$

It is further assumed that the relative size of the inclusions has a negligible effect on the globally observed properties and that the inner radius has a constant value, a_{ave}. The coating fraction for each family of inclusions then relates the inclusion and

coating volume fractions to total volume fraction of the family having the same outer radius (and therefore coating fraction) with the following relations.

$$f^{C,i} = \varphi_i \gamma_i \tag{IV.3.16}$$

$$f^{I,i} = \varphi_i - f^{C,i} = \varphi_i (1 - \gamma_i) \tag{IV.3.17}$$

It is important to note that the above relations also hold for ellipsoidal inclusions (though it would be admittedly difficult to experimentally determine the coating fraction for non-spherical inclusions). For a true composite material, it is obvious that the coating thickness will be found in some distribution that can be related to a measured distribution of outer radii through Equation (IV.3.15). From this measured distribution, $p(\gamma)$, the normalized distribution, $n(\gamma)$, is calculated by using Equation (IV.3.10). The resulting expression of the SC model for the case of varying coating thicknesses is then written:

$$\hat{\mathbf{C}}^{eff} = \hat{\mathbf{C}}^{M} + \varphi \left[\frac{\int_{-\infty}^{\infty} p(\gamma) \left\{ (1-\gamma) \Delta \hat{\mathbf{C}}^{IM} : \hat{\mathbf{A}}^{I}(\gamma) + \gamma \Delta \hat{\mathbf{C}}^{CM} : \hat{\mathbf{A}}^{C}(\gamma) \right\} d\gamma}{\int_{-\infty}^{\infty} p(\gamma) d\gamma} \right] \tag{IV.3.18}$$

$$\hat{\mathbf{C}}^{eff} \approx \hat{\mathbf{C}}^{M} + \varphi \sum_{j=1}^{N} n(\gamma_j) \left\{ (1-\gamma_j) \Delta \hat{\mathbf{C}}^{IM} : \hat{\mathbf{A}}^{I}(\gamma_j) + \gamma_j \Delta \hat{\mathbf{C}}^{CM} : \hat{\mathbf{A}}^{C}(\gamma_j) \right\} \Delta\gamma \tag{IV.3.19}$$

The expression given in Equation (IV.3.18) is a continuous function of γ though the strain localization tensors, $\hat{\mathbf{A}}^{\chi}$, cannot be integrated for the case of ellipsoidal inclusions since they are not analytic functions. Equation (IV.3.19) must therefore be employed for correct implementation for those cases or for simplified direct

application in the case of spherical inclusions as the coating distribution function may yield integration extremely difficult or impossible for the case of spherical coated inclusions.

4.3.5.1 Comparison with experiment

The use of DSCT for the case of a distribution of coating thicknesses will be verified by implementing Equation (IV.3.19) to calculate the TL of a 2.5 cm thick slab of viscoelastic material containing coated micro-inclusions submerged in water. The results are compared with the experimental data of Baird *et al* [76] as well as the SC approximation which only uses the average coating thickness hypothesis. The viscoelastic composite material in question is composed of the "soft" viscoelastic polymer and 10% by volume coated inclusions. The material properties of each phase are given in Table 4-1. The coating fraction distribution is assumed to be well approximated by the Rayleigh distribution given below based on heuristic grounds and through "initial measurements" by Baird *et al* [76]. The average coating fraction is $\bar{\gamma} = 2.5 \times 10^{-2}$.

$$p(\gamma) = \frac{n_0 \pi \gamma}{2\bar{\gamma}^2} \exp\left(-\frac{\pi}{4}\left(\frac{\gamma}{\bar{\gamma}}\right)^2\right) \quad \Rightarrow \quad n(\gamma) = \frac{p(\gamma)}{\int p(\gamma) d\gamma} \qquad \text{(IV.3.20)}$$

This distribution is then used to calculate the complex effective stiffness tensor of the viscoelastic composite through Equation (IV.3.19) and the TL is then calculated by employing relations (IV.3.3)-(IV.3.7). The material is fully described by the two Lamé coefficients since the inclusions are spherical and the composite is therefore globally isotropic. It is also important to point out that due to the distribution of shell thicknesses, the equation expressing the effective density of the composite, (IV.3.6), must be calculated by the law of mixtures relationship below.

$$\rho^{eff} = \rho^{M}(1-\varphi) + \varphi \sum_{j=1}^{N} n(\gamma_j)\left[(1-\gamma_j)\rho^{I} + \gamma_j \rho^{C}\right]\Delta\gamma \qquad \text{(IV.3.21)}$$

Figure 4-25 shows the results of the SC model as modified with DSCT for the case of a variation in coating thickness when applied to the "soft" polymer composite material with 10% coated inclusions tested by Baird *et al* [76]. Included on the plot is the curve resulting from implementation of the uniform coating thickness model given by Haberman *et al* [53].

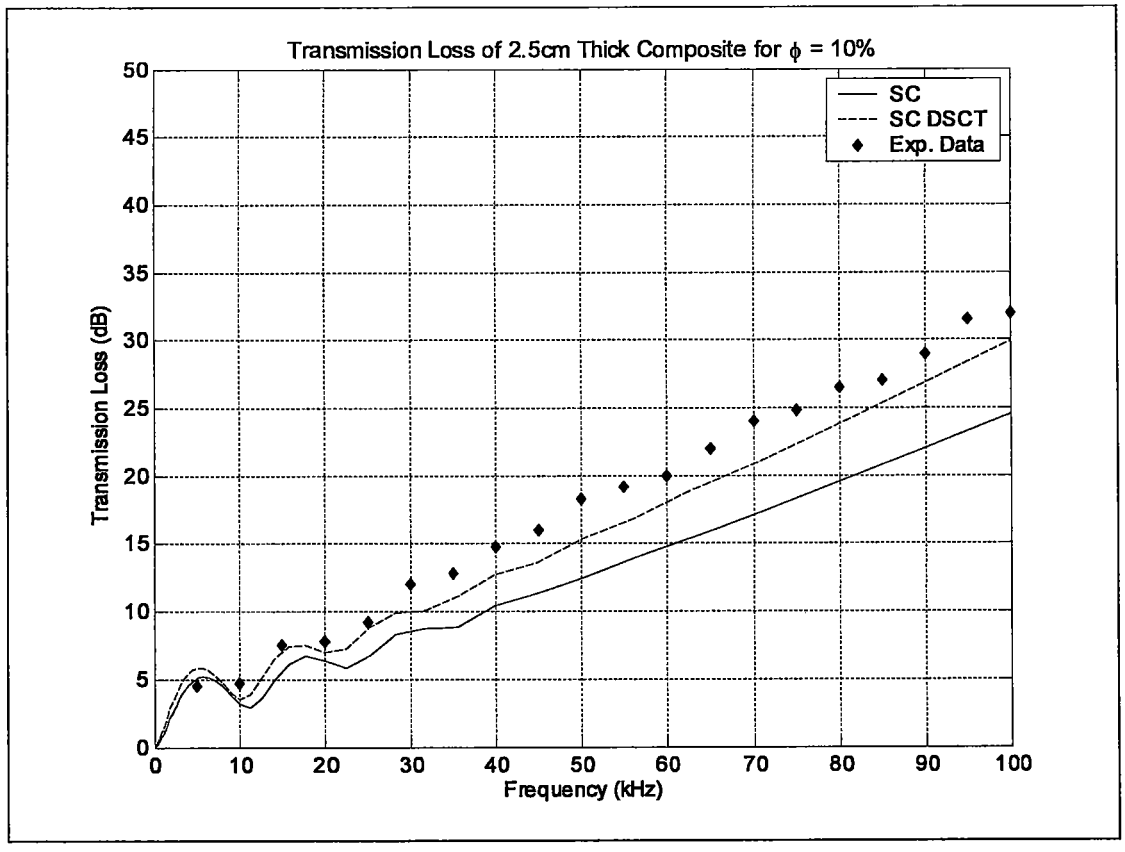

Figure 4-25: Transmission loss calculated using SC and SC DSCT with experimental data from reference [76].

As can be clearly seen in the plot, the agreement of the model with the experimental data is improved. The slope of the high frequency regime is very nearly the same as the trend observed in the data which is a marked improvement over the uniform

thickness model. Further, the value of the TL approximation in general is within 2-3 dB across the full range of frequencies inspected: 0–100 kHz.

4.4 Comments on numerical implementation of SC model

Successful SC model implementation depends on the ability to numerically evaluate the implicit problem given in Equations (III.2.73), (III.2.75), and (III.2.76). These equations represent a tensor relationship whose solution must be found implicitly. The implicit nature requires a careful consideration of numerical root-finding and/or minimization techniques to find the effective viscoelastic stiffness tensor, $\hat{\mathbf{C}}^{eff}$. For the case of spherical isotropic coated inclusions embedded in an isotropic matrix, the resulting effective properties will also be isotropic and Equations (III.2.73), (III.2.75), and (III.2.76) can be reduced to two implicit equations for the effective Lamé constants, μ^{eff} and λ^{eff}. These relations are given in Appendix A of Haberman *et al* [53]. Solutions to this set of equations can be obtained by using a two-dimensional Newton-Raphson numerical root-finding scheme. This technique for the isotropic effective material is very robust and no convergence problems have been observed regardless of material contrasts or volume fraction of coated inclusions.

The implicit solution to the general anisotropic case is neither simple nor is it guaranteed to converge for all combinations of material stiffness contrasts, inclusion aspect ratios, or volume fractions. One approach to finding an approximate solution of the composite's effective viscoelastic properties is through minimization. The first step in the minimization process it the re-arrangement of the SC tensor equations into a vector function to be minimized to an acceptable level of accuracy. Orthotropic materials are fully described by nine independent viscoelastic constants and therefore the coefficients of the effective stiffness tensor can be re-arranged as a 9x1 vector,

$\hat{\mathbf{C}}^{eff} \rightarrow \vec{\mathbf{v}}^{eff}$. The SC model and the approximate solution can then be used to create the function shown below in Equation (IV.4.1).

$$h\left(\vec{\mathbf{v}}^{eff}\right) = SC\left(\vec{\mathbf{v}}^{eff}\right) - \vec{\mathbf{v}}^{eff} \tag{IV.4.1}$$

In this relationship, $h\left(\mathbf{v}^{eff}\right)$ is the function to be minimized and $SC\left(\mathbf{v}^{eff}\right)$ is understood to represent the result, represented in vector form, of the SC model given in Equations (III.2.73), (III.2.75), and (III.2.76) for an input of $\vec{\mathbf{v}}^{eff} \rightarrow \hat{\mathbf{C}}^{eff}$. It is also important to point out that the evaluation of $\hat{\mathbf{T}}^{I}\left(\hat{\mathbf{C}}^{z}\right)$, given in Equation (III.2.40), is required for correct evaluation of the strain localization tensors, $\hat{\mathbf{A}}^{I}$ and $\hat{\mathbf{A}}^{C}$. This is achieved through numerical integration of the modified Green's tensor, $\hat{\Gamma}^{z}_{ijkl}\left(\mathbf{r}-\mathbf{r}'\right)$, through an n-point Gauss-Legendre quadrature integration, after using Fourier transform techniques to transform the ellipsoidal inclusions into spheres in the Fourier domain as outlined in the Appendix A. A nine dimensional simplex method is then used to minimize the implicit relationship given in Equation (IV.4.1) [160]. The simplex method is robust and effective because it does not require the calculation of rates of change in the function with respect to each individual variable. The technique involves the evaluation of the SC model at ten points suspected to surround the solution in the 9-dimensional space. During implementation, these points are chosen by varying each of the nine elements of $\vec{\mathbf{v}}^{eff}$ of the previous volume fraction step by a small percentage (1% used for this evaluation) thus yielding nine initial guess points and then using the unaltered elements of $\vec{\mathbf{v}}^{eff}$ for the tenth point. The algorithm then uses a series of reflections and contractions of the ten points until an acceptable level of convergence is found. Though the technique is robust, it is not guaranteed to converge to the correct solution and calculation time can be significant for a high volume fraction of inclusions.

Several factors can cause significant problems in the convergence of the numerical evaluation of the general SC model. Therefore, a few qualitative observations may help for successful implementation of the method. The parameter that has the strongest influence on the convergence of the model is the contrast of the moduli of the constituent phases. If the moduli of the inclusion materials are significantly lower than that of the matrix (as is the case with voids or air inclusions) the numerical scheme has great difficulty in converging to the correct solution. This convergence difficulty is still observed when the inclusions are coated. Indeed, glass coated voids embedded in a soft matrix prove to be one of the most difficult set of parameters for the resolution of the general self-consistent model. Another parameter that has strong influence on the convergence of the general model is the aspect ratio of the inclusions. As the aspect ratio (either a/b or a/c) increases, the likelihood of poor convergence behavior also increases. It should be noted that poor convergence due to the inclusion aspect ratio is coupled with the contrast of the material properties, the higher the material contrast the less stable the SC method for any given aspect ratio. However, no obvious practical guidelines can be given. Here it is emphasized that, even with large aspect ratios, the model is strictly valid in the low-ka regime. Yet another parameter that can influence convergence, though to a lesser extent, is the ratio of $\Delta a/a$, i.e., the normalized coating thickness. It has been observed that values of this parameter below 10^{-3} can lead to poor convergence behavior, though, like the effect of the aspect ratio, the influence of $\Delta a/a$ on the convergence is coupled to the material contrast and therefore smaller ratios can be tolerated for lower contrast situations. Other known issues are usual user defined parameters of root-finding techniques, such as the initial values for the numerical search algorithm, the volume fraction step size, and the number of points chosen for Gauss-Legendre evaluation of the integral of the modified Green's tensor.

Despite numerical difficulties manifest in the coated-inclusion SC model this chapter has shown, through comparison with experiment and parametric studies, the generality and precision of the SC model. The SC model has been shown to reliably

approximate the lossy behavior of viscoelastic composites. This ability is a great improvement over scattering based models because of the enhanced flexibility to include material anisotropy and the effects of inclusion orientation which is afforded by the micromechanical approach. The enhanced level of generality makes the SC micromechanical model a strong candidate to play a role in a material by design strategy. The next chapter will present a simple multiscale modeling application that employs the SC model to enhance absorptive properties of a structure through variation of material microstructure.

CHAPTER V

TOWARDS SELF-CONSISTENT MODEL IMPLEMENTATION IN A MATERIAL BY DESIGN STRATEGY

5.1 Overview

Material selection, traditionally a key component of the design process [19], is a very limiting aspect of design. Indeed the systems design approach, which pervades the design community, assumes that component design will be restricted by the physical properties of available materials [20]. This paradigm is changing as the systems approach is being extended to include the design of materials for multi-functional and multi-physics applications [14, 15]. This approach is called inductive design. Inductive material design aims to design materials for manufacture, while traditional methods manufacture materials that will be used in design, a deductive approach [21]. One very important aspect of this emerging design approach is the development of robust multiscale material models that can be employed to inform the material design process [14]. Models capable of bridging the disparate length and time scales interest to material design (length scales ranging from atomistic to macroscopic and time scales ranging from pico-seconds to years) are far beyond the reach of current modeling approaches. Instead, researchers currently employ a nested hierarchy of different models, each of which is capable of making one or more scale transitions [20]. One of the most prominent problems with this approach is the lack of information about, and/or the extremely complex behavior of, material models in the design space [21]. These problems restrict the efficient implementation of many

material models in an overarching material design scheme. One way this shortcoming can be overcome is by solving simple multiscale problems in order to observe trends that can inform future material by design strategies. Another approach would be to employ metamodels that approximate material behavior between two specific scales when models based on more rigorous physical considerations impede the design process. The metamodel approach could be employed in material design, for example, to approximate the scale transition between atomistic and continuum behavior. These modeling simplifications permit an efficient means to perform behavioral studies of a model or investigate the design space at multiple scales [22]. Regardless of the method employed, any material design process will require not only robust multiscale models, but also the profound understanding of the material behavior in the design space that a well developed model yields. The aim of this chapter is to provide an introductory level example of self-consistent (SC) model implementation in the design of a lossy structure. This is accomplished by studying the damping properties of a simple structure: a vibrating sandwich plate. The results of this study provide preliminary insight into the role the quasi-static SC model can play in a material design strategy and lay the groundwork for more detailed research. Metamodel implementation is left for future work.

5.2 Multiscale windshield modeling

Structural applications for layered sandwich plates are numerous and typically aim to reduce overall weight while simultaneously maintaining structural rigidity. Some examples of such sandwich structure applications include aircraft wings and fuselage [2] or reinforcement and noise isolation in automobiles [1, 5]. One consequence of sandwich plate geometry is a pronounced ability to provide acoustic and thermal isolation [80]. An example of a structural element that fulfills all of the roles highlighted above is the automobile windshield. Current windshield design is a

layered structure consisting of two identical high performance glass layers sandwiching an absorptive viscoelastic layer. From a mechanical perspective, the interior viscoelastic layer serves the dual purpose of holding glass fragments in place in the event of projectile impact while simultaneously providing enhanced structural vibration dissipation and sound isolation qualities during normal operating conditions. The ability to reduce sound transmission has become one of the many requirements placed on the automobile windshield. This requirement stems from a desire to reduce driver noise annoyance and to eliminate structural vibrations of the automobile frame as a whole.

The case study presented in this chapter aims to model sandwich plate behavior as a multiscale structure consisting of four distinct length scales. These length scales are, from shortest to longest: (*i*) the constituent material microstructure, (*ii*) the macroscopic plate material, (*iii*) the sandwich plate, and (*iv*) the constrained sandwich plate. In so doing, this study introduces the key variables which define the design space and provides an important study of their interaction and influence on the behavior of the structure. Figure 5-1 illustrates the multiscale windshield modeling approach employed. The study begins with part level modeling. A simple sandwich plate model is introduced and the mechanisms that enhance flexural wave damping are discussed in the context of strain energy. Several parametric studies investigating optimal damping design of a sandwich plate complete the part level modeling study. Following this analysis the structural level model considered is the modal response of a viscoelastically constrained plate and beam. The simple layered plate model is incorporated into this modal analysis and results are compared with a sophisticated finite element model. Finally, the study considers the effect of microstructural behavior on structural level damping through SC homogenization. The aim of this study is to observe the capability of microstructural behavior to increase the overall absorptive properties of the plate while limiting negative effects on its structural rigidity role. The present study thus provides insight to multiscale modeling for damping applications.

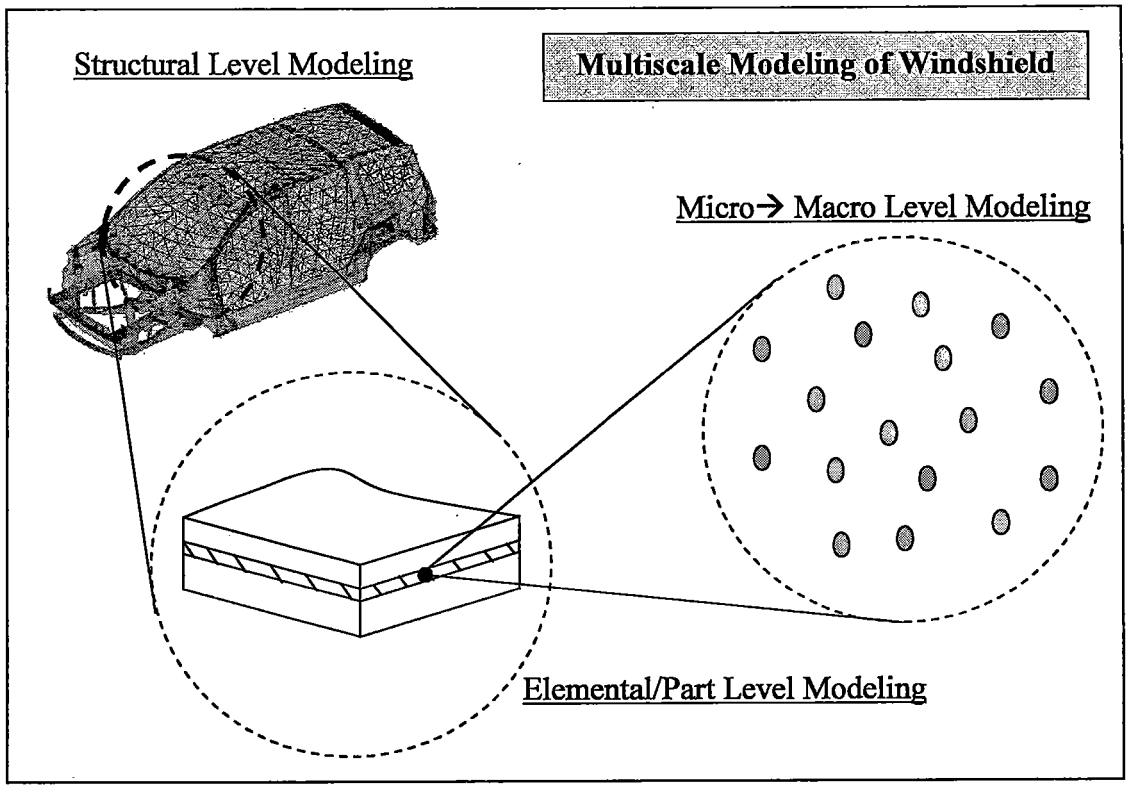

Figure 5-1: Multiscale windshield modeling approach.

5.3 Part level modeling: Damped flexural waves in a sandwich plate

The three layer structure of a windshield capitalizes on the lossy properties of the sandwiched viscoelastic layer, the interlayer, by inducing high shear strains in the material upon vibrational excitation [5]. The high shear strain in the interlayer results from the viscoelastic material's relatively low shear resistance as compared to that of the sandwiching plates and its location at the center of the layered plate. The high shear compliance of the constrained viscoelastic layer means that shear stresses resulting from an imposed bending moment will translate into large deformations in the interlayer [81]. The ultimate consequence of this geometric configuration is an increase in vibrational and acoustical energy damping capacity coupled with the structural advantage of being highly shatter resistant [1].

The study of sandwich structures is not a recent development. As early as 1959 Kerwin presented an analytic three-layered plate model [161]. The plates he studied consisted of three isotropic layers and had no restriction on layer thicknesses or symmetries. Following this introductory model, Ross, Kerwin, and Ungar derived a more general analytic model that describes the flexural behavior of a three layered plate to approximate the lossy behavior of structures with viscoelastic treatments such as external viscoelastic layers and non-symmetric or symmetric viscoelastic sandwich structures [81, 162]. Their model was followed by many other constrained plate analytical models that are applicable to plates having simple boundary conditions. Representative examples include Ditaranto's layered beam model [84], Mead and Markus's model of the forced vibration of a layered beam [85] , Yan and McDowell's work on the dynamic behavior of constrained layer plates [87] , and Cupial and Niziol seminal work on the damping of a three layered plate [82]. The strength of analytical models lies in their ability to quantitatively compare the behavior of different sandwich structures with relative ease of implementation. For many cases, however, such models are not applicable because they are limited to simple geometries and simple boundary conditions (BC). True engineering problems often present complexities that analytical models cannot take into account. It is for this reason that many researchers have concentrated on the development of sandwich structure finite element (FE) models which approximate dynamic lossy behavior. Representative works in this area are those of Soni [86], Johnson and Kienholz [163], Rikards and Chate [164], and Daya and Potier-Ferry [83]. For an excellent review of a significant developments in constrained layer damping models, see Austin [165]. FE models are more precise and provide a richer analysis of the dynamic stress and strain states in a layered plate. Further, they can be implemented in structural analysis of higher order structures, such as the structural behavior of an automobile as a whole. However, the aim of this chapter is not to provide a detailed analysis of a complex structure but rather to give an introductory level study of the effect of microstructure on the structural damping properties of the multiscale modeling approach. It is for this

reason that FE studies will only be employed in this study for quantitative qualitative verification of analytical studies.

5.3.1 Approximation of the effective bending modulus of a sandwich plate

The concise study of the microstructural effects on the damping capacity of a layered plate as a structural element first requires the selection of the appropriate part-level model. The analytic model developed by Ross, Kerwin, and Ungar (RKU) [81] is ideal for our present study. This model is computationally light and provides reasonable estimates of the enhanced damping capacity of a constrained layer plate as a function of frequency, material properties, and plate geometry [166].

The proceeding discussion has pointed out that the constrained layer geometry and material stiffness contrast lead to the enhanced damping capacity of the layered plate. These both contribute by inducing large shear deformation in the absorptive central layer. This increased deformation leads to a large increase in strain energy located in the lossy material thereby increasing the damping capacity of the layered plate as a whole [162]. Kerwin [161] showed that the flexural behavior of such a layered plate is reasonably approximated as a uniform plate having an effective complex bending, or flexural, modulus. The real part of this modulus describes the resistance to flexure due to an imposed time-varying bending moment and the imaginary part is a descriptor of the composite plate's capacity to absorb flexural wave energy [81, 161]. For an out of plane flexural disturbance, $\hat{w}(x,t)$, propagating in the $+x$ direction of a layered plate the damped wave is described using Equations (V.3.1) and (V.3.2) below. These expressions are analogous to Equation (IV.3.2) for pressure wave propagation.

$$\hat{w}(x,t) = \hat{A}e^{j\left(\omega t - \hat{k}^{flex}x\right)} = \hat{A}e^{\hat{\alpha}^{flex}x}e^{j\left(\omega t - \hat{k}^{flex,'}x\right)} \qquad \text{(V.3.1)}$$

where:

$$\hat{k}^{flex} = \hat{k}^{flex,'} - j\hat{\alpha}^{flex} = \left(\frac{\omega^2 \rho^{eff} h^{tot}}{\hat{B}^{eff}} \right)^{\frac{1}{4}} \qquad \text{(V.3.2)}$$

In the above expressions $\hat{A}$ is the complex amplitude, ω is the angular frequency, $\hat{k}^{flex,'}$ and $\hat{\alpha}^{flex}$ are components of the frequency dependent complex flexural wavenumber, $\hat{k}^{flex}$, ρ^{eff} is the effective density of the entire plate, h^{tot} is the thickness of the entire plate, and $\hat{B}^{eff}$ represents the complex effective frequency dependent bending modulus of the layered plate. Note also that the present study treats structural vibrations. Therefore, *in keeping with the conventions of the vibrations community, the '$e^{j\omega t}$' convention is employed in this section.* The RKU model aims to provide an accurate approximation of the effective bending modulus of the plate which takes the exaggerated interlayer shearing into account. This is accomplished by writing equations of motion for the plate element shown below in Figure 5-2.

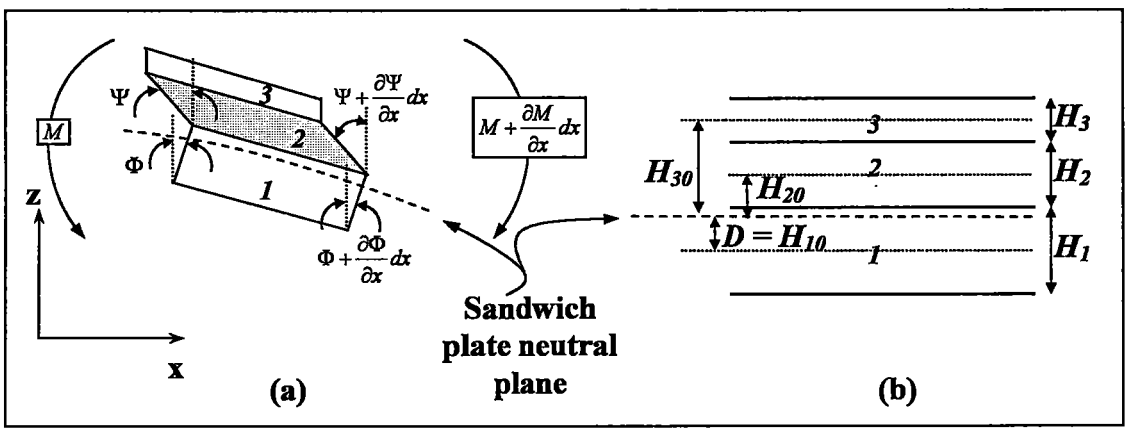

Figure 5-2: (a) Differential element of a sandwich plate ; (b) Cross sectional geometry.

The RKU model results from solving the wave equation for the out of plane flexural disturbance described by Equation (V.3.3) together with the moment equation, (V.3.4).

$$\nabla^4 \hat{w}(x) - \frac{\omega^2 \rho^{eff} h^{tot}}{\hat{B}^{eff}} \hat{w}(x) = \frac{\hat{p}(x)}{\hat{B}^{eff}} \tag{V.3.3}$$

$$\hat{M}(x) = \hat{B}^{eff} \frac{\partial \hat{\Phi}(x)}{\partial x} = \sum_{i=1}^{3} \hat{M}_i(x) + \sum_{j=1}^{3} \hat{F}_j H_{j0} \tag{V.3.4}$$

In these expressions $\hat{p}(x)$ represents the frequency dependent and spatially varying forcing pressure, $\hat{M}(x)$ denotes the total flexural moment applied to the plate, $\hat{M}_i(x)$ is the resulting moment in each layer, $\hat{F}_j(x)$ is the net transverse force in each layer, and H_{j0} represents the distance from the center j^{th} of the layer to the neutral plane of the composite [81].

This resulting model has many restrictions for implementation which are listed here [81]:

1) The Young's modulus of the upper and lower layers (*1* and *3*) must be much larger than that of layer *2*.

2) The flexural, shear, and longitudinal wavelengths of the composite plate must be much larger than the total thickness of the plate.

3) The slope of the neutral plane must be very small, $\Phi(x) << 1$.

4) The thickness of the interlayer (layer *2*) remains fixed (no standing waves within the interlayer).

Ross *et al* derived their model for the effective bending modulus of a three layer plate using these simplifying assumptions. The resulting RKU model does not have any restrictions regarding material or geometric symmetries. If symmetry is required, thereby creating a "sandwich" plate, the following additional assumptions must be added [167]:

5) Layers *1* and *3* have identical material properties and geometries. The Young's modulus is denoted as E, the density ρ, and the thickness h ($H_1 = H_3 = h$).

The result of these many simplifying assumptions is the set of the implicit relations (V.3.5), (V.3.6), and (V.3.7) describing the complex effective bending modulus of the layered plate.

$$\hat{B} = \frac{1}{6}\hat{E}h^3\left(1 + 6Y\left(\frac{\hat{g}}{1+2\hat{g}}\right)\right) = \hat{B}'\left(1 + j\hat{\eta}_p\right) \qquad \text{(V.3.5)}$$

Here Y represents a variable called the geometric parameter and $\hat{g}$ is the complex shear parameter. This simple equation satisfies physical intuition about the behavior of a layered plate since the term $\hat{E}h^3/6$ represents the bending rigidity of two plates of thickness h about their base. The term within the parenthesis increases the bending rigidity based on geometry and the interlayer's shear resistance. The geometry and shear parameters are defined in Equations (V.3.6) and (V.3.7) below.

$$Y = (1+H)^2 \quad \text{with} \quad H = \frac{H_2}{h} \qquad \text{(V.3.6)}$$

$$\hat{g} = \frac{1}{h^2}\left(\frac{\hat{\mu}_2}{\hat{E}H}\right)\sqrt{\frac{1}{\omega^2}\frac{\hat{B}^{eff}}{h^{tot}\rho^{eff}}} = \hat{g}'\left(1 + j\hat{\gamma}\right) \qquad \text{(V.3.7)}$$

In the above relationships, $\hat{\mu}_2$ is the interlayer's complex shear modulus, $\hat{\mu}_2 = \hat{\mu}_2'\left(1 + j\hat{\beta}\right)$, and the effective density of the composite plate is calculated using the law of mixtures.

$$\rho^{eff} = \left(1 - H_2/h^{tot}\right)\rho + \left(H_2/h^{tot}\right)\rho_2 \qquad \text{(V.3.8)}$$

Ross *et al* further observed that assumption (*2*) listed above requires that $\hat{g}'$ be larger than unity. As previously stated, this model yields an implicit solution for the

effective bending modulus. Appendix D details a numerical solution scheme for RKU model implementation.

It is now interesting to show constrained layer damping behavior as approximated by the RKU model. For this purpose, consider a symmetric plate composed of two identical glass layers sandwiching a Saflex© PVB (viscoelastic) layer [168]. The layer geometry and material properties are given in Table 5-1. The values chosen represent PVB complex moduli corresponding to observed behavior at 1 kHz and 20°C. Frequency dependent PVB shear modulus values were approximated from Havriliak-Negami (HN) fits [148] of DMTA data, see Figure 5-3. The HN model is given in Equation (V.3.9) and the HN coefficients for this PVB material were found to be: $\mu_\infty = 2.35\times10^8$, $\mu_0 = 4.79\times10^5$, $\alpha_{HN} = 0.46$, $\beta_{HN} = 0.1946$, and $\tau_0 = 0.3979$.

$$\mu^*(\omega) = \mu_\infty + (\mu_0 - \mu_\infty)\left[1 + (j\omega\tau_0)^{1-\alpha}\right]^{-\beta} \qquad \text{(V.3.9)}$$

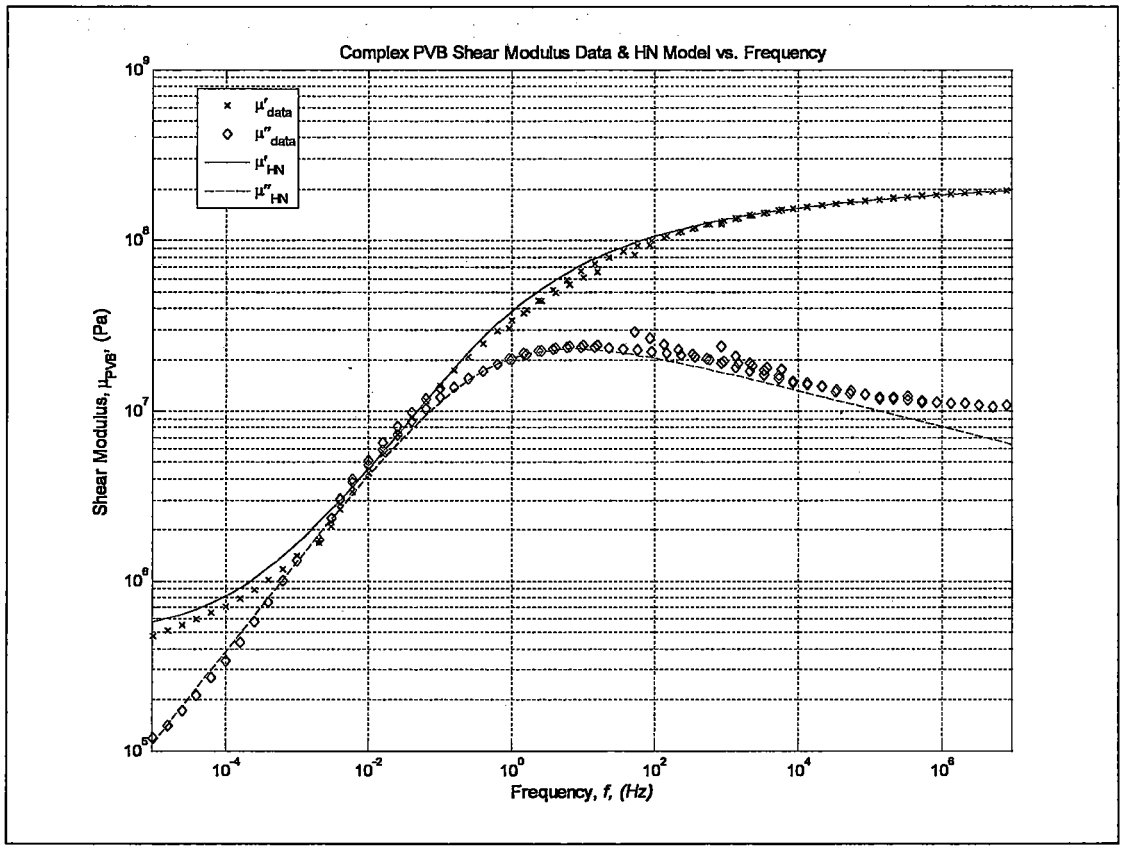

Figure 5-3: DMTA data and HN curve fits for PVB material.

Table 5-1: Layer properties representing windshield constituent properties and geometry.

	H_x (m)	$\mu'(1+j\beta)$ (GPa)	$E(1+j\eta)$ (GPa)	ρ (kg/m^3)	f (Hz)
Layers 1&3	2.0×10^{-3}	$29.5(1+0.02j)$	$72(1+0.02j)$	2469	1000
Layer 2	8.0×10^{-4}	$0.133(1+0.13j)$	$0.396(1+0.13j)$	1115	1000

The plots below show parametric studies of the effective sandwich plate bending modulus, $\hat{B}$, shear parameter, $\hat{g}$, and flexural wavenumber, $\hat{k}^{flex}$, as a function of the thickness ratio, H.

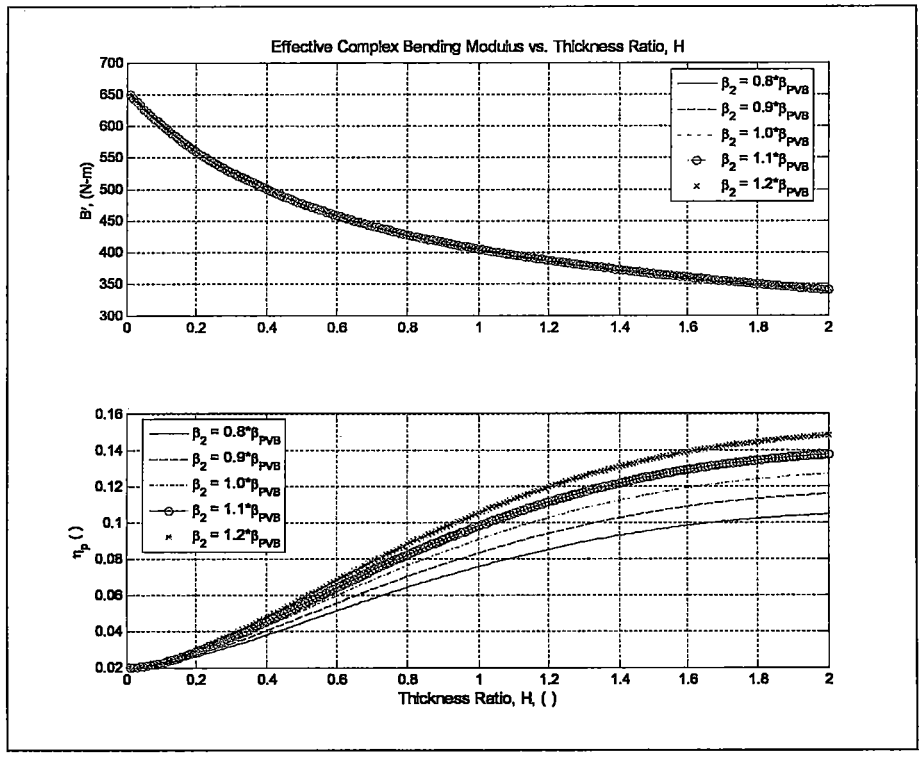

Figure 5-4: Variation of sandwich plate complex bending modulus as a function of the thickness ratio, *H*. Parametric study on the shear loss factor of the interlayer.

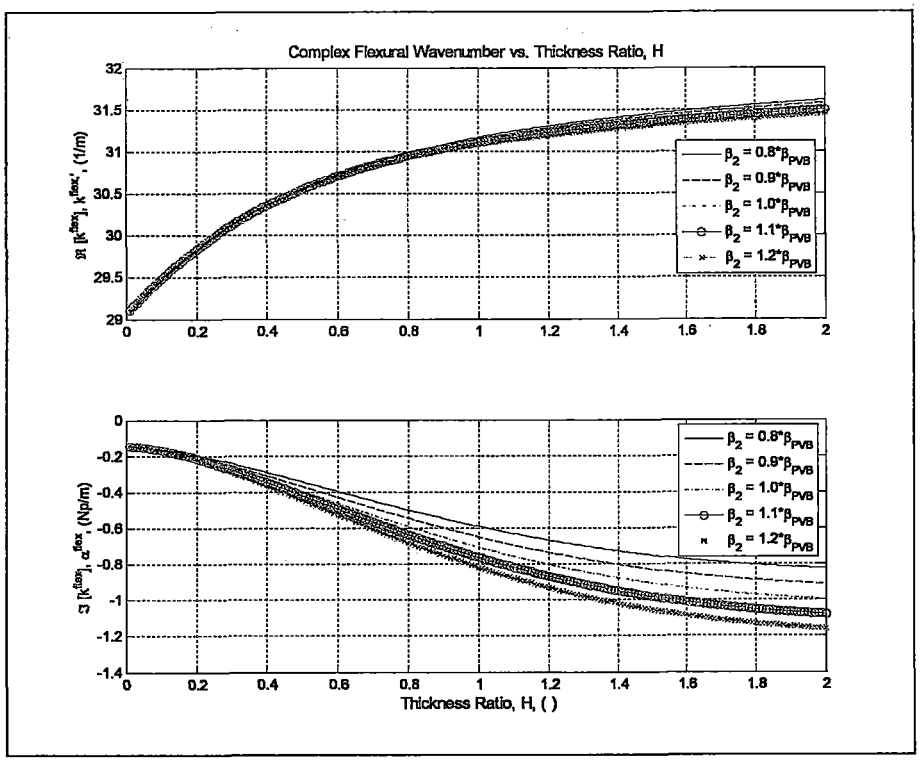

Figure 5-5: Variation of sandwich plate complex flexural wavenumber as a function of the thickness ratio, *H*. Parametric study on the shear loss factor of the interlayer.

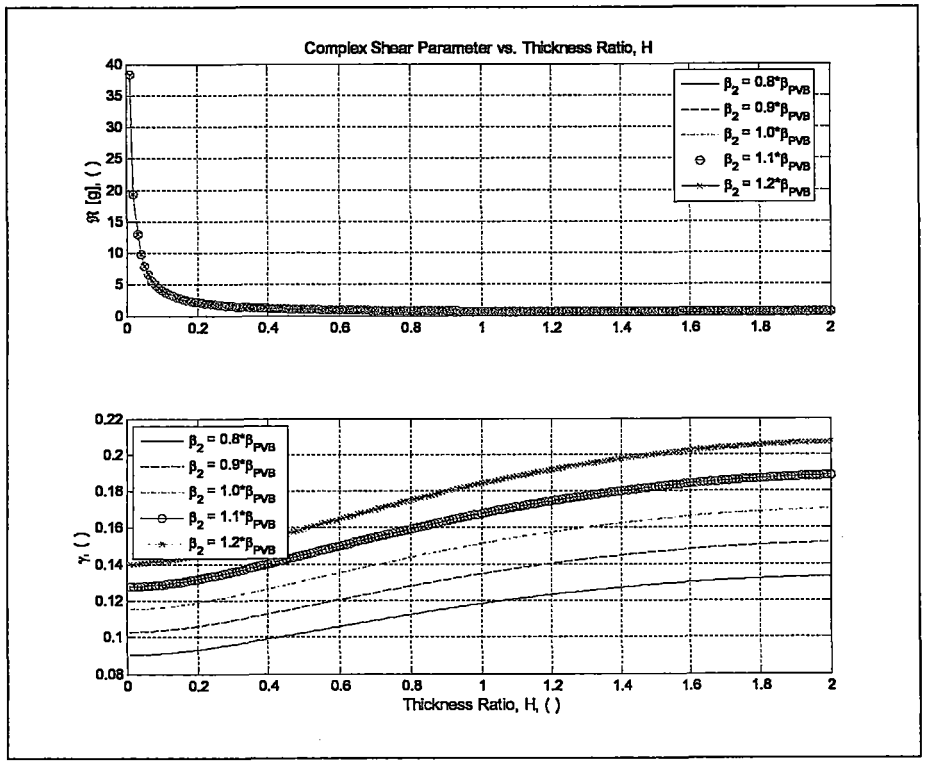

Figure 5-6: Variation of sandwich plate complex shear parameter as a function of the thickness ratio, *H*. Parametric study on the shear loss factor of the interlayer.

Several physically intuitive behaviors are apparent from these plots. Figure 5-4 shows that the plate's resistance to flexure decreases with increasing H. Coupled with this reduction in flexural rigidity is an increase in flexural loss factor. The increased damping capacity results from augmented strain energy located in the lossy interlayer. The increases in the magnitude of the flexural wavenumber and attenuation coefficient shown in Figure 5-5 are the result of a complex combination of increasing frequency and sandwich plate flexural compliance. Figure 5-6 illustrates that the shear parameter's loss factor also increases with increasing H and also as the shear loss factor of the interlayer, $\hat{\beta}_2$, increases. One very important observation is that the RKU model is *not* valid for small values of $|\hat{g}|$.

It is also interesting to inspect the flexural modulus variation as a function of the shear parameter's loss factor, $\hat{\gamma}$ while keeping H constant. Figure 5-7 shows the results of such a study.

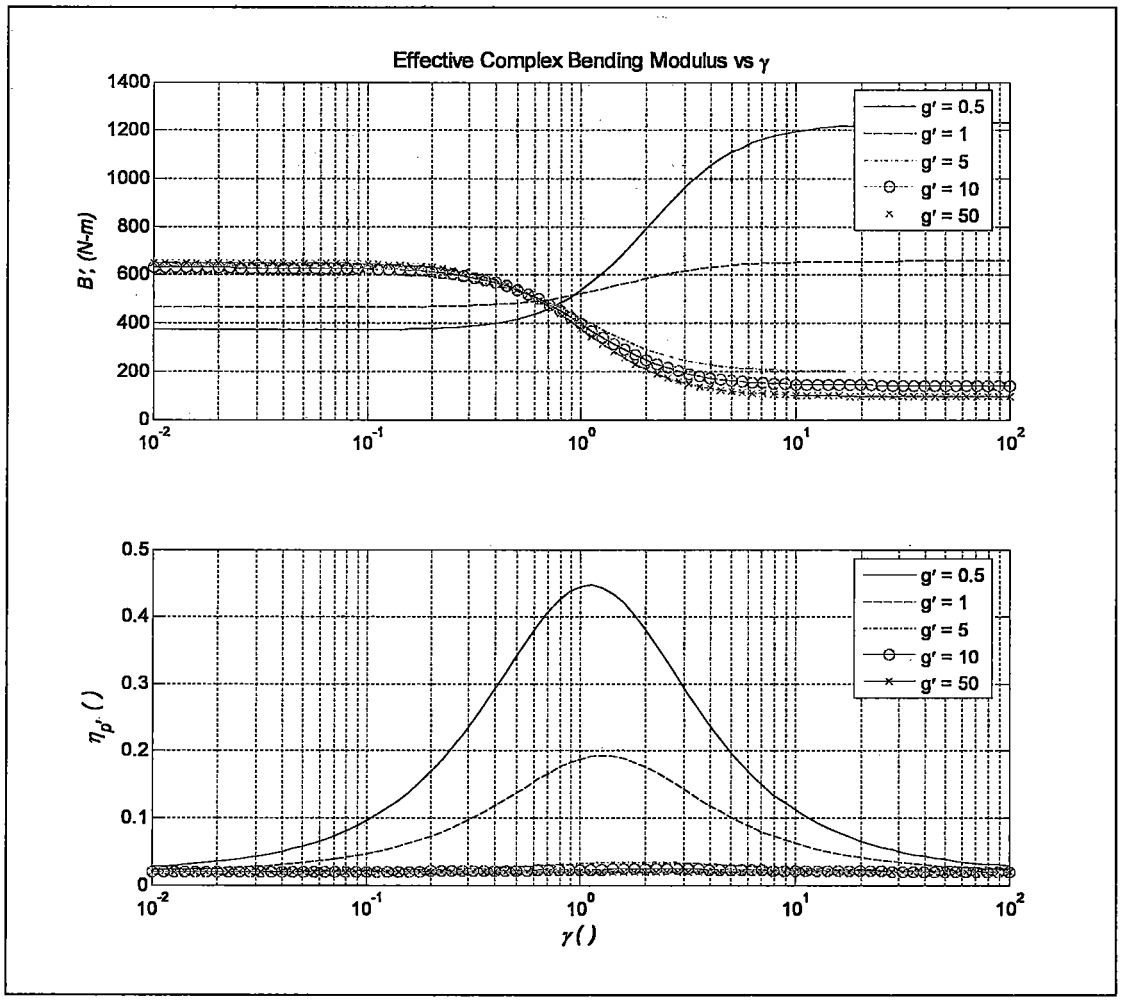

Figure 5-7: Complex effective flexural modulus calculated with BKT model as a function of the shear parameter's loss factor, γ for fixed values of g'.

This figure clearly shows that at a given frequency, ω, there exists some value of $\hat{\gamma}$ for each value of $\hat{g}'$ that yields optimal damping properties for a sandwich plate in flexure, $\hat{\eta}_p^{opt}$. If all other parameters are fixed, this optimal value of $\hat{\gamma}$ can be found through inspection of the partial derivative $\partial\hat{\eta}_p/\partial\hat{\gamma}$. Figure 5-8 shows the complex effective bending modulus for a large range of $\hat{g}'$ values when the associated value loss factor is optimal, $\hat{\gamma}^{opt}$. Mathematically stated, the value of $\hat{B}$ is calculated as a function of $\hat{g}'$ when the associated value of $\hat{\gamma}$ is such that $\partial\hat{\eta}_p/\partial\hat{\gamma}\big|_{\hat{\gamma}^{opt}} = 0$.

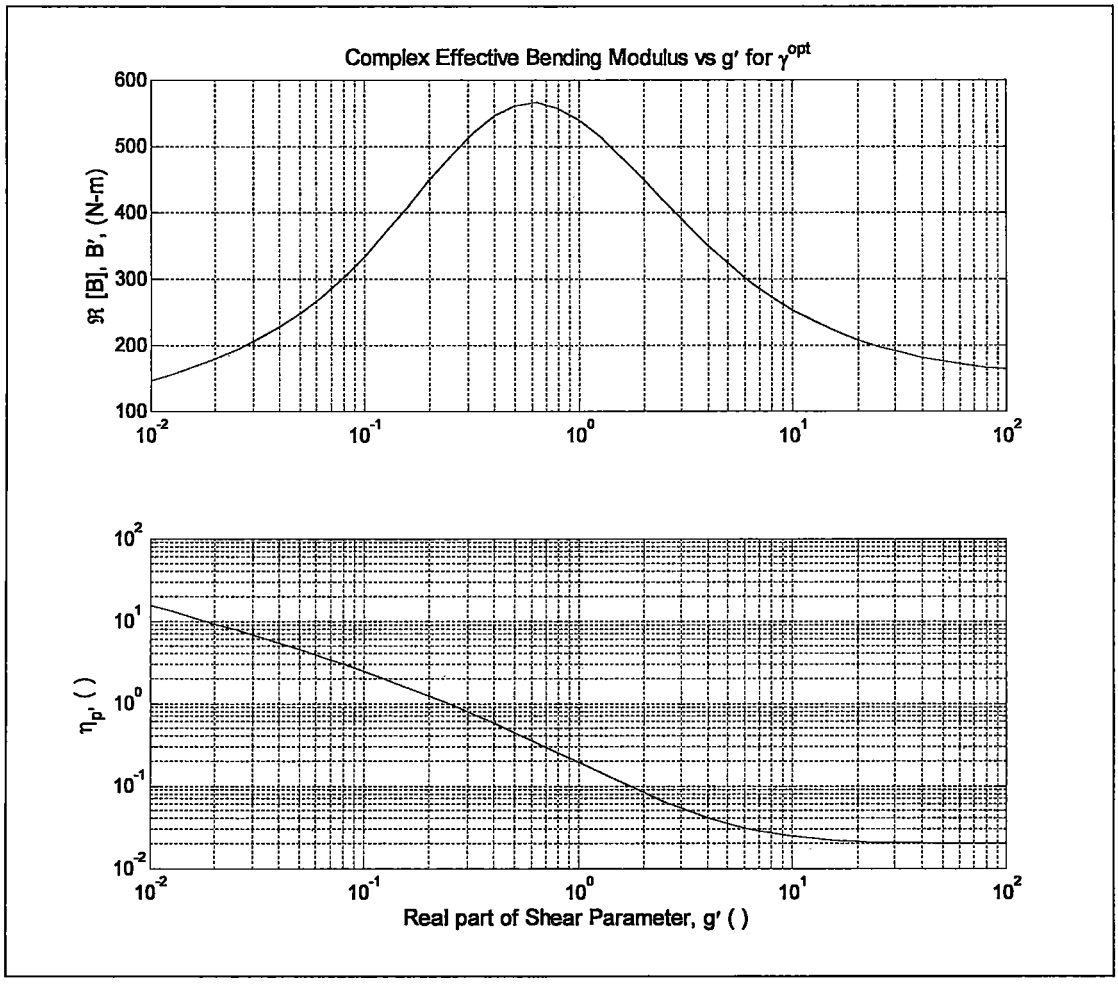

Figure 5-8: Optimally lossy complex effective bending modulus calculated as a function of $\hat{g}'$. The material properties employed are those given in Table 5-1

This plots clearly show that highest damping is expected with decreasing values of $\hat{g}'$. It is imperative to keep in mind, however, that the RKU model is not valid for small values of $\hat{g}'$. It is also important to observe that variations in $\hat{g}'$ have large effects on the plates overall resistance to flexural deformation. Large reductions in flexural rigidity, though ideal for damping applications, are not acceptable for such real-world applications as windshields which must fulfill multiple, often conflicting, design requirements [1]. The ideal solution for such an application is a more robust design that considers both the flexural rigidity, $\hat{B}'$, and damping capacity, $\hat{\eta}_p$, in an effort to find the highest damping capacity with a minimal reduction in rigidity.

5.3.2 RKU Model Sensitivity Analysis

The automobile windshield is a good example of a structural element requiring both structural rigidity and absorptive qualities. One simple manner to approach this optimization problem is through sensitivity analysis of important variables. The materials and geometry given in Table 5-1 are representative of actual values in current windshield design, however, Figure 5-6 shows that they yield a shear parameter far from optimal across all frequencies of interest: $H = 0.4$, $\hat{g}' \approx 2$, and $\hat{\gamma} \approx 0.13$ while $\hat{\gamma}^{opt} \approx 1.1$. All of the above information suggests that the most efficient means to increase the damping capacity of the plate while having a minimal effect on the flexural rigidity as a whole is to increase $\hat{\gamma}$ while minimally decreasing the real part of the shear parameter, $\hat{g}'$. It is assumed that structural design constraints require the total thickness and the real parts of the material properties remain constant. Therefore, the two remaining variables that can influence the plate's lossy behavior are the thickness ratio, H, and shear loss factor of the interlayer, $\hat{\beta}_2$. Figure 5-9 shows the results of this sensitivity analysis.

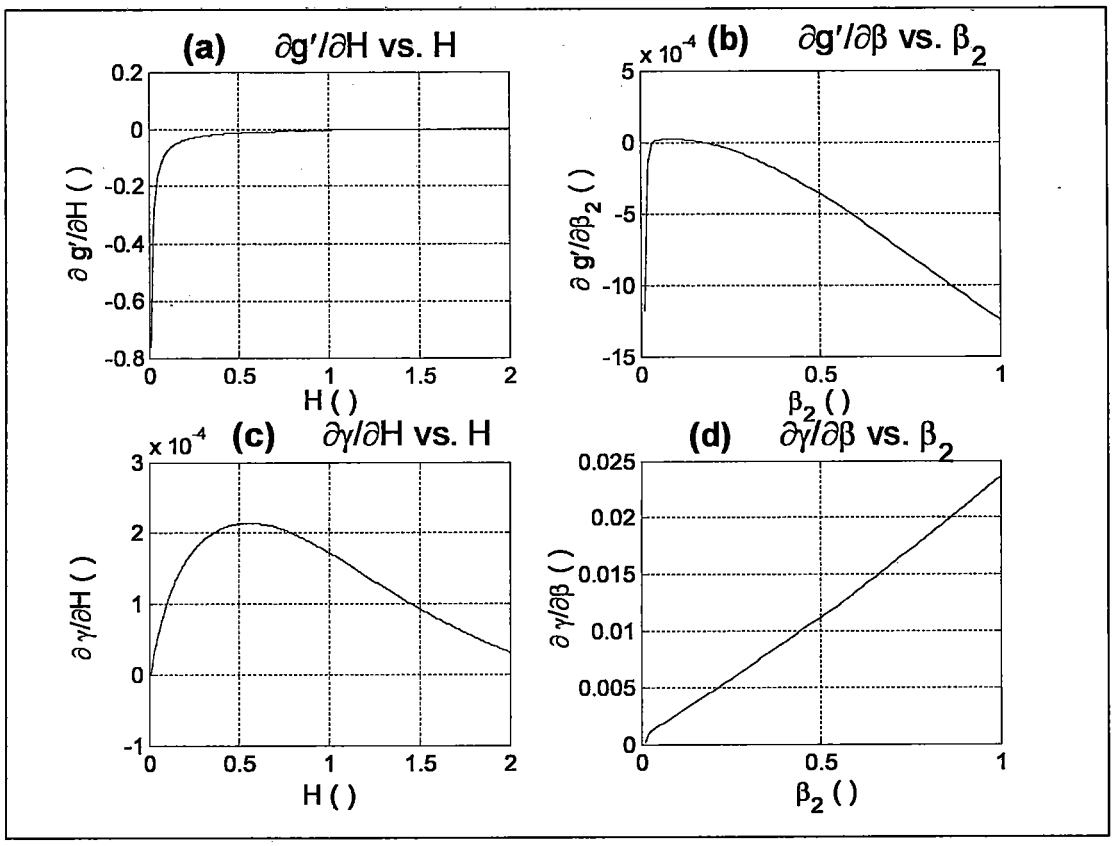

Figure 5-9: Sensitivity of the complex shear parameter to changes in the thickness ratio and the shear loss factor of the interlayer. Partial derivatives of g' and γ with respect to H and β_2 are shown. For (a) and (c), $\beta_2 = 0.13$; for (b) and (d), $H = 0.4$.

Figure 5-9a and Figure 5-9c show that varying the thickness ratio has a strong negative effect on the stiffness, analogous to a decrease in $\hat{g}'$, with minimal improvement of the damping capacity. On the other hand, it is obvious that an increase of the shear loss factor of the interlayer will have a notable effect on the damping capacity, $\hat{\gamma}$, with a minimal increase in compliance. Indeed, Figure 5-9d suggests that $\hat{\gamma}$ quadratically as a function of interlayer shear loss factor, $\hat{\beta}_2$. The previous chapter has shown that introducing inhomogeneities into a viscoelastic material can change the macroscopic damping capacity significantly. Section 5.5 will employ the SC model to investigate such microstructural effects on structural damping behavior. It should also be noted that the dependence of the complex shear parameter on the stiffness ratio, $\hat{\mu}_2'/\hat{E}'$, has also been studied. The results show, however, that when in the RKU's domain of applicability, specifically restriction (*1*),

variations of this ratio have little influence on the plate's damping capacity as a whole.

This section has shown that a simple analytical model for the effective bending modulus of a sandwich plate can yield considerable knowledge about the design space of a sandwich plate. The influence and interaction of design space variables has been investigated resulting in several guidelines for the design of the constituent materials. In short, the part level modeling performed here has given insight and a few "design handles" for lossy structure design. Further knowledge can be gained by exploring damping behavior on the structural level, the subject of the following section.

5.4 Structure level modeling

The previous section has shown that much information about constrained layer damping is gained from part level modeling and analysis. In application, however, such plates will be mounted in structures which excite structural vibration. The resulting structure level frequency response is governed by the part level behavior and the plate's boundary conditions [169]. Both the BC and the constitutive lossy behavior of the plate have a significant effect on the damping capacity of the structure as a whole. The analysis below extends the present analysis to forced vibration of beams and plates with viscoelastic BC. The study examines the independent influence of BC and plate lossy behavior on structural modal damping. It is limited to the vibration of *flat* constrained layer sandwich structures with simple plate geometries. The aim of this study is to approximate the behavior of a windshield mounted in a rubbery material in order to observe modal loss factor trends resulting from variations in the plate and BC material behavior. These trends are studied and it is shown how this information can be used to inform design on the part and microstructural scales. It is important to stress that the work presented here is an

elementary step in the material by design approach. It is submitted more as a proof of concept for SC model application as a material by design tool rather than as an exhaustive study. More advanced modeling techniques, such as finite element modeling, should be employed to approximate true BC and complex plate geometries which occur in reality. It is also instructive to study in-depth the systems approach to material design by Seepersad [20].

One initial validation of RKU model implementation into structural level models is a comparison of resonant frequency approximations and experimental observations. The results of acoustic Transmission Loss (TL) tests of four sandwich structures can be used for this purpose. The sandwich structures, prepared by Pacific Northwest National Laboratory (PNNL), were geometrically identical but each has slightly different viscoelastic interlayer materials. Generic sample geometry and material properties are given below in Table 5-2. The exact material properties of each interlayer material were not provided, but are known to be very close the PVB values provided in Table 5-2.

Table 5-2: Generic layer and plate properties used to approximate resonant behavior. ν ~ Poisson ratio, L ~ sample length, and W ~ sample width.

	H_x (mm)	$\mu(1+j\beta)$ (GPa)	ν ( )	ρ (kg/m^3)	L (cm)	W (cm)
Layers 1&3	2.0	29.5(1 + 0.02j)	0.23	2469	30.5	30.5
Layer 2	0.8	0.133(1 + 0.13j)	0.49	1115	30.5	30.5

Two resonant frequency approximations, one corresponding to a Law of Mixtures (LOM) homogenization and the other to RKU modeling of sandwich plate material properties, are given below in Table 5-3. These values were calculated using the information in Table 5-2 and eigenvalues based found through Rayleigh-Ritz methods provided by Angloulvant [170].

Table 5-3: Approximate sandwich plate resonant frequencies from LOM and RKU model homogenization.

Part-Level Model	*Resonant Frequency of 1st Six modes (Clamped Boundaries)*					
	f_{11} (Hz)	f_{12} (Hz)	f_{22} (Hz)	f_{13} (Hz)	f_{23} (Hz)	f_{33} (Hz)

LOM	580	1100	1620	1900	2390	3150
RKU	518	970	1418	1648	2100	2780

TL testing was done for third-octave bands between 125 Hz and 8 kHz in accordance with SAE J1400 [171]. Samples were mounted in the test window between the reverberant chamber and the semi-anechoic chamber of the Integrated Acoustics Laboratory (IAL) at Georgia Institute of Technology in Atlanta. Figure 5-10 shows a schematic of the test setup and Figure 5-12 shows an image of the test window.

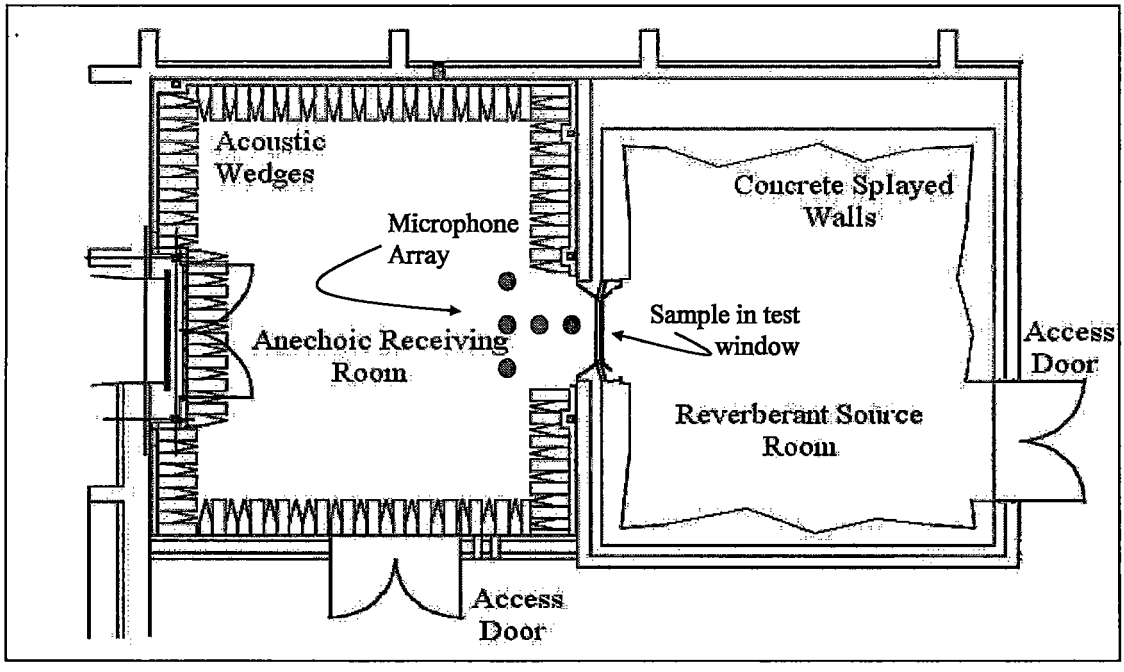

Figure 5-10: Schematic of general set-up used for SAE J1400 TL testing.

Figure 5-11 plot experimental TL results of the four different glass-viscoelastic sandwich plates. This experimental data shows two important facts: (1) an increase in the interlayer damping capacity (S4) leads to a notable increase in TL and (2) incorporation of RKU part level modeling into structural models yields increased accuracy in the approximation of the first and second resonant frequencies. The first point validates the discussion given in the previous section and the second validates employment of the RKU model in structural models such as modal analysis.

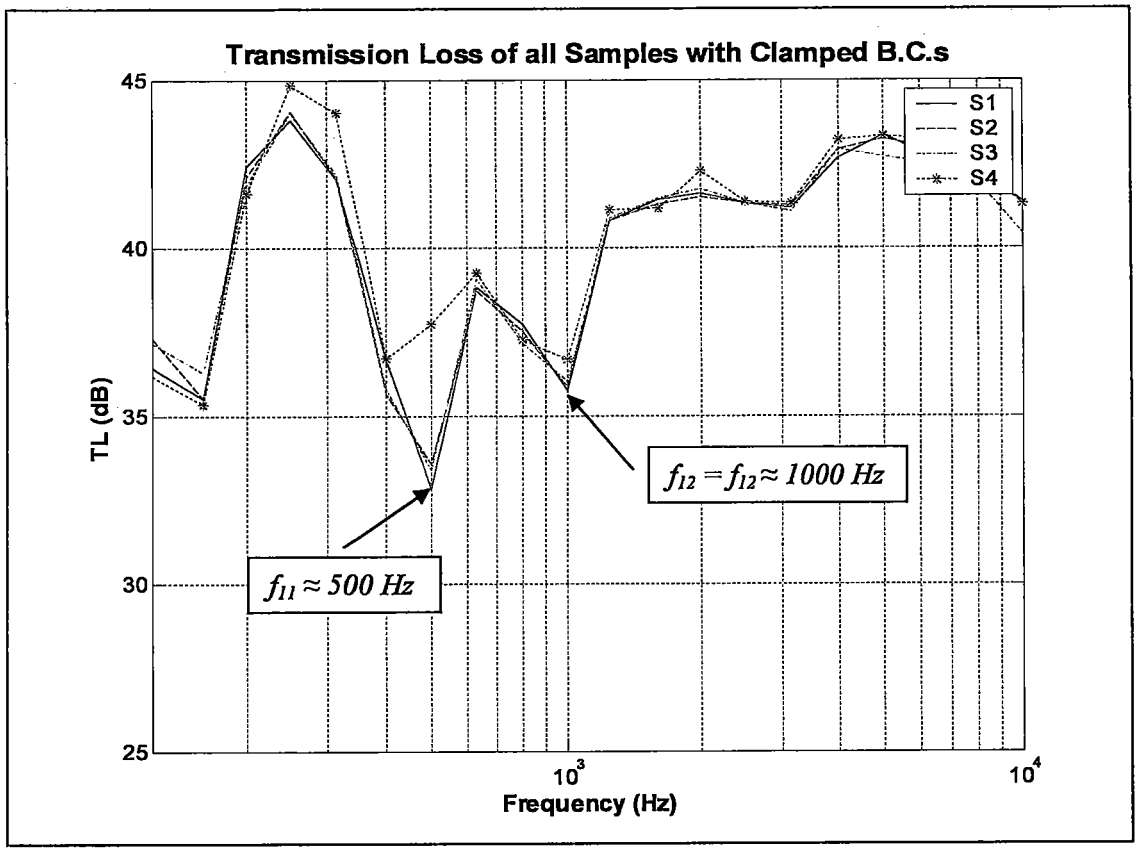

Figure 5-11: TL due to four different windshield samples. Notches in TL at ~ 500 Hz and ~ 1000 Hz agree well with RKU model approximation.

One further validation provided by these experiments is the effect of BC on observed TL. The experimental data in Figure 5-11 was taken with samples having clamped BC as shown in Figure 5-12.

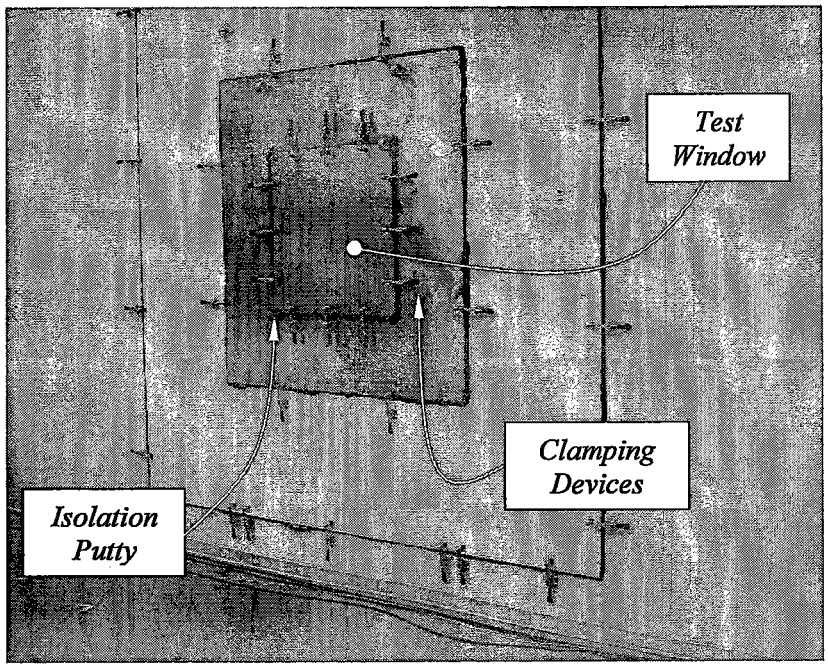

Figure 5-12: TL experimental setup. Sample window contains stainless steel plug. Note red clamps and isolation putty around exterior of test window.

The clamped conditions were modified in another set of tests by releasing the red clamps seen above in Figure 5-12 to approximate viscoelastic boundary conditions. The exact conditions are very difficult to quantify because the samples were held in place only by isolation putty whose purpose is to seal air gaps between the reverberant and semi-anechoic chambers. Though they are difficult to quantify analytically, the experimentally observed quantitative difference in TL near the first resonant frequency is significant (~ *-4dB re 20μPa*), see the results for S1 shown in Figure 5-13. These results also show the expected reduction in resonant frequency resulting from the decreased "stiffness" of the structure as a whole resulting from the viscoelastic BC.

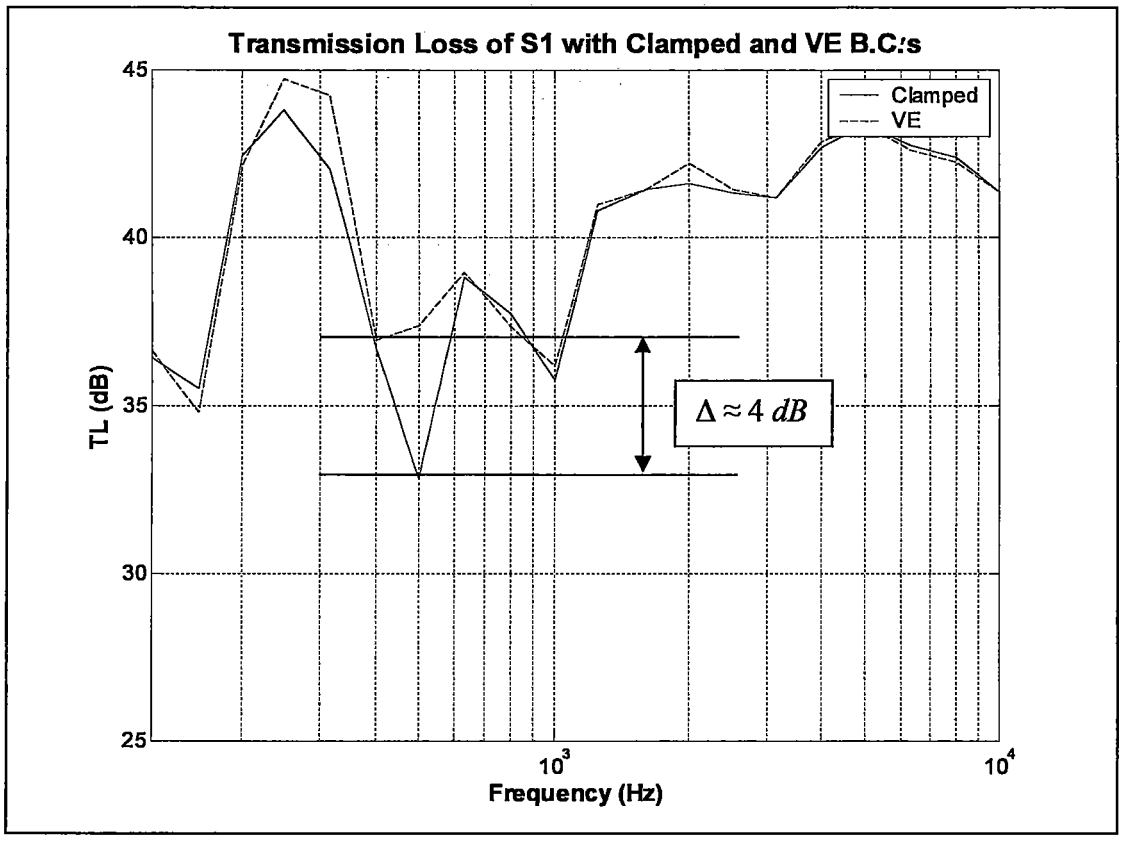

Figure 5-13: TL results for S1 with different boundary conditions. Viscoelastic BC show a substantial increase in observed TL.

5.4.1 Analysis of the lossy behavior of simplified structures

The TL study results shown in Figure 5-13 illustrate the need to incorporate plate boundary conditions into structural level models. The inclusion of influence of BC on the structural level lossy behavior adds another degree of freedom to the design space and more closely approximates real-life applications. This sub-section inspects the influence of viscoelastic boundaries on the lossy behavior of two simplified structures, a viscoelastically constrained beam and a viscoelastically constrained circular plate, through modal analysis. The ultimate aim of this study is to allow the approximation of changes in the structural level lossy behavior as a function of variations in constituent material microstructure. Such an analysis gives a clearer picture of how microstructural variations propagate to higher length scales and thereby illustrates the value of SC micromechanical modeling in the design process.

5.4.1.1 Forced vibration of a beam with elastic boundary conditions

One of the simplest ways to quantify the modal loss factor of a uniform beam due to different boundary conditions is to find the solution for the general case of a vibrating beam with elastic boundary conditions as shown below in Figure 5-14. The present analysis finds this solution for a beam of uniform cross-section and material properties as a function of x. The present work is also limited to classic plate theory, which is discussed at length elsewhere [172].

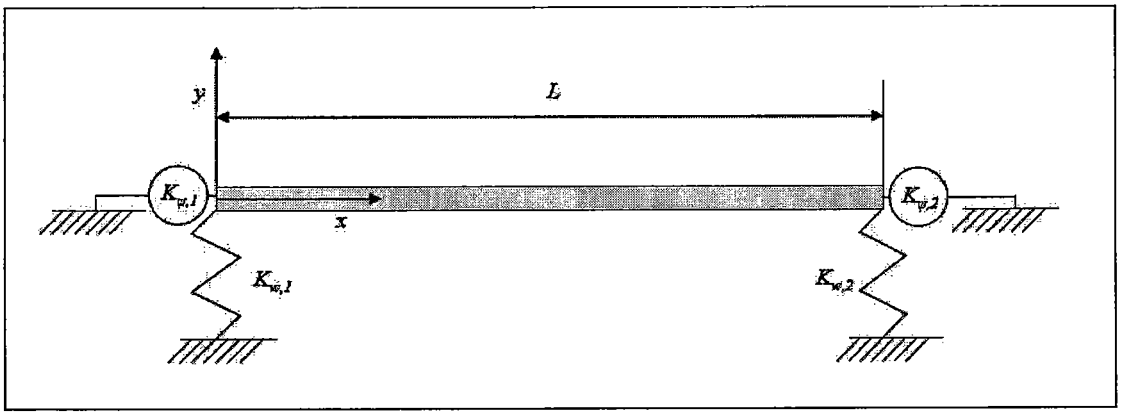

Figure 5-14: Schematic of an elastically constrained beam.

The advantage of finding a solution to the forced vibration of such a beam is that it can easily be modified to approximate many different boundary conditions by changing the values associated with the linear displacement springs, $K_{w1,2}$ [N/m], the rotational displacement springs, $K_{\psi 1,2}$ [N·m], or both, see Appendix E for examples and model validation. Figure 5-15 shows one approach to approximating these coefficients, representing viscoelastic boundary conditions at the extents of the beam, from the viscoelastic material constants in which the beam is embedded and the boundary geometry. Through application of the elastic-viscoelastic correspondence principle the boundary conditions can be altered to study the effects of different

viscoelastic boundary conditions and interlayer materials on modal damping. The derivation of the general solution is given in Appendix E.

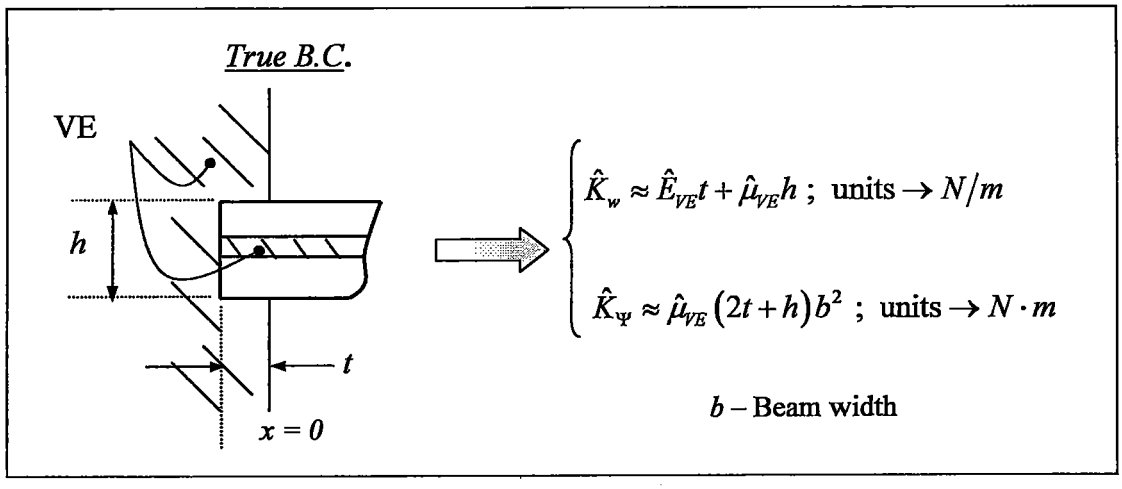

Figure 5-15: Approximation of viscoelastic boundary conditions as linear and rotational springs.

One way to check this nested analytic multiscale modeling approach is to compare modal analysis results from the analytic models above to FE approximations. Figure 5-16 shows the results of a study that employed these two different approximations methods. The subject of study is a sandwich beam with a length $L+t$, a total thickness h, and a width b. The beam is embedded at $x = 0$ in a viscoelastic medium which has the same material properties as the beam interlayer. The beam dimensions and material properties are given in Table 5-4. For this study the beam is excited using a time varying spatially uniform pressure on the top surface thereby simultaneously exciting all modes of vibration.

Table 5-4: Sandwich beam geometry and properties for analytic and FE study in Figure 5-16.

	$H\,(m)$	$L\,(m)$	$t\,(m)$	$b\,(m)$	$\mu\,(GPa)$	$\nu\,()$	ρ (kg/m^3)
Layer 1&3	2.0×10^{-3}	0.100	1.0×10^{-2}	0.01	29.5	0.23	2469
Layer 2	1.0×10^{-3}	0.100	1.0×10^{-2}	0.01	$0.133+0.13j$	0.49	1115
BC	5.0×10^{-3}	---	1.0×10^{-2}	0.01	$0.133+0.13j$	0.49	1115

The analytical approach employed approximates sandwich beam behavior using the RKU model and the resulting effective bending modulus is used in model

general vibrating beam model derived in Appendix E. It is important to stress that the value used for the Poisson ratio, ν_{12}, is that of the glass plate material, $\nu_{1,3}$, for implementation of the model derived in Appendix E. The analytic model results were compared to FE analysis to validate employing such a simplified multiscale modeling approach. The FE results were calculated using the sophisticated FE model of Daya and Potier-Ferry [83] where the viscoelastic boundaries were *not* approximated as linear and rotational springs, but as an embedding material, and therefore represent reality much more closely. In both cases the modal loss factor was estimated using the half-power beam width method from the calculated beam frequency response [169].

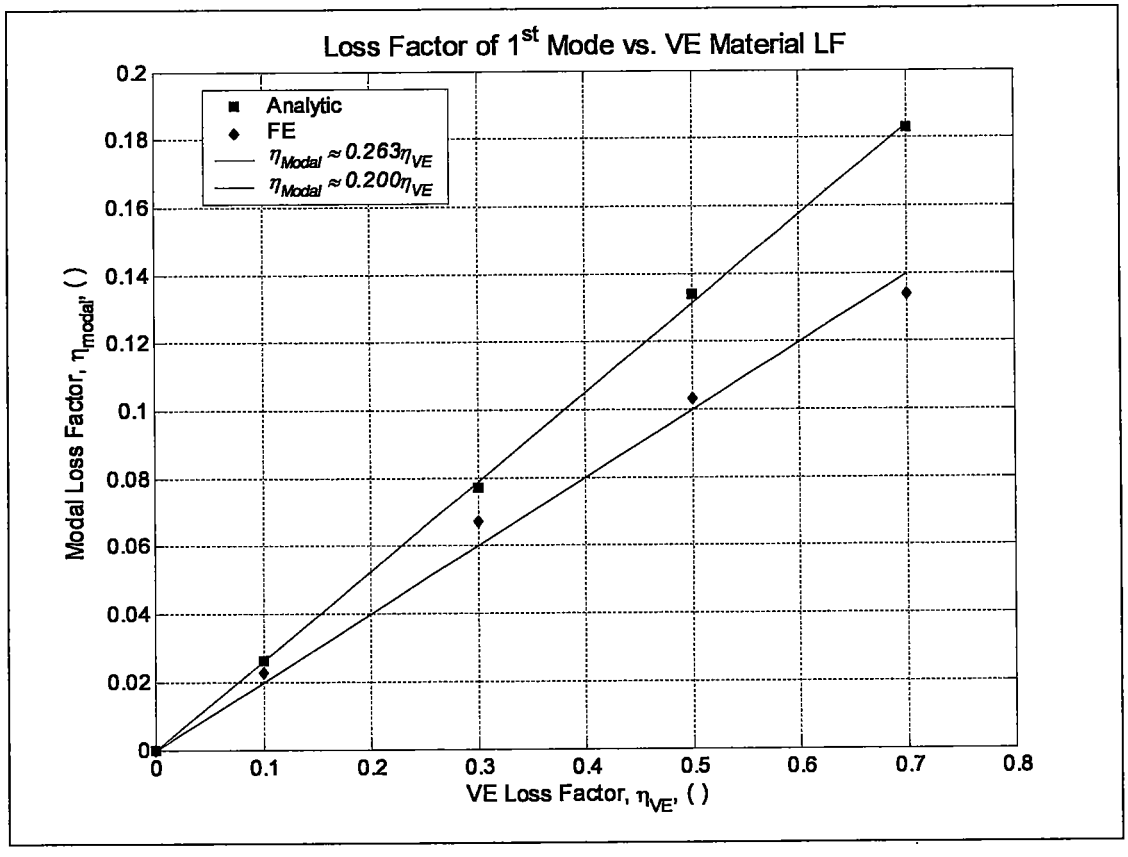

Figure 5-16: Viscoelastically constrained beam LF as function of the LF of constraining and interlayer materials. Multiscale model comparison with FEA model derived by Daya and Potier-Ferry [83]

The results shown above have several encouraging points. First, it is obvious that the viscoelastic material lossy behavior has a linear effect on the macroscopic

damping properties of the structure for *low* loss factor values. This is to be expected [169]. When the value of the loss factor increases the analytic approach presented here will no longer be valid and more involved analytic models or FE models are required. Indeed the plot suggests that the validity of the proposed method is questionable for η_{VE} values exceeding ~ 0.5. Another encouraging point is the agreement between this simple analytic approach and the FE model. Considering all of the simplifying approximations, especially those concerning the viscoelastic boundaries, the estimates provided by the analytic model are quite close. The over-estimation provided by the analytic model is in part explained by the well-known fact that the RKU model generally provides superior damping estimates to those observed in reality [165]. More importantly, this comparison validates using the RKU model in such a multiscale approach. The analytical nature of this nested multiscale model approach permits efficient study of the influence of different BC, constituent material properties, and microstructures on structural damping behavior, thereby reducing the overall computational load. It is for this reason that it is attractive as a first step in the design of absorptive materials.

5.4.1.2 Forced vibration of an elastically constrained circular plate

It is instructive to study a two dimensional plate in order to move closer to true windshield structure. This is most easily accomplished through analytical methods by studying the vibration of a circular plate. Due to symmetries, the circular plate solution can be found through analytical methods thus eliminating the need for Rayleigh-Ritz schemes which are inherent in two-dimensional rectangular plate models [169, 172]. This fact simultaneously reduces modeling complexity and computational load. Further, the main objective of the following study is to show the effects of component viscoelasticity on the system response so the actual geometry is unimportant as long as the plate is two dimensional. As with prior beam problem, it is

essential to first find the solution for the general case of a plate having cross-section and material properties which are uniform in the plane of the plate with elastic boundary conditions at $r = a$. Figure 5-17 illustrates this geometry. A detailed derivation of the general solution of a vibrating circular plate with elastic BC is given in Appendix E.

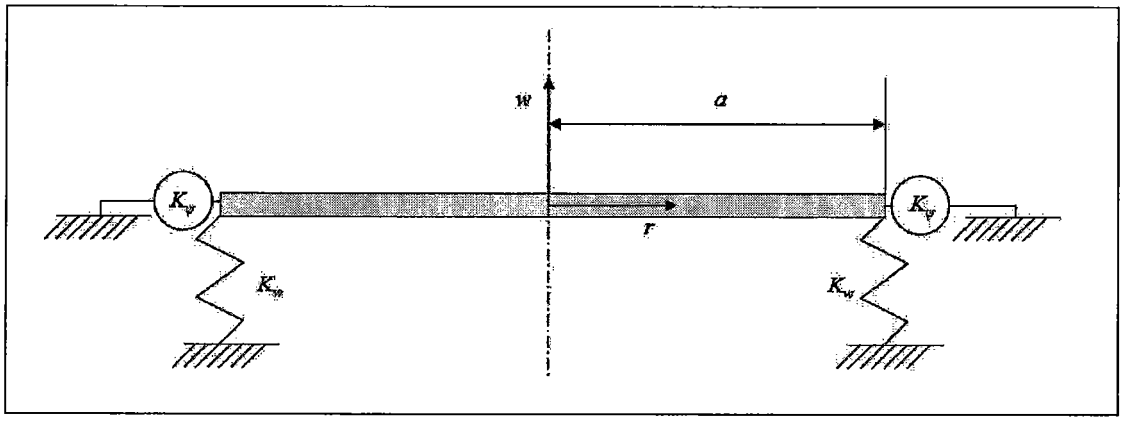

Figure 5-17: Schematic of elastically constrained circular plate.

The advantage of the resulting solution is that it is easily modified to represent many different boundary conditions by changing the values associated with the distributed linear displacement spring, K_w [N/m^2], the distributed rotational displacement spring, K_ψ [N], or both. These coefficients are chosen to represent elastic boundary conditions at $r = a$ by relating them to the material constants in which the plate is embedded and the geometry of the plate-boundary interface. A simple approximation scheme is shown below in Figure 5-18. Their effect on the modal damping can then be studied by assigning complex values to the elastic BC and plate materials.

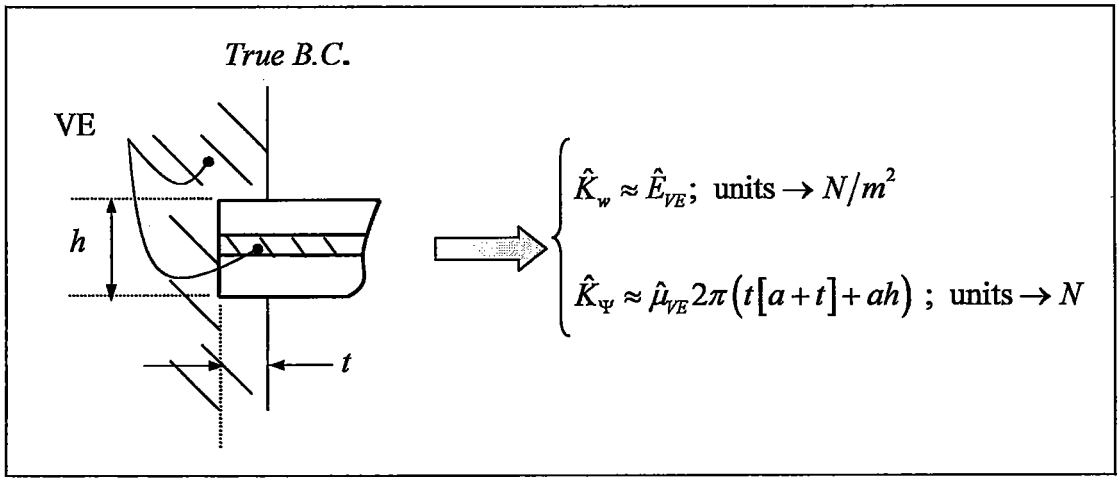

Figure 5-18: Approximation of viscoelastic boundary conditions as linear and rotational springs.

One of the main objectives of design is efficiency. Design efficiency refers to the ability to arrive at a design that fulfills all requirements though minimal design iterations and by *reducing* variables in the design space. Keeping this in mind, it is interesting to study the relative effect each "component" contributes to damping plate vibration at the first resonant frequency. The following study investigates the independent effects of lossy behavior of the plate, linear spring, and rotational spring on the modal loss factor of a viscoelastic constrained circular plate. This is done in an effort to shed light on the most efficient means of damping resonant behavior and is accomplished via three different studies. The plate geometry and material properties employed in these parametric studies are detailed in Table 5-5. It is important to note that the plate studied in each of these studies *is not* a sandwich structure and therefore only the effects of lossy plate behavior are studied.

In the first parametric study the plate is pinned at $r = a$ ($K_w \rightarrow \infty$) and the plate material is a homogeneous non-lossy glass. The values for the rotational spring are calculated according to the equation given in Figure 5-18 using shear modulus values given in the PS1 row of Table 5-5. Shear modulus loss factor values are varied between *0* and *1* and the half-power bandwidth method is employed to calculate the loss factor of the first mode. For the second parametric study the slope of the plate is required to be zero at $r = a$ ($K_\psi \rightarrow \infty$) and the plate material is again a homogeneous

non-lossy glass. The linear spring values are calculated from the equation given in Figure 5-18 using shear modulus values given in the PS2 row of Table 5-5. Again the shear modulus loss factor values are varied from *0* to *1* and the results of the structural model yield the modal loss factor of the first mode via the half-power bandwidth method. The final study represents the behavior of a clamped ($K_w \to \infty$ and $K_\psi \to \infty$) viscoelastic plate where the plate material loss factor is varied between *0* and *1*. The results of these three studies are given in Figure 5-19.

Table 5-5: Plate geometry and material properties for parametric studies of component influence on structural damping.

	$a\ (m)$	$h\ (m)$	$t\ (m)$	μ_{VE} (GPa)	$\nu_{VE}\ ()$	E_p (GPa)	$\nu_p\ ()$	K_w (N/m^2)	$K_\psi\ (N)$
PS1	0.100	0.005	0.010	0.133 $(1+\eta j)$	0.49	72.0	0.23	$1\text{x}10^{10}$	calc $\in \mathbb{C}$
PS2	0.100	0.005	0.010	0.133 $(1+\eta j)$	0.49	72.0	0.23	calc $\in \mathbb{C}$	$1\text{x}10^{10}$
PS3	0.100	0.005	0.010	0.133	0.49	72.0 $(1+\eta j)$	0.23	$1\text{x}10^{10}$	$1\text{x}10^{10}$

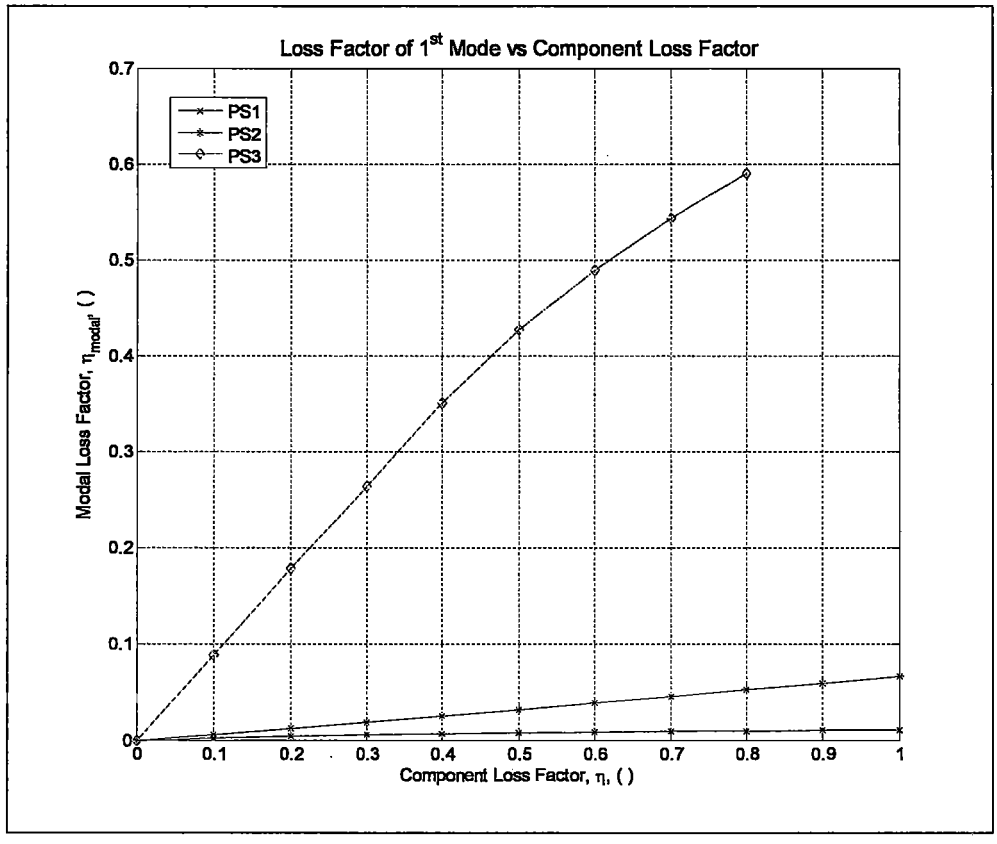

Figure 5-19: Modal loss factor of vibrating plate as a function of each contributing element. PS1 indicates the influence of the rotational spring loss factor, PS2 indicates the effect of the linear spring's loss factor, and PS3 indicates the beam loss factor's influence.

The results of these parametric studies clearly show that lossy plate behavior dominates damping behavior on a structural scale. It is therefore obvious that the most efficient means to achieve increased acoustic and vibrational isolation with a constrained plate is to increase the plate material loss factor. It must be stated that this study assumes that all other parameters remain equal, which is often difficult to achieve in reality. Indeed, increasing the material loss factor *usually* implies an undesired decrease in material strength: the classic dichotomy of material strength versus damping. Recent research suggests, however, that the introduction of certain trace microstructural heterogeneities can have marked effects on material damping behavior while minimally affecting material strength [9, 10, 12]. For this reason it is very interesting to study the present nested multiscale modeling approach and its capacity to capture micro-scale influence on the structure-level damping behavior.

5.5 Microstructural influence on structural damping capacity

The final validation step for the proposed multiscale modeling approach is to inspect the influence of microstructural changes on structure level damping. The results of such a study will provide a complete picture of the role of microstructure in structure-level damping of a vibrating sandwich plate. It will also illustrate how multiscale modeling lends designers high levels of control and insight at each individual scale and how changes at one level propagate through length scales. This section, therefore, endeavors to incorporate the quasi-static SC micromechanical model developed in Chapter III into the multiscale model detailed in the prior sections and to show microstructural influence on structural behavior.

Previous sections have investigated the influence of material loss factors and sandwich geometry have on structural damping. Chapter IV made it abundantly

obvious that changes in material microstructure can greatly increase material damping capacity by altering the amount of strain energy present in lossy material phases under identical loading conditions. The loads applied to windshield sandwich plates result from air-structure coupling, frame vibrations, and projectile impacts. All of these loads are fixed force/stress loads, as opposed to displacement or strain based loads. The simplest way to increase strain energy in lossy material components for such loading is to increase their compliance. Chapter IV illustrated that this can be achieved by introducing inclusions into a viscoelastic material which are less rigid than the host. Voiding a material is the most efficient known means of increasing a composite viscoelastic compliance [28] and therefore voided viscoelastic material is subject of this study. The scope of this study, however, is limited to isotropic bi-phase particulate composites resulting from a viscoelastic host material containing spherical voids.

Several points must be raised in regards to such a treatment for an automobile windshield. Voiding a windshield interlayer material has both positive and negative aspects. The most apparent drawback is that introducing heterogeneities of any kind will have a negative impact on the light transmission. The same scattering phenomena addressed in Chapter II with respect to acoustic waves are applicable to light waves when there is a material discontinuity. The major difference is that for light waves the ka value will be much larger and, consequentially, light scattering effects will be pronounced. Light scattering leads to poor windshield transparency and is a *major* restriction to the introduction of voids to achieve elevated windshield damping capacity. However, the physical mechanisms leading to enhanced energy dissipation, namely increasing strain energy in lossy components, are not restricted to voids. Ideally a material can be found to take the place of voids which has weak elastic constants but an index of refraction similar to the viscoelastic interlayer. This would eliminate light scattering problems. It is also possible that materials can be found which can analogously increase lossy behavior through the addition of only infinitesimal amounts of heterogeneity. A positive aspect of introducing voids into

the interlayer material is that the resulting sandwich windshield will have a lower density. Lower overall density translates to increased energy efficiency which is a very desirable consequence.

5.5.1 Microstructure → Part level modeling

To study void fraction effect on part level behavior, it is interesting to re-visit the parametric studies shown in Section 5.3.1. Figure 5-4 – Figure 5-6 of that section investigated changes in the complex effective bending modulus, the flexural wavenumber, and the shear parameter as a function of the thickness ratio for several values of interlayer shear loss factor. The plots showed that increasing interlayer material loss factor has a positive influence on the plate damping capacity. The most desirable result shown was that by only varying the material loss factor, i.e. no change in shear stiffness, the bending loss factor increased while only slight change was observed in the real part of the effective bending modulus. Similar plots are shown below where the interlayer void fraction is varied in order to observe the effect on the complex effective flexural behavior.

Figure 5-20 clearly shows that the void fraction has a strong influence on the effective complex bending modulus. The reduction in real part, $\hat{B}'$, is rapid with increasing void fraction for any fixed thickness ratio, H. This is an undesirable result of adding voids to the interlayer material. Conversely, the bending modulus loss factor, $\hat{\eta}_p$, quickly increases as a function of void fraction.

Table 5-6: Material properties used to produce Figure 5-20 - Figure 5-24 and Figure 5-26. The viscoelastic properties are calculated from (V.3.9) and the HN coefficients given in the associated paragraph for an exciting frequency of 1 kHz.

	μ_{VE} (GPa)	ν_{VE} ()	ρ (kg/m^3)	E_p (GPa)	ν_p ()	ρ (kg/m^3)	μ_{void} (GPa)	ν_{void} ()	ρ (kg/m^3)
Property	0.133 (1+0.13j)	0.49	1115	72.0 (1+0.02j)	0.25	2469	1×10^{-8}	0.45	1.21

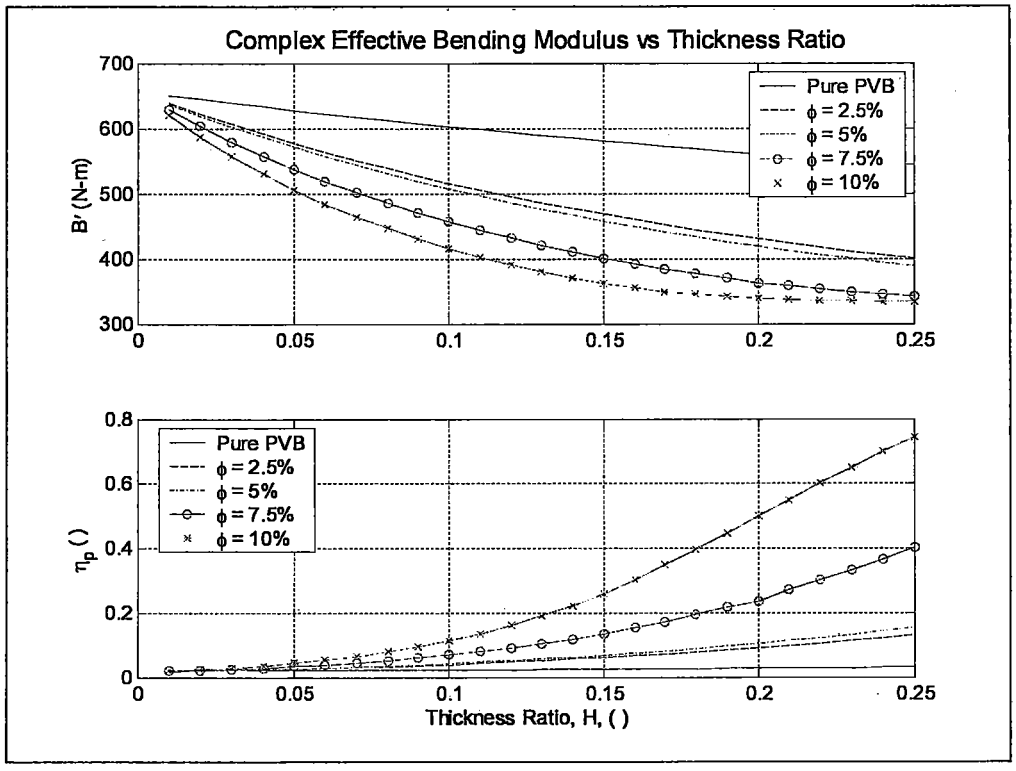

Figure 5-20: Effective bending modulus as a function of layer thickness ratio for varying values of interlayer void fraction at f = 1 kHz.

The increased damping capacity is further evidenced by inspecting the results in Figure 5-21 and Figure 5-22. The prior shows the effective complex flexural wave number and the latter a measure of the attenuation per flexural wavelength suggested by Kinsler *et al* [88], $\hat{\alpha}^{flex}/\hat{k}^{flex,'}$. The wavenumber plot shows two interesting aspects. The most obvious observation is that the magnitude of the flexural attenuation coefficient, $\hat{\alpha}^{flex}$, monotonically increases both for a fixed void fraction with increasing thickness ratio and for a fixed thickness ratio with increasing void fraction. This is due to the fact that both changes, increasing void fraction and increasing thickness ratio, result in increased plate flexural compliance. The increased compliance augments the strain energy present in the viscoelastic material for a fixed applied moment/stress, thereby increasing the damping capacity of the plate. The less obvious result is the non-monotonic behavior of the real part, $\hat{k}^{flex,'}$. For a fixed frequency, an increase in real part of the wavenumber implies a decrease in the wave speed, $\hat{c}^{flex}$, since $\hat{k} = \omega/\hat{c}$. Because the flexural wave speed is related

indirectly to the inverse of the modulus through Equation (V.3.2), it would seem apparent that a decrease in the real part of the flexural modulus would likewise lead to an increase in the real part of the wavenumber. However, for high loss factor values, this is not always the case. The relationship between the real parts of these two quantities is *not* independent of the flexural modulus loss factor. It is for this reason that Figure 5-22 shows non-monotonic curves for $\hat{k}^{flex,'}$ and that the maximum value is observed for consecutively smaller thickness ratio values as the void fraction increases. The non-dimensional measure of attenuation plotted in Figure 5-22 clearly shows that the attenuation efficiency is a monotonic function of both the thickness ratio and the void fraction despite the increased wave speed for all values inspected. One further observation of effective plate behavior concerns the shear parameter. Figure 5-23 shows that values of $\hat{g}'$ decrease rapidly with increasing void fraction and thickness ratio. The RKU model is only valid when $\hat{g}' > 1$ implying that the RKU model may give erroneous values for thickness ratios exceeding ≈ 0.2.

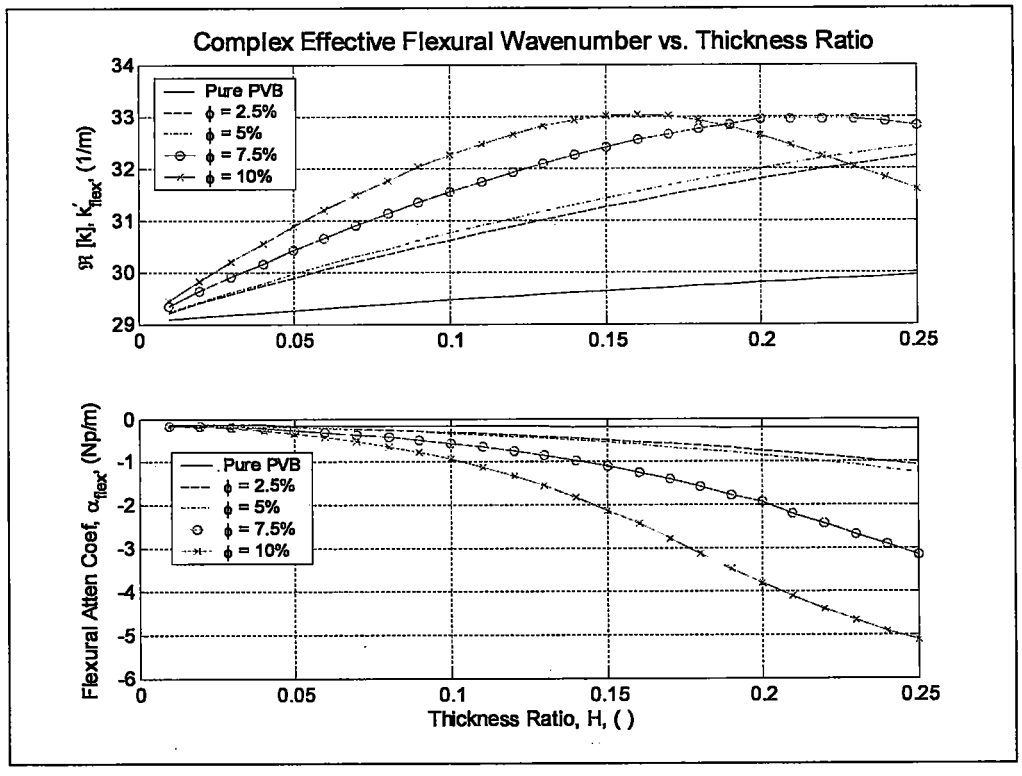

Figure 5-21: Effective flexural wavenumber as a function of the thickness ratio at $f = 1$ kHz for a several different void fractions.

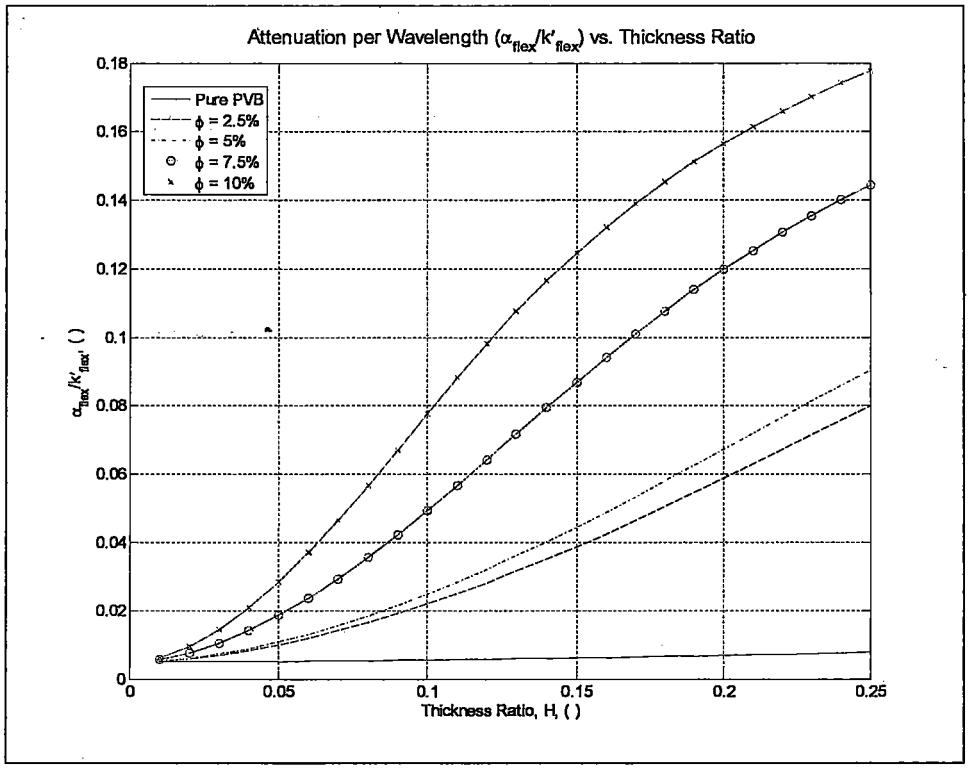

Figure 5-22: Measure of damping amplitude attenuation per flexural wavelength for layered plate homogenized using RKU model with a voided interlayer.

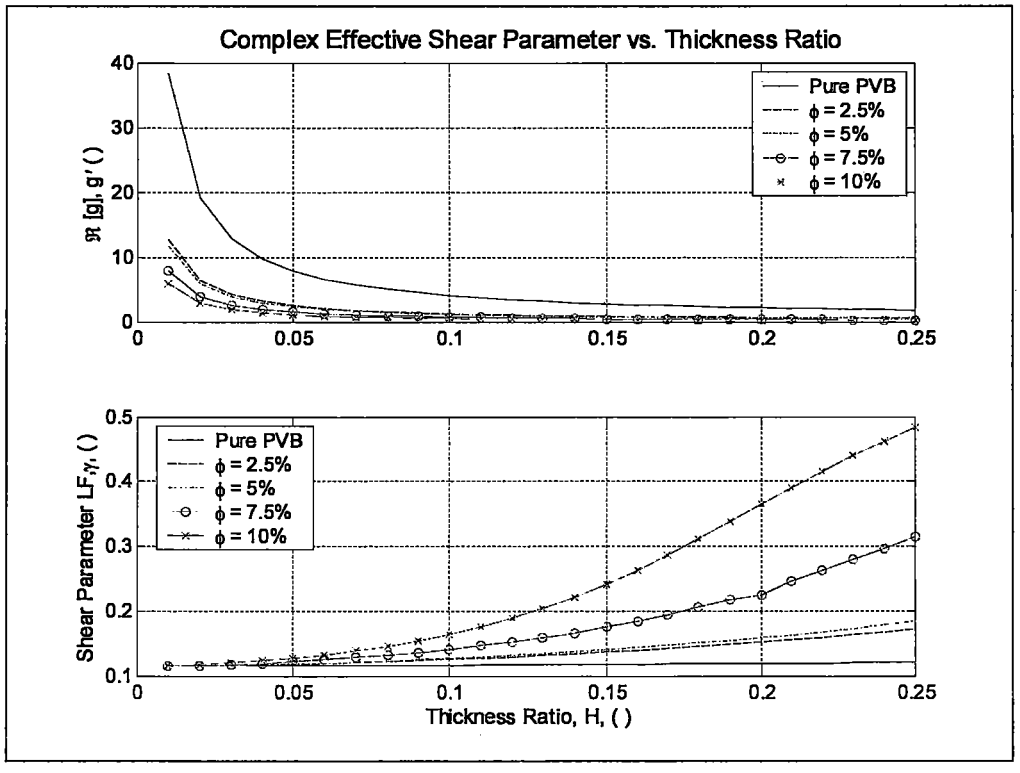

Figure 5-23: Effective shear parameter as a function of the layer thickness ratio for several values of interlayer void fraction at f = 1 kHz.

5.5.2 Microstructure → Structure level modeling

The final subject of interest is the influence of microstructural changes, in the form of void fraction, on structure-level damping. The results are presented in two different ways. First changes in the modal loss factor of a vibrating circular sandwich plate as a function of viscoelastic interlayer and boundary void fraction are shown. This yields insight into the increased capacity of the sandwich structure to damp resonant behavior. The second study approximates windshield transmission loss for an incident plane wave as a function of frequency. The results of this study illustrate relative acoustic isolation improvements of a voided interlayer.

Section 5.4.1.2 presented the effects of different lossy elements on the damped behavior of a viscoelastically constrained circular plate. Though it was shown that the most efficient means to damp flexural vibrations is by elevating the beam loss factor, it is of interest to demonstrate the generality of the nested multiscale approach through a study that take into account the behavior of voided viscoelastic boundary conditions and sandwich interlayer. For this purpose the following studies the damped 1st resonance of a circular sandwich plate embedded at $r = a$ in a voided viscoelastic material. The interlayer material is also assumed to contain voids with the same volume fraction. For this study the same materials and geometries are employed as those presented in Table 5-5 and the modal loss factor was again approximated using the half-power bandwidth method. Figure 5-24 shows interlayer and boundary material void fraction effects on the modal loss factor of the first mode. The plot clearly shows a quadratic correspondence, as was suggested in the RKU model sensitivity analysis presented in Section 5.3.2. This quadratic correspondence is due to the introduction of voids in the interlayer material, thereby increasing the loss factor of that layer. Section 5.4.1 showed that viscoelastic plate and B.C. behavior has only a quasi-linear influence on the modal loss factor, therefore the quadratic tendency observe in Figure 5-24 is a result of constrained layer damping of

the sandwich plate. These results are encouraging and show that microstructural inhomogeneities can have noticeable influence on structure-level behavior.

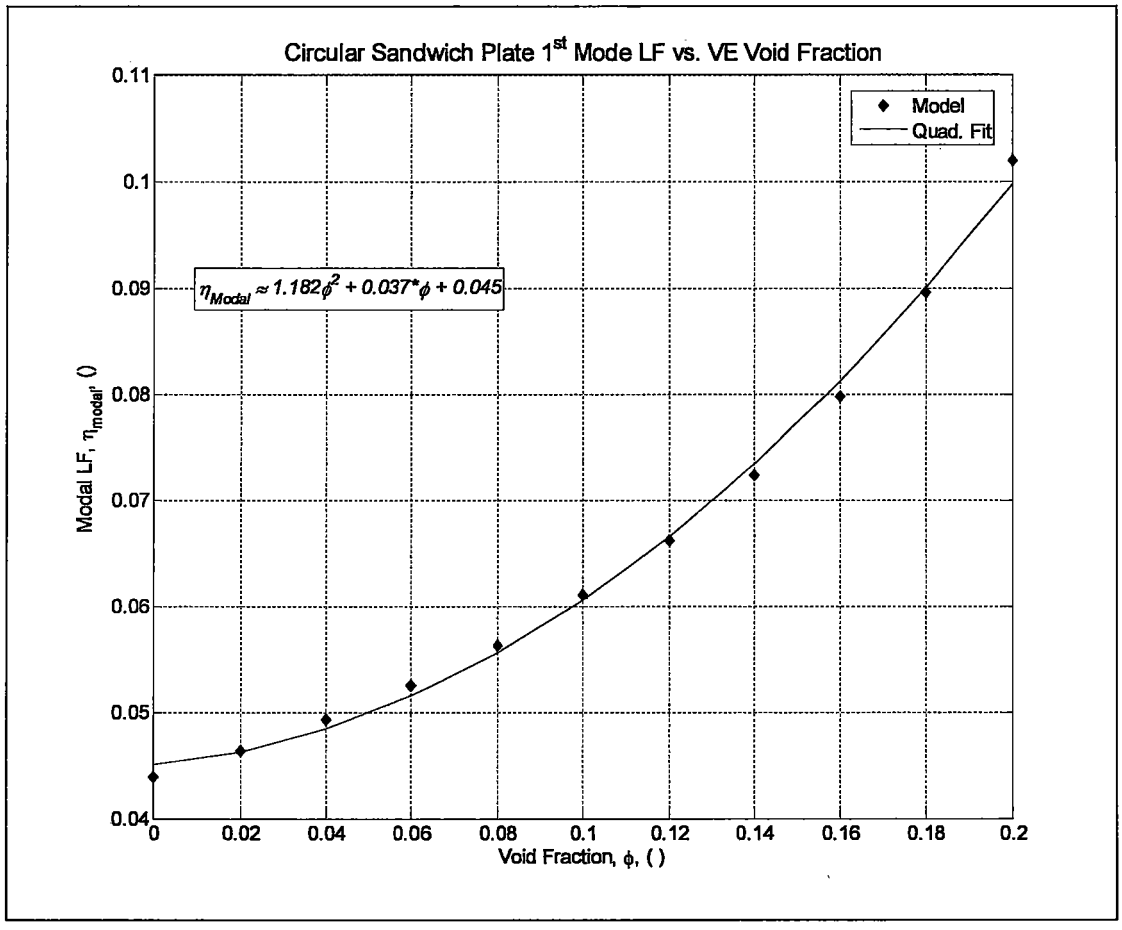

Figure 5-24: Variation of the loss factor of the 1st mode of vibration for a cantilever beam as a function of interlayer void fraction, ϕ.

Noise in an automobile interior has two distinctly different sources. A major contributing source is sound radiated by structure borne vibrations that originate from engine vibrations and, more importantly, the interaction between the road and the automobile [1]. The efficiency with which the windshield radiates this vibrational energy in the form of sound is dominated by its modal response. For this noise source, the previous study is applicable. Figure 5-24 has clearly shown that increasing the void fraction of the viscoelastic interlayer and boundary materials displays a desirable enhanced ability to reduce resonant behavior. The second source of noise is sound originates outside the vehicle which is consequently transmitted

through the windshield and other acoustic paths. The quality of noise isolation is usually measured by the transmission loss (TL) discussed in previously. For a panel, homogeneous, sandwich, or otherwise, the general characteristics of TL as a function of frequency are shown in Figure 5-25 [166].

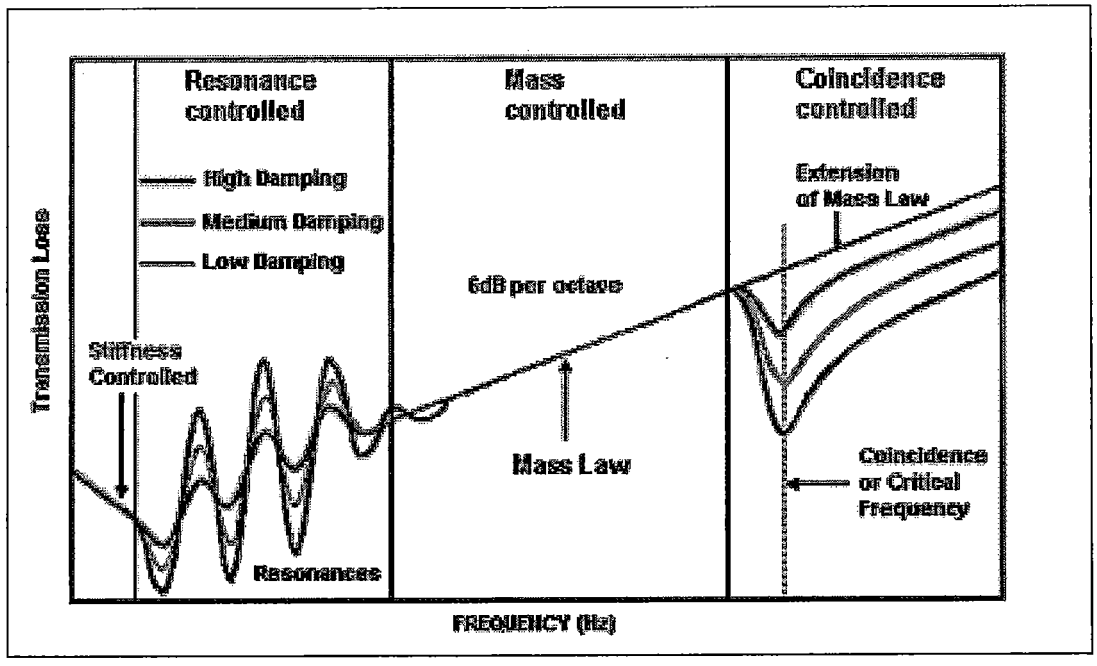

Figure 5-25: General characteristics of TL versus frequency for a panel (figure from Buerhle *et al* [166]).

Figure 5-25 illustrates the four regimes of panel transmission loss. From left to right, the first is the stiffness controlled domain which represents the quasi-static case for the *plate*, meaning acoustic wavelengths are much larger than the panel of interest. This regime is not of interest in the present work. The second regime, resonance controlled, is similar to the case studied above. It is reasonable to assume that behavior due to air-borne waves exciting resonance behavior will be damped in the same manner as structure borne vibrations and therefore this case was treated by the previous study. In the mass controlled TL regime, acoustic wavelengths are much smaller than panel dimensions and the panel is therefore approximated as a limp hanging panel with a known mass per unit area. The pressure gradient of the incident sound wave causes the panel to move as a whole and radiate sound on the other side.

In this regime TL is dominated by the panel mass and a doubling the frequency leads to a 6 *dB* TL increase [89]. It is obvious from this behavior that high density panels are ideal for noise isolation. The final TL regime is the coincidence controlled regime. In this frequency range the incident wavelength projected onto the panel matches the wavelength of flexural waves in the panel. Coincidence occurs when these two wavelengths match, resulting in near perfect transmission and a greatly diminished TL. The result is a sharp decrease in observed TL at a specific frequency depending on the air-borne plane wave angle of incidence. This region of high sound transmission is called the coincidence notch and the behavior is sometimes simply termed coincidence [89].

Microstructural effects of resonant behavior were previously shown for a vibrating plate so it is now interesting to inspect the effect of microstructural changes on windshield TL in the mass-controlled and coincidence-controlled regimes. Panel behavior in this frequency range is well approximated using the set of equations below [89].

$$\hat{\omega}_{coinc} = \frac{c_{air}^2}{\sqrt{\hat{K}}} \quad \text{where} \quad \hat{K} = \frac{\hat{B}^{eff}}{\rho^{eff} h^{tot}} \tag{V.5.1}$$

$$\hat{Z}_p = \omega \rho^{eff} h^{tot} \left\{ \hat{\eta}_p \left(\frac{\omega}{\hat{\omega}_{coinc}} \right)^2 \sin^4 \theta_I - i \left[1 - \left(\frac{\omega}{\hat{\omega}_{coinc}} \right)^2 \sin^4 \theta_I \right] \right\} \tag{V.5.2}$$

$$TL = 20 \log_{10} \left[\left| 1 + \frac{\hat{Z}_p}{2(\rho c)_{air}} \cos \theta_I \right|^2 \right] \tag{V.5.3}$$

In these expressions c_{air} and ρ_{air} represent the speed of sound (343 *m/s*) and density (1.21 kg/m^3) of air, respectively, $\hat{\omega}_{coinc}$ is the coincidence frequency, $\hat{Z}_p$ represents the plate impedance, and the other variables have been previously introduced. Figure

5-26 shows the TL calculated from Equations (V.5.1)-(V.5.3) for a sandwich windshield consisting of the same materials and geometry as for the resonance behavior discussed in Section 5.5.1. These results clearly show the expected mass and coincidence-controlled regimes. In the mass controlled regime the interlayer void fraction is small enough to have no detrimental effects on the TL. It also shows that the non-voided interlayer material already provides substantial coincidence notch reduction. The voided materials do enhance damping in this frequency range, but improvements are marginal at best, ~ 2 *dB re 20μPa*, and surely beyond the limits of human perceptibility in noise reduction.

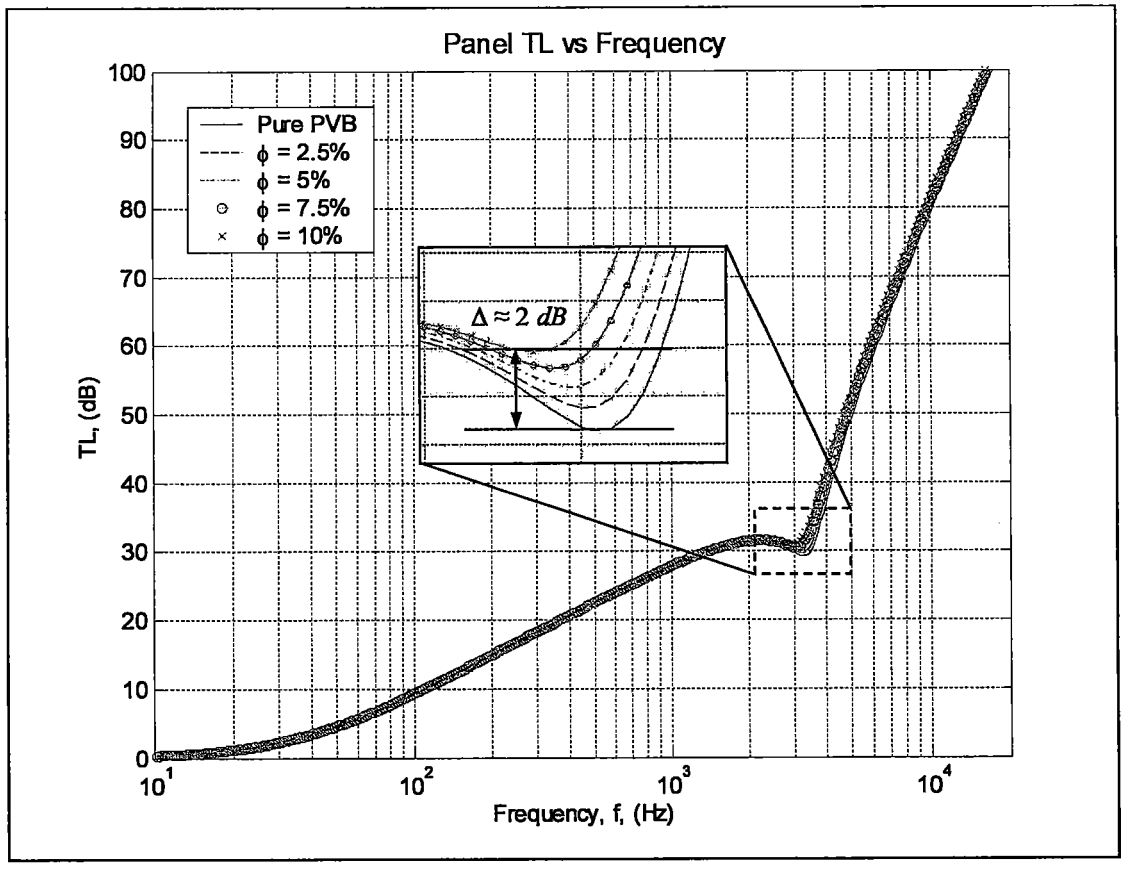

Figure 5-26: Theoretical TL of layered windshield as a function of frequency for an incident angle of $\theta_I = 60°$. Slight improvements are predicted for voided PVB near coincidence frequency.

Unfortunately, the results of this study show only marginal damping improvements at the structure-level. This can be attributed to the fact that only traditional materials have been investigated. It is very possible that non-conventional

inclusion materials or trace interlayer material treatments could translate to large effects on the structure-level damping capacity. One specific inclusion behavior leading to increased macroscopic material damping are negative stiffness inclusions. Lakes *et al* [9, 10, 12] have shown that "snap-through" phenomena observed in instable inclusion materials can be approximated as a negative stiffness. Their work has clearly shown that this extreme damping is due to large strains induced in the neighborhood of inclusions which exhibit "snap-through" behavior. The most significant increases in macroscopic lossy behavior results from inclusions whose modulus, $\hat{\mu}_I$, is related to the matrix modulus, $\hat{\mu}_M$, as $\hat{\mu}_I \approx -1.1\hat{\mu}_M$ [9]. It has been shown theoretically [9] and experimentally [10, 12] that treatments using inclusions displaying negative stiffness behavior can significantly increase lossy behavior with only trace amounts of the inhomogeneities. Indeed, Lakes called such treatment "homeopathic." Figure 5-27 investigates structural behavior, in the form of sandwich windshield TL, when the interlayer contains small volume fractions of hypothetical negative stiffness inclusions whose modulus obeys $\hat{\mu}_I \approx -1.1\hat{\mu}_{PVB}$ at each frequency while all other materials and geometry are identical to those used to produce Figure 5-26.

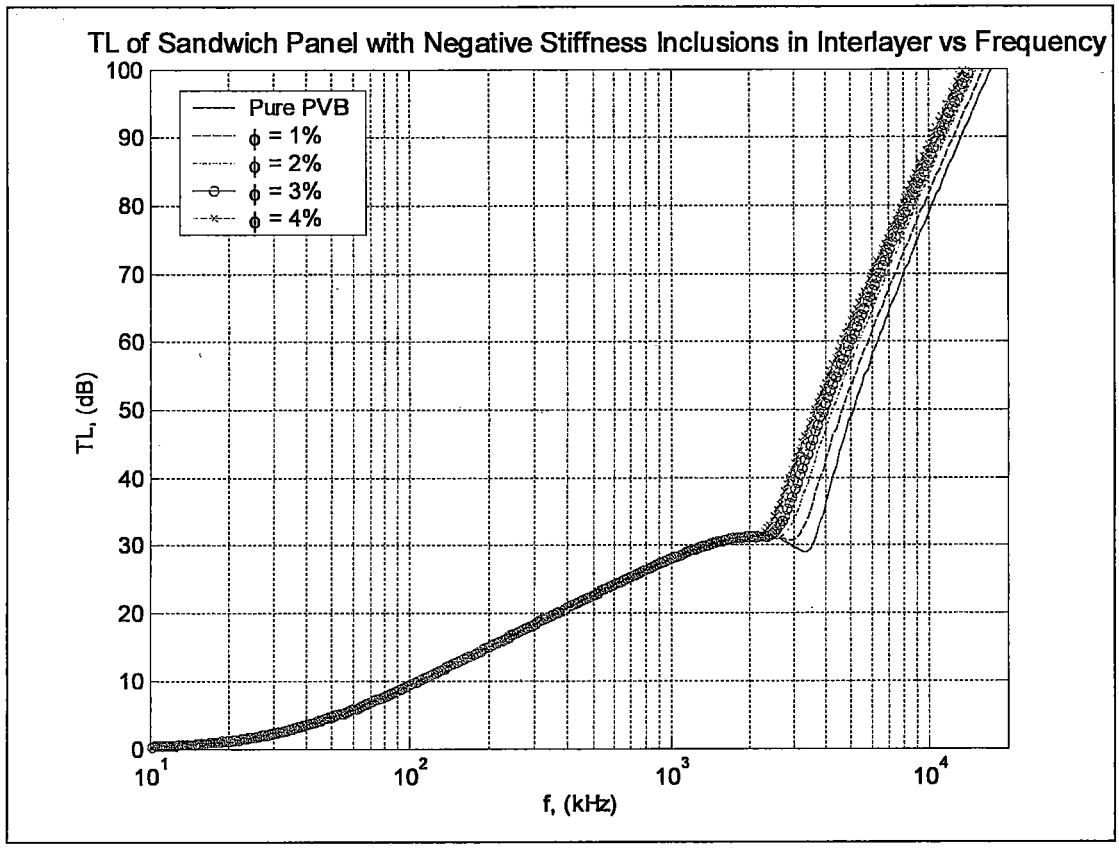

Figure 5-27: Transmission Loss of sandwich panel when PVB interlayer contains small volume fractions of negative stiffness inclusions ($\mu_I = -1.1\mu_{PVB}$). Coincidence notch moves to dramatically lower frequencies and nearly vanishes.

This plot shows a dramatic increase in observed structural level energy dissipation at coincidence. Indeed, the introduction of such inclusions nearly eliminates the coincidence notch while simultaneously moving coincidence phenomena to lower frequencies. Though the behavior shown in this plot is for a hypothetical material, it is very interesting for future research to show that such behavior can be captured by a nested multiscale modeling technique such as the one presented in this chapter. It also encourages further research in the design of materials with negative stiffness, or "snap-through," behavior for use as treatments in structures when energy dissipation is important. More importantly for this work, the above study validates the incorporation of the SC micromechanical model as a tool for a material by design strategy. The study also clears the way for more intense research of microstructural behaviors which have more pronounced effects on

structural level damping. Such a search will provide microstructural specifications for the design of absorptive materials.

CHAPTER VI

CONCLUSIONS, PERSPECTIVES, AND SUGGESTIONS FOR FUTURE WORK

6.1 General conclusion and perspectives

Classic design methods require the selection of materials which conform to the needs of a preconceived whole [19]. This design methodology is well developed and well understood. Unfortunately, this approach is often limited by the lack of available materials that meet the needs of the structure which, in turn, limits the entire design processes [14, 15]. An elegant solution to this classic problem is the creation of materials specifically conceived for structural demands [21]. This new approach, material by design, not only creates materials for specific needs but also includes the creation into the design of the system as a whole [90].

Material by design, or simply material design, is currently a very active area of research. One well accepted material design approach aims to extend either optimal or robust systems design to include the concurrent design of materials for specific high importance components [14, 21, 91]. Extending the systems approach to include material design is very natural as materials themselves can easily be viewed as multiscale structures [90, 92]. This new methodology is very attractive because it ensures structure functionality while simultaneously giving ultimate control to the designer.

The development and study of multiscale material models is one of the many areas of material design which requires further research before the method can become tractable. This thesis aimed to derive, develop, and validate a quasi-static

self-consistent micromechanical model for implementation as a tool in the design of high loss materials. Achievement of this objective required three distinct steps. The first step was the derivation of a robust quasi-static frequency domain micromechanical model for application to a wide range of viscoelastic particulate composite materials. Chapter III addressed model derivation by extending Cherkaoui's static SC coated inclusion model [23, 24] to include viscoelastic behavior of the constituent phases. The model was further developed via DSCT tensor formulation, thereby permitting the approximation of a broad range of viscoelastic particulate composites. The second step was the validation of the quasi-static SC model through comparisons with complex bounds and experimental data which was the subject of Chapter IV. This chapter ensured that no laws were violated in model derivation and displayed model accuracy for both static and quasi-static applications. The final step in achieving the thesis objective was integration of the SC model into a multiscale structural model. This was achieved by modeling the dynamic behavior of a viscoelastically constrained sandwich plate, representing an automobile windshield, through a hierarchy of nested models. The result is an initial contribution to the area of material design coupled with a well developed and understood quasi-static micromechanical model. The following summarizes the important contributions and developments of each section of this thesis, gives perspectives on the results, and suggests future avenues for detailed study.

6.1.1 Quasi-static model development

Frequency dependent approximations of heterogeneous material damping properties depend strongly on the frequency range of interest. This thesis has been restricted to applications where the mechanical loading is well represented as varying with time at some frequency, ω, but being spatially homogeneous. It has been shown that this frequency range corresponds to heterogeneity length scales, a, which are much smaller than the incident wavelengths, λ. This frequency domain is called the

"low frequency" limit, low *ka* scattering, or the Rayleigh scattering limit. Material behavior in this domain can be captured through static models by applying the elastic-viscoelastic correspondence principle. Based on this reasoning, this thesis proposed a micromechanical modeling approach rather than a scattering based model. Micromechanical modeling approximates macroscopic frequency dependent behavior uniquely through constituent material behaviors and neglects inertial effects present in scattering models. Despite the fact that such an approach limits modeling to the quasi-static domain, it greatly enhances the range of heterogeneous materials whose frequency dependent effective behavior is accurately approximated. It is for this reason that the micromechanical approach has been chosen to be developed as a tool for the design of absorptive materials.

The micromechanical model derived in Chapter III is an extension of the static coated inclusion self-consistent model introduced by Cherkaoui *et al* [23, 24]. Section 3.2 derived a model for the simple case of coated ellipsoidal inclusions embedded in an infinite viscoelastic matrix. The model approximates the presence of inhomogeneities as a spatial variation of elastic constants in accordance with Zeller and Dederichs [34]. In the static domain, this approach yields an integral equation based on Green's formalisms for the local strain field. The kernel of this integral equation is a Green's function that relates material stiffness contrast between matrix, inclusion, and coating phases to a distribution of volume forces. Extension of the static model to the quasi-static frequency domain requires this distribution of volume forces vary in time at some frequency, ω, and integrates the static integral equation across all frequencies. Finally, application of interfacial operators and volume averaging of the local strain fields yields a quasi-static SC micromechanical model for viscoelastic particulate composites containing coated ellipsoidal inclusions.

The quasi-static model derived in Section 3.2 is limited to the approximation of effective material behavior resulting from a host containing identical spherical or ellipsoidal inclusions. The model is further restricted to applications where the inclusions are identically orientated in space when the inclusions are ellipsoidal. This

limitation is addressed in Section 3.3 where the model is generalized by expanding the representative volume element to include multiple coated inclusion families. Each coated inclusion family possesses identical viscoelastic behavior, inclusion geometry, and spatial orientation. Generalization is achieved through a dilute strain concentration tensor (DSCT) approximation scheme. Generalization by DSCT yields a much more flexible model which is capable of accommodating a vast range of materials containing coated inclusions with various viscoelastic behaviors, ellipsoidal geometries, and spatial orientation distributions.

6.1.2 Model validation

The quasi-static micromechanical model derived in Chapter III was first validated before attempting implementation of the model as a material design tool. Model validation and application was the aim of Chapter IV. The chapter first compared quasi-static SC estimates to complex bounds from the literature. Comparison with bounds has a two fold purpose. Bounds on the effective behavior of composite materials describe the limits of possible effective material properties based on minimal and maximal energy restrictions. They are dependent on constituent material properties and the volume fractions of each phase. Disagreement with bounds invalidates a material model as it implies that physical laws have been violated during model derivation. For this reason, verification that a proposed effective medium theory (EMT) falls within accepted bounds is a first order check of model validity. The second purpose for comparison with bounds is to check composite material optimality. Bounds provide information concerning the optimality of effective material behavior because they are derived from upper and lower energy restrictions. For this reason, proximity to an upper or lower bound gives a measure of how nearly optimal the phase composition, inclusion geometry, inclusion orientation, or any combination of these factors renders the effective behavior of the composite

[67]. The quasi-static SC model was compared with three specific complex bounding methods taken from the literature for these reasons. Section 4.2.1 clearly shows that the three phase model falls within the bounds proposed by Roscoe [65, 66] as a function of frequency and inclusion volume fraction. The two-phase isotropic SC model was then successfully compared with the variational and translational bounds for complex shear and bulk modulus introduced by Gibiansky and Lakes [72] and Milton and Berryman [71], respectively. These studies validate the derivation given in Chapter III as well as the implementation of the resulting model in the quasi-static frequency domain.

6.1.2.1 Homogenization of composites containing oriented ellipsoidal inclusions

Section 4.3.2 employed the SC model to evaluate the effective viscoelastic constants of an isotropic viscoelastic matrix containing coated, ellipsoidal elastic inclusions. The lossy behavior of the resulting anisotropic composite was captured by introducing complex frequency dependent matrix material moduli. The section investigated the effects of constituent phase properties, inclusion orientation, and inclusion aspect ratios through a series of parametric studies and comparison with experiment. This validation step first investigated the transmission loss (TL) of a plane wave normally incident on a slab of viscoelastic composite material submerged in water for oblate, coated, inclusions with aspects ratios ranging from 1.0 (spherical) to 2.5. For the range of material properties used, the effect of the inclusion geometry on the TL was modest, less than 2 dB, but agreement with the spherical inclusion approximation and experimental data taken from Baird *et al* [76] was good. The variation of plane-wave attenuation coefficient was then studied as a function of inclusion orientation angle for the same constituent material properties presented in the TL study. Directional dependence in accordance with the physical dissipation mechanisms were shown to be captured by the quasi-static SC model. The complex

effective sound speed of the material was then evaluated as a function of frequency, inclusion aspect ratio, and volume fraction. The effects of different inclusion geometries such as penny-shaped, needle-shaped, oblate, and prolate have also been studied. The results of all these studies clearly showed that the quasi-static SC model predicts directional variations of lossy composite material behavior induced by aligned ellipsoidal inclusions. The calculations and discussion of Section 4.3.2 verified that the quasi-static micromechanical model allows for a level of generality in modeling of lossy composites where scattering based approaches are limited. As such, it was concluded that it could be a useful tool in the design of new anisotropic damping materials for numerous applications, including cases where the anisotropy of such materials is induced due to loading conditions or manufacturing processes.

6.1.2.2 Homogenization through DSCT formulation: Orientation distribution, multiple scale modeling, and coating thickness variations

The next validation step presented was an inspection of the quasi-static SC DSCT model. The SC model was modified in Section 3.3 to allow the approximation of the effective properties of composites with many disparate coated-inclusion properties, geometries, and orientation distributions. To illustrate the improved modeling flexibility of the DSCT formulation, several cases studies were presented in Sections 4.3.3, 4.3.4, and 4.3.5. Section 4.3.3.1 showed that SC DSCT approximation of the lossy properties of globally isotropic composites containing uniform orientational distributions of ellipsoidal inclusions has good qualitative agreement with a model proposed by Berryman [51]. The formulation was then shown in Section 4.3.3.2 to capture the effects of varying the orientational preference of ellipsoidal inclusions through a parametric study on the compressional wave attenuation coefficient of a bi-phase lossy composite. The ability to correctly capture preferential inclusion orientation was then verified by comparison with experiment in

Section 4.3.3.3. That section showed, through comparison with experimental values from Jones and Wang [77], that the SC DSCT model has the ability to accurately homogenize composites containing multiple inclusion types together with preferential orientations of select inclusion phases. In Section 4.3.4, the multiscale capability of the SC DSCT model was illustrated. A SiC-Al composite studied be Ledbetter and Datta [79] was idealized as consisting of three distinct length scales. The effective stiffness coefficients calculated using this formulation were shown to have good agreement with experimental values and the multiple scattering model Ledbetter and Datta [79]. Sections 4.3.3.3 and 4.3.4.1 showed another strength of the coated-inclusion SC DSCT formulation, that being the simple extension to the form of a generalized SC model for bi-phase composites. The GSC scheme shows slight improvements of approximation without adding modeling difficulty. Finally, the SC DSCT model was shown capable of improving the accuracy of TL approximations for a previously studied composite [50, 53, 76] by taking variations in inclusion coating thickness into account.

The comparisons detailed above illustrate the flexibility and level of generality achievable using the quasi-static SC DSCT model. The model is not without its drawbacks, however, and several points of caution must be addressed. First, it is known that SC models can display some numerical instability due to its implicit form. This drawback was discussed at length in Section 4.4 and must be considered when modeling composites with high contrast phases. Another drawback of the model, which is also linked to its implicit nature, are the singularities observed in the imaginary part of the complex wavenumber around the threshold of rigidity for high contrast composites. With these drawbacks in mind, the level of achievable generality and accuracy of the SC DSCT model displayed in this chapter far outweigh these negative aspects. Indeed, the ability of this generalized model to capture the effects of complex material microstructure in the static and quasi-static regimes make the SC DSCT model an ideal candidate for the design of absorptive materials.

6.1.3 Towards the implementation of the SC model as a material by design tool

Chapter V investigated quasi-static SC model implementation as a material design tool by presenting and studying the damping behavior of a multiscale structure. The aim of this chapter was to provide an introductory level example of quasi-static SC model implementation in the design of a lossy structure. This was accomplished by presenting a case study of the damping properties of a simple structure: a vibrating sandwich plate. A vibrating sandwich plate was chosen to represent an automobile windshield, a common structural element. Such a choice clearly shows practical implementation and the potential wide-range impact of the material by design approach. This case study provided preliminary insight into the role the quasi-static SC model can play in a material design strategy and laid the groundwork for more detailed research.

A constrained sandwich plate was idealized as consisting of four distinct length scales. These length scales are, from shortest to longest: (*i*) the constituent material microstructure, (*ii*) the macroscopic plate material, (*iii*) the sandwich plate, and (*iv*) the constrained sandwich plate. Length scales (*iii*) and (*iv*) are referred to as the structural element, or part, level and structure level length scales, respectively. The lossy behavior of this multiscale structure was modeled using a nested hierarchy of models where each model was capable of making one or more scale transitions.

The damped behavior of the structure as a whole was approximated with the loss factor of the first mode of vibration calculated for a viscoelastically constrained sandwich plate or beam. Modal analysis was performed via classic methods discussed by Liessa [172]. This study quantified lossy behavior at the highest length scale. Modeling behavior at the structure level required information about part level behavior, in other words, this model made the scale transition from length scales (*iii*) → (*iv*).

The structural element of interest to this case study was represented by a sandwich plate and was modeled using a simple constrained layer damping model

introduced by Ross, Kerwin, and Ungar (RKU) [81]. This simple analytic model yielded insight into lossy sandwich plate behavior based on constituent layer material behavior and geometry. The RKU model was successfully employed to model effective sandwich plate behavior as a function of frequency and made the scale transition from macroscopic plate materials and geometry to structural element, represented as scale transition (*ii*) → (*iii*).

The final model employed was the SC model which has already been discussed in detail and which performed the scale transition from constituent material microstructure to macroscopic material behavior, length scales (*i*) → (*ii*). This section showed that the SC model adds design variables, design flexibility, and behavioral insight to the design process. Multiscale structural behavior approximated via this nested hierarchy of models was verified through comparison with finite element approximations employing a sophisticated model proposed by Daya and Potier-Ferry [83].

The final section of this chapter investigated the employment of the SC model to yield insight in order to enhance part and structural level damping capacity. This study aimed to quantify the effects of microstructural variations on damping properties at the part and structural levels. This was done by studying the effect of introducing voids into the viscoelastic interlayer of the sandwich plate. Structural element level effects were first studied. The introduction of 10% voids into the interlayer material yielded 5 – 10% increases in sandwich plate damping capacity. The damping capacity measure employed was the amplitude attenuation per flexural wavelength, $\hat{\alpha}^{flex}/\hat{k}^{flex,'}$. Though this is significant on the part level, the effects observed at the structural length scale were marginal. Circular sandwich plate modal loss factor calculations showed a quadratic dependence on void fraction, but the magnitude of this influence was minimal. Indeed, 10% interlayer void fraction was only shown to increase modal loss factor by ~2% over the non-voided interlayer case. Further, the sandwich plate suffers a simultaneous significant reduction in flexural resistance upon introduction of voids. The effects of interlayer void fraction on the

frequency dependent TL of the sandwich plate was also inspected. The TL approximation was made using the nested multiscale modeling approach coupled with fundamental acoustic relationships given by Pierce [89]. Interlayer voiding showed minimal TL improvement at coincidence. The improvement calculated was merely 2 *dB*, a level imperceptible to human hearing. Though the modeling approach was validated by this case study and microstructural influence was observed to propagate through lengths scales, these results were discouraging in terms of design benefit.

Fortunately, new research suggests that very small volume fractions of instable microstructural inclusions yield extreme increases in macroscopic damping behavior [9, 10, 12]. The set of material models was therefore employed to approximate windshield TL for a sandwich plate whose interlayer contained trace amounts of a hypothetical instable material. The results of this multiscale study showed the propagation of these microstructural variations through multiple length scales finally manifesting in very effective increases in structural level damping. Additions of only 1% instable inclusions nearly removed the TL coincidence notch, and 4% inclusions were shown completely damp coincidence phenomena. Though the material studied was hypothetical, such broadband material damping has been experimentally observed by Lakes *et al* [10, 12], and these results are therefore very encouraging for the design of high loss materials.

6.2 Perspectives and suggestions for future work

This thesis has derived, developed, and validated a quasi-static self-consistent micromechanical model and presented a simple multiscale problem within the framework of material by design. However, this work represents but a small contribution to the complex material by design research area which remains rich for study. It has been shown that micromechanical modeling as a material by design tool can easily be incorporated into a nested hierarchy of models thereby simultaneously

approximating structural behavior at many different levels. This approach gives considerable information and freedom to the design process and represents an initial step towards the integration of material by design into the overall design of any structure. This thesis has shown that development and study of micromechanical models is extremely important to this emergent design process. These models give substantial insight into the influence of material microstructures which translate into desirable structural behavior while also being a key tool to approximate final design performance. Indeed, the robust quasi-static self-consistent model derived, developed, and validated in this thesis has been shown to enhance knowledge of absorptive behavior and the influence of microstructural behavior on damping at macroscopic, elemental, and structural length scales. This work has therefore given promising results for future development of micromechanical tools for application in strategies to design absorptive materials.

6.2.1.1 Suggestions for future work

It has been previously stated that the domain of material by design is rich for study. Future research in this domain could include a vast range of areas including the study of detailed overarching design strategies, fabrication processes and variability, computationally efficient design, collaborative systems design, nano→micro scale modeling, and molecular dynamics or quantum approximations of sub-continuum material behavior. For this reason, the suggestions for future research given here are limited to the development of micromechanical tools for the material by design process with a specific emphasis on the design of high loss materials.

One limitation of the micromechanical model presented in this thesis is its limitation to quasi-static applications. This problem is specifically important when investigating high frequency wave propagation applications where the quasi-static approximation is no longer valid. This problem could be addressed using an approach

similar to the micromechanical approach presented by this thesis without neglecting inertial terms in the first stages of model development. This is not a trivial modeling problem. Successful evaluation of this problem would, however, yield a model capable of approximating both quasi-static and non-quasi-static material behavior while maintaining the generality of the quasi-static SC model presented in this work.

Another interesting research area in the domain of EMT is the development of more tractable complex bounding techniques. The present complex bounds are either not restrictive enough or give too little information. Roscoe's bounds provide the ability to inspect effective complex material behavior as a function of frequency or volume fraction, but are too admissive to study composite optimality. Bounds derived from variational and translational techniques, on the other hand, provide a very accurate restriction on permissible effective values. Unfortunately, these bounding techniques do no lend themselves easily to EMT comparison as a function of frequency or volume fraction. The development of bounds for complex composite materials which can be easily implemented for a wide range of exciting frequencies, volume fractions, and constituent material properties is therefore attractive.

Future research of micromechanical modeling tools for material design applications must include implementation of meta, or surrogate, models to map the effects of microstructural behavior to macroscopic behavior. Meta-models are design tools that permit efficient exploration of the design space [20]. For example meta-models approximating submicron material behavior as the result of localized macro-scale loading can be used as an input to existing micromechanical models (see Figure 6-1). This approach is a powerful method to evaluate macroscopic and constituent material behavior while limiting computational loads usually required for precise evaluation of behavior at such small scales [22]. The meta-modeling approach gives extremely important information regarding the effects of submicron material behavior and geometry on the macro-scale. This information is of high importance for a material design strategy [22]. An example of this approach with respect to damping behavior would be the implementation of meta-models to approximate various

negative-stiffness behaviors. Meta-models can be created to mimic instable behavior resulting from macroscopic thermomechanical loading localized to the microstructural scale. These models could subsequently be integrated into the SC model derived and validated in this thesis in order to further inform the design of high loss materials.

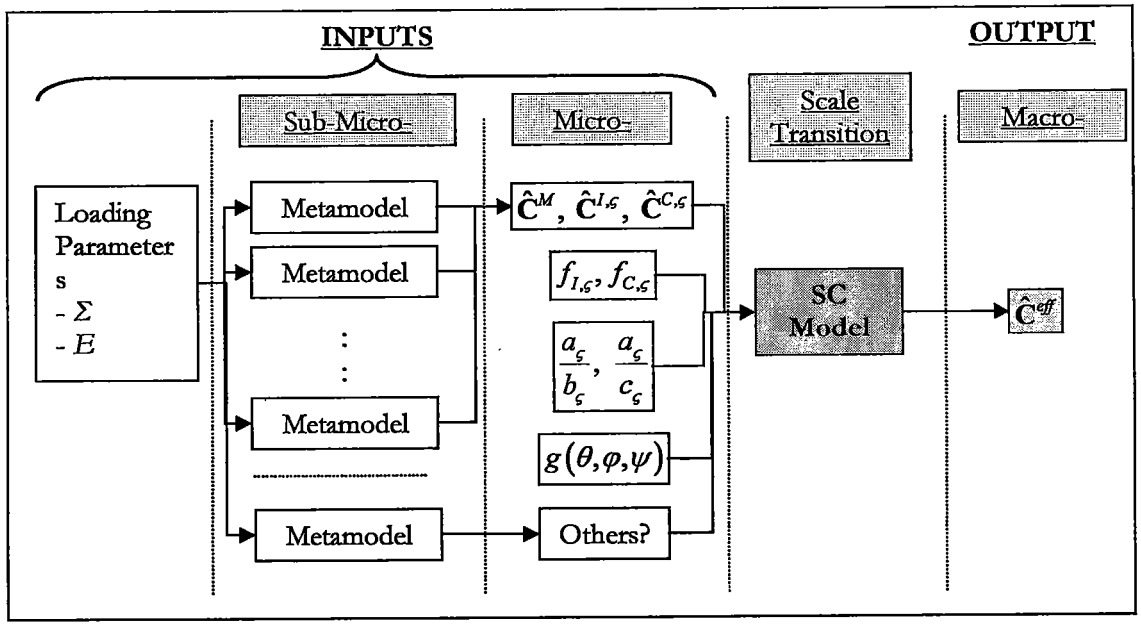

Figure 6-1: Schematic of a meta-model mapping procedure. The microscale variables represent, from top to bottom, the constituent material properties, the volume fractions, the inclusion form, the inclusion orientation, and any other variables to be defined.

A related area of considerable interest for lossy material design is detailed research on instable material behavior at small scales (micron-, submicron-, or nano-scales). This thesis has shown that instable behavior leads to extreme damping at the macroscopic scale even when volume fractions of materials displaying this behavior are miniscule. Research regarding the onset of instable behavior as well as methods to introduce instable materials into a host is of utmost interest. Another very interesting aspect that must be studied with regards to material instability is the ability to stabilize such phases under nominal operating conditions while eliciting instable behavior upon slight loading changes in preferential directions or along certain loading paths. These, and many other behavioral trends, should be first explored through a meta-modeling approach and finally implemented into a material design scheme.

6.2.1.2 Comments on material by design

Material by design is an emergent and extremely ambitious research field with the potential for considerable impact in many fields of science and engineering. The elementary study provided in the Chapter V clearly illustrated this point by showing efficient enhancement in the absorptive behavior of a simple structural element through a limited material design approach. This was accomplished through application of knowledge obtained from the quasi-static self-consistent model and the nested hierarchy multiscale models. The result of the work done in this thesis is, therefore, a well developed material design tool which has provided insight into the microstructural mechanisms that lead to enhanced damping behavior across length scales. It has further provided a tool to be integrated into a multiscale and multi-physics material design scheme. The combination of this research with other studies that target key areas of material by design will provide this exciting field with significant information and bring designers closer to its practical implementation.

APPENDIX A

FOURIER TRANSFORMATION APPROXIMATION OF $\hat{\mathbf{T}}^{I}\left(\hat{\mathbf{C}}^{X}\right)$

Implementation of the SC technique requires the numerical approximation of the modified Green's tensor for cases where the surrounding matrix is anisotropic (this includes cases when the actual material phases are anisotropic or when the inclusions are ellipsoidal and oriented). The numerical evaluation is done via Fourier transform techniques as explained in Mura and Berveiller *et al* [26, 37]. For evaluation using the FT technique, the assumption is made that the displacement field caused by the presence of the inclusion can be represented by the superposition of an infinite sum of spatially regular displacement fields. This assumption, by the very nature of the Fourier transform, implies that the spacing of inclusions is regular. Though this can be a gross estimate, the method has been proven to provide very good approximations to true composite material behavior [26]. The method employed is rather involved, but stated simply it involves using the Fourier integral to transform the ellipsoid into a sphere in Fourier domain. The transform variable in this case represents the "wave number" of the strain field with spatial regularity in an infinite homogeneous medium due to the presence of inclusions. The transformation allows for numerical integration around a spherical volume using numerical techniques to evaluate Equation (III.2.40).

Let the Fourier transform of the Green's tensor in the reference material X and its inverse be defined as follows:

$$\hat{\bar{G}}_{km}^{X}\left(\vec{k}\right)=\int_{-\infty}^{\infty}\hat{G}_{km}^{X}\left(\vec{r}\right)e^{i\vec{k}\cdot\vec{r}}d\vec{r}$$
$$\hat{G}_{km}^{X}\left(\vec{r}\right)=\frac{1}{\left(2\pi\right)^{3}}\int_{-\infty}^{\infty}\hat{\bar{G}}_{km}^{X}\left(\vec{k}\right)e^{-i\vec{k}\cdot\vec{r}}d\vec{k} \tag{A.1}$$

where the vector $\vec{k}$ is the "wave-number" of the displacement (and therefore strain) field in an infinite homogeneous medium due to the presence of the coated inclusion. Integrating through all frequencies and then applying the Fourier transform to Equation (III.2.7) gives:

$$\hat{C}_{ijkl}^{X}k_{l}k_{j}\hat{\bar{G}}_{km}^{X}\left(\vec{k}\right)=\delta_{im} \tag{A.2}$$

If the inclusion is ellipsoidal, it is convenient to introduce the following change of variables:

$$\vec{r}=\begin{cases}x_1\\x_2\\x_3\end{cases}\Rightarrow\vec{R}=\begin{cases}X_1=x_1\\X_2=\dfrac{a}{b}x_2\\X_3=\dfrac{a}{c}x_3\end{cases}\quad\text{and}\quad\vec{k}=\begin{cases}k_1\\k_2\\k_3\end{cases}\Rightarrow\vec{K}=\begin{cases}K_1=k_1\\K_2=\dfrac{b}{a}k_2\\K_3=\dfrac{c}{a}k_3\end{cases} \tag{A.3}$$

The following equalities are then useful:

$$\vec{k}\cdot\vec{r}=\vec{K}\cdot\vec{R} \tag{A.4}$$

$$k_i=\Phi_{it}K_t\quad\text{where: }\left[\Phi_{it}\right]=\begin{bmatrix}1&0&0\\0&\dfrac{a}{b}&0\\0&0&\dfrac{a}{c}\end{bmatrix} \tag{A.5}$$

Equation (A.2) can then be expressed as for the case of an ellipsoidal inclusion:

$$\hat{C}^X_{ijkl} K_t \Phi_{lt} K_u \Phi_{ju} \hat{\bar{G}}^X_{km}\left(\vec{k}\right) = \delta_{im} \tag{A.6}$$

Then, defining $K_t = K\chi_t$, where K is the magnitude and χ_t are the direction cosines, leads to:

$$\begin{aligned} \hat{C}^X_{ijkl} \Phi_{lt} \Phi_{ju} \chi_t \chi_u &= \hat{M}_{ki} \\ K^2 \hat{\bar{G}}^X_{km}\left(\vec{K}\right) &= \hat{M}^{-1}_{km} \end{aligned} \tag{A.7}$$

which depends only on the magnitude of the vector K. This expression can then be substituted into the inverse Fourier transform in order to evaluate $\hat{\mathbf{t}}^I$, and therefore $\hat{\mathbf{T}}^I\left(\hat{\mathbf{C}}^X\right)$ as follows:

$$\begin{aligned} \hat{t}^I_{klmj} &= \frac{abc}{3} \int_0^{\pi} \sin\theta d\theta \int_0^{2\pi} \left[K^2 \hat{\bar{G}}^X_{km}\left(\vec{K}\right) \right] \chi_t \Phi_{lt} \chi_u \Phi_{ju} d\varphi \\ \hat{T}^I_{klmj}\left(\hat{C}^X\right) &= \frac{1}{2}\left\{ \hat{t}^I_{klmj} + \hat{t}^I_{lkmj} \right\} \end{aligned} \tag{A.8}$$

For efficient and accurate numerical evaluation of the integral in Equation (A.8), an n point Gaussian–Legendre quadrature has been employed. It was found that, for most cases studied, 10-point quadrature was sufficient. Finally, it should be reiterated that the integral of the modified Green's tensor is related to Eshelby's tensor through the following relationship.

$$\hat{\mathbf{S}} = \hat{\mathbf{T}}^{I}\left(\hat{\mathbf{C}}^{X}\right) : \hat{\mathbf{C}}^{X} \tag{A.9}$$

APPENDIX B

TENSOR ROTATION AND EULER ANGLES

According to Euler's rotation theorem, any rotation may be described using three angles. If the rotations are written in terms of rotation matrices **B**, **C**, and **D**, then a general rotation can be written as the product of those rotations [149].

$$\mathbf{R} = \mathbf{BCD} \tag{B.1}$$

The three angles giving the three rotation matrices are called Euler angles. There are several conventions for Euler angles, depending on the axes about which the rotations are carried out. One of the most common conventions is the "x"-convention which has been employed in this thesis and is illustrated in Figure B-1.

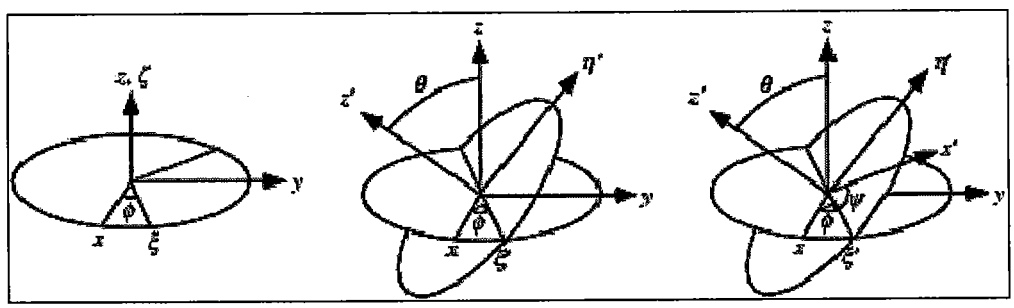

Figure B-1: Visualization of Euler angles employed in the x-convention [149].

The rotations associated with this convention consist of a rotation, φ, about the z-axis, followed by a rotation, θ, about the rotated x-axis and finally a rotation, ψ, about the rotated z-axis. In general the Euler angles, (φ, θ, ψ), can take the following values:

$$\begin{aligned} \varphi &\in [0 \quad 2\pi] \\ \theta &\in [0 \quad \pi] \\ \psi &\in [0 \quad 2\pi] \end{aligned} \tag{B.2}$$

The individual rotation matrices are defined in Equations (B.3), (B.4), and (B.5).

$$\mathbf{B} = \begin{bmatrix} \cos\psi & \sin\psi & 0 \\ -\sin\psi & \cos\psi & 0 \\ 0 & 0 & 1 \end{bmatrix} \tag{B.3}$$

$$\mathbf{C} = \begin{bmatrix} 1 & 0 & 0 \\ 0 & \cos\theta & \sin\theta \\ 0 & -\sin\theta & \cos\theta \end{bmatrix} \tag{B.4}$$

$$\mathbf{D} = \begin{bmatrix} \cos\varphi & \sin\varphi & 0 \\ -\sin\varphi & \cos\varphi & 0 \\ 0 & 0 & 1 \end{bmatrix} \tag{B.5}$$

The resulting components of the rotation matrix **R** are detailed in Equations (B.6).

$$\begin{aligned} R_{11} &= \cos\psi\cos\varphi - \cos\theta\sin\varphi\sin\psi \\ R_{12} &= \cos\psi\sin\varphi + \cos\theta\cos\varphi\sin\psi \\ R_{13} &= \sin\psi\sin\theta \\ R_{21} &= -\sin\psi\cos\varphi - \cos\theta\sin\varphi\cos\psi \\ R_{22} &= -\sin\psi\sin\varphi - \cos\theta\cos\varphi\cos\psi \\ R_{31} &= \sin\theta\sin\varphi \\ R_{32} &= -\sin\theta\cos\varphi \\ R_{33} &= \cos\theta \end{aligned} \tag{B.6}$$

The rotation of any second order tensor, X_{rs}, from one coordinate system to its representation in another, $\tilde{X}_{ij}$, using the rotation matrix, **R**, is shown in Equation (B.7).

$$\tilde{X}_{ij} = R_{ir} R_{js} X_{rs} \tag{B.7}$$

The rotation of any fourth order tensor, X_{nmpq}, from one coordinate system to its representation in another, $\tilde{X}_{ijkl}$, which is related by the above Euler angles is given in Equation (B.8).

$$\tilde{X}_{ijkl} = R_{im} R_{jn} R_{kp} R_{lq} X_{nmpq} \tag{B.8}$$

APPENDIX C

SUMMARY OF COMPLEX BOUNDS

Complex bounds proposed by Roscoe

The equations used to derive the complex bounds the proposed by Roscoe are analogous to statements of potential energy used as the basis for the extremum principles which yield the bounds for elastic composites, see Voigt [110] and Reuss [111]. The following analysis employs the notation used by Roscoe. First the isotropic and deviatoric parts of the relevant tensors are separated in order to simplify the derivation. Doing so yields the following classic relations for the stress and strain in a material.

$$\sigma_{ij} = \sigma\delta_{ij} + s_{ij} \tag{C.1}$$

$$\sigma_{ij} = \varepsilon\delta_{ij} + e_{ij} \tag{C.2}$$

In the equations above the hydrostatic and deviatoric stress values are denoted as σ and $\mathbf{s}$ respectively, the analogous strain values are assigned the variables ε and $\mathbf{e}$, respectively, and δ_{ij} is the Kronecker delta function. In the low frequency limit the elastic-viscoelastic correspondence principle can be employed and the well-known stress-strain relationship for the rth phase is given as [65, 66].

$$\mathbf{s}_r = 2\mu_r^*\mathbf{e}_r \qquad \sigma_r = 3\kappa_r^*\varepsilon_r \tag{C.3}$$

$$\mathbf{e}_r = \frac{1}{2} j_r^* \mathbf{s}_r \qquad \varepsilon_r = \frac{1}{3} l_r^* \sigma \tag{C.4}$$

In these expressions an asterisk, *, denotes that the quantity has a complex value, μ_r and κ_r represent the shear and bulk moduli and j_r and l_r represent the deviatoric and isotropic compliances of the rth phase. The two elementary extremum principles used for classic elastic composites [110, 111] and applied here to viscoelastic composites are summarized with the two points below.

1. Assume $\langle s \rangle = s_r$ and $\langle \sigma \rangle = \sigma_r$ for each phase, r, where $\langle s \rangle$ and $\langle \sigma \rangle$ are the global deviatoric and isotropic stresses respectively.
2. Assume $\langle \mathbf{e} \rangle = \mathbf{e}_r$ and $\langle \varepsilon \rangle = \varepsilon_r$ for each phase, r, where $\langle \mathbf{e} \rangle$ and $\langle \varepsilon \rangle$ are the global deviatoric and isotropic strains respectively.

Applying assumption 1 to the expression for strain energy yields Equation (C.5) below.

$$\frac{1}{2} j_{eff}^* \langle s_{ij} \rangle \langle \bar{s}_{ij} \rangle + \frac{1}{3} l_{eff}^* \langle \sigma_{ij} \rangle \langle \bar{\sigma}_{ij} \rangle = \frac{1}{V} \sum_r \int \left(\frac{1}{2} j_r^* s_{ij} \bar{s}_{ij} + \frac{1}{3} l_r^* \sigma_{ij} \bar{\sigma}_{ij} \right) dV_r \tag{C.5}$$

A bar over any quantity in the above expression denotes the complex conjugate of that quantity and V_r is the volume of the rth phase with $V = \sum_r V_r$. Similarly, for assumption 2, the strain energy relationship is written:

$$2\mu_{eff}^* \langle e_{ij} \rangle \langle \bar{e}_{ij} \rangle + 3\kappa_{eff}^* \langle \varepsilon_{ij} \rangle \langle \bar{\varepsilon}_{ij} \rangle = \frac{1}{V} \sum_r \int \left(2\mu_r^* e_{ij} \bar{e}_{ij} + 3\kappa_r^* \varepsilon_{ij} \bar{\varepsilon}_{ij} \right) dV_r \tag{C.6}$$

It is important to note that Equations (C.5) and (C.6) each represent two separate relationships each of which relate the real or imaginary parts of macroscopic material behavior and mechanical loading to the analogous quantities of the constituent phases. Denoting the real and imaginary parts of a complex quantity as $x^* = x' + ix''$, these relationships are shown below.

$$\frac{1}{2} j_{eff}^{*} \langle s_{ij} \rangle \langle \bar{s}_{ij} \rangle + \frac{1}{3} l_{eff}^{*} \langle \sigma_{ij} \rangle \langle \bar{\sigma}_{ij} \rangle = \frac{1}{V} \sum_r \int \left(\frac{1}{2} j_r^{*} s_{ij} \bar{s}_{ij} + \frac{1}{3} l_r^{*} \sigma_{ij} \bar{\sigma}_{ij} \right) dV_r \qquad \text{(C.7)}$$

$$2\mu_{eff}^{*} \langle e_{ij} \rangle \langle \bar{e}_{ij} \rangle + 3\kappa_{eff}^{*} \langle \varepsilon_{ij} \rangle \langle \bar{\varepsilon}_{ij} \rangle = \frac{1}{V} \sum_r \int \left(2\mu_r^{*} e_{ij} \bar{e}_{ij} + 3\kappa_r^{*} \varepsilon_{ij} \bar{\varepsilon}_{ij} \right) dV_r \qquad \text{(C.8)}$$

viscoelastic analogues to the elastic Reuss and Voigt bounds are then found by matching terms on the LHS and RHS of relations (C.7) and (C.8). These bounds are simply the weighted harmonic average and weighted average of the constituent phase properties given below:

$$\mu_{RL}^{*} = \left(\sum_r \frac{f_r}{\mu_r^{*}} \right)^{-1} \qquad \kappa_{RL}^{*} = \left(\sum_r \frac{f_r}{\kappa_r^{*}} \right)^{-1} \qquad \text{(C.9)}$$

$$\mu_{RU}^{*} = \sum_r f_r \mu_r^{*} \qquad \kappa_{RU}^{*} = \sum_r f_r \kappa_r^{*} \qquad \text{(C.10)}$$

In the above relationships, *RL* and *RU* denote Roscoe's lower and upper bounds, respectively. It is now important to note that due to energy considerations the following is true:

$$\begin{aligned} \mu_{RU}^{*} &\geq \mu_{eff}^{*} \quad & \kappa_{RU}^{*} &\geq \kappa_{eff}^{*} \\ j_{RL}^{*} &\geq j_{eff}^{*} \quad & l_{RL}^{*} &\geq l_{eff}^{*} \end{aligned} \qquad \text{(C.11)}$$

An important aspect of these complex bounds is the lack of restrictions with respect to the frequency inspected, the total number of constituent viscoelastic phases, r, or the total volume fraction, φ. This logic leads to the following restrictions on the possible values for the effective viscoelastic moduli:

$$\begin{aligned} \mu_{RL}^{'''}(\omega,\varphi) \le \mu_{eff}^{'''}(\omega,\varphi) \le \mu_{RU}^{'''}(\omega,\varphi) \\ \kappa_{RL}^{'''}(\omega,\varphi) \le \kappa_{eff}^{'''}(\omega,\varphi) \le \kappa_{RU}^{'''}(\omega,\varphi) \end{aligned} \tag{C.12}$$

where ω is the frequency of interest and φ is the total volume fraction of inclusion phases. Note: $f_{matrix} = 1-\varphi$.

Complex bulk modulus bounds

According to the work of Gibiansky and Lakes [72], the effective complex valued bulk modulus of the isotropic viscoelastic composite is constrained to a "lens-shaped" region in the complex bulk modulus plane. This region is bounded by the outer-most pair of four circular arcs, each of which correspond to the four min-max variational principles proposed by Cherkaev and Gibiansky [67] and Milton [68]. The equations defining these arcs are calculated from Equations (C.13) – (C.17)below.

$$\kappa^{(n)}(f,\gamma) = f\kappa_1 + (1-f)\kappa_2 - \frac{f(1-f)(\kappa_1-\kappa_2)^2}{(1-f)\kappa_1 + f\kappa_2 + y^{(n)}(\gamma)} \tag{C.13}$$

for $\quad n = 1, 2, 3, 4$

For this relation f, where $f \in [0,1]$ and represents the volume fraction of phase *2*, is fixed and γ varies along the real axis from [0, 1]. Functions $y^{(n)}(\gamma)$ are the previously mentioned *Y*-transforms and are defined for the bulk modulus as shown below.

$$y^{(1)} = \frac{4}{3}(\gamma\mu_1 + (1-\gamma)\mu_2) \tag{C.14}$$

$$y^{(2)}(\gamma) = \frac{4}{3}\left(\frac{\gamma}{\mu_1} + \frac{(1-\gamma)}{\mu_2}\right)^{-1} \tag{C.15}$$

$$\begin{aligned} y^{(3)}(\gamma) = \quad & -\kappa_1 + \left[\left(\frac{4\mu_1}{3} + \kappa_1\right)\left(\frac{4\mu_2}{3} + \kappa_1\right)\right] * \\ & \left[\gamma\left(\frac{4\mu_2}{3} + \kappa_1\right) + (1-\gamma)\left(\frac{4\mu_1}{3} + \kappa_1\right)\right]^{-1} \end{aligned} \tag{C.16}$$

$$\begin{aligned} y^{(4)}(\gamma) = \quad & -\kappa_2 + \left[\left(\frac{4\mu_1}{3} + \kappa_2\right)\left(\frac{4\mu_2}{3} + \kappa_2\right)\right] * \\ & \left[\gamma\left(\frac{4\mu_2}{3} + \kappa_2\right) + (1-\gamma)\left(\frac{4\mu_1}{3} + \kappa_2\right)\right]^{-1} \end{aligned} \tag{C.17}$$

Complex Shear modulus bounds

Milton and Berryman derived bounds for the complex shear modulus of a bi-phase isotropic complex composite material using the variational principles introduced by Cherkaev et Gibiansky [67]. Application of these bounds is achieved through the following algorithm. Given the complex valued bulk and shear moduli of the constituent phases, κ_1, κ_2, μ_1, μ_2, the algorithm calculates the bounds in the transformed complex plane. Note that the same notation for viscoelastic composite composition and material properties is used for these bounds as for the complex bulk modulus bounds derived by Gibiansky and Lakes [72]. The algorithm begins by

defining a range of angles which represent the phase angle of the shear modulus bounds in Y-transform space must be defined [71]:

$$\theta \in [\theta_L \quad \theta_U]$$

with (C.18)

$$\begin{cases} \theta_L = -\pi + \max\{\arg(\kappa_1), \arg(\kappa_2), \arg(\mu_1), \arg(\mu_2)\} \\ \theta_U = \min\{\arg(\kappa_1), \arg(\kappa_2), \arg(\mu_1), \arg(\mu_2)\} \end{cases}$$

Because both real and imaginary parts of the moduli are forced to be positive for the evaluation of these bounds, the values of θ_U and θ_L will always fall between 0 and π, and $-\pi$ and 0, respectively. In the Y-transform space the bounds are defined by some single valued function, $f^{+,-}$, represented in Equation (C.19) in the most general terms possible [71].

$$y = f^{+,-}(x), \quad \text{if and only if } z^{+,-} = x + iy \in \partial B^{+,-} \tag{C.19}$$

$\partial B^{+,-}$ in Equation (C.19) represents the upper and lower boundary, respectively, of the set of all admissible values of $z^{+,-}$ in complex Y-space, x and y are the real and imaginary parts of the complex shear modulus in Y-space on that boundary, and the complex number, $z^{+,-}$, is some as function of the viscoelastic composite's constituent properties and composition. The resulting bounds can now be plotted either in the Y-transformed space or complex shear modulus space via the relationships given below. First, $z^{+,-}$ must be defined in terms of the viscoelastic constituent properties and the - Y-space phase angle θ with the equations below [71]:

$$z^{-}(\theta)=\frac{\mu_i(8+9c_1)}{6(2+c_1)}+\frac{5(\kappa_j-c_1\mu_i)}{3(2+c_1)^2}$$

$$z^{+}(\theta)=\left[\frac{6(2+c_2)}{\mu_k(8+9c_2)}+\frac{60c_2}{(8+9c_2)}\left(\frac{c_2}{\kappa_l}-\frac{1}{\mu_k}\right)\right]^{-1} \tag{C.20}$$

where

$$c_1=\frac{\mathrm{Im}\left[\kappa_j e^{-i\theta}\right]}{\mathrm{Im}\left[\mu_i e^{-i\theta}\right]} \text{ and } c_2=\frac{\mathrm{Im}\left[e^{i\theta}/\mu_k\right]}{\mathrm{Im}\left[e^{i\theta}/\kappa_l\right]} \tag{C.21}$$

For z^{-}, the variables μ_i and κ_j are defined as:

$$\mu_i=\begin{cases}\mu_1, & \text{if } \mathrm{Im}\left[(\mu_1-\mu_2)e^{-i\theta}\right]\le 0\\ \mu_2, & \text{otherwise}\end{cases}$$
$$\kappa_j=\begin{cases}\kappa_1, & \text{if } \mathrm{Im}\left[(\kappa_1-\kappa_2)e^{-i\theta}\right]\le 0\\ \kappa_2, & \text{otherwise}\end{cases} \tag{C.22}$$

and, for z^{+}, the variables μ_k and κ_l are defined as:

$$\mu_k=\begin{cases}\mu_1, & \text{if } \mathrm{Im}\left[(1/\mu_1-1/\mu_2)e^{i\theta}\right]\ge 0\\ \mu_2, & \text{otherwise}\end{cases}$$
$$\kappa_l=\begin{cases}\kappa_1, & \text{if } \mathrm{Im}\left[(1/\kappa_1-1/\kappa_2)e^{i\theta}\right]\ge 0\\ \kappa_2, & \text{otherwise}\end{cases} \tag{C.23}$$

Upon implementation of this algorithm either $c_1 \rightarrow \infty$ or $c_2 \rightarrow \infty$. The former occurs when one of the shear moduli determines either of the limiting angles in Equation (C.21) and the latter occurs when one of the bulk moduli determines either of the limiting angles in the same equation. It should also be noted that the despite this problem evaluation of the above equations does not always lead to a closed space. This problem is eliminated by extending tangent lines from the limiting angles using the following relationships [71]:

$$z^{-} = z^{-}(\theta_U) + se^{i\theta_U}, \qquad z^{-} = z^{-}(\theta_L) - se^{i\theta_L} \tag{C.24}$$

$$z^{+} = \left[z^{+}(\theta_U) + se^{-i\theta_U}\right]^{-1}, \qquad z^{+} = \left[z^{+}(\theta_L) - se^{-i\theta_L}\right]^{-1} \tag{C.25}$$

The variable s in Equations (C.24) and (C.25) represents a real variable that can takes any value in the range $[0\ \infty)$ required to close the upper and lower bounds. The Y-transform space bounds given by Equations (C.18) – (C.25) can then be transformed to the complex shear modulus space using the following relationship [71].

$$\mu^{+,-} = \sum_{n=1}^{2}\left[\frac{f_n}{\mu_n + z^{+,-}}\right]^{-1} - z^{+,-} \tag{C.26}$$

In the above expression, f_n and μ_n denote the volume fraction and shear modulus of phase n.

APPENDIX D

RKU MODEL EVALUATION ALGORITHM

The effective flexural modulus relation derived by Ross *et al* [81] is given in Equations (D.1) – (D.3). In order to efficiently evaluate these implicit equations and to simplify sensitivity analyses, it is desirable to find analytical expressions for both the real and imaginary parts of the bending modulus and shear parameter denoted as: $\hat{B}^{eff,'}$, $\hat{\eta}_p$, $\hat{g}'$, and $\hat{\gamma}'$.

$$\hat{B}^{eff} = \frac{1}{6}\hat{E}h^3\left(1+6Y\left(\frac{\hat{g}}{1+2\hat{g}}\right)\right) = \hat{B}^{eff,'}\left(1+j\hat{\eta}_p\right) \tag{D.1}$$

In the above expression Y denotes the geometric parameter and $\hat{g}$ is the complex shear parameter. These parameters are calculated using Equations (D.2) and (D.3), respectively.

$$Y = (1+H)^2 \tag{D.2}$$

$$\hat{g} = \frac{1}{h^2}\left(\frac{\hat{\mu}_2}{\hat{E}H}\right)\sqrt{\frac{1}{\omega^2}\frac{\hat{B}^{eff}}{h^{tot}\rho^{eff}}} = \hat{g}'\left(1+j\hat{\gamma}\right) \tag{D.3}$$

In these equations, H is the ratio of interlayer thickness to the thickness of the top and bottom plates ($H = H_2/h$), $\hat{\mu}_2$ is the complex shear modulus of the viscoelastic interlayer where $\hat{\mu}_2 = \hat{\mu}_2'\left(1+j\hat{\beta}\right)$, $\hat{E}$ is the complex Young's modulus of the upper

and lower plates with $\hat{E} = \hat{E}'(1 + j\hat{\eta})$, ω is the frequency of interest, h^{tot} is the thickness of the sandwich plate, and ρ^{eff} is the effective sandwich plate density.

Given the material properties and sandwich plate geometry, a rough estimate of the sandwich plate effective bending modulus is: $B^{eff,i} \approx \frac{1}{6}Eh^2 = B^{eff,i}\left(1 + j\eta_p^i\right)$. This represents the resistance of the top and bottom plates to flexure about their bottom plane. Using this estimate the evaluation loop described by Equations (D.4) – (D.11) will yield the effective flexural modulus at each frequency and plate geometry of interest. Note: frequency dependence denoted by "^" is not included in these equations.

$$Y = (1 + H)^2 \tag{D.4}$$

Define:

$$x = \sqrt{1 + \sqrt{1 + \eta_p^i}} \tag{D.5}$$

$$g'^{,i} = \frac{1}{h^2}\frac{\mu_2'}{EH}\sqrt{\frac{B'^{,i}}{\omega^2 h_{tot}\rho_{eff}}}\left\{\frac{\sqrt{2}}{2}\left(\frac{1}{1+\eta^2}\right)\left[x\left(1+\eta_p^i\beta\right) - \frac{\eta_p^i}{x}(\beta - \eta)\right]\right\} \tag{D.6}$$

$$\gamma^i = \left\{x^i(\beta - \eta) + \frac{1}{x^i}\eta_p^i(1 + \eta\beta)\right\} \Big/ \left\{x^i(1 + \eta\beta) - \frac{1}{x^i}\eta_p^i(\beta - \eta)\right\} \tag{D.7}$$

$$A_r^i = \left\{g'^{,i}\left(1 + 2g'^{,i}\right) + 2g'^{,i}\left(\gamma^i\right)^2\right\} \Big/ \left\{\left(1 + 2g'^{,i}\right)^2 + \left(2g'^{,i}\gamma^i\right)^2\right\} \tag{D.8}$$

$$A_s^i = \left\{\gamma\left(1 + 2g'^{,i}\right) - 2g'^{,i}\gamma^i\right\} \Big/ \left\{\left(1 + 2g'^{,i}\right)^2 + \left(2g'^{,i}\gamma^i\right)^2\right\} \tag{D.9}$$

$$B'^{,i+1} = \frac{1}{6}E'h^3\left[1 + 6Y\left(A_r^i - \eta A_s^i\right)\right] \tag{D.10}$$

$$\eta_p^{i+1} = \left\{\eta\left(1+6A_r^iY\right)+6A_s^iY\right\}\Big/\left\{1+6Y\left(A_r^i-\eta A_s^i\right)\right\} \tag{D.11}$$

$$B^{eff,i+1} = B^{',i+1}\left(1+j\eta_p^{i+1}\right)$$

This model is well-behaved and simple root finding techniques such as bi-section reliably converge. One suggested convergence criteria is given in (D.12).

$$\varepsilon = \frac{\left\|B^{eff,i+1}\right| - \left|B^{eff,i}\right\|}{\left|B^{eff,i}\right|} \tag{D.12}$$

APPENDIX E

FORCED VIBRATION OF ELASTICALLY CONSTRAINED BEAMS AND CIRCULAR PLATES

This section finds the solution for the y-displacement for a uniform forcing pressure as a function of frequency for the general case of a beam with uniform cross-section and material properties in the x-direction and elastic boundary conditions at $x = 0$ and $x = L$. The diagram in Figure E-1 shows this case:

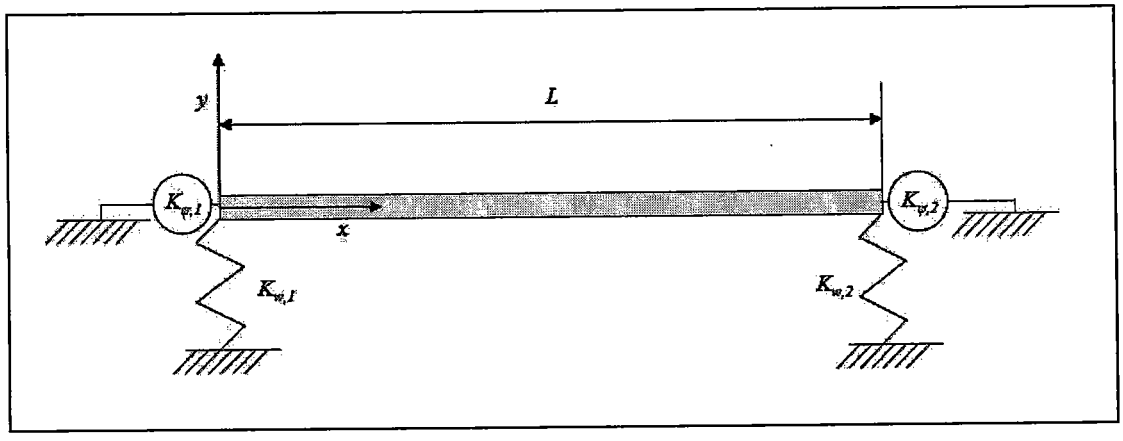

Figure E-1: Schematic of elastically constrained beam.

The well known differential equation for the space and time varying out of plane displacement, $y(x,t)$, for a vibrating beam of uniform cross section and material properties along its length, which is found via the dynamics of beam elements using the Euler-Bernoulli beam bending assumptions [169], is given below in Equation (E.1).

$$EI\frac{\partial^4 y(x,t)}{\partial x^4} + \rho bh\frac{\partial^2 y(x,t)}{\partial t^2} = p(x,t)b \qquad \text{(E.1)}$$

In this equation E is the Young's modulus of the beam, I is the beam's area moment of inertia ($I = bh^3/12$), ρ is the mass per unit volume of the beam, b is the width of the beam cross section, h is the beam's height, and $p(x,t)$ is the space and time varying forcing pressure. The first step in solving this partial differential equation to first take the Fourier transform of the out of plane displacement with respect to time, yielding the non-homogeneous ordinary differential equation below.

$$\frac{d^4\hat{y}(x)}{dx^4} - \beta^4\hat{y}(x) = \frac{\hat{p}(x)b}{EI} \tag{E.2}$$

Where $\beta^4 = \omega^2\rho bh/EI = 12\omega^2\rho/Eh^2$ and represents the flexural wave number in the beam. One arrives at the solution to this ordinary differential equation through the resolution of the homogeneous and particular parts. For simplification of the solution of the particular part, exciting pressure is assumed to be constant in space and a harmonic of the form $p(r,\theta,t) \rightarrow p(t) = p_o\cos(\omega t) = \mathrm{Re}\left[p_o e^{-i\omega t}\right]$. The resulting general solution is shown below in Equation (E.3).

$$y(x,t) = \left[b_1\cos(\beta x) + b_2\sin(\beta x) + b_3\cosh(\beta x) + b_4\sinh(\beta x) - \frac{p_o}{\omega^2\rho h}\right]\cos(\omega t) \tag{E.3}$$

The undetermined coefficients of the relationship given in Equation (E.3) are dependent on the specific boundary conditions of the beam, and are found through the resolution of the following four boundary conditions.

Resolution of System for Elastic boundary conditions

For the elastically constrained beam shown in Figure E-1, the determination of the coefficients $b_1 - b_4$ require expressions for the shear and moment at the extents of

the beam. The boundary conditions are expressed below in the four relations given in (E.4).

$$\begin{aligned} &(i)\ \ M(0,t) = -K_{\psi,1}\frac{dy(0,t)}{dx} \quad &&(iii)\ \ M(L,t) = K_{\psi,2}\frac{dy(L,t)}{dx} \\ &(ii)\ \ \mathrm{V}(0,t) = K_{w,1}y(0,t) \quad &&(iv)\ \ \mathrm{V}(L,t) = -K_{w,1}y(L,t) \end{aligned} \tag{E.4}$$

Where $K_{\psi,1,2}$ are the rotational spring coefficients on the left and right limits respectively (having the units of N·m) and $K_{w,1,2}$ are the linear displacement spring coefficients at the left and right limits respectively (having units of N/m). Approximate values for the linear and rotational springs are approximated using the conventions shown in Figure E-2. These shear and moment sign conventions for beam bending shown below in Figure E-3.

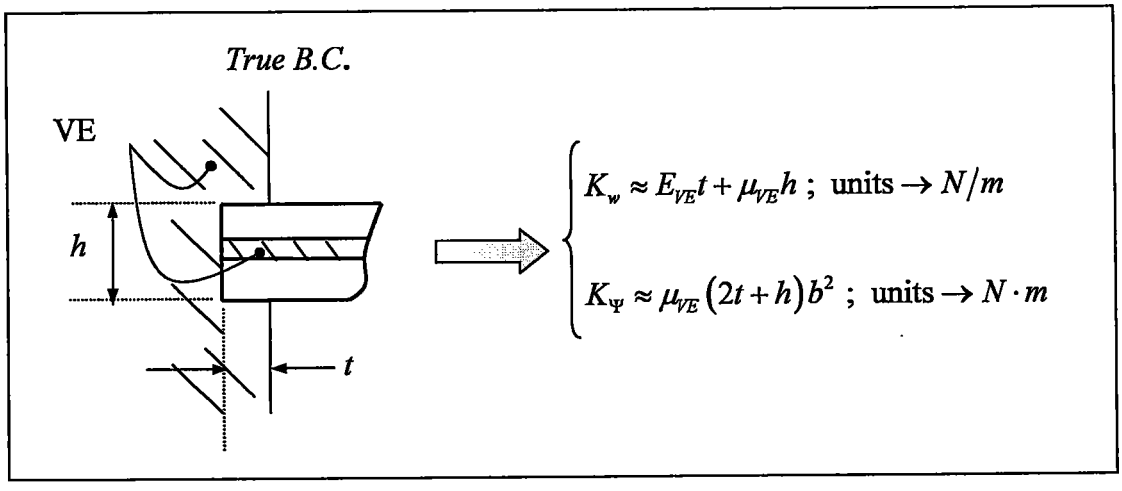

Figure E-2: Approximation of boundary conditions as linear spring and rotational spring. *b* is the beam width.

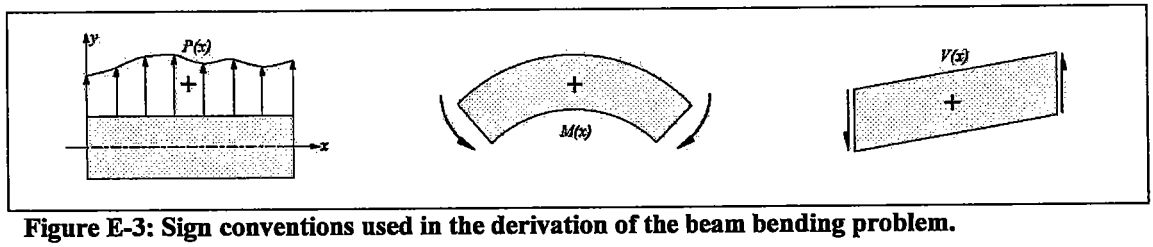

Figure E-3: Sign conventions used in the derivation of the beam bending problem.

Expressions for the shear and moment can also be derived from the deflection expression using the following [173].

$$M(x,t) = EI\frac{\partial^2 y(x,t)}{\partial x^2}$$

$$V(x,t) = \frac{\partial M(x,t)}{\partial x} = EI\frac{\partial^3 y(x,t)}{\partial x^3} \tag{E.5}$$

Inserting expression (E.3) for the out of plane displacement into the RHS of the boundary conditions given in Equations (E.4) where the LHS is determined using the relations for shear and moment given in equations (E.5) yields a system of four equations having four unknowns. These four unknowns are the undetermined coefficients $b_{1,\ldots,4}$ and can be resolved in terms of the specific beam material and geometry specified by E, ρ, b, h, and L, the elastic boundary conditions: $K_{w,1,2}$, and $K_{\psi,1,2}$, and the loading conditions p_o, and ω. Useful in this derivation are the following spatial derivations.

$$\frac{d\hat{y}(x)}{dx} = -b_1\beta\sin(\beta x) + b_2\beta\cos(\beta x) + b_3\beta\sinh(\beta x) + b_4\beta\cosh(\beta x)$$

$$\frac{d^2\hat{y}(x)}{dx^2} = -b_1\beta^2\cos(\beta x) - b_2\beta^2\sin(\beta x) + b_3\beta^2\cosh(\beta x) + b_4\beta^2\sinh(\beta x) \tag{E.6}$$

$$\frac{d^3\hat{y}(x)}{dx^3} = b_1\beta^3\sin(\beta x) - b_2\beta^3\cos(\beta x) + b_3\beta^3\sinh(\beta x) + b_4\beta^3\cosh(\beta x)$$

Using all of this information, the following system of equations results:

$$\begin{bmatrix} -EI\beta & K_{\psi,1} & EI\beta & K_{\psi,1} \\ -K_{w,1} & -EI\beta^3 & -K_{w,1} & EI\beta^3 \\ -EI\beta\cos(\beta L) + K_{\psi,2}\sin(\beta L) & -EI\beta\sin(\beta L) - K_{\psi,2}\cos(\beta L) & EI\beta\cosh(\beta L) - K_{\psi,2}\sinh(\beta L) & EI\beta\sinh(\beta L) - K_{\psi,2}\cosh(\beta L) \\ EI\beta^3\sin(\beta L) + K_{w,2}\cos(\beta L) & -EI\beta^3\cos(\beta L) + K_{w,2}\sin(\beta L) & EI\beta^3\sinh(\beta L) + K_{w,2}\cosh(\beta L) & EI\beta^3\cosh(\beta L) + K_{w,2}\sinh(\beta L) \end{bmatrix} \begin{Bmatrix} b_1 \\ b_2 \\ b_3 \\ b_4 \end{Bmatrix} = \begin{Bmatrix} 0 \\ -K_{w,1} \\ 0 \\ K_{w,2} \end{Bmatrix} \frac{p_o}{\rho h \omega^2} \tag{E.7}$$

The system is characterized as a function of frequency by solving this system of equations for the unknown coefficients ($\{b\} = [A]^{-1}\{c\}$) at each exciting frequency. Or, more simply, a search for the zeros of the characteristic equation of the *[A]* matrix yields the resonant frequencies for any system that can be simulated using the elastic boundary conditions above (which includes, cantilevered, simply-supported – simply supported, clamped – simply-supported, etc). Using this system of equations, the above model was verified by checking the first three calculated eigenvalues, βL, with those tabulated in the literature [170] which employs an Rayleigh quotient method. This is summarized in Table E-1 below.

Table E-1: First three eigenvalues taken from literature and comparison with current model.

	Cantilevered (C. – F.)		S.S. – S.S.		C. – S.S.	
	Ref. [170]	Model	Ref. [170]	Model	Ref. [170]	Model
$(\beta L)_1$	1.875	1.875	π	3.142	3.927	3.927
$(\beta L)_2$	4.694	4.694	2π	6.286	7.069	7.069
$(\beta L)_3$	7.855	7.855	3π	9.425	10.210	10.210

It is important to note that the conditions at $x = 0$ and $x = L$ required to approximate a clamped B.C. were that $K_{w,1,2} = 1 \times 10^{10}$ N/m and $K_{\psi,1,2} = 1 \times 10^{10}$ N·m, and for the simply-supported B.C., $K_{w,1,2} = 1 \times 10^{10}$ N/m and $K_{\psi,1,2} = 0$ N·m were used. As can be seen from this table, this model is easily adaptable to different boundary conditions by simply varying the values of the elastic constants at the extents of the beam. This can now be employed in order to study the effects of viscoelastic elements on the modal damping of the system. The most straightforward manner to quantify modal damping using the system response relations above is the half-power bandwidth method.

Frequency response of an elastically constrained circular plate

The general case of a plate having uniform cross-section and material properties in the r- and θ-directions and having elastic boundary conditions at $r = a$. The diagram in Figure E-4 shows this case:

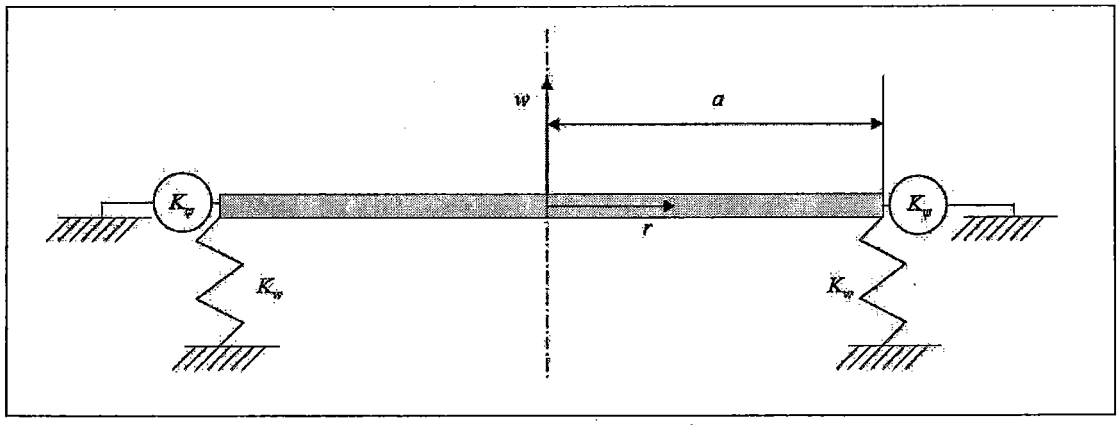

Figure E-4: Schematic of elastically constrained circular plate.

For a vibrating plate of uniform cross section and material properties in the *r*- and θ-directions, the well known differential equation for the space and time varying out of plane displacement, *w(x,t)*, which is found via the dynamics of plate elements using classic Kirchhoff plate theory [172], is given below in Equation (E.8).

$$\hat{B}\nabla^4\hat{w}(r,\theta,t)+\rho h\frac{\partial^2\hat{w}(r,\theta,t)}{\partial t^2}=\hat{p}(r,\theta,t) \tag{E.8}$$

Where B is the frequency dependent bending modulus described by the relationship $\hat{B}=\hat{E}h^3/12(1-\nu^2)$, w is the out of plane displacement, ρ is the mass per unit volume, h is the thickness of the plate, and p is the forcing pressure. Now, making the simplifying assumption that the forcing pressure is a harmonic and constant in space as shown in Equation (E.9)

$$\hat{p}(r,\theta,t)\rightarrow\hat{p}(t)=p_o\cos(\omega t)=\mathrm{Re}\left[\hat{p}_o e^{-i\omega t}\right] \tag{E.9}$$

Taking the Fourier transform with respect to time of Equation (E.8), the result is Equation (E.10).

$$\nabla^4 \hat{w}(r,\theta) - \hat{k}^4 \hat{w}(r,\theta) = \frac{\hat{p}}{\hat{B}} \tag{E.10}$$

Where $\hat{k}^4 = \rho h \omega^2 / \hat{B}$ and is the bending wave number. The general solution to this partial differential equation is done by first finding the solution to the homogeneous part as follows. The LHS of the above equation can first be factored into two Laplacian operator relations.

$$\left(\nabla^2 - \hat{k}^2\right)\left(\nabla^2 + \hat{k}^2\right)\hat{w}_h(r,\theta) = 0 \tag{E.11}$$

Now, due to symmetry, we know that $\hat{w}_h$ must be periodic in θ i.e. $\hat{w}(r,\theta=0) = \hat{w}(r,\theta=2\pi)$. Therefore, in taking a separation of variables approach such that $\hat{w}_h(r,\theta,t) = R(r)\Theta(\theta)e^{-i\omega t}$, it is apparent that $\Theta(\theta)$ must be of the form:

$$\Theta(\theta) = \begin{Bmatrix} \cos(n\theta) \\ \sin(n\theta) \end{Bmatrix} \tag{E.12}$$

Then, returning Equation (E.11), the two similar relations below will require solutions:

$$\nabla^2\{R(r)\Theta(\theta)\} - \hat{k}^2\{R(r)\Theta(\theta)\} = 0 \tag{E.13}$$

$$\nabla^2\{R(r)\Theta(\theta)\} + \hat{k}^2\{R(r)\Theta(\theta)\} = 0 \tag{E.14}$$

Now, applying the Laplacian operator in cylindrical coordinates and noting that the form of $\Theta(\theta)$ given in equation (11) requires $\Theta''(\theta) = -n^2\Theta(\theta)$, the following two equations result.

$$R''(r)+\left(\frac{1}{r}\right)R'(r)-\left(\hat{k}^2+\frac{n^2}{r^2}\right)R(r)=0 \tag{E.15}$$

$$R''(r)+\left(\frac{1}{r}\right)R'(r)+\left(\hat{k}^2-\frac{n^2}{r^2}\right)R(r)=0 \tag{E.16}$$

These are identified as equations whose solutions are respectively the regular and modified Bessel and Neuman functions of the first kind. The complete solution for the homogeneous out-of-plane displacement is therefore described with the following complete solution.

$$\hat{w}_h(r,\theta,t)=\left[\begin{Bmatrix} J_n(\hat{k}r) \\ N_n(\hat{k}r) \end{Bmatrix}+\begin{Bmatrix} I_n(\hat{k}r) \\ K_n(\hat{k}r) \end{Bmatrix}\right]\begin{Bmatrix} \cos(n\theta) \\ \sin(n\theta) \end{Bmatrix}e^{-i\omega t} \tag{E.17}$$

Now, the solution can be simplified by noting specifics of the geometry. First, due to the symmetry about the z-axis, we can discard one of the two functions in θ. Secondly, because the plate is continuous at $r = 0$, the regular and modified Neuman functions must be discarded. This leaves the following relationship for the solution to the homogeneous part of Equation (E.10).

$$\hat{w}_h(r,\theta,t)=\left\{\sum_{n=0}^{\infty}\left[A_nJ_n(\hat{k}r)+B_nI_n(\hat{k}r)\right]\cos(n\theta)\right\}e^{-i\omega t} \tag{E.18}$$

Note that there are two unknown coefficients which must be determined from the shear and moment boundary conditions imposed at $r = a$.

To find the particular solution, we must take into account that the exciting pressure is uniform in space and harmonic. This leads to the simple hypothesis that

the particular solution be simply of the form $\hat{w}_p(r,\theta,t) \rightarrow \hat{w}_p(t) = C\cos(\omega t) = \mathrm{Re}\left[Ce^{-i\omega t}\right]$. Substituting this solution into Equation (E.10), we have the following.

$$\nabla^4\left(\hat{C}e^{-i\omega t}\right) - \hat{C}\hat{k}^4 e^{-i\omega t} = \frac{p_o}{\hat{B}}e^{-i\omega t} \tag{E.19}$$

The first term on the LHS of Equation (E.19) is zero, and the remaining terms yield an expression for the constant, C, in terms of the forcing pressure. The final general solution of (E.10) is then given below.

$$\hat{w}(r,\theta,t) = \left\{\sum_{n=0}^{\infty}\left[A_n J_n\left(\hat{k}r\right) + B_n I_n\left(\hat{k}r\right)\right]\cos(n\theta) - \frac{p_o}{\rho h\omega^2}\right\}e^{-i\omega t} \tag{E.20}$$

Resolution of system for elastic boundary conditions

For the elastically constrained plate shown in Figure E-4, the determination of the coefficients A_n and B_n require expressions for the shear and moment at the extents of the plate. The boundary conditions are expressed below in relations (E.21) and (E.22).

$$\hat{M}_r(a,\theta,t) = K_\psi \frac{\partial \hat{w}(a,\theta,t)}{\partial r} \tag{E.21}$$

$$\hat{V}_r(a,\theta,t) = -K_w \hat{w}(a,\theta,t) \tag{E.22}$$

Where the linear and rotational spring values are approximated from the true boundary conditions using the convention shown in Figure E-5.

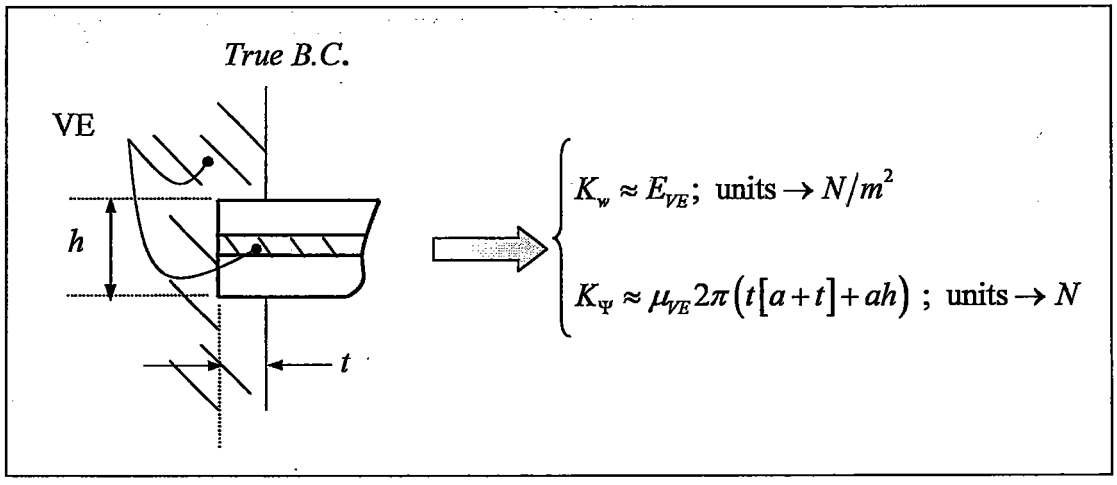

Figure E-5: Approximation of boundary conditions as linear spring and rotational spring. *a* is the plate radius, *h* is the plate thickness, and *t* is the radial thickness that the plate is embedded in the elastic boundary.

As was done in the previous example, the resolution of the problem requires expressions relating the shear and moment to the displacement equation derived above and given in Equation (E.20). The necessary classic plate relations for this problem were taken from Liessa [172] and are given below in Equations (E.23) – (E.26) describing the plate bending moments, the transverse shearing forces, and the Kelvin-Kirchhoff edge reactions in terms of the out-of-plane displacement.

$$\hat{M}_r = -\hat{B}\left[\frac{\partial^2 \hat{w}}{\partial r^2} + \nu\left(\frac{1}{r}\frac{\partial w}{\partial r} + \frac{1}{r^2}\frac{\partial^2 \hat{w}}{\partial \theta^2}\right)\right] \tag{E.23}$$

$$\hat{M}_{r\theta} = -\hat{D}(1-\nu)\frac{\partial}{\partial r}\left(\frac{1}{r}\frac{\partial \hat{w}}{\partial \theta}\right) \tag{E.24}$$

$$\hat{Q}_r = -\hat{B}\frac{\partial}{\partial r}\left(\nabla^2 \hat{w}\right) \tag{E.25}$$

$$\hat{V}_r = \hat{Q}_r + \frac{1}{r}\frac{\partial \hat{M}_{r\theta}}{\partial \theta} \tag{E.26}$$

The evaluation of the boundary conditions will lead to two simultaneous equations at $r = a$ that can then be solved for the undetermined coefficients A_n and B_n. The system of equations is given below in Equations (E.27) – (E.31).

$$\begin{bmatrix} \hat{L}_n(\hat{k}a) & \hat{M}_n(\hat{k}a) \\ \hat{R}_n(\hat{k}a) & \hat{S}_n(\hat{k}a) \end{bmatrix} \begin{Bmatrix} \hat{A}_n \\ \hat{B}_n \end{Bmatrix} = \begin{Bmatrix} 0 \\ 1 \end{Bmatrix} \frac{K_w p_o}{\hat{B}k^3 \rho h \omega^2} \tag{E.27}$$

Where the frequency dependent functions in the matrix of the LHS are specified below. Note that in the following the "^" designation has been removed for clarity, but that all entities are still dependent on the frequency:

$$L_n(ka) = J_n''(ka) + \left(\frac{\nu}{ka} + \frac{K_\psi a}{Bka}\right) J_n'(ka) - \frac{\nu n^2}{(ka)^2} J_n(ka) \tag{E.28}$$

$$M_n(ka) = I_n''(ka) + \left(\frac{\nu}{ka} + \frac{K_\psi a}{Dka}\right) I_n'(ka) - \frac{\nu n^2}{(ka)^2} I_n(ka) \tag{E.29}$$

$$R_n(ka) = J_n'''(ka) + \frac{1}{ka} J_n''(ka) - \frac{1+\nu n^2}{(ka)^2} J_n'(ka) + \left\{\frac{n^2(1+\nu)}{(ka)^3} - \frac{K_w a^3}{B(ka)^3}\right\} J_n(ka) \tag{E.30}$$

$$S_n(ka) = I_n'''(ka) + \frac{1}{ka} I_n''(ka) - \frac{1+\nu n^2}{(ka)^2} I_n'(ka) + \left\{\frac{n^2(1+\nu)}{(ka)^3} - \frac{K_w a^3}{B(ka)^3}\right\} I_n(ka) \tag{E.31}$$

Solving relationship (E.27) for A_n and B_n in terms of the forcing function and the elastic boundary conditions yields the following expressions.

$$A_n = \frac{-p_o K_w}{Bk^3 \rho h \omega^2} \frac{M_n(ka)}{\Delta(ka)} \tag{E.32}$$

$$B_n = \frac{p_o K_w}{Bk^3 \rho h \omega^2} \frac{L_n(ka)}{\Delta(ka)} \tag{E.33}$$

Where $\Delta(ka)$ is the characteristic equation of the matrix in Equation (E.27).

$$\Delta(ka) = L_n(ka) S(ka) - M_n(ka) R_n(ka) \tag{E.34}$$

From Equations (E.32) – (E.34) it is obvious that resonance is reached when the characteristic equation of the coefficient matrix of Equation (E.27) is equal to zero as would be expected. Equations (E.27) – (E.34) give a complete solution for a thin circular plate with a uniform harmonic exciting pressure and allow modeling of the forced frequency response of the system for a large variety of boundary conditions. It is important to note that for simple implementation of these relationships, it is convenient to use the following recursion relationships for the regular and modified Bessel functions taken from Blackstock [105].

$$\mathrm{X}_{n+1}(ka) = \frac{2n}{ka} \mathrm{X}_n(ka) - \mathrm{X}_{n-1}(ka) \tag{E.35}$$

$$\mathrm{X}_n'(ka) = \frac{1}{2}\left[\mathrm{X}_{n-1}(ka) - \mathrm{X}_{n+1}(ka)\right] \tag{E.36}$$

$$\frac{d}{d(ka)}\left[(ka)^n \mathrm{X}_n(ka)\right] = (ka)^n \mathrm{X}_{n-1}(ka) \tag{E.37}$$

Where $X_n(ka)$ represents either the regular or modified Bessel or Neumann function of the first kind.

To verify the formulation outlined by Equations (E.27) – (E.34), the first few eigenvalues of circular plates having different boundary conditions has been checked with models derived by Leissa [172] for the specific case given. The results are given below in Table E-2, Table E-3, and Table E-4.

Table E-2: First four eigenvalues of clamped circular plate taken from literature [172] and comparison with current model. ν = 0.30

	Plate Clamped at $r = a$, with ν = 0.30					
	n = 0		n = 1		n = 2	
$\beta^2_{n,s}$	Ref. [172]	Model	Ref. [172]	Model	Ref. [172]	Model
$\beta^2_{n,0}$	10.2	10.22	21.2	21.26	34.8	34.80
$\beta^2_{n,1}$	39.7	39.76				

Table E-3: First four eigenvalues of a simply-supported circular plate taken from literature [172] and comparison with current model. ν = 0.30

	Plate Simply-Supported at $r = a$, with ν = 0.30					
	n = 0		n = 1		n = 2	
$\beta^2_{n,s}$	Ref. [172]	Model	Ref. [172]	Model	Ref. [172]	Model
$\beta^2_{n,0}$	4.9	4.94	13.9	13.90	25.6	25.61
$\beta^2_{n,1}$	29.7	29.72				

Table E-4: First five eigenvalues of free circular plate taken from literature [172] and comparison with current model. ν = 0.25

	Free Plate with ν = 0.25							
	n = 0		n = 1		n = 2		n = 3	
$\beta^2_{n,s}$	Ref. [172]	Model	Ref. [172]	Model	Ref. [172]	Model	Ref. [172]	Model
$\beta^2_{n,0}$					5.513	4.600	12.75	12.71
$\beta^2_{n,1}$	8.892	8.884	20.41	19.97	35.28	33.60		

1Here the index s indicates the number of nodal circles on the plate (not including the boundary). It is important to note that the conditions at $r = a$ required to approximate a clamped B.C. were that $K_w = 1 \times 10^9$ N/m^2 and $K_\psi = 1 \times 10^9$ N, and for the simply-supported B.C., $K_w = 1 \times 10^9$ N/m^2 and $K_\psi = 0$ N were used. As can be seen from the

results, the model derived here yields results for three extremely different boundary conditions which are acceptably close, though not identical, to the specific individual models of Liessa [172]. The model is therefore ideal for studies on the effects of various elastic (and viscoelastic) boundary conditions on the lossy behavior of the system.

REFERENCES

1. Moore, T.C. and Lovins, A.B. *Vehicle design strategies to Meet and Exceed PNGV goals*. in *SAE Future Transportation Technology Conference*. 1995. Costa Mesa, CA: Society of Automotive Engineers.

2. Mixson, J.S. and Powell, C.A., *Review of recent research on interior noise of propeller aircraft*. Journal of Aircraft, 1985. **22**(11): p. 931-949.

3. Wilson, C.E., *Noise Control: Measurement, Analysis, and Control of Sound and Vibration*. 1994, Melbourne, FL: Krieger Publishing Co.

4. Varanasi, K.K. and Nayfeh, S.A. *Vibration damping by coupling to lossy low-wave-speed media*. in *Smart Structures and Materials: Damping and Isolation*. 2003. San Diego, CA: SPIE.

5. Lilly, J.G., *Recent advances in acoustical glazing*, in *Sound and Vibration*2004. p. 8-13.

6. Jarzynski, J., *A Review of the Mechanisms of Sound Attenuation in Materials*. Sound and Vibration Damping with Polymers, ed. R.D. Corsaro and L.H. Sperling. Vol. 424. 1990, Washington D.C.: American Chemical Society. 116-207.

7. Christensen, R.M., *Viscoelastic properties of heterogeneous media*. Journal of the Mechanics and Physics of Solids, 1969. **17**: p. 23-41.

8. Hashin, Z., *Viscoelastic behavior of heterogeneous media*. Journal of Applied Mechanics, 1965. **32**: p. 630-635.

9. Lakes, R.S., *Extreme damping in composite materials with a negative stiffness phase*. Physical Review Letters, 2001. **86**(13): p. 2897-2900.

10. Lakes, R.S., *Extreme damping in compliant composites with a negative-stiffness phase*. Philosophical Magazine Letters, 2001. **81**(2): p. 95-100.

11. Wang, Y.-C. and Lakes, R.S., *Stable extremely-high-damping discrete viscoelastic systems due to negative stiffness elements*. Applied Physics Letters, 2004. **84**(22): p. 4451-4453.

12. Lakes, R.S., et al., *Extreme damping in composite materials with negative-stiffness inclusions*. Nature, 2001. **410**: p. 565-567.

13. Wang, Y.C., Ludwigson, M., and Lakes, R., *Deformation of extreme viscoelastic metals and composites*. Materials Science and Engineering A, 2004. **370**: p. 41-49.

14. McDowell, D.L. and Story, T.L., *New Directions in Materials Design Science and Engineering (MDS&E)*, 1999, U.S. National Science Foundation Workshop Report: Georgia Institute of Technology Materials Council, Atlanta, GA.

15. Olson, G.B., *Designing a new material world*. Science, 2000. **288**(5468): p. 993-998.

16. Ungar, E.E. and Kerwin, E.M., *Loss factors of viscoelastic systems in terms of strain energy*. Journal of the Acoustical Society of America, 1962. **34**(2): p. 954-958.

17. Cherkaev, A.V., Cherkaev, E., and Slepyan, L., *Transition waves in bistable structures. I: Delocalization of dampage.* Journal of the Mechanics and Physics of Solids, 2005. **53**(2): p. 383-405.

18. Slepyan, L., Cherkaev, A.V., and Cherkaev, E., *Tansition Waves in bistable structures II: Anyalytical solution, wave speed, and energy dissipation.* Journal of the Mechanics and Physics of Solids, 2004. **53**(2): p. 407-436.

19. Ashby, M.F., *Materials Selection in Mechanical Design.* 1999, Oxford, UK: Butterworth-Heinmann.

20. Seepersad, C.C., *A Robust Topological Preliminary Design Exploration Method with Materials Design Applications, Ph.D. Dissertation,* 2004, Mechanical Engineering, Georgia Institute of Technology, p. 526.

21. Mistree, F. *Are We Designing Materials?* in *Workshop on Inverse Techniques in Materials Design.* 2004. Atlanta, GA.

22. Qian, Z., et al., *Building surrogate models based on detailed and approximate simulations.* Journal of Mechanical Design, 2005, *in Press.*

23. Cherkaoui, M., Sabar, H., and Berveiller, M., *Micromechanical Approach of the coated inclusion problem and applications to composite materials.* Journal of Engineering Materials and Technology, 1994. **116**: p. 274-278.

24. Cherkaoui, M., Sabar, H., and Berveiller, M., *Elastic composites with coated reinforcements: A micromechanical approach for nonhomothetic topology.* International Journal of Engineering Science, 1995. **33**(6): p. 829-843.

25. Böhm, H.J., *A short introduction to basic aspects of continuum micromechanics,* 1998, A Report to: The Vienna Institute of Technology: Christian Doppler Labratory for Functionally Oriented Materials: Vienna, Austria.

26. Mura, T., *Micromechanics of Defects in Solids.* 2nd ed. 1987: Kluwer Academic.

27. Christensen, R.M., *Mechanics of Composite Materials.* Reprint ed. 1991, Melbourne, FL: Krieger Publishing Company. 348.

28. Wu, T.T., *The effect of inclusion shape on the elastic moduli of a two-phase material.* International Journal of Solids and Structures, 1966. **2**: p. 1-8.

29. Lu, Y. and Liaw, P.K., *Effects of particle orientation in silicon carbide particulate reinforced aluminum matrix composite extrusions on ultrasonic velocity measurement.* Journal of Composite Materials, 1995. **29**(8): p. 1096-1116.

30. Kröner, E., *Elastic moduli of perfectly disordered composite materials.* Journal of the Mechanics and Physics of Solids, 1967. **15**(5): p. 319-329.

31. Kröner, E., *Berechnug der elastishen konstanten des vielkristalles aus den konstanten des einkristalls.* Zeitschrift fur Physik, 1958. **151**: p. 504-518.

32. Budiansky, B., *On the elastic moduli of some heterogeneous materials.* Journal of the Mechanics and Physics of Solids, 1965. **13**(4): p. 223-227.

33. Mori, T. and Tanaka, K., *Average stress in the matrix and average elastic energy of materials with misfitting inclusions.* Acta Metallurgica, 1973. **21**: p. 571-574.

34. Zeller, R. and Dederichs, P.H., *Elastic constants of polycrystals.* Physica Status Solidi B, 1973. **55**: p. 831-842.

35. Mura, T., *Displacement and plastic distortion fields produced by dislocations in anisotropic media.* Journal of Applied Mechanics, 1971. **38**: p. 865-868.

36. Willis, J.R., *Stress fields produced by dislocations in anisotropic media.* Philosophical Magazine, 1970. **21**: p. 931-949.

37. Berveiller, M., Fassi-Fehri, O., and Hihi, A., *The problem of two plastic and heterogeneous inclusions in an anisotropic medium.* International Journal of Engineering Science, 1987. **25**(6): p. 691-709.

38. Walpole, L.J., *The elastic field of an inclusion in an anisotropic medium.* Proceedings of the Royal Society of London, A, 1967. **300**: p. 270-289.

39. Hill, R., *Interfacial operators in the mechanics of composite media.* Journal of the Mechanics and Physics of Solids, 1983. **31**(4): p. 347-357.

40. Cherkaoui, M., et al., *Thermoelastic behavior of composites with coated reinforcements: a micromechanical approach and applications.* Computational Materials Science, 1996. **5**(1-3): p. 45-52.

41. Nemat-Nasser, S. and Hori, M., *Micromechanics: Overall properties of heterogeneous materials.* 1999, Amsterdam, Netherlands: Elsevier.

42. Molinari, A. and Mouden, M.E., *The problem of elastic inclusions at finite concentration.* International Journal of Solids and Structures, 1996. **33**(20-22): p. 3131-3150.

43. Hill, R., *A self-consistent mechanics of composite materials.* Journal of the Mechanics and Physics of Solids, 1965. **13**: p. 213-222.

44. Hill, R., *Continuum micro-mechanisms of elastoplastic polycrystals.* Journal of the Mechanics and Physics of Solids, 1965. **13**(2): p. 89-101.

45. Christensen, R.M. and Lo, K.H., *Solutions for effective shear properties in three phase sphere and cylinder models.* Journal of the Mechanics and Physics of Solids, 1979. **27**(4): p. 315-330.

46. Chaban, I.A., *Self-consistent field approach to calculation of the effective parameters of microinhomogeneous media.* Soviet Physical Acoustics, 1965. **10**: p. 298-304.

47. Kuster, G.T. and Toksöz, M.N., *Velocity and attenuation of seismic waves in two-phase media: Theoretical Formulation.* Geophysics, 1974. **39**: p. 587-606.

48. Gaunaurd, G.C. and Überall, H., *Theory of resonant scattering from spherical cavities in elastic and viscoelastic media.* Journal of the Acoustical Society of America, 1978. **63**(6): p. 1699-1712.

49. Gaunaurd, G.C. and Überall, H., *Resonance theory of the effective properties of perforated solids.* Journal of the Acoustical Society of America, 1982. **71**(2): p. 282-295.

50. Haberman, M., Berthelot, Y., and Cherkaoui, M., *Transmission loss of viscoelastic materials containing oriented, ellipsoidal, coated microinclusions.* Journal of the Acoustical Society of America, 2005. **118**(5): p. 2984-2992.

51. Berryman, J.G., *Long-wavelength propagation in composite elastic media II. Ellipsoidal Inclusions.* Journal of the Acoustical Society of America, 1980. **68**(6): p. 1820-1831.

52. Haberman, M., Berthelot, Y., and Cherkaoui, M., *Micromechanical modeling of particulate composites for damping of acoustic waves.* Journal of Engineering Materials and Technology, *Accepted for publication November* 2005.

53. Haberman, M., et al., *Micromechanical modeling of viscoelastic composites in the low frequency approximation.* Journal of the Acoustical Society of America, 2002. **112**(5): p. 1937-1943.

54. Cherkaoui, M.? *Ph.D. Dissertation*? Departement de Genie Mécanique, Université de Metz, p.

55. Bradshaw, R.D., Fisher, F.T., and Brinson, L.C., *Fiber waviness in nanotube-reinforced polymer composites - II: modeling via numerical approximation of the dilute strain concentration tensor.* Composites Science and Technology, 2003. **63**: p. 1705-1722.

56. Fisher, F.T., Bradshaw, R.D., and Brinson, L.C., *Fiber waviness in nanotube-reinforced polymer composites-I: Modulus predictions using effective nanotube properties.* Composites Science and Technology, 2003. **63**: p. 1689-1703.

57. Odegard, G.M., et al., *Constitutive modeling of nanotube-reinforced polymer composites.* NASA/CR-2002-211760, ICASE Report No. 2002-27, 2002.

58. Hashin, Z. and Shtrikman, S., *A variational approach to the theory of the elastic behavior of multi-phase materials.* Journal of the Mechanics and Physics of Solids, 1963. **11**: p. 127-140.

59. Walpole, L.J., *On the bounds for the overall elastic moduli of inhomogeneous systems I.* Journal of the Mechanics and Physics of Solids, 1966. **14**: p. 151-162.

60. Hill, R., *The elastic behavior of a crystalline aggregate.* Proceedings of the Physical Society, A, 1952. **65**: p. 349.

61. Hill, R., *Elastic Properties of reinforced solids: some theoretical principles.* Journal of the Mechanics and Physics of Solids, 1963. **11**: p. 357-372.

62. Hashin, Z., *Analysis of composite materials.* Journal of Applied Mechanics, 1983. **50**: p. 481-505.

63. Hashin, Z., *Complex moduli of viscoelastic composites - I: General theory and application to particulate composites.* International Journal of Solids and Structures, 1970. **6**: p. 539-552.

64. Hashin, Z., *Complex moduli of viscoelastic composites II: Fiber reinforced materials.* International Journal of Solids and Structures, 1970. **6**: p. 797-807.

65. Roscoe, R., *Bounds for real and imaginary parts of the dynamic moduli of composite viscoelastic systems.* Journal of the Mechanics and Physics of Solids, 1969. **17**: p. 17-22.

66. Roscoe, R., *Improved bounds for real and imaginary parts of complex moduli of isotropic viscoelastic composites.* Journal of the Mechanics and Physics of Solids, 1972. **20**: p. 91-99.

67. Cherkaev, A.V. and Gibiansky, L.V., *Variational principles for complex conductivity, viscoelasticity, and similar problems I: Media with complex moduli.* Journal of Mathematical Physics, 1994. **35**(1): p. 127-145.

68. Milton, G.W., *On characterizing the set of possible effective tensors of composites: The variational method and the translation method.* Communs Pure Applied Mathematics, 1990. **43**: p. 63-125.

69. Miller, M.N., *Bounds for effective electrical, thermal, and magnetic properties of heterogeneous materials.* Journal of Mathematical Physics, 1969. **10**: p. 1988-2005.

70. Gibiansky, L.V. and Milton, G.W., *On the effective viscoelastic moduli of two-phase media. I: Rigorous bounds on the complex bulk modulus.* Proceedings of the Royal Society of London, A, 1993. **440**: p. 163-188.

71. Milton, G.W. and Berryman, J.G., *On the effective viscoelastic moduli of two-phase media. II: Rigorous bounds on the complex shear modulus in three dimensions.* Proceedings of the Royal Society of London, A, 1997. **453**: p. 1849-1880.

72. Gibiansky, L.V. and Lakes, R.S., *Bounds on the complex bulk modulus of a two-phase viscoelastic composite with arbitrary volume fractions of the components.* Mechanics of Materials, 1993. **16**: p. 317-331.

73. Gibiansky, L.V. and Lakes, R.S., *Bounds on the complex bulk and shear moduli of a two-dimensional two-phase viscoelastic composite.* Mechanics of Materials, 1997. **25**: p. 79-95.

74. Gibiansky, L.V. and Torquato, S., *New method to generate three-point bounds on effective properties of composites: Application to viscoelasticity.* Journal of the Mechanics and Physics of Solids, 1998. **46**(4): p. 749-783.

75. Lakes, R.S., *Viscoelastic Solids*. Mechanical Engineering. Vol. 9. 1998, New York, NY: Taylor & Francis CRC Press. 496.

76. Baird, A.M., Kerr, F.H., and Townend, D.J., *Wave propagation in a viscoelastic medium having fluid-filled microspheres.* Journal of the Acoustical Society of America, 1999. **105**: p. 1527-1538.

77. Jones, L.E.A. and Wang, H.F., *Ultrasonic velocities in Cretaceous shales from the Williston Basin.* Geophysics, 1981. **46**: p. 288-297.

78. Hornby, B.E., Schwartz, L.M., and Hudson, J.A., *Anisotropic effective-medium modeling of the elastic properties of shales.* Geophysics, 1994. **59**(10): p. 1570-1583.

79. Ledbetter, H.M. and Datta, S.K., *Effective wave speeds in an SiC-particle reinforced Al composite.* Journal of the Acoustical Society of America, 1986. **79**(2): p. 239-248.

80. Davies, J.M., *Lightweight Sandwich Construction.* 2001: Blackwell Science, Ltd. 370.

81. Ross, D., Ungar, E.E., and Kerwin, E.M., *Damping of Plate Flexural Vibrations by Means of Viscoelastic Laminae*, in *Structural Damping - A Colloquium held at the ASME Annual Meeting*, A.S.o.M. Engineers, 1959, American Society of Mechanical Engineers: Atlantic City, New Jersy. p. 49-87.

82. Cupial, P. and Niziol, J., *Vibration and damping analysis of thee-layer composite plate with viscoelastic mid-layer.* Journal of Sound and Vibration, 1995. **183**(1): p. 99-114.

83. Daya, E.M. and Potier-Ferry, M., *A shell finite element for viscoelastically damped sandwich structures.* Revue Européene des Eléments Finis, 2002. **11**(1): p. 39-56.

84. Ditaranto, R.A. and Blasingame, W., *Composite damping of vibrating beams.* Journal of Engineering Industry, 1967. **89B**: p. 633-638.

85. Mead, D.J. and Markus, S., *The forced vibration of three-layer damped sandwich beam with arbitrary boundary conditions.* Journal of Sound and Vibration, 1969. **10**: p. 163-175.

86. Soni, M.L., *Finite element analysis of viscoelastically damped sandwich structures.* Shock and Vibration Bulletin, 1981. **55**(1): p. 97-109.

87. Yan, M.J. and McDowell, E.H., *Governing equations for vibrating constrained-layer damping sandwich plates and beams.* Journal of Applied Mechanics, 1972. **94**: p. 1041-1047.

88. Kinsler, L.E., et al., *Fundamentals of Acoustics*. 4th ed. 2000, Hoboken, NJ: John Wiley & Sons, Inc. 560.

89. Pierce, A.D., *Acoustics, and Introduction to Its Physical Principles and Applications*. 5th ed. 1991, Woodbury, NY: Acoustical Society of America.

90. Olson, G.B., *Computational Design of Hierarchically Structured Materials.* Science, 1997. **277**(5330): p. 1237-1242.

91. Seepersad, C.C., et al., *Design of Multifunctional Honeycomb Materials.* AIAA Journal, 2004. **42**(5): p. 1025-1033.

92. Smith, C.S., *A Search for Structure*. 1981, Cambridge, MA: MIT Press.

93. 3M, *3M Microspheres*, 2003.

94. Haddad, Y.M., *Viscoelasticity of Engineering Materials*. 1st ed. 1995: Chapman & Hall.

95. Ferry, J., *Viscoelastic Properties of Polymers*. 1970, New York, NY: John Wiley & Sons.

96. Christensen, R.M., *Restrictions Upon Viscoelastic Relaxation Functions and Complex Moduli.* Transactions of the Society of Rheology, 1972. **16**(4): p. 603-614.

97. Hwang, S.J. and Gibson, R.F., *The use of strain energy-based finite element techniques in the analysis of various aspects of damping of composite materials and structures.* Journal of Composite Materials, 1992. **26**(17): p. 2585-2605.

98. Hwang, S.J. and Gibson, R.F., *Micromechanical modeling of damping in discontinuous fiber composites using a strain energy/finite element approach.* Journal of Engineering Materials and Technology, 1987. **109**(1): p. 47-52.

99. Guan, H. and Gibson, R.F., *Micromechanical models for damping in woven fabric-reinforced polyer matrix composites.* Journal of Composite Materials, 2001. **35**(16): p. 1417-1434.

100. Lin, R.M. and Lim, M.K., *Complex eigensensitivity-based characterization of structures with viscoelastic damping.* Journal of the Acoustical Society of America, 1995. **100**(5): p. 3182-3191.

101. Sun, C.T. and Lu, Y.P., *Vibration Damping of Structural Elements.* 1995, Englewood Cliff, NJ: Prentice Hall.

102. Nashif, A.D., *Control of Noise and Vibration with Damping Materials,* in *Sound and Vibration Magazine*1983. p. 28-36.

103. McDaniel, J.G. and Ginsberg, J.H., *A simple test of the modal strain energy method.* Journal of the Acoustical Society of America, 1993. **93**(4): p. 2388.

104. Malvern, L.W., *Introduction to the Mechanics of a Contiuous Medium.* 1st ed. 1977, Englewood Cliff, NJ: Prentice Hall. 713.

105. Blackstock, D.T., *Fundamentals of Physical Acoustics.* 2000, New York: Wiley.

106. Achenbach, J.D., *Wave propagation in elastic solids.* 7th ed. Applied Mathematics and Mechanics, ed. J.D. Achenbach, et al. Vol. 16. 1999, Amsterdam, NL: North-Holland - Elsevier. 426.

107. LeGonidec, Y., Gibert, D., and Proust, J.-N., *Multiscale analysis of waves reflected by complex interfaces: Basic principles and experiments.* Journal of Geophysical Research - Solid Earth, 2002. **107**(B9): p. 2184.

108. Eshelby, J.D., *The determination of the elastic field of an ellipsoidal inclusion, and related problems.* Proceedings of the Royal Society of London, A, 1957. **241**: p. 376-396.

109. Song, G.Q., Sun, Q.P., and Cherkaoui, M., *Micromechanics modeling of composite with ductile matrix and SMA reinforcement.* International Journal of Solids and Structures, 2000. **37**: p. 1577-1594.

110. Voigt, W., *Uber die beziehung zurischen den beiden elastizitäts konstanten isotroper körper.* Wied. Ann, 1889. **38**.

111. Reuss, A., *Berechnung der fliessgrenze von mischkristallan auf grund der plastizitätsbedingung fur einkristall.* Z. Ang. Math. Mech., 1929. **9**.

112. Berveiller, M. and Zaoui, A. *Méthodes self-consistentes en mécanique des solides hétérogènes.* in *15e Colloque du Groupe Français de Rhéologie: Comportement Rhéologique des Matériaux.* 1980.

113. Jasiuk, I. and Kouider, M.W., *The effect of an inhomogeneous interphase on the elastic constants of transversly isotropic composites.* Mechanics of Materials, 1993. **15**(1): p. 53-63.

114. Hervé, E. and Zaoui, A., *n-layered inclusion-based micromechanical modeling.* International Journal of Engineering Science, 1993. **31**(1): p. 1-10.

115. Lipinski, P., Barhdadi, E.H., and Cherkaoui, M., *Micromechanical modeling of an arbirary ellipsoidal multi-coated inclusion.* Philosophical Magazine, 2006. **86**(10): p. 1305-1326.

116. Ying, C.F. and Truell, R., *Scattering of plane longitudinal waves by a spherical obstacle in an isotropically elastic fluid.* Journal of the Acoustical Society of America, 1956. **27**: p. 1086-1097.

117. Kligman, R.L., Madigosky, W.M., and Barlow, J.R., *Effective dynamic properties of composite viscoelastic materials.* Journal of the Acoustical Society of America, 1981. **70**(5): p. 1437-1444.

118. Kerr, F., *The scattering of a plane elastic wave by a spherical elastic inclusions.* International Journal of Engineering Science, 1992. **30**: p. 169-186.

119. Mal, A.K. and Knopoff, L., *Elastic wave velocities in two-component systems.* Journal of the Institute of Mathematics and its Applications, 1967. **3**: p. 376-387.

120. Norris, A.N., *Scattering of elastic waves by spherical inclusions with applications to low frequency wave propagation in composites.* International Journal of Engineering Science, 1986. **24**: p. 1271-1282.

121. Aggelis, D.A., Tsinopoulos, S.V., and Polyzos, D., *An iterative effective medium approximation (IEMA) for wave dispersion and attenuation predictions in particulate composites, suspensions, and emulsions.* Journal of the Acoustical Society of America, 2004. **116**(6): p. 3343-3452.

122. Berryman, J.G., *Long-wavelength propagation in composite elastic media I: Spherical Inclusions.* Journal of the Acoustical Society of America, 1980. **68**(6): p. 1809-1819.

123. Anson, L.W. and Chivers, R.C., *Ultrasonic scattering from spherical shells including viscous and thermal effects.* Journal of the Acoustical Society of America, 1993. **93**(4): p. 1687-1699.

124. Varadan, V.K., Ma, Y., and Varadan, V.V., *A multiple scattering theory for elastic wave propagation in discrete random media.* Journal of the Acoustical Society of America, 1985. **77**: p. 375-385.

125. Foldy, L.L., *The multiple scattering of waves.* Physical Review Letters, 1945. **67**: p. 107-119.

126. Lax, M., *Multiple scattering of waves.* Reviews of Modern Physics, 1952. **23**: p. 287-310.

127. Waterman, P.C. and Truell, R., *Multiple scattering of waves.* Journal of Mathematical Physics, 1961. **2**: p. 513-537.

128. Bose, S.K. and Mal, K., *Elastic waves in a fiber-reinforced composite.* Journal of the Mechanics and Physics of Solids, 1976. **22**: p. 217-229.

129. Lloyd, P. and Berry, M.V., *Wave propagation through an assembly of spheres. IV: Relations between different multiple scattering theories.* Proceedings of the Royal Society of London, A, 1967. **91**: p. 678-688.

130. Twersky, V., *On scattering of waves by random distributions. I: Free-space scatterer formalism.* Journal of Mathematical Physics, 1962. **3**(4): p. 700-724.

131. Twersky, V., *On scattering of waves by random distributions, II: Two-space scatterer formalism.* Journal of Mathematical Physics, 1962. **3**(4): p. 724-734.

132. Twersky, V., *Multiple scattering of waves and optical phenomena.* Journal of the Optical Society of America, 1962. **52**: p. 145-171.

133. Epstein, P.S. and Carhart, R.R., *The absorption of sound in suspensions and emulsions. I: Water fog in Air.* Journal of the Acoustical Society of America, 1953. **51**(5): p. 553-565.

134. Allegra, J.R. and Hawley, A., *Attenuation of sound in suspensions and emulsions, theory and experiment.* Journal of the Acoustical Society of America, 1972. **51**: p. 1545-1564.

135. Anson, L.W. and Chivers, R.C., *Ultrasonic propagation in suspensions: A comparison of a multiple scattering and effective medium approach.* Journal of the Acoustical Society of America, 1989. **85**(2): p. 535-540.

136. Yang, R.-B., *A dynamic generalized self-consistent model for wave propagation in particulate composites.* Journal of Applied Mechanics, 2003. **70**(4): p. 575-582.

137. Pahl, G. and Beitz, W., *Engineering Design: A Systematic Approach.* 2nd ed. 1996, New York, NY: Springer-Verlag.

138. Ashbey, M.F., *Materials Selection in Mechanical Design.* 1999, Oxford, UK: Butterworth-Heinmann.

139. Cohen, M., *Unknowables in the essence of materials science and engineering.* Materials Science and Engineering, 1976. **25**: p. 3-4.

140. *Innovations in Ultrahigh-Strength Steel Technology*, ed. G.B. Olson, M. Azrin, and E.S. Wright. 1990, Washington, DC: Government Printing Office (GPO).

141. Stupp, S.I. and Braun, P.V., *Molecular manipulation of microstructures: Biomaterials, ceramics, and semiconductors.* Science, 1997. **277**(f): p. 1242-1248.

142. Cochran, J.K., et al. *Low density monolithic honeycombs by thermal chemical processing.* in *4th Conference on Aerospace Materials, Processes, and Environmental Technology.* 2000. Huntsville, AL.

143. Randle, V., *http://www.swan.ac.uk/mateng/microstructure/*, 2004.

144. Piscanec, S., *http://www-g.eng.cam.ac.uk/edm/index.html*, 2004.

145. Eshelby, J.D., *Elastic Inclusions and Inhomogeneities.* Progress in Solid Mechanics. Vol. 2. 1961, Amsterdam: North-Holland. 140.

146. Lipinski, P., Barhdadi, E.H., and Cherkaoui, M., *Micromechanical modeling of an arbirary ellipsoidal multi-coated inclusion.* Philosophical Magazine, *submitted March* 2005.

147. Cherkaoui, M., *Comportement Thermoélastique Global des Composites à Renforts Enrobés: Modélisation Micromécanique et Applications, Ph.D. Dissertation*, 1995, Université de Metz, p.

148. Havriliak, S. and Negami, S., *A complex plane analysis of α-dispersions in some polymer systems.* Journal of Polymer Science: Part C, 1966. **14**: p. 99-117.

149. Weisstein, E.W., *CRC Conscise Encyclopedia of Mathematics*. 2nd ed. 2003, Boca Raton, FL: Chapman & Hall/CRC. 3252.

150. Willis, J.R., *Bounds and self-consistent estimates for the overall properties of anisotropic composites.* Journal of the Mechanics and Physics of Solids, 1977. **25**: p. 185-202.

151. Krönig, R. and Kramers, A., *Absorption and dispersion in X-Ray spectra.* Zeitschrift fur Physik, 1928. **48**: p. 174.

152. Yeh, P., *Optical Waves in Layered Media.* 1988, New York, NY: John Wiley & Sons.

153. Ferry, J.D., *Viscoelastic Properties of Polymers*. 3rd ed. 1980, New York, NY: Wiley & Sons.

154. Christensen, R.M., *A critical evalutation for a class of micromechanics models.* Journal of the Mechanics and Physics of Solids, 1990. **38**(3): p. 379-404.

155. Mavko, G., Mukerji, T., and Dvorkin, J., *The Rock Physics Handbook: Tools for Seismic Analysis of Porous Media.* 2003, New York, NY, USA: Cambridge University Press.

156. Merkel, S., et al., *Equation of state, elasticity and shear strength of pyrite under high pressure.* Physics and Chemistry of Minerals, 2002. **29**: p. 1-9.

157. Spearot, D.E., Jacob, K.I., and McDowell, D.L., *Non-local seperation constitutive laws for interfaces and their relation to nanoscale simulations.* Mechanics of Materials, 2004. **36**(9): p. 825-847.

158. Dvorak, G.J. and Srinivas, M.V., *New Estimates of Overall Properties of Heterogeneous Solids.* Journal of the Mechanics and Physics of Solids, 1999. **47**: p. 899-920.

159. Odegard, G.M., *Constitutive Modeling of Piezoelectric Polymer Composites.* Acta Materiala, 2004. **52**(18): p. 5315-5330.

160. Press, W.H., et al., *Numerical Recipes in Fortran: The Art of Scientific Computing.* 1992, New York, NY: Press Syndicate of the University of Cambridge.

161. Kerwin, E.M., *Damping of Flexural Waves by a constrained viscoelastic layer.* Journal of the Acoustical Society of America, 1959. **31**(7): p. 952-962.

162. Ungar, E.E., *Structural Damping*, in *Noise and Vibration Control Engineering: Principles and Applications*, L.L. Beranek and I.L. Vér, Editors. 1992, Wiley-Interscience: Hoboken, NJ.

163. Johnson, C.D. and Kienholz, D.A., *Finite element prediction of damping in beams with constrained viscoelastic layer.* Shock and Vibration Bulletin, 1981. **51**(1): p. 71-81.

164. Rikards, R., Chate, A., and Barkanov, E., *Finite element analysis of damping the vibrations of laminated composites.* Computers and Structures, 1993. **46**(6): p. 1005-1015.

165. Austin, E.M., *Variations on Modeling of Constrained-Layer Damping Treatments*, in *The Shock and Vibration Digest*1999. p. 275-280.

166. Buehrle, R.D., Klos, J., and Gibbs, G.P. *Damped windows for aircraft interior noise control.* in *Noise-Con 2004*. 2004. Baltimore, Maryland.

167. Haberman, M., et al. *Modèlisation des plaques sandwiches pour l'amélioration de la performance acoustique.* in *17ème Congrès Français de Mécanique*. 2005. Troyes, France.

168. Williams, D.E., *Technical Memo: Saflex 3G Master Curves*, 2001.

169. Tongue, B.H., *Principles of Vibrations*. 2nd ed. 2002, New York, NY: Oxford University Press. 518.

170. Angloulvant, F., *Caractérisation dynamique des matériaux composites: Étude de l'amortissement, Ph.D. Dissertation*, 1998, Génie Mécanique, Université de Maine, p. 243.

171. S.A.E., *J1400: Laboratory Measurement of the Airborne Sound Barrier Performance of Automotive Materials and Assemblies*, A.M. Committee, 1990, Society of Automotive Engineers International.

172. Leissa, A., *Vibration of Plates*. 1993, Melville, NY: American Institute of Physics.

173. Gere, J.M., *Mechanics of Materials*. 5th ed. 2003, Toronto, Canada: Thomson-Engineering.